Universidade de Aveiro Departamento de Engenharia Mecânica
Ano 2015

DEVARAJ
RAMASAMY

Extensão de sítios eletroquimicamente ativos em PCOSs e EOSs

Extension of Electrochemically Active Sites in SOFCs and SOECs

Universidade de Aveiro Departamento de Engenharia Mecânica
Ano 2015

DEVARAJ RAMASAMY

Extensão de sítios eletroquimicamente ativos em PCOSs e EOSs

Extension of Electrochemically Active Sites in SOFCs and SOECs

Tese apresentada à Universidade de Aveiro para cumprimento dos requisitos necessários à obtenção do grau de Doutor em Nanociências e Nanotecnologia, realizada sob a orientação científica do Doutor Duncan Paul Fagg, Investigador Principal do Departamento de Engenharia Mecânica da Universidade de Aveiro.

PTDC-CTM-105424-2008
Extension of Electrochemically Active
Sites in SOFC anodes (E-a-s-i Anode)

Dedicated to My Beloved Family

o júri

presidente

Prof. Doutor Fernando Manuel Bico Marques
Professor Catedrático, Universidade de Aveiro

Doutor Domingo Manuel Pérez Coll
Investigador Ramón y Cajal, Instituto de cerámica y Vidrio – CSIC, Madrid, Espanha

Doutora Carmen Mireya Rangel Archila
Investigadora Coordenadora, Laboratório Nacional de Energia e Geologia, Lisboa

Doutor Aleksey Yaremchenko
Investigador Principal, Centro de Investigação em Materiais Cerâmicos e Compósitos- CICECO, Universidade de Aveiro

Doutor Joao Carlos de Castro Abrantes
Superior de Tecnologia e Gestão de Viana do Castelo, Instituto Politécnico de Viana do Castelo

Doutor Duncan Paul Fagg
Investigador Principal, Universidade de Aveiro

agradecimentos

I sincerely express my deep gratitude to my research supervisor Dr. Duncan Paul Fagg for his invaluable guidance and encouragement throughout my Ph.D.

Special thanks to the late Professor Dr. José Grácio for his continuous inspiration and Professor Dr. Antonio Sousa for the incredible support, at TEMA, DEM.

A special gratitude to my friends Suraj Charan and Tao Yang for their great support all the time, I am really grateful.

I would like to thank my friends and colleagues Dr. Jose Torre, Dr. Sergey Mikhalev, Dr. Aliaksandr L. Shaula, Isabel Antunes, Narendar Nasani, Francisco A Loureiro, Dr. Pukazh Selvan, Sofia Soares. Also, I wish to thank Ricardo Beja, Carla Lopes and Dr. Budhendra Singh for their help and friendly conversations in the office.

I would like to express my gratitude to all my friends for their constant support and wishes.

Last but not least, I am extremely grateful to my beloved family who are waiting for my success. My deepest thanks are extended to my father Ramasamy Nadar and my mother Arumugakani, for their great support and prayers throughout my life. Thank you very much, my brother Kannan and sisters Tamil Selvi, Sumathi and Revathi for their support and prayers during each step. And, I extend all my sweet love to my nieces and nephews at my home. I love you all!

palavras-chave

Camada de proteção, Condutores iónicos e electrónicos mistos, PCOS, EOS, Fronteira de fase tripla, Estrutura K_2NiF_4, Resistência de polarização, Condutividade, Cinética de eléctrodos, Spin coating, Óxido de cério dopado.

resumo

As pilhas de combustível e eletrolisadores de óxido sólido (PCOSs e EOSs) têm sido promovidas a tecnologias promissoras para estabelecer o abastecimento de combustível e sua utilização futura em sistemas de energia limpa. As PCOSs são dispositivos que produzem energia elétrica pela oxidação de combustíveis como o hidrogénio ou de hidrocarbonetos de elevada eficiência. Alternativamente, as EOSs funcionam de maneira inversa, na qual podem ser gerados combustíveis sintéticos ao fornecer energia eléctrica renovável ao sistema. É, pois, devido a esta natureza semelhante e ainda que inversa, que estes dispositivos têm sido tradicionalmente construídos a partir de materiais compatíveis.

No entanto, a entrada no mercado destas tecnologias encontra-se ainda condicionada por diversos factores. Um dos mais limitantes, está associado a problemas de estabilidade química entre os constituintes da célula, que podem reduzir a longevidade a elevadas temperaturas de operação e/ou a um desempenho eletroquímico insuficiente. Normalmente, tais problemas de compatibilidade são minimizados pela introdução de uma camada de proteção muito fina constituída por um material condutor puramente iónico, na interface elétrodo/eletrólito. Deste modo, o objetivo deste trabalho é avaliar se modificando as propriedades de transporte destas camadas de proteção se pode conduzir ao aumento das propriedades de cinética do elétrodo, através da introdução de catiões polivalentes.

A introdução de condutividade eletrónica menor na superfície do electrólito foi anteriormente relatada apresentando uma melhoria muito considerável das zonas eletroquimicamente activas para a permuta de oxigénio, reduzindo, desta forma, as perdas de resistência de polarização.

Resumo (cont.)

Assim, esta dissertação tem por objetivo desenvolver este conhecimento para adaptar uma camada de proteção bifuncional que consiga evitar os problemas de interação química e ao mesmo tempo aumentar a cinética dos elétrodos.

Esta dissertação apresenta um cenário típico de um eletrólito à base de zircónia estabilizada com ítrio combinado com um elétrodo de oxigénio contendo lantanídeos. Foram investigados como materiais de proteção, os sistemas de céria dopada com gadolínio, térbio e praseodímio. As propriedades inerentes à condução eletrónica e iónica mista (MIEC) dos materiais dopados foram analisadas e agrupadas. Posteriormente, foi realizada uma análise detalhada sobre o impacto das camadas de proteção na cinética do elétrodo de oxigénio em dispositivos PCOS e EOS. Foi dada especial atenção às potenciais relações entre as propriedades de transporte da camada proteção e subsequente desempenho do elétrodo. O trabalho também avalia o desempenho eletroquímico de cátodos de K_2NiF_4 com diferentes estruturas, depositadas sobre a camada de proteção que apresentou melhor desempenho, isto é, a céria dopada com praseodímio, assim como a influência da espessura da camada e da fração de Pr presente na céria. Demonstrou-se que a introdução de camadas de proteção à base de MIECs levou a um aumento drástico no desempenho do elétrodo, nomeadamente pelos MIECs de maior condutividade ambipolar. Estas camadas de proteção utlizadas provaram ser também eficazes em manter o papel de inibidores de interactividade química na interface elétrodo/eletrólito.

.

keywords

Buffer layer, Mixed ionic electronic conductors, SOFC, SOEC, Triple phase boundary, K_2NiF_4 structure, Polarization resistance, Conductivity, Electrode kinetics, Spin coating, Doped-Cerium Oxides.

abstract

Solid oxide fuel (SOFCs) and electrolyzer (SOECs) cells have been promoted as promising technologies for the stabilization of fuel supply and usage in future green energy systems. SOFCs are devices that produce electricity by the oxidation of hydrogen or hydrocarbon fuels with high efficiency. Conversely, SOECs can offer the reverse reaction, where synthetic fuels can be generated by the input of renewable electricity. Due to this similar but inverse nature of SOFCs and SOECs, these devices have traditionally been constructed from comparable materials.

Nonetheless, several limitations have hindered the entry of SOFCs and SOECs into the marketplace. One of the most debilitating is associated with chemical interreactions between cell components that can lead to poor longevities at high working temperatures and/or depleted electrochemcial performance. Normally such interreactions are countered by the introduction of thin, purely ionic conducting, buffer layers between the electrode and electrolyte interface. The objective of this thesis is to assess if possible improvements in electrode kinetics can also be obtained by modifying the transport properties of these buffer layers by the introduction of multivalent cations.

The introduction of minor electronic conductivity in the surface of the electrolyte material has previously been shown to radically enhance the electrochemically active area for oxygen exchange, reducing polarization resistance losses. Hence, the current thesis aims to extend this knowledge to tailor a bi-functional buffer layer that can prevent chemical interreaction while also enhancing electrode kinetics.

Abstract (cont.)

The thesis selects a typical scenario of an yttria stabilized zirconia electrolyte combined with a lanthanide containing oxygen electrode. Gadolinium, terbium and praseodymium doped cerium oxide materials have been investigated as potential buffer layers. The mixed ionic electronic conducting (MIEC) properties of the doped-cerium materials have been analyzed and collated. A detailed analysis is further presented of the impact of the buffer layers on the kinetics of the oxygen electrode in SOFC and SOEC devices. Special focus is made to assess for potential links between the transport properties of the buffer layer and subsequent electrode performance. The work also evaluates the electrochemical performance of different K_2NiF_4 structure cathodes deposited onto a peak performing Pr doped-cerium buffer layer, the influence of buffer layer thickness and the Pr content of the ceria buffer layer. It is shown that dramatic increases in electrode performance can be obtained by the introduction of MIEC buffer layers, where the best performances are shown to be offered by buffer layers of highest ambipolar conductivity. These buffer layers are also shown to continue to offer the bifunctional role to protect from unwanted chemical interactions at the electrode/electrolyte interface.

INDEX

List of Figures

List of Tables

List of Abbreviations and Symbols

AC	Alternating Current
CGO	Cerium Gadolinium Oxide
CPO	Cerium Praseodymium Oxide
CTO	Cerium Terbium Oxide
EDS	Energy dispersive X-ray spectroscopy
EMF	Electromotive Force
MIEC	Mixed Ionic Electronic Conductor
OCV	Open circuit voltage
OP	Oxygen Permeability
pO_2	Oxygen partial pressure
SEM	Scanning Electron Microscopy
SOEC	Solid Oxide Electrolyser Cell
SOFC	Solid Oxide Fuel Cell
TEM	Transmission Electron Microscopy
TPB	Triple Phase Boundary
XRD	X-Ray Diffraction
YSZ	Yttria Stabilized Zirconia
D_k	diffusion coefficient
E_a	activation energy
$J(O_2)$	specific oxygen permeability
K_s	surface exchange coefficient
R_p	Polarization resistance of electrodes
δ	oxygen nonstoichiometry
σ	total conductivity
σ_{amb}	ambipolar conductivity

1. Introduction

Energy is at the center of the development of today's world, with an increasing demand directly related to population growth and increased global life quality. Crucial focus has, therefore, turned to the development of alternative energy sources to provide this energy demand in an environmentally sustainable manner. Growing concerns regarding increasing greenhouse gas emissions and diminishing fossil fuel reserves have underscored the importance of a combined approach to energy management that involves both improved fuel efficiency and a shift to carbon neutral renewable energy [1]. With respect to the former, fuel cells have been proposed to fulfill a vital role in future electrochemical power generation due to their ability to offer higher efficiencies than conventional combustion processes and to offer potentially environmental friendly and clean routes to electrical energy production. A fuel cell is an electrochemical device that directly converts chemical energy into electrical energy through chemical reaction with an oxidant. Hence, fuel cells can continuously generate electricity as long as they are supplied with sufficient fuel and oxidant for the specific electrochemical reactions to progress. Different types of fuel cells are available and are defined by the nature of their electrolyte, such as polymer electrolyte fuel cells (PEFCs), alkaline fuel cells (AFCs), phosphoric acid fuel cell (PAFCs), molten carbonate fuel cells (MCFCs) and solid oxide fuel cells (SOFCs) [2]. The nature of their electrolyte, furthermore, dictates their specific operating temperatures due to the requirement to provide fast ionic migration. The SOFC has received a large attention due to the beneficial character of a solid electrolyte that can eliminate difficulties arising from liquid electrolyte evaporation, material corrosion and delicate water management. In addition, SOFCs are especially applicable to large scale stationary power applications, given their unique combination of high efficiency, low dependence on precious metal catalysts, simplicity and fuel flexibility [3].

Hydrogen has been promoted as an attractive fuel to be utilized in fuel cells due to the potential for zero emissions and its natural abundance. Nonetheless, several debilitating limitations are associated with this concept. The storage of hydrogen is problematic due to its poor volumetric energy density and its potential explosion risk, with the pursuit of safe and alternative hydrogen storage solutions being an active and critical area of ongoing research [4]. A further complication is that, on earth, hydrogen is only found bonded with additional elements in compounds such as water or hydrocarbons. Thus, in order to use pure hydrogen as a fuel, it is necessary to firstly dissociate hydrogen from these structures [5]. Such dissociation can be performed in several ways, such as biological, electrolytic, chemical, photolytic and thermo-chemical [6]. One of most common methods of hydrogen production is that of steam reforming of natural gas. However, this process has the disadvantage that it contributes to the emission of greenhouse gases and perpetuates an undesirable dependence on fossil fuels. In contrast, a cleaner method to produce hydrogen may be that of water dissociation. Of potential methods of water dissociation, the production of hydrogen by high temperature steam electrolysis offers one of the cleanest, simple and most thermodynamically viable approaches. Electrolysis is an electrochemical process that can dissociate hydrogen from water or steam by the input of electrical energy.

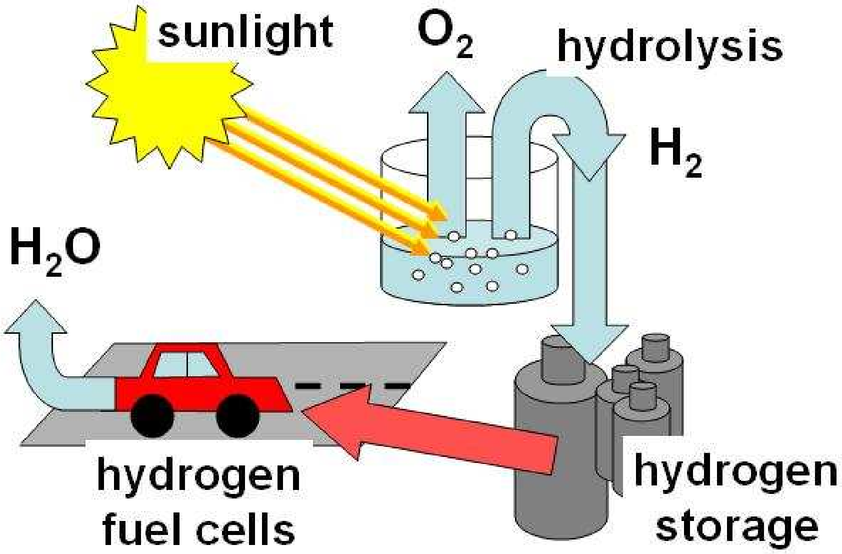

Figure 1.1. Hydrogen energy cycle.

If the rehired electrical energy demand is provided by renewable sources, this process can also offer a way to normalize the intermittency of these sources, by the formation of hydrogen during periods of peak renewable electricity production that can be stored and transported for later conversion to electrical energy in fuel cells far from the original renewable energy source (Figure 1.1) [7].

1.1. SOFCs and SOECs

A Solid Oxide Fuel Cell (SOFC) is a solid state device that can produce electricity by the electrochemical oxidation of hydrogen or hydrocarbon fuels, Figure 1.2. In contrast, a Solid Oxide Electrolyser Cell (SOEC) is a device that can electrochemically reverse this process to dissociate fully oxidized chemicals (such as CO_2 or H_2O) by the application of electrical current. In its simplest operation mode, the production of hydrogen from the dissociation of steam at elevated temperatures is shown schematically in Figure 1.2. In Figure 1.2, the electrochemical reactions performed by an SOFC and an SOEC can be noted to be simply the reverse of each other. Due to this similarity, SOFC and SOEC devices have been typically constructed from similar materials [8]. Both SOFCs and SOECs consist of three main components, a hydrogen electrode, an electrolyte and an oxygen electrode, where the electrolyte is sandwiched between the electrodes, Figure 1.2.

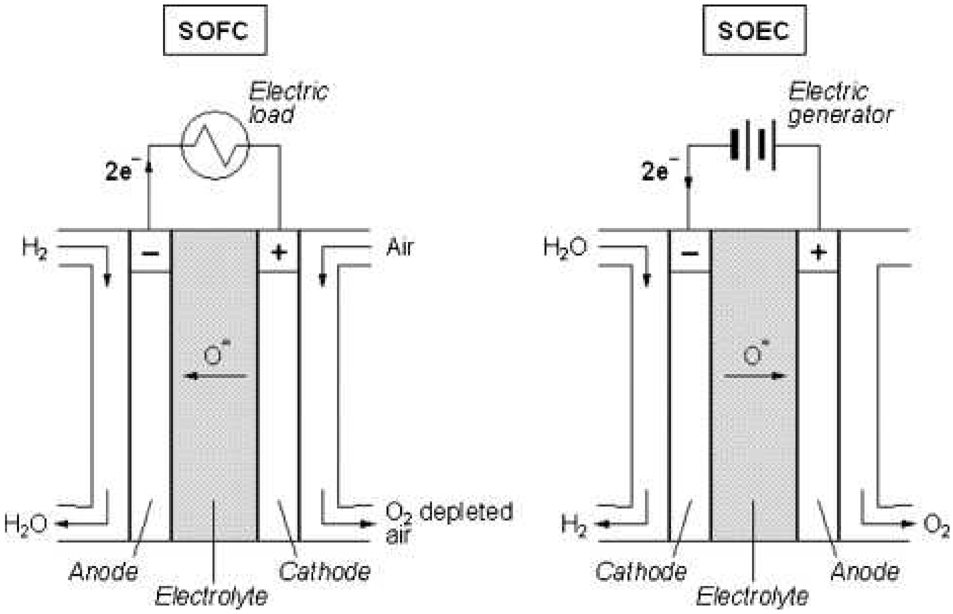

Figure 1.2. Schematic diagram of SOFCs and SOECs.

1.2 Electrochemical cell performance

In this section the basic thermodynamic and electrochemical principles behind the electrochemical cell performance is described. To understand more clearly the ideal and practical operation of fuel cells also illustrated. The influence of temperature, pressure and gas constituents on fuel cell also discussed.

At constant operating temperature and pressure, the maximum electrical work (W_{el}) attainable from fuel cell can be explained by the change in Gibbs free energy (ΔG) of the electrochemical reaction [2];

$$W_{el} = \Delta G = -nFE \qquad (1.1)$$

where n is the number of electrons participating in the reaction, F is Faraday´s constant and E is the ideal potential of the cell. Moreover, ΔG can be expressed by the following equation:

$$\Delta G = \Delta G^0 + RT\ ln \frac{f_C^c f_D^\delta}{f_A^\alpha f_B^\beta} \qquad (1.2)$$

where ΔG^0 is the Gibbs free energy change of reaction at temperature T, standard state pressure (1 atm) and f_i is the fugacity of species i. Therefore equation (1.2) can be written as:

$$E = E^0 + \frac{RT}{nF}\ ln \frac{f_C^c f_D^\delta}{f_A^\alpha f_B^\beta} \qquad (1.3)$$

Also, the above equation can written as more general form of Nernst equation,

$$E = E^0 + \frac{RT}{nF}\ ln \frac{\Pi[reactant\ fugacity]}{\Pi[product\ fugacity]} \qquad (1.4)$$

Generally, fuel cells will operate at pressures low enough that the fugacity can be approximated by the partial pressure. The Nernst potential E provide the ideal open circuit cell potential and sets the upper limit or maximum performance achievable by a fuel cell. The fuel cell reactions corresponding to the anode (equation 1.5) and cathode (equation 1.6) reactions for conventional hydrogen fuel can be expressed as follow [2]:

$$H_2 + O^{=} \rightarrow H_2O + 2e^{-} \qquad (1.5)$$

$$\frac{1}{2}O_2 + 2e^{-} \rightarrow O^{=} \qquad (1.6)$$

The Nernst equation represents the relationship between the ideal standard potential E^0 for the fuel cell reaction and the ideal equilibrium potential E at other pressures and temperatures of reactants and products. Therefore, the overall fuel cell reaction and the corresponding Nernst equation can be written as:

$$H_2 + \frac{1}{2}O_2 \rightarrow H_2O \quad (1.7)$$

$$E = E^0 + \frac{RT}{2F} \ln \frac{[P_{H_2}]}{[P_{H_2O}]} + \frac{RT}{2F} \ln [P_{O_2}^{1/2}] \quad (1.8)$$

Therefore, the cell potential increases with an increase in the partial pressure of reactants and a decrease in the partial pressure of products. For example, the Nernst equation for hydrogen oxidation, the ideal cell potential at a given temperature can be increased by operating the cell at higher reactant pressures. The variation of the fuel cell ideal potential as a function of temperature is shown in figure 1.3.

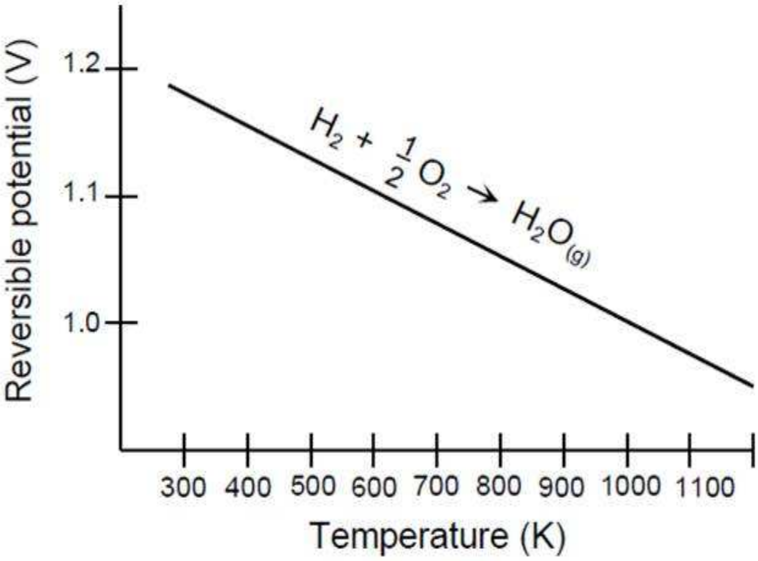

Figure 1.3. The Ideal potential as a function of temperature of an H_2/O_2 fuel cell [2].

In reality the actual performance of fuel cell is quite different from ideal one. The actual cell potential is lower than the ideal potential because of irreversible losses due to a variety of reasons. Many factors can contribute to the irreversible losses in a practical fuel cell, nonetheless, three main losses normally account for this potential difference [2].

(i) Activation losses: The activation polarization is due to slow electrochemical reactions at the electrode surface of fuel cell and it is directly related to the rate at which fuel or oxidant is oxidized or reduced. Moreover, the activation loss is directly proportional to the current flow. Therefore, the activation polarization can be expressed as,

$$\eta_{act} = \frac{RT}{\alpha nF} \ln \frac{i}{i_o} \quad (1.9)$$

Where η_{act} is the activation polarization, α the charge transfer coefficient, i the current density and i_o is the exchange current density. Activation losses are mainly dependent on material selection, microstructure, and reactant activities and weakly on current density.

(ii) Ohmic losses: The ohmic losses are caused by the resistance to the flow of ions in the electrolyte and electrodes, as well as the resistance of current collectors, interconnect and contacts. The ohmic losses vary proportionally to the increase in current density.

$$\eta_{\Omega} = iR \tag{1.10}$$

where i is the current and R is the total cell resistance. The ohmic losses depend on materials selection, stack geometry and temperature. Although, the dominant ohmic loss is mainly due to that coming from the electrolyte, which can be reduced by decreases in electrolyte thickness and the electrode separation or by enhancing the ionic conductivity of the electrolyte.

(iii) Concentration losses: Concentration losses occur over the entire range of current density and are predominant when the gas flow to the fuel cell reaction sites is hindered. The concentration polarization can be expressed as,

$$\eta_{con} = \frac{RT}{nF} ln\, 1 - \frac{i}{i_L} \tag{1.11}$$

where η_{con} is the concentration polarization and i_L is the limiting current density.

The variation between the ideal and actual performance of an electrochemical cell with respect to voltage and current is, therefore, shown in figure 1.4.

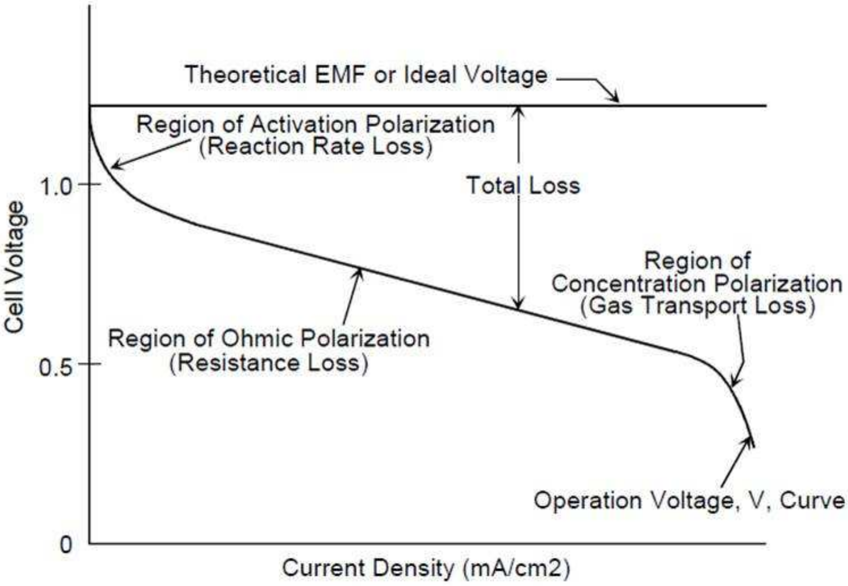

Figure 1.4. Ideal and actual performance of electrochemical cell with respect to voltage/current characteristic [2].

1.3. Component Requirements

The previous section outlined that achievement of high efficiencies in electrochemical devices is highly dependent on the ability to minimize polarization losses, being those both ohmic in nature and also those arising due to electrochemical reactions occurring at the electrodes. Realization of this goal is normally accomplished by a combination of materials tailoring and microstructural control. The main requirements include the stability of materials under oxidizing or reducing environments, chemical and mechanical compatibility with adjacent components, the formation of dense electrolytes and well bonded electrodes that are porous enough to facilitate gas transport to reaction sites whilst retaining percolation pathways.

1.3.1. Electrolyte material

The electrolyte is the defining component in electrochemical devices from which compatible electrode materials are subsequently selected. For SOFCs and SOECs the electrolyte must be thin enough to reduce ohmic losses, while being sufficiently dense to avoid gas phase diffusion through pores and to provide high ionic conduction. Based on the mobile conducting species, ceramic electrolytes are typically categorized into two distinct types (i) Oxide-ion conducting (ii) Proton conducting [9].

(i) Oxide ion conducting electrolyte:

Oxide-ion conducting electrolytes are materials that offer fast ionic motion of oxide-ion though their crystallographic structure with minimal electronic leakage. Such oxide-ion conduction is found mainly in ionic oxides with highly ordered symmetry such as the cubic perovskite structure or the cubic defect fluorite crystal structure. The most commonly known oxide-ion conducting solid electrolytes are those based on ZrO_2, CeO_2, ThO_2, Bi_2O_3 and $LaGaO_3$.

Of these, the most widely used ionic electrolyte is that of yttria stabilized zirconia (YSZ), due to its high oxide-ion conductivity and wide electrolytic domain that persists from oxidizing to very low oxygen partial pressures. This material is also very inert and offers good mechanical properties [10]. At room temperature, pure ZrO_2 has a monoclinic crystal structure that changes to tetragonal form above 1200^oC. Above 2300^oC the cubic form is obtained. These polymorphic changes of zirconia are associated with large volume changes. Such unwanted phase changes can be prevented by stabilizing the cubic phase of ZrO_2 to lower temperatures by doping with impurities such as MgO, CaO and Y_2O_3. These acceptor dopants also create oxygen vacancies as charge compensating defects that can beneficially lead to oxide-ion conduction. The fluorite structure is a face centered cubic arrangement of cations with the anions occupying all tetrahedral sites, Figure 1.5. At elevated temperatures the oxygen vacancies can migrate through the crystal structure by exchanging position with surrounding oxide-ions.

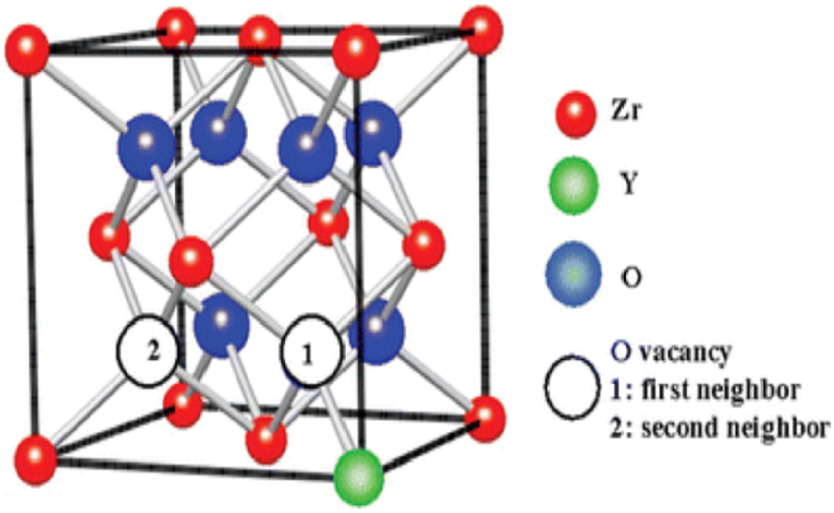

Figure 1.5. Structure of yttria-stabilized zirconia [11].

When Y_2O_3 dissolved in to ZrO_2, the defect equilibrium equation can be written by Kröger-Vink notation,

$$Y_2O_3 \leftrightarrow 2Y_{Zr}^{\prime} + V_O^{\bullet\bullet} + 3O_O^x \tag{1.12}$$

Ionic conductivity increases with increasing dopant level until a maximum is reached (at around 8 mol% Y_2O_3 at 1000ºC) from which conductivity begins to decrease due to an impaired mobility of oxygen vacancies that arises due to defect ordering. Sc-Stabilized Zirconia (ScSZr) is possible alternative for YSZ solid electrolyte due to its slightly higher ionic conductivity with similar wide electrolytic domain [12,13]. Nonetheless, a drawback of the ScSZr systems is their elevated cost.

Ceria-based solid electrolytes are useful alternatives to zirconia-based solid electrolytes due to offering a higher ionic conductivity than YSZ in the lower temperature range. However, the main disadvantage of ceria-based electrolytes is that Ce^{4+} can be partially reduced to Ce^{3+} under strongly reducing environments, limiting the electrolytic domain by an increase in electronic conductivity and also producing undesirable chemical expansion that can lead to potential mechanical failure [14,15].

The cubic phase Bi_2O_3 shows the highest ionic conductivity of all known fluorite oxide-ion conductors at high temperature. Nevertheless, pure Bi_2O_3 reverts to the monoclinic phase at lower temperature (< 777^{o}C), leading to poor conductivities. The addition of yttrium oxide or heavy-rare-earth can stabilize the Bi_2O_3 cubic phase at lower temperatures retaining high levels ionic conductivity to these conditions. Nevertheless, in spite of their high ionic conductivity, Bi_2O_3-based electrolytes are easily reduced to Bi-metal under reducing environments, limiting potential application, and leading to poor mechanical strength. A further problem of these materials is their undesirable high vapor pressures [16].

Apart from the fluorite material, the perovskite composition $La_{0.85}Sr_{0.15}Ga_{0.80}Mg_{0.20}O_{2.825}$ (LSGM) is also known to offer good ionic conductivity at intermediate temperatures [17]. Nonetheless its high reactivity with typical Ni-based electrodes to form lanthanum nicklates is one of the main disadvantages to its widespread use.

(ii) Proton conducting electrolyte:

Besides traditional oxide-ion conducting electrolytes, proton conducting ceramics can also be used as an electrolyte for SOFC and SOEC applications and are attractive for use at lower temperatures due to their higher levels of ionic conduction under these conditions. The most well-known ceramic-oxide proton-conducting protonic materials are perovskite oxides (ABO_3) with large basic A cations (e.g. Ba, Sr) and tetravalent B cations (e.g., Zr, Ce) due to their high proton conductivities. Unfortunately, due to their high basicity, the cerate materials offer poor tolerance to CO_2 and steam, rapidly decomposing to form the carbonates, $BaCO_3$, $SrCO_3$ or hydroxides at intermediate temperatures [18]. In contrast, yttrium-doped barium zirconate (BZY) offers higher stability in these conditions, while offering high bulk proton conductivity [19,20]. However, the drawbacks to the zirconate materials are their high grain boundary resistivity's coupled with poor densification and grain growth. Mixed cerate and zirconate materials, such as $Ba(Ce,Zr)_{1-x}Y_xO_{3-\delta}$ have, therefore, been suggested as a compromise solution to offer high total conductivities, and improved processing [21].

1.3.2. Electrode materials

From figure 1.2 it is clear that the nomenclature chosen to describe the electrodes in SOFC and SOEC devices is non-trivial due to their opposite directions of ionic flow. For example, in an SOFC the anode is that of the H_2/steam side, while in an SOEC the H_2/steam side represents the cathode. Vice versa, the oxygen side of an SOFC is that of the cathode, while the oxygen side of a SOEC is that of the anode. Hence, to simplify discussion in the following text the nomenclature "oxygen electrode" and "hydrogen electrode" are chosen to describe these electrodes; terms that are independent of the chosen operating regime.

(i) Hydrogen electrode:

The hydrogen electrode in SOFCs and SOECs (involving the oxidation or formation of fuels, respectively) needs to meet the following important requirements in order to ensure high cell efficiency, (i) Sufficient porosity to facilitate gas phase transport of the fuel to minimize diffusion polarization losses, (ii) Chemically stable with respect to the electrolyte and interconnect materials during cell operation, (iii) Matching thermal expansion coefficient with adjacent components, (iv) High electrocatalytic activity, (v) High wettability.

Most current hydrogen electrodes are based on Spacil's patent that suggested a fine distribution of Ni particles in an ion-conducting ceramic oxide matrix (a cermet structure) [22]. This type of cermet structure can successfully limit polarization losses by maximizing the three phase boundary length (TPB) by maximizing the interface between the ion-conducting, the electronic-conducting and the gaseous phases, Figure 1.6a.

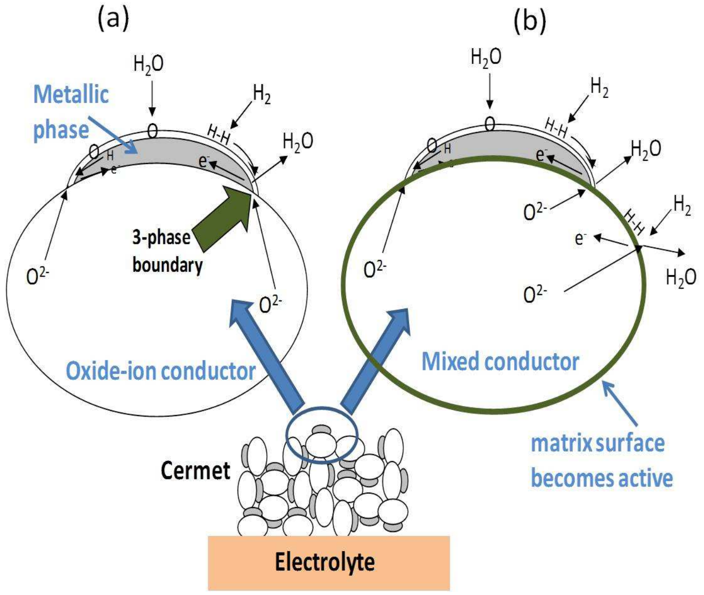

Figure 1.6. Schematic of typical cermet anode (a), showing extension of electrochemically active sites when cermet matrix phase offers mixed electronic and ionic conduction (b).

The Ni-YSZ cermet is most widely used hydrogen electrode because it fulfils most requirements of the electrode, such as high electrocatalytic activity, chemical stability and closely matching TEC with conventional YSZ electrolytes and low cost. A large body of theoretical research exists to indicate that the electrode performance of such structures should increase as the microstructure becomes finer, as long as enough porosity is maintained to prevent gas phase limitations [23]. Thus, nanoscale control of cermet electrode microstructure has recently become a hot topic [24]. Nonetheless, nanostructuration is often shown to be incompatible with the additional anode requirements of high mechanical strength, sufficient gas phase diffusion, high ionic conductivity and longevity [24]. These problems still plague cermet electrode design for these devices and continue to hinder their implementation in the marketplace. Furthermore, the Ni-YSZ cermet shows additional disadvantages like, poor redox stability [25], nickel agglomeration during long time cell operation [26] and upon operation in hydrocarbon fuels, low tolerance to sulphur and carbon deposition [27]. Authors have attempted to address these limitations by alloying of the Ni-cermet and also by alteration of the ceramic composite phase. Some examples of these modifications are given by Lee et al. [28] who studied anode-based Cu-Ni and Cu-Co bimetallics with YSZ electrolyte, showing that the use of bimetallics increased cell performance in H_2, and Martínez-Arias et al.[29] who exchanged doped-cerium based oxides for YSZ as the ceramic phase of cermet anodes for SOFC application, leading to an improvement in conductivity that was suggested to be due to an extension of electrochemically active sites when the cermet matrix phase offers mixed electronic and ionic conduction, Figure 1.6b [29].

(ii) Oxygen electrode:

The oxygen electrode in these devices must offer (i) low activation polarization losses (ii) chemical and mechanical compatibility with adjacent parts like electrolyte and interconnect (iii) chemical and structural stability under oxidizing atmospheres and (iv) sufficient porosity to facilitate gas phase transport [30].

In the past platinum and other noble materials were suggested as potential oxygen electrodes due to their high catalytic activity. This practice is still common in the case of low temperature polymer fuel cells and electrolysers where the presence of these noble metals is necessary to achieve acceptable electrocatalytic properties. In contrast, an important advantage of high temperature fuel cells and electrolysers is the enhanced electrode kinetics at higher temperatures that negate the need for expensive noble metal catalysts. Instead, perovskite-type (ABO_3) oxides have been widely suggested for the oxygen electrode in these devices, typically containing A-site cations such as La, Sr, Ca, Ba, etc., and B cations such as Ni, Fe, Co, Mn, etc.

Of these materials, lanthanum manganite ($LaMnO_{3-\delta}$) based oxides have been the most widely used oxygen electrodes, due to their high electronic conductivities under these conditions [31]. Nonetheless, lanthanum manganite has been shown to react with YSZ electrolytes to form the pyrochlore phase $La_2Zr_2O_7$ at the electrode/electrolyte interface at high operating temperatures, resulting in depleted cell performance [32]. Thus, many researchers have used Sr-doped $LaMnO_{3-\delta}$ (LSM) as an oxygen electrode. Here, Sr is compatible with the $LaMnO_{3-\delta}$ system due to a good size match between the ionic radii of Sr and La [33,34], while its substitution for La ($La_{1-x}Sr_xMnO_{3-d}$) also leads to an increased electronic conductivity up to the concentration of x = 0.5 [35]. Although the presence of Sr slightly lowers the chemical reactivity, LSM is still reported to react with the electrolyte (YSZ) at 1000°C to form poorly conducting composite layers at the electrode/electrolyte interface [36,37]. Other work on this system is given by Tatsumi et al. [38] who systematically studied $Ln_{0.6}Sr_{0.4}MnO_3$ (Ln = La, Pr, Nd, Sm, Gd, Yb, and Y) cathodes, noting that Sr-doped $PrMnO_3$ offered the superior cathode performance at intermediate temperatures. Building on this work, state of the art SOFC cathodes are suggested to be composite materials consisting of $(ZrO_2)_{0.92}(Y_2O_3)_{0.08}$, YSZ, a classical ionic conductor, and LSM [39]. Although the pure LSM phase performs adequately at 1000°C, its poor oxide ionic transport hinders electrode kinetics at lower temperatures, thereby, necessitating combination with YSZ, forming a LSM-YSZ composite, to retain acceptable electrochemical performance [40].

Mixed ionic-electronic conductive (MIEC) materials also have been studied as potential oxygen electrodes [41], as well as for many other applications such as three-way catalysts [42], oxygen sensors [43], oxygen permeation membranes [44], and ultraviolet ray absorbents [45]. In the case of practical oxygen separation membranes, the perovskite-type mixed ionic-electronic conductive materials $Ba_xSr_{1-x}Co_{0.8}Fe_{0.2}O_{3-\delta}$ (BSCF) and $La_{0.5}Sr_{0.5}Fe_{1-x}Co_xO_{3-\delta}$ (LSCF) have shown high oxygen permeability and attractive methane conversion characteristics [46,47]. However, the main disadvantages of these oxides are their high thermal and chemical expansion coefficients and low chemical stability [48,49]. Fluorite-type doped cerium oxides are another important class of MIEC materials due to their high rates of oxygen exchange, diffusion and good stability in repeated redox cycles [50–52]. In reducing conditions, ceria based oxides show extensive mixed conductivity via small polaronic hopping due to partial reduction of Ce^{4+} to Ce^{3+} [53]. Increased oxygen permeation fluxes in oxidising conditions can also be obtained by doping ceria with multivalent cations like Tb and Pr [54].

In the case of oxygen electrodes for SOFCs and SOECs, mixed conductivity is an attractive property due to enlargement of the electrochemical reaction zone, subsequently lowering polarization losses [55]. For this reason, the good mixed ionic and electronic conductors BSCF and LSCF have also shown promise as potential oxygen electrodes [56,57]. BSCF has been shown to exhibit attractive electrochemical performance as a SOFC cathode, even though, its high thermal expansion coefficient (TEC) places limits on its practical application [58,59]. Of these MIECs, LSCF has been the most widely used as an oxygen electrode due to its low cost and good performance [39,60], offering high electronic (230 S cm^{-1} at 900°C) and ionic conductivities (0.2 S cm^{-1} at 900°C) [40]. Mirroring the composite concept of YSZ-LSM, several pure ionic conductors have also been combined with LSCF to make a composite cathode, such as $(ZrO_2)_x(Sc_2O_3)_{1-x}$ (ScSZ), $La_{1-x}Sr_xGa_{1-y}Mg_yO_{3-(x+y)/2}$ (LSGM) or $(CeO_2)_{1-x}(GdO_{1.5})_x$ (CGO). These materials offer the advantage of superior ionic conductivity at intermediate temperatures (by up to an order of magnitude) in comparison to that of YSZ. Nevertheless, the chemical instability of LSGM [61] and the reported interaction of LSCF with ScSZ, to form strontium zirconate ($SrZrO_3$) and lanthanum zirconate ($La_2Zr_2O_7$), as well as high cost, make these solutions problematic [62]. Against this background, there are clear advantages for the use of CGO as the secondary cathode component, regarding its good chemical compatibility, price and high ionic conductivity. Thus, several works can be found in literature concerning the electrochemical behavior of the composite cathode material, LSCF-CGO. Murray et al.[40] assessed the electrode performance of different fractions of CGO in the LSCF-CGO composite, showing the composition LSCF-CGO (50 wt% of CGO) to offer the lowest Rp value of 0.33 Ω cm^2, at 600°C in air. In contrast, the work of Dusastre et al. [63] placed peak performance at a CGO content of 30 wt% with an improvement of 4 times in Rp over that of the pure LSCF phase. Dusastre et al. further outlined that the compositional dependence of peak performance is intricately linked to the electrode microstructure, with the CGO/LSCF ratio needed for peak electrochemical performance, increasing with decreasing porosity [63].

A further promising MIEC material for this application is that of K_2NiF_4-type structure oxides [64]. This materials type is generally described as $A_2BO_{4+\delta}$, in which perovskite ABO_3 layers alternate with rock salt AO layers in the c-direction (figure 1.7).

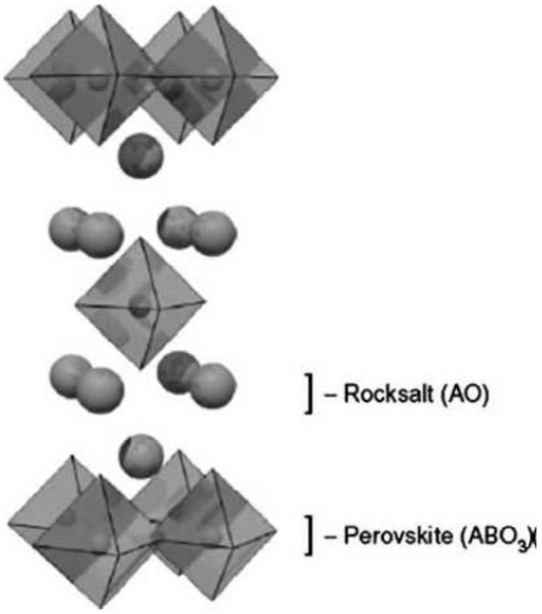

Figure 1.7. $A_2BO_{4+\delta}$ type structure showing alternating AO and ABO_3 Layers [65].

Mauvy et al. [66] studied $Ln_2NiO_{4-\delta}$ based materials (Ln = La, Nd and Pr) as potential cathodes for SOFCs, showing to exhibit good electrochemical performance with lower overpotential losses than obtainable in conventional LSM electrodes. Nonetheless, Hermandez et al. [67] systematically studied the thermal stability of $Ln_2NiO_{4-\delta}$ (Ln = La, Pr and Nd) and its chemical compatibility with YSZ and CGO electrolytes and noted chemical reaction between $La_2NiO_{4-\delta}$ electrode with YSZ and CGO electrolyte at below 900^{o}C as well as decomposition of $Pr_2NiO_{4-\delta}$ (PNO) after annealing for 24 h at 700^{o}C. The Nd analogue was shown to offer higher stabilities; nevertheless, chemical reaction with both solid electrolytes was still shown above 900ºC.

1.4. Kinetics of SOFC cathodes

Development of SOFC cathodes has been extensive of the past two decades. Nonetheless, the mechanism of the oxygen electrode reaction mechanism still remains a key issue to be understood to focus materials selection. Several parameters may impact the mechanism of oxygen reduction, where the most discussed issues have been based on clarifying whether the limiting steps to electrode kinetics are controlled by chemical or electrochemical processes [68]. Amongst those different propositions, Adler [69] is one of the early researchers who treated the SOFCs cathode reaction as a pure chemical process.

From Fig.1.8, we can see the overall cathode reaction was suggested to occur via three physically separated interfacial reactions

(1) Charge-transfer of oxygen ion vacancies across the mixed conductor/electrolyte interface.

(2) Charge-transfer of electrons across the current-collector/mixed conductor interface.

(3) Chemical exchange of oxygen at the gas/mixed-conductor interface.

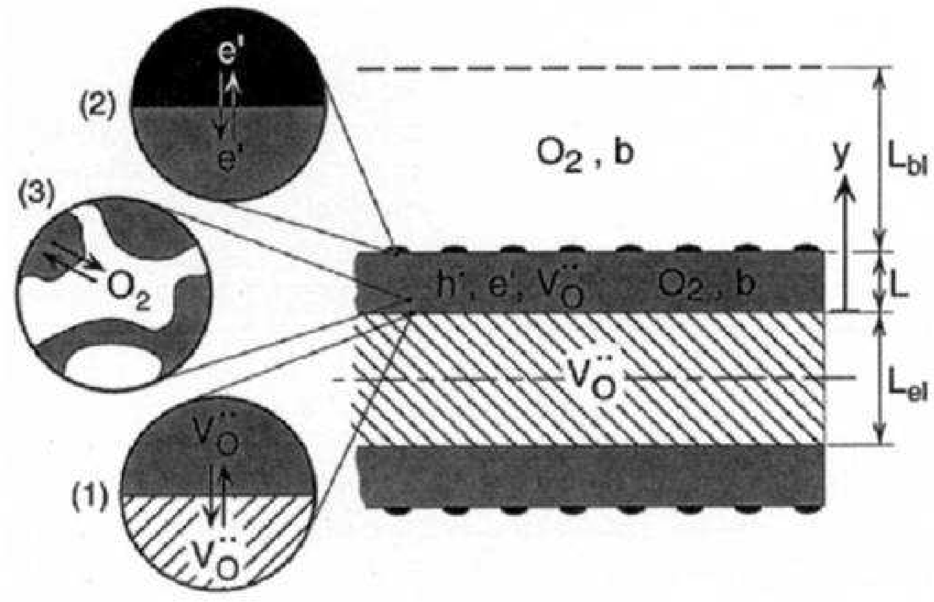

Figure 1.8. Cell geometry model by Adler [69].

For the third reaction, the gas/mixed conductor (MC) interface includes the entire internal surface area of the porous MC and also the boundary between the porous region and the gas-phase boundary layer. All these interfacial reactions are linked indirectly by diffusion of oxygen molecule inside the pores of the catalyst and in the gas-phase boundary layer and also the transport of oxide-ions and electrons (or holes) in the MC. The contribution to cathode kinetics was suggested by Adler to be predominantly limited by the diffusion of oxygen and exchange of O_2 from the gas/MC interface [69]. Thus, these non-charge-transfer steps were considered as the rate limited processes of the entire cathode reaction. In such a case, when the surface exchange and solid state diffusion were dominating, the total cell impedance would reduce to:

$$Z = R_{chem}\sqrt{\frac{1}{1 - j\omega t_{chem}}} \tag{1.13}$$

Whereas, when the gas phase diffusion became limiting, the total cell impedance would be given by:

$$Z = \frac{R_{gas}}{1 - j\omega R_{gas} C_{gas}} \tag{1.14}$$

where R_{chem} and R_{gas} are characteristic resistance, t_{chem} is a time constant and C_{gas} is the effective capacitance with gas phase diffusion polarization. The results of Adler showed that the bulk transport properties of the cathode material could quantitatively affect the electrode kinetics. Additionally, Adler also introduced the concept of a characteristic distance that corresponds to the extension of the reaction zone beyond the three-phase boundary. The chemical resistances corresponding to different characteristic distances were calculated, and the optimal extension distance was shown to be just a few microns for common perovskite MIEC electrodes [69]. Moreover, the model from Adler showed the oxygen reduction reaction including the processes of “charge-transfer” and “non-charge-transfer” could only happen on the electrode/gas interface since matter cannot pass through a truly three-phase boundary. It was noted that “charge-transfer” always occurs at a rate proportional to the current, whereas, “non-charge-transfer” processes occur at a rate independent of current because they are driven by gradients in chemical potential, only involving neutral species or neutral combinations of species [69].

In contrast to the work of Adler at open circuit conditions, Svensson et al.[70,71] introduced an overpotential bias into their simulation to express the departure of the surface exchange reaction occurring at electrolyte surface from that occurring at equilibrium. Svensson et al. built a physical model to show the possible oxygen transport pathways, where, as shown in Fig. 1.9, the first step of oxygen reduction is adsorption and desorption of neutral, monatomic oxygen at the gas/cathode and gas/electrolyte interfaces.

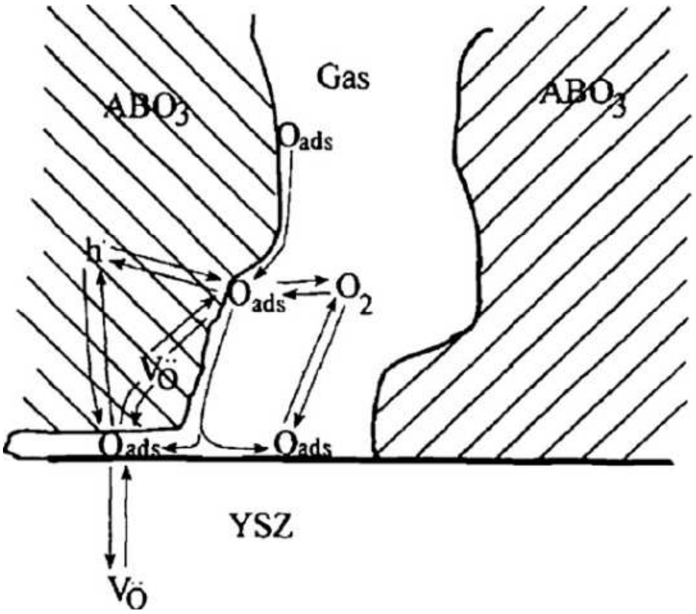

Figure 1.9. Two step reactions at cathode by Svensson´s [71].

The absorbed oxygen atom will then combine with the vacancy to form an oxide-ion. The two step reaction can be, therefore, be written as:

$$O_2(g) + 2ads \underset{K_{des}}{\overset{K_{ads}}{\rightleftarrows}} 2O_{ads} \tag{1.15}$$

$$O_{gas} + V_O^{\bullet\bullet}\, ads \underset{K_o}{\overset{K_r}{\rightleftarrows}} ads + 2h^{\bullet} + O_O^x \tag{1.16}$$

Svensson pointed out that the interface between cathode and electrolyte contained adsorbed intermediate oxygen species that would combine with the vacancies of the cathode material or the vacancies of the electrolyte material. The reaction occurring at the gas/cathode interface was considered to be chemical in nature since no interfacial charge-transfer was involved, while the one occurring at the electrolyte surface was considered as an electrochemical process [70,71].

Another influential model was developed by Liu and Winnick [72], who investigated the reactions occurring at the MIEC/gas interface. The oxygen reduction and evolution at MIEC/gas interfaces were considered electrochemical reactions where one of its charge-transfer steps is the rate limiting process to the overall reaction. These authors suggested that oxygen reduction or evolution might involve [72]:

(i) Adsorption (ad) or desorption (des) of oxygen molecules on the surface of MIEC;

(ii) Dissociation (diss) of oxygen molecules to atoms or combination (comb) of atoms to molecules;

(iii) Surface diffusion of adsorbed atoms from the adsorption sites to the active sites for electrochemical reactions or vice versa;

(iv) Charge transfer processes converting atomic or molecular species to ionic species or vice versa;

(v) Combination of oxygen ions with oxygen vacancies or removal of oxygen ions from regular lattice sites to form oxygen vacancies.

These possible reaction pathways are shown in Figure 1.10,

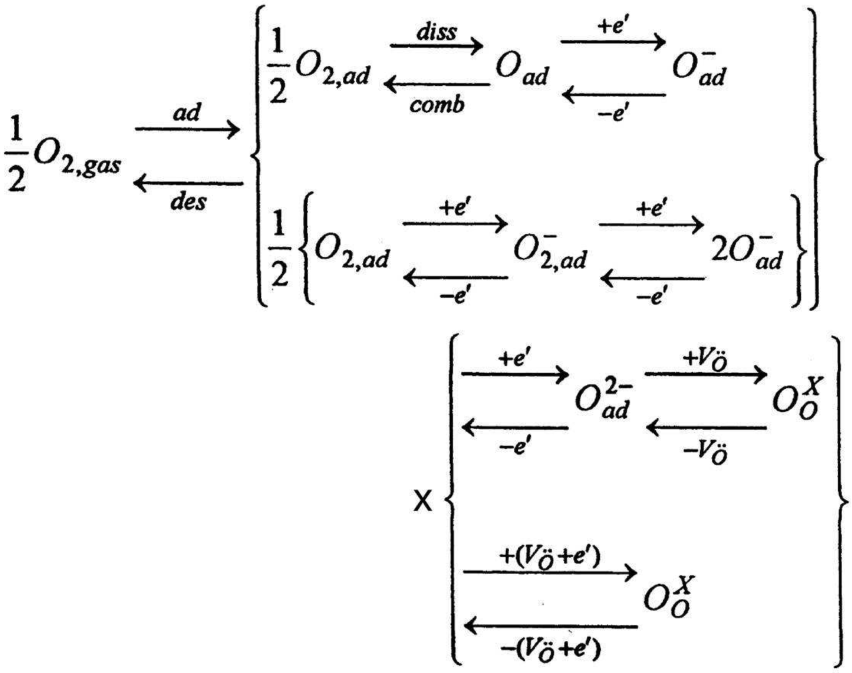

Figure 1.10. Possible reaction pathways by Liu [72].

The authors noted that, if one of the charge transfer steps influences the rate of the overall reaction, the reaction should be considered electrochemical in nature. For instance, one of the charge transfer steps in (iv) such as $O_{ad} + e' \rightarrow O^-_{ad}$ or $O^-_{ad} + e' \rightarrow O^{2-}_{ad}$ is an example of electrochemical reaction [72].

1.5. Degradation Issues

Degradation of SOFC and SOEC devices upon cell fabrication and/or during operation is a critical problem facing these high temperature applications. In general, degradation issues occur either due to interreaction of cell components, elemental migration, chemical or thermal expansion mismatch or due to cell failure under polarization. An example of typical degradation issues facing the hydrogen electrode is given by the work of Simwonis et al. [26] who studied nickel coarsening in porous Ni/8YSZ cermets upon exposure to hydrogen. These authors noted agglomeration of metallic particles after prolonged operation (4000 h) at 1000^{o}C leading to a decrease of 33% in the electrical conductivity. Supporting microstructural studies revealed that the Ni-particle size distribution had increased significantly with increasing exposure time [33]. With respect to the oxygen electrode, section 1.3 outlined several examples where chemical reaction between the electrolyte and oxygen electrode had led to impaired performance. Such interreaction between cell components and elemental migration is, unfortunately, a very common problem that has been regularly noted between many electrolyte materials (e.g. CGO, YSZ) and potential lanthanide containing electrode compositions (e.g. LnSCF, Ln_2NiO_4 etc). For example, Mitterdorfer et al [73] analysed the characterization of interface between LSM and YSZ electrolyte by high resolution transmission electron microscopy (HRTEM), electrochemical impedance spectroscopy (EIS), and atomic force microscopy (AFM), showing reaction of LSM with YSZ to form a $La_2Zr_2O_7$ (LZO) layer at the electrode/electrolyte interfaces after only a few minutes of sintering. Nonetheless, these authors noted that reduction in sintering temperature and doping with excess manganese could overcome the formation of LZO.

Ultimately, such degradation issues have slowed the entry of SOFC/SOEC devices into the market. Due to this importance, Koehler et al. [74] has summarized typical degradation issues for SOFC and SOEC components, as shown in Table 1.1.

Table 1.1. Degradation; Mode, Mechanisms and Stressors relationships [74].

Component Part	**Failure Modes** (visual symptoms)	**Degradation Mechanisms** (causes of the damage)	**Degradation Stressors** (mechanism activation agents)	**Mechanism and Stressor** (What should be measured to detect degradation?)

Electrolyte	Cracked, warpage/bowing surface fractures	High thermal stress, reduced strength of material	Thermal coefficient mismatch with another material, deleterious material interactions	Elongation/strain of materials, temperature (T) profiling, acoustic emission (AE) of Components.
	Cracked, warpage/bowing surface fractures	Mechanical stress (materials are not flat)	Pressure too high on cell stack or material too brittle	Measure force on stack and response (strain/deflection) of cell component, material properties
	Cracked, warpage/bowing surface fractures	High stress	Sealing material contacted electrolyte	Viscosity of sealing material, T profile, microstructure of electrolyte, AE of components
Cathode	Low power output, degrading performance	High activation polarization	Low O_2 activity/pressure at reaction sites.	p(O_2) at interface, gas chromatography or p(O2) sensor, impedance spectroscopy
Anode	Low power output, degrading performance	High activation polarization	Low fuel activity, low pressure at reaction site	p(fuel) at interface, GC, T profile
	Low power output, degrading performance	High concentration polarization	Fuel leaks/reactants not making it to the reaction site	Fuel utilization, differential pressure (dp) of fuel and O2 T profile, IS
Interface	Cracking.	Heat gradient. Chemical expansion mismatch	Fuel leaks/fuel took alternate path or the path is obstructed	Thermal profile across the cell, volumetric check of exhaust gasses, fuel flow balance
	Formation of resistive phases	High interfacial polarization losses	Chemical interreaction at electrolyte/electrode interface.	
Interconnect	Cracking	Heat gradient at the interface	Fuel took alternate path or the path is obstructed	Thermal profile across the cell; fuel flow balance

Although plentiful research has focused on these issues, the elimination of degradation issues remains one of the most important challenges facing these devices [75–79].

In recent years, many researchers have aimed to limit the chemical reactivity between electrode/electrolyte interfaces by introducing thin buffer layers or barrier layers. Doped-ceria materials have been most widely used materials for this task to date. Hong et al.[80] suggested that a lanthanum–doped ceria (LDC) buffer layer could effectively prevent chemical reaction between Ni-based samarium-doped ceria (SDC) composite anode and Sr-Mg-doped $LaGaO_3$ (LSGM) electrolyte, using a sintering temperature of 1350^oC. Later [81], these authors used Co as a sintering aid with LDC (LDC+Co) buffer layer in order to reduce the sintering temperature from 1350^oC to 1250^oC with a subsequently improved cell performance reported.

Besides a LDC buffer layer, Mesguich et al.[82] and Ogier et al.[83] used yttria-doped ceria (YDC) buffer layers between $Nd_2NiO_{4+\delta}$/YSZ and $Pr_2NiO_{4+\delta}$/YSZ electrode/electrolyte layers respectively. These authors observed that the buffer layer structure lead to enhanced electrochemical properties compared to the electrode without any interlayer and this was reported to be due to the absence of interfacial reaction products. Mesguich et al.[84] and Bassat et al. [85] observed that a Gd-doped ceria and undoped ceria buffer layer used between $Nd_2NiO_{4+\delta}$/YSZ and $Pr_2NiO_{4+\delta}$/YSZ electrode/electrolyte layers, respectively, showed better electrochemical performance than a YDC buffer layer.

Sm-doped ceria (SDC) has also been used as a buffer layer to prevent chemical reaction between electrode/electrolyte interface and enhance cell performance in a cell containing BSCF electrode and YSZ electrolyte [86]. More recently, Xie et al.[87] studied the electrochemical properties of a double perovskite oxide, $Sr_2Mg_{1-x}Ni_xMoO_{6-\delta}$ (SMNM), as a hydrogen electrode with a LSGM electrolyte for SOFC. Without a buffer layer the SMNM electrode slightly reacts with LSGM electrolyte. Nevertheless, using SDC buffer layer this reaction could be prevented resulting improved cell efficiency.

Of all suggested buffer layers, Gadolinium-doped ceria (CGO) has been the most widely used, with literature examples showing the successful prevention of chemical interreaction between YSZ electrolytes and a very large range of potential oxygen electrodes; Sr-doped lanthanum cobaltite (LSC), Sr-doped samarium cobaltite (SSC), LSCF, BSCF and Pr_2NiO_4 with subsequently improved electrochemical performance [88–92]. Further to these examples, Choi et al. [93] fabricated a CGO+Gd_2O_3 composite buffer layer between YSZ electrolyte and LSCF+GDC composite electrode, showing the CGO composite buffer layer to offer higher power density than a conventional CGO buffer layer. From these works, it is clear that, in general, an improved electrochemical performance can be obtained by the inclusion of a buffer layer to prevent chemical interreaction at the electrode/electrolyte interface. A notable exception to this trend, however, is the work of Hansen et al. who prepared a CGO buffer layer on a YSZ electrolyte by spin coating, followed by a LSM+YSZ composite electrode deposited by slurry spraying. These authors reported an increased polarization resistance for this buffer layer, leading to poor cell performance. Apart from ceria-based buffer layers, more recently Lei et al. [94] used a pure YSZ buffer layer between an Al_2O_3-doped-YSZ electrolyte and Ni-YSZ electrode, in order to avoid the formation of $NiAl_2O_4$.

1.6. Scope of this thesis

As noted in the previous section, the use of ceria based buffer layers is commonly found in the literature as an attempt to prevent chemical interreaction at the electrolyte/electrode interface. In the current work we show how this approach can also serve an additional role to radically reduce polarization resistance upon tailoring the transport properties of the ceria-based buffer layer.

The possibility to modify electrode kinetics by alteration of the electrolyte surface is not a new concept. Indeed, works can be found dating from the 1990s which have provided circumstantial evidence to suggest that implantation of the YSZ electrolyte surface by multivalent ions, such as Fe, could lower polarization resistance [95,96]. As stated in section 1.4, the overall reaction occurring at the oxygen electrode of a SOFC is given by the equation,

$$\frac{1}{2}O_2\,(gas) + 2e^-\,(electronic) \rightarrow O^{2-}\,(ionic) \tag{1.17}$$

whilst the reverse reaction occurs for a SOEC. From this equation, it can be seen that three phases would be necessary for the progression of the reaction, a gas phase, an electronically conducting component and an ionically conducting component. The classical three phase boundary (TPB) is, therefore, described to correspond to sites where this combination of phases is met. Equation 1.17 is usually broken down into further multistep to describe the overall polarization mechanism, with the most common steps described schematically in Fig. 1.11 (modified from the work of Fleig [97]).

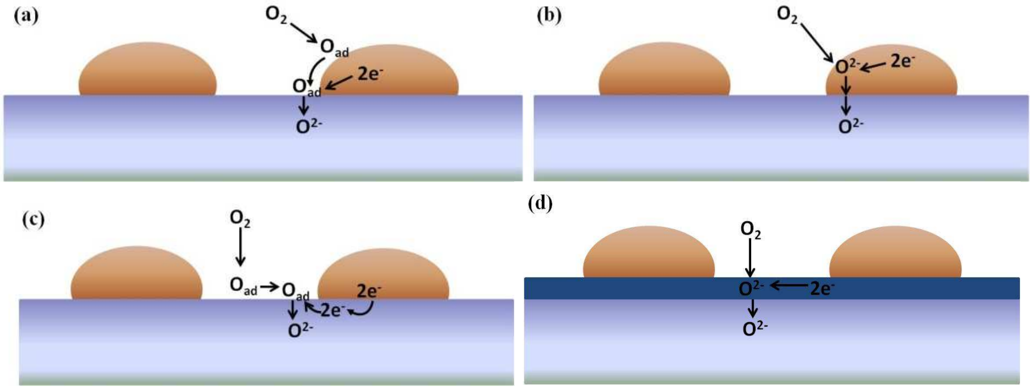

Figure 1.11. Schematics of the reaction path of the oxygen reduction and incorporation reaction a) electrode surface path b) bulk path c) electrolyte surface path and d) extended electrolyte path. i) electrode, ii) electrolyte iii) mixed conducting layer.

For a purely electronic conducting electrode, the location of the TPB would, thus, be limited closely to the interface between the electrode, the electrolyte and the gas phase, as indicated in Fig. 1.11a. The electrolyte surface path Fig. 1.11c is normally limited to a similar geometry, with charge transfer occurring close to the TPB, due to limited electronic conductivity in the electrolyte surface. The concept of these early works is that the observed improvement in electrode kinetics could be related to an enhancement on electronic conductivity in the electrode surface which would result in an extension of the electrochemically active zone beyond that of the classical three phase boundary to the entire interface, Fig. 1.11d. As an alternative theory, Adler suggested that the improved electrode kinetics of these early works could be described by an electrochemical kinetic effect that enhances the existent rate processes close to the TPB rather than extension of the mechanism to include an electrolyte surface route [98]. Adler’s reasoning was that minor impregnation of the electrolyte surface would be insufficient to transport electrons through the electrolyte to appreciable distances from the electrode, Fig. 1.11c.

Several works exist where these concepts have been extended to homogenous doping of the electrolyte with mixed valent cations, for example doping YSZ with 10 mol% of Pr, Mn, Co [99], or more recently by doping Gadolinium doped ceria (CGO) with small amounts (2 mol%) of Co [100–102]. In these works, the addition of small fractions of multivalent dopants aimed to raise the level of electronic conductivity in the electrolyte, while maintaining predominantly ionic behavior. Moreover, as the selected dopants enhance levels of p-type conductivity, the electronic enhancement would be primarily located at the side of the electrolyte exposed to the most oxidizing conditions. As such, parallels can be drawn with that generated by impregnation of the electrolyte surface in the more classical literature [95,96], with analogous improvements in the kinetics of the oxygen electrode observed in every case [99–102]. The level of enhancement in p-type conductivity by doping CGO with small fractions of cobalt has been shown to be in the region of 8-30 times that of the undoped composition in the temperature range 600-900ºC [103,104]. On the other hand, this material is still shown to be predominantly an ionic conductor with an oxide-ion transference number (to) measured in air at 650°C of around 0.98 [103,104]. An article by Fagg et al. analysed oxygen reduction kinetics using a Pt electrode of fixed geometry on Co-CGO to assess whether this small enhancement in electronic conductivity could be sufficient to extend the electrochemically active area beyond that of the classical TPB [100]. The work showed a large reduction in polarization resistance for the Co-containing electrolyte in comparison to that of a Co-free electrolyte, and this improvement in electrode performance was related to a decrease in current constriction resistance in the Co-containing case [100]. In other words, this work reinforced the theory of the classical literature, by demonstrating that an improvement in electrode kinetics could be induced by enhancements in the electronic conductivity at the electrolyte surface, which could produce an extension of the electrochemically active zone beyond that of the classical three phase boundary. In agreement, similar improvements in electrode kinetics have been reported for mixed conducting electrode materials, such as $La_2NiO_{4+\delta}$, when deposited on CGO electrolytes containing comparable concentrations of Co-additions. Identical to that noted for fixed electrode geometry, valuable improvements in electrode kinetics could be obtained in the Co-containing cases [101][102]. This suggests that useful gains in performance can be obtained by considering the transport properties of the electrode surface, even for state of the art mixed conducting electrodes that offer an additional bulk transport path for the electrochemical reaction, Fig. 1.11b.

The current work, therefore, studies if possible improvements in electrode kinetics could also be obtained by doping buffer layers with multivalent cations, in an analogous way to that achieved by the electrolyte doping methods outlined above. To fulfill this aim the first two chapters of this assess the bulk transport properties of a selection of ceria based materials and the ability to tailor these properties by compositional selection. The remaining chapters of the thesis show how the implementation of these mixed conducting materials as buffer layers between the electrolyte/electrode interface can radically improve polarization behavior.

1.7. References

[1] Z. Li, L. Chang, D. Gao, P. Liu, E.N. Pistikopoulos, Hydrogen energy systems, in: process systems engineering 5 (2011)125–157.

[2] Fuel Cell Handbook, 5th ed., EG&G Services Parsons, Inc. Science Applications Intl Corp, 2000.

[3] S.C. Singhal, Solid oxide fuel cells for power generation, Wiley Interdisciplinary Reviews: Energy and Environment 3 (2014) 179–194.

[4] N. Armaroli, V. Balzani, The hydrogen issue., ChemSusChem 4 (2011) 21–36.

[5] M.A. Laguna-Bercero, Recent advances in high temperature electrolysis using solid oxide fuel cells: A review, Journal of Power Sources 203 (2012) 4–16.

[6] A. Haryanto, S. Fernando, N. Murali, S. Adhikari, Current status of hydrogen production techniques by steam reforming of ethanol : A Review, Energy & Fuels 19 (2005) 2098–2106.

[7] C. Graves, S.D. Ebbesen, M. Mogensen, K.S. Lackner, Sustainable hydrocarbon fuels by recycling CO_2 and H_2O with renewable or nuclear energy, Renewable Sustainable Energy Review 15 (2011) 1–23.

[8] M.A. Laguna-Bercero, Recent advances in high temperature electrolysis using solid oxide fuel cells: A review, Journal of Power Sources 203 (2012) 4–16.

[9] L. Malavasi, C.A.J. Fisher, M.S. Islam, Oxide-ion and proton conducting electrolyte materials for clean energy applications: structural and mechanistic features., Chemical Society Reviews 39 (2010) 4370–4387.

[10] S.C. Singhal, Advances in solid oxide fuel cell technology, 135 (2000) 305–313.

[11] J. Caputo, C.-C. Chao, Z. Huang, Oxygen ion diffusion in Yttria-stabilized Zirconia, Introduction to molecular simulation; Final report (2007)1–17.

[12] D. Lee, W. Kim, S. Choi, J. Kim, H. Lee, J. Lee, Characterization of ZrO co-doped with ScO and CeO electrolyte for the application of intermediate temperature SOFCs, Solid State Ionics 176 (2005) 33–39.

[13] H. Huang, C.-H. Hsieh, N. Kim, J. Stebbins, F. Prinz, Structure, local environment, and ionic conduction in scandia stabilized zirconia, Solid State Ionics 179 (2008) 1442–1445.

[14] S.R. Bishop, H.L. Tuller, Y. Kuru, B. Yildiz, Chemical expansion of nonstoichiometric $Pr_{0.1}Ce_{0.9}O_{2-\delta}$: Correlation with defect equilibrium model, Journal of the European Ceramic Society 31 (2011) 2351–2356.

[15] S.R. Bishop, Chemical expansion of solid oxide fuel cell materials: A brief overview, Acta Mechanica Sinica 29 (2013) 312–317.

[16] L.E. A. Karl Gschneidner, Handbook on the Physics and Chemistry of Rare Earths, Volume 28, Elsevier, 2000.

[17] L. Cong, T. He, Y. Ji, P. Guan, Y. Huang, W. Su, Synthesis and characterization of IT-electrolyte with perovskite structure $La_{0.85}Sr_{0.15}Ga_{0.80}Mg_{0.20}O_{2.825}$ by glycine–nitrate combustion method, Journal of Alloys and Compounds 348 (2003) 325–331.

[18] M.J. Scholten, J. Schoonman, Synthesis of strontium and bariium cerate and their reaction with carbon dioxide, Solid State Ionics 61 (1993) 83–91.

[19] J. Li, J.-L. Luo, K.T. Chuang, A.R. Sanger, Chemical stability of Y-doped $Ba(Ce,Zr)O_3$ perovskites in H_2S-containing H_2, Electrochimica Acta 53 (2008) 3701–3707.

[20] E. Fabbri, D. Pergolesi, S. Licoccia, E. Traversa, Exploring highly Yttrium doped Barium Zirconate proton conductor electrolytes for application in intermediate temperature solid oxide fuel cells (IT-SOFCs), in: ECS Transactions 25 (2009) 1745–1752.

[21] E. Fabbri, A. Depifanio, E. Dibartolomeo, S. Licoccia, E. Traversa, Tailoring the chemical stability of $Ba(Ce_{0.8-x}Zr_x)Y_{0.2}O_{3-\delta}$ protonic conductors for intermediate temperature solid oxide fuel cells (IT-SOFCs), Solid State Ionics 179 (2008) 558–564.

[22] H.S. Spacil, U.S:Patent 3, (1970) 809.

[23] C.W. Tanner, The effect of porous composite electrode structure on solid oxide fuel cell performance, Journal of The Electrochemical Society 144 (1997) 21–30.

[24] R.J. Gorte, J.M. Vohs, Nanostructured anodes for solid oxide fuel cells, Current Opinion in Colloid & Interface Science 14 (2009) 236–244.

[25] Y. Zhang, B. Liu, B. Tu, Y. Dong, M. Cheng, Redox cycling of Ni–YSZ anode investigated by TPR technique, Solid State Ionics 176 (2005) 2193–2199.

[26] H. Tagawa, D. Simwonis, F. Tietz, D. Stover, Nickel coarsening in annealed Ni/8YSZ anode substrates for solid oxide fuel cells, Solid State Ionics 132 (2000) 241–251.

[27] Y. Matsuzaki, I. Yasuda, The poisoning effect of sulfur-containing impurity gas on a SOFC anode: Part I. Dependence on temperature, time, and impurity concentration, Solid State Ionics 132 (2000) 261–269.

[28] S.-I. Lee, J.M. Vohs, R.J. Gorte, A study of SOFC anodes based on Cu-Ni and Cu-Co bimetallics in CeO_2-YSZ, Journal of The Electrochemical Society 151 (2004) A1319–A1323.

[29] A. Martínez-Arias, A.B. Hungría, M. Fernández-García, A. Iglesias-Juez, J.C. Conesa, G.C. Mather, et al., Cerium–terbium mixed oxides as potential materials for anodes in solid oxide fuel cells, Journal of Power Sources 151 (2005) 43–51.

[30] Fuel Cell Handbook, 7th ed., EG&G Technical Services, Inc., 2004.

[31] C. Sun, R. Hui, J. Roller, Cathode materials for solid oxide fuel cells: a review, Journal of Solid State Electrochemistry 14 (2009) 1125–1144.

[32] S.P. Jiang, J.G. Love, J.P. Zhang, M. Hoang, Y. Ramprakash, A.E. Hughes, The electrochemical performance of LSM/zirconia – yttria interface as a function of a-site non-stoichiometry and cathodic current treatment, Solid State Ionics 121 (1999) 1–10.

[33] A. Princivalle, E. Djurado, Nanostructured LSM/YSZ composite cathodes for IT-SOFC: A comprehensive microstructural study by electrostatic spray deposition, Solid State Ionics 179 (2008) 1921–1928.

[34] R. Tian, J. Fan, Y. Liu, C. Xia, Low-temperature solid oxide fuel cells with $La_{1-x}Sr_xMnO_3$ as the cathodes, Journal of Power Sources 185 (2008) 1247–1251.

[35] J. Vanroosmalen, J. Huijsmans, L. Plomp, Electrical conductivity in $La_{1-x}Sr_xMnO_{3+\delta}$, Solid State Ionics 66 (1993) 279–284.

[36] M.J.L. Ostergard, C. Clausen, C. Bagger, M. Mogensen, Manganite-Zirconia composite cathodes SOFC:Influence of structure and composition, Electrochimica Acta 40 (1995) 1971–1981.

[37] M. Chen, Y.-L. Liu, A. Hagen, P. V. Hendriksen, F.W. Poulsen, LSM–YSZ reactions in different atmospheres, Fuel Cells 9 (2009) 833–840.

[38] T. Ishiham, T. Kudo, H. Matsuda, Y. Takita, Doped perovskite oxide, $PrMnO_3$, as a new cathode for solid-oxide fuel cells that decreases the operating temperature, Journal of the American Ceramic Society 77 (1994) 1682–1684.

[39] C. Sun, R. Hui, J. Roller, Cathode materials for solid oxide fuel cells: a review, Journal of Solid State Electrochemistry 14 (2009) 1125–1144.

[40] E.P. Murray, M.J. Sever, S.A. Barnett, Electrochemical performance of (La, Sr) (Co, Fe)O_3–(Ce, Gd)O_3 composite cathodes, Solid State Ionics 148 (2002) 27–34.

[41] J.M. Serra, V.B. Vert, O. Büchler, W.A. Meulenberg, H.P. Buchkremer, IT-SOFC supported on mixed oxygen ionic-electronic conducting composites, Chemistry of Materials 20 (2008) 3867–3875.

[42] S. Bernal, J.J. Calvino, G.A. Cifredo, D. Finol, J.M. Gatica, C.J. Kiely, C. López-Cartes, J.G. Zheng, H. Vidal, Study of the structural modifications induced by reducing treatments on a $Pd/Ce_{0.8}Tb_{0.2}O_{2-x}/La_2O_3-Al_2O_3$ catalyst by means of X-ray diffraction and electron microscopy techniques, Chemistry of Materials 14 (2002) 1405–1410.

[43] P. Jasinski, T. Suzuki, H.U. Anderson, Nanocrystalline undoped ceria oxygen sensor, Sensors and Actuators B: Chemical 95 (2003) 73–77.

[44] J. Sunarso, S. Baumann, J.M. Serra, W.A. Meulenberg, S. Liu, Y.S. Lin, Mixed ionic–electronic conducting (MIEC) ceramic-based membranes for oxygen separation, Journal of Membrane Science 320 (2008) 13–41.

[45] T. Morimoto, H. Tomonaga, A. Mitani, Ultraviolet ray absorbing coatings on glass for automobiles, Thin Solid Films 351 (1999) 61–65.

[46] G.X. Zongping Shao, Weishen Yang, You Cong, Hui Dong, Jianhua Tong, Investigation of the permeation behavior and stability of a $Ba_{0.5}Sr_{0.5}Co_{0.8}Fe_{0.2}O_{3-\delta}$ oxygen membrane,", Journal of Membrane Science 172 (2000) 177–188.

[47] H.J.M. Bouwmeester, Dense ceramic membranes for methane conversion, Catalysis Today 82 (2003) 141–150.

[48] S. Svarcova, Structural instability of cubic perovskite $Ba_xSr_{1-x}Co_{1-y}Fe_yO_{3-\delta}$, Solid State Ionics 178 (2008) 1787–1791.

[49] H. Lein, K. Wiik, T. Grande, Thermal and chemical expansion of mixed conducting $La_{0.5}Sr_{0.5}Fe_{1-x}Co_xO_{3-\delta}$ materials, Solid State Ionics 177 (2006) 1795–1798.

[50] X. Qi, Y.S. Lin, Electric conductivity and oxygen permeability of modified cerium oxides, Journal of Materials Science 8 (2003) 1073–1079.

[51] G.Z. and R.J. Gorte, Thermodynamic investigation of the redox properties for ceria-hafnia, ceria-terbia, and ceria-praseodymia solid solutions, Journal of Physical Chemistry B 112 (2008) 9869–9875.

[52] D.P. Fagg, D. Pérez-Coll, P. Núñez, J.R. Frade, A.L. Shaula, A.A. Yaremchenko, V.V. Kharton, Ceria based mixed conductors with adjusted electronic conductivity in the bulk and/or along grain boundaries, Solid State Ionics 180 (2009) 896–899.

[53] I.K. Naik, T.Y. Tien, Small-polaron mobility in nonstoichiometric cerium dioxide, Journal of Physics and Chemistry of Solids 39 (1978) 311–315.

[54] C. Chatzichristodoulou, P. V. Hendriksen, Electronic and ionic transport in $Ce_{0.8}Pr_xTb_{0.2-x}O_{2-\delta}$ and evaluation of performance as oxygen permeation membranes, Journal of Electrochemical Society 159 (2012) E162–E170.

[55] A.J. Burggraaf, L. Cot, H.J.M. Bouwmeester, Chapter 10 Dense ceramic membranes for oxygen separation, Membrane Science and Technology 4 (1996) 435–528.

[56] Z. Shao, S.M. Haile, A high-performance cathode for the next generation of solid-oxide fuel cells, Nature 431 (2004) 170–3.

[57] Z. Duan, A. Yan, B. Tu, M. Cheng, Optimization of IT-SOFC with $Ba_{0.5}Sr_{0.5}Co_{0.8}Fe_{0.2}O_3$ cathode, in: Proceedings of the 1st European Fuel Cell Technology and Applications Conference 2005 - Book of Abstracts, 2005:179.

[58] Q. Zhu, T. Jin, Y. Wang, Thermal expansion behavior and chemical compatibility of $Ba_xSr_{1-x}Co_{1-y}Fe_yO_{3-\delta}$ with 8YSZ and 20GDC, Solid State Ionics 177 (2006) 1199–1204.

[59] B. Wei, Z. Lü, X. Huang, J. Miao, X. Sha, X. Xin, Crystal structure, thermal expansion and electrical conductivity of perovskite oxides $Ba_xSr_{1-x}Co_{0.8}Fe_{0.2}O_{3-\delta}$ ($0.3 \leq x \leq 0.7$), Journal of the European Ceramic Society 26 (2006) 2827–2832.

[60] C. Xia, M. Liu, Novel cathodes for low-temperature solid oxide fuel cells, Advanced Materials 14 (2002) 521–523.

[61] W. Wang, M. Mogensen, High-performance lanthanum-ferrite-based cathode for SOFC, Solid State Ionics 176 (2005) 457–462.

[62] J. J. Peña-Martínez, D. Marrero-López, C. Sánchez-bautista, A.J. Dos santos-garcía, J.C. Ruiz-Morales, J. Canales-vazquez, Effect of a CGO buffer layer on the

performance of $(La_{0.6}Sr_{0.4})_{0.995}Co_{0.2}Fe_{0.8}O_{3-\delta}$ cathode in YSZ-Based SOFC, Bol. La Soc. Española Cerámicay Vidrio 49 (2010) 15–22.

[63] V. Dusastre, J.A. Kilner, Optimisation of composite cathodes for intermediate temperature SOFC applications, Solid State Ionics 126 (1999) 163–174.

[64] S.J. Skinner, J.A. Kilner, Oxygen diffusion and surface exchange in $La_{2-x}Sr_xNiO_{4+\delta}$, Solid State Ionics 135 (2000) 709–712.

[65] C. Munnings, S. Skinner, G. Amow, P. Whitfield, I. Davidson, Oxygen transport in the LaNiCoO system, Solid State Ionics 176 (2005) 1895–1901.

[66] F. Mauvy, C. Lalanne, J.M. Bassat, J.C. Grenier, H. Zhao, P. Dordor, Oxygen reduction on porous $Ln_2NiO_{4+\delta}$ electrodes, Journal of the European Ceramic Society 25 (2005) 2669–2672.

[67] A. Montenegro-Hernández, J. Vega-Castillo, L. Mogni, A. Caneiro, Thermal stability of $Ln_2NiO_{4+\delta}$ (Ln:La, Pr, Nd) and their chemical compatibility with YSZ and CGO solid electrolytes, Int. Journal of Hydrogen Energy 36 (2011) 15704–15714.

[68] L. Yihong, R. Gemmen, X. Liu, Oxygen reduction and transportation mechanisms in solid oxide fuel cell cathodes, Journal of Power Sources 195 (2010) 3345–3358.

[69] S.B. Adler, J.A. Lane, B.C.H. Steele, Electrode kinetics of porous mixed-conducting oxygen electrodes, Journal of Electrochemical Society 143 (1996) 3554–3564.

[70] A.M. Svenssona, S. Sundeb, K. Nisancioglu, A mathematical model of the porous SOFC cathode, Solid State Ionics 86-88 (1996) 1211–1216.

[71] A.M. Svensson, Mathematical modeling of oxygen exchange and transport in air-perovskite-YSZ interface regions, Journal of The Electrochemical Society 144 (1997) 2719.

[72] M. Liu, J. Winnick, Fundamental issues in modeling of mixed ionic-electronic conductors (MIECs), Solid State Ionics 118 (1999) 11–21.

[73] A. Mitterdorfer, L.J. Gauckler, $La_2Zr_2O_7$ formation and oxygen reduction kinetics of the $La_{0.85}Sr_{0.15}Mn_yO_3$, O_2(g)/YSZ system, Solid State Ionics 111 (1998) 185–218.

[74] T.M. Koehler, D.B. Jarrell, L.J. Bond, High temperature ceramic fuel cell measurement and diagnostics for application to solid oxide fuel cell systems, 2001.

[75] M.J. Jérgensen, P. Holtappels, C.C. Appel, Durability test of SOFC cathodes, Journal of Applied Electrochemistry 30 (2000) 411–418.

[76] H. Tu, U. Stimming, Advances, aging mechanisms and lifetime in solid-oxide fuel cells, Journal of Power Sources 127 (2004) 284–293.

[77] S.N. Rashkeev, M. V. Glazoff, Control of oxygen delamination in solid oxide electrolyzer cells via modifying operational regime, Applied Physics Letters 99 (2011) 173506-173508.

[78] M.A. Laguna-Bercero, R. Campana, A. Larrea, J.A. Kilner, V.M. Orera, Electrolyte degradation in anode supported microtubular yttria stabilized zirconia-based solid oxide steam electrolysis cells at high voltages of operation, Journal of Power Sources 196 (2011) 8942–8947.

[79] F. Tietz, D. Sebold, A. Brisse, J. Schefold, Degradation phenomena in a solid oxide electrolysis cell after 9000 h of operation, Journal of Power Sources 223 (2013) 129–135.

[80] J.-E. Hong, T. Inagaki, T. Ishihara, Preparation of $LaGaO_3$ thin film for intermediate temperature SOFC by screen printing method (I), Ionics 18 (2012) 433–439.

[81] J.-E. Hong, S. Ida, T. Ishihara, Decreased sintering temperature of anode-supported solid oxide fuel cells with La-doped CeO_2 and Sr-and Mg-doped $LaGaO_3$ films by Co addition, Journal of Power Sources 259 (2014) 282–288.

[82] D. Mesguich, J.-M. Bassat, C. Aymonier, A. Brüll, L. Dessemond, E. Djurado, Influence of crystallinity and particle size on the electrochemical properties of spray pyrolyzed $Nd_2NiO_{4+\delta}$ powders, Electrochimica Acta 87 (2013) 330–335.

[83] T. Ogier, J.M. Bassat, F. Mauvy, S. Fourcade, J.C. Grenier, K. Couturier, Enhanced performances of structured oxygen electrodes for high temperature steam electrolysis, Fuel Cells 0 (2013) 1–6.

[84] D. Mesguich, C. Aymonier, J. Bassat, F. Mauvy, E. You, J.J. Watkins, Low-temperature deposition of undoped ceria thin films in $ScCO_2$ as improved interlayers for IT-SOFC, Chemistry of Materials 23 (2011) 5323–5330.

[85] J.M. Bassat, D. Mesguich, C. Ferchaud, Y. Zhang-Steenwinkel, F.V, Berkel, C. Aymonier, J.J. Watkins, J.C. Grenier, Doped/Undoped ceria buffer layers for improved LT-SOFC performances with Pr_2NiO, ECS Transactions 35 (2011) 1945–1954.

[86] W. Zhang, B. Yu, J. Xu, Investigation of single SOEC with BSCF anode and SDC barrier layer, International Journal of Hydrogen Energy 37 (2012) 837–842.

[87] Z. Xie, H. Zhao, Z. Du, T. Chen, N. Chen, Electrical, chemical, and electrochemical properties of double perovskite oxides $Sr_2Mg_{1-x}Ni_xMoO_{6-\delta}$ as anode materials for solid oxide fuel cells, The Journal of Physical Chemistry C 118 (2014) 18853–18860.

[88] C. Benel, A.J. Darbandi, R. Djenadic, A. Evans, R. Tölke, M. Prestat, Synthesis and characterization of nanoparticulate $La_{0.6}Sr_{0.4}CoO_{3-\delta}$ cathodes for thin-film solid oxide fuel cells, Journal of Power Sources 229 (2013) 258–264.

[89] Y. Min Park, H. Kim, Porous Gd-doped ceria barrier layer on solid oxide fuel cell with $Sm_{0.5}Sr_{0.5}CoO_{3-\delta}$ Cathodes, Ceramics International 39 (2013) 2037–2043.

[90] D. Wang, J. Wang, C. He, Y. Tao, C. Xu, W.G. Wang, Preparation of a $Gd_{0.1}Ce_{0.9}O_{2-\delta}$ interlayer for intermediate-temperature solid oxide fuel cells by spray coating, Journal of Alloys and Compounds 505 (2010) 118–124.

[91] Y.-M. Kim, P. Kim-Lohsoontorn, J. Bae, Effect of unsintered gadolinium-doped ceria buffer layer on performance of metal-supported solid oxide fuel cells using unsintered barium strontium cobalt ferrite cathode, Journal of Power Sources 195 (2010) 6420–6427.

[92] C. Ferchaud, J.-C. Grenier, Y. Zhang-Steenwinkel, M.M.A. van Tuel, F.P.F. van Berkel, J.-M. Bassat, High performance praseodymium nickelate oxide cathode for low temperature solid oxide fuel cell, Journal of Power Sources 196 (2011) 1872–1879.

[93] J.-J. Choi, D.-S. Park, B.-G. Seong, H.-Y. Bae, Low-temperature preparation of dense $(Gd,Ce)O_{2-\delta}$–Gd_2O_3 composite buffer layer by aerosol deposition for YSZ electrolyte-based SOFC, Int. Journal of Hydrogen Energy 37 (2012) 9809–9815.

[94] L. Lei, Y. Bai, J. Liu, Ni-based anode-supported Al_2O_3-doped-Y_2O_3-stabilized ZrO_2 thin electrolyte solid oxide fuel cells with Y_2O_3-stabilized ZrO_2 buffer layer, Journal of Power Sources 248 (2014) 1312–1319.

[95] B.A. van Hassel, B. Boukamp, A. Bourggraaf, Electrode polarization at the Au, O_2(g)/Fe implanted yttria-stabilized zirconia interface, Solid State Ionics 51 (1992) 161–174.

[96] B.A. van Hassel, B.A. Boukamp, A.J. Burggraaf, Oxygen transfer properties of ion-implanted yttria-stabilized zirconia, Solid State Ionics 53-56 (1992) 890–903.

[97] J. Fleig, Solid oxide fuel cell cathodes:Polarization mechanisms and modeling of the electrochemical performance, Annual Review of Material Research 33 (2003) 361–382.

[98] S.B. Adler, Factors governing oxygen reduction in solid oxide fuel cell cathodes, Chemical Review 104 (2004) 4791–4843.

[99] P. Bohac, A. Orliukas, L. Gauckler, Lowering of the cathode overpotential of SOFC by electrolyte doping, in: Electroceramics IV, II, 1994:771–774.

[100] D.P. Fagg, V. V. Kharton, J.R. Frade, Transport in ceria electrolytes modified with sintering aids: effects on oxygen reduction kinetics, Journal of Solid Stat Electrochemistry 8 (2004) 618–625.

[101] D. Pérez-Coll, A. Aguadero, M.J. Escudero, P. Núñez, L. Daza, Optimization of the interface polarization of the La_2NiO_4-based cathode working with the $Ce_{1-x}Sm_xO_{2-\delta}$ electrolyte system, Journal of Power Sources 178 (2008) 151–162.

[102] D. Pérez-Coll, A. Aguadero, M.J. Escudero, L. Daza, Effect of DC current polarization on the electrochemical behaviour of $La_2NiO_{4+\delta}$ and $La_3Ni_2O_{7+\delta}$-based systems, Journal of Power Sources 192 (2009) 2–13.

[103] D.P. Fagg, V.V. Kharton, J.R. Frade, P-Type Electronic Transport in $Ce_{0.8}Gd_{0.2}O_{2-\delta}$: The effect of transition metal oxide sintering aids, Journal of Electroceramics 9 (2002) 199–207.

[104] D.P. Fagg, J.C.C. Abrantes, D. Pérez-Coll, P. Núñez, V.V. Kharton, J.R. Frade, The effect of cobalt oxide sintering aid on electronic transport in $Ce_{0.80}Gd_{0.20}O_{2-\delta}$ electrolyte, Electrochimical Acta 48 (2003) 1023–1029.

2. Experimental

2.1. Synthesis and ceramic processing

(i) Hydrothermal synthesis: Doped-cerium oxide compositions of 20 mol% gadolinium (CGO), Terbium (CTO), or Praseodymium (CPO) were prepared by a hydrothermal method, using cerium (III) nitrate hexahydrate ($Ce(NO_3)_3.6H_2O$, Aldrich, 99% pure) with gadolinium (III) nitrate hexahydrate ($Gd(NO_3)_3.6H_2O$, 99.9% pure), Alfa Aesar), terbium (III) nitrate pentahydrate ($Tb(NO_3)_3.5H_2O$, 99.9% pure, Aldrich), or praseodymium (III) nitrate hexahydrate ($Pr(NO_3)_3.6H_2O$, 99.9% pure, Aldrich), respectively, as a starting materials. Stoichiometric amounts of the starting precursors were dissolved separately in distilled water under mild stirring and combined. After complete mixing, excess ammonium hydroxide was added dropwise until the solution reached ~ pH 10, upon which co-precipitation occurred. The precipitated gels were sealed in Teflon-lined steel autoclaves and heated at 250°C for 5 h with 5°C/min heating and cooling rates. The resulting slurry was filtered off and thoroughly washed with deionised water and dried in air at 70°C for 12 h. The resultant powder was ball-milled in nylon mill with zirconia balls with slow speed (150 rpm) for about 5 h to break weak agglomerates. Addition of cobalt oxide (2 mol%) sintering aid was added in the form of an aqueous solution of nitrate, $Co(NO_3)_2.6H_2O$ (>98% pure, Aldrich), with ultrasonication for 1 h and subsequent drying. The powder was ground using an agate mortar and pestle until fine powders were obtained. These cobalt containing analogues of the doped ceria samples are labeled CGO+Co, CTO+Co and CPO+Co, for the gadolinium and praseodymium materials, respectively.

(ii) Combustion method: Perovskite-type $Nd_2NiO_{4+\delta}$ and $Pr_2NiO_{4+\delta}$ powders were prepared by the citrate route using neodymium oxide (99.9% pure, Aldrich), praseodymium hexahydrate (99.9% pure, Sigma-Aldrich) and nickel (II) nitrate hexahydrate (>98.5% pure, Aldrich). Stoichiometric amounts of the precursors were dissolved in distilled water and with a small amount of nitric acid. After addition of citric acid (>99.5% pure, Aldrich), the solution was stirred vigorously for 30 mins. to obtain a clear solution. Then, the solution was dehydrated at 120°C and slowly heated until self-combustion occurred. The calcination of the produced power was performed at 1100°C for

12 h to obtain pure phases. The powder was ball-milled at 250 rpm for about 5 h to break weak agglomerates.

2.2. Preparation of electrochemical cells via spin coating

To prepare electrochemical cells, pre-densified 8 mol% yttria stabilized-zirconia pellets were used as the electrolyte. The buffer layers (CGO+Co, CTO+Co, or CPO+Co) and electrode ($Nd_2NiO_{4+\delta}$) or ($Pr_2NiO_{4+\delta}$) were fabricated by the spin coating technique (Spin coater - Laurell Technology Corporation) on these substrates. To prepare stable suspensions, absolute ethanol was used as the solvent with a polyvinylpyrrolidone (PVP) binder. These suspensions were ball milled at 350 rpm for 2 h followed by ultrasonication (Ultrasons-H,JP SELECTA, Abrera, Spain) for 1h. Buffer layers were spin coated on the YSZ electrolyte substrates at a rotation speed of 3000 rpm for 30 s to coat a centrally located unmasked area of approximately 6 mm. The resultant electrolyte/buffer layer assemblies were sintered at 900°C for 5 h. Subsequently, $Nd_2NiO_{4+\delta}$ or $Pr_2NiO_{4+\delta}$ electrodes were spin coated to cover an identical unmasked area on top of the buffer layer assemblies, using the same conditions as before. Repeated coatings of the $Nd_2NiO_{4+\delta}$ or $Pr_2NiO_{4+\delta}$ electrodes were made with intermediate, in-situ, dryings in air at room temperature to build up the desired thickness. The number of coatings was kept constant for every sample tested. Finally, the cell was sintered at 900°C for 10 h. Porous platinum paint was coated on the other side of the electrolyte as a counter electrode, with identical area and symmetrically placed with respect to the working electrode [1]. Pt was also employed as a reference electrode in the form of a ring located around the working electrode, at a distance greater than three electrolyte thicknesses from the edge of the working electrode; an arrangement that has been previously documented to ensure negligible interference by current fluxes at the reference [2]. The platinum electrodes were sintered at 850°C for 10mins. A schematic of the formed cell is shown in Figure 2.1.

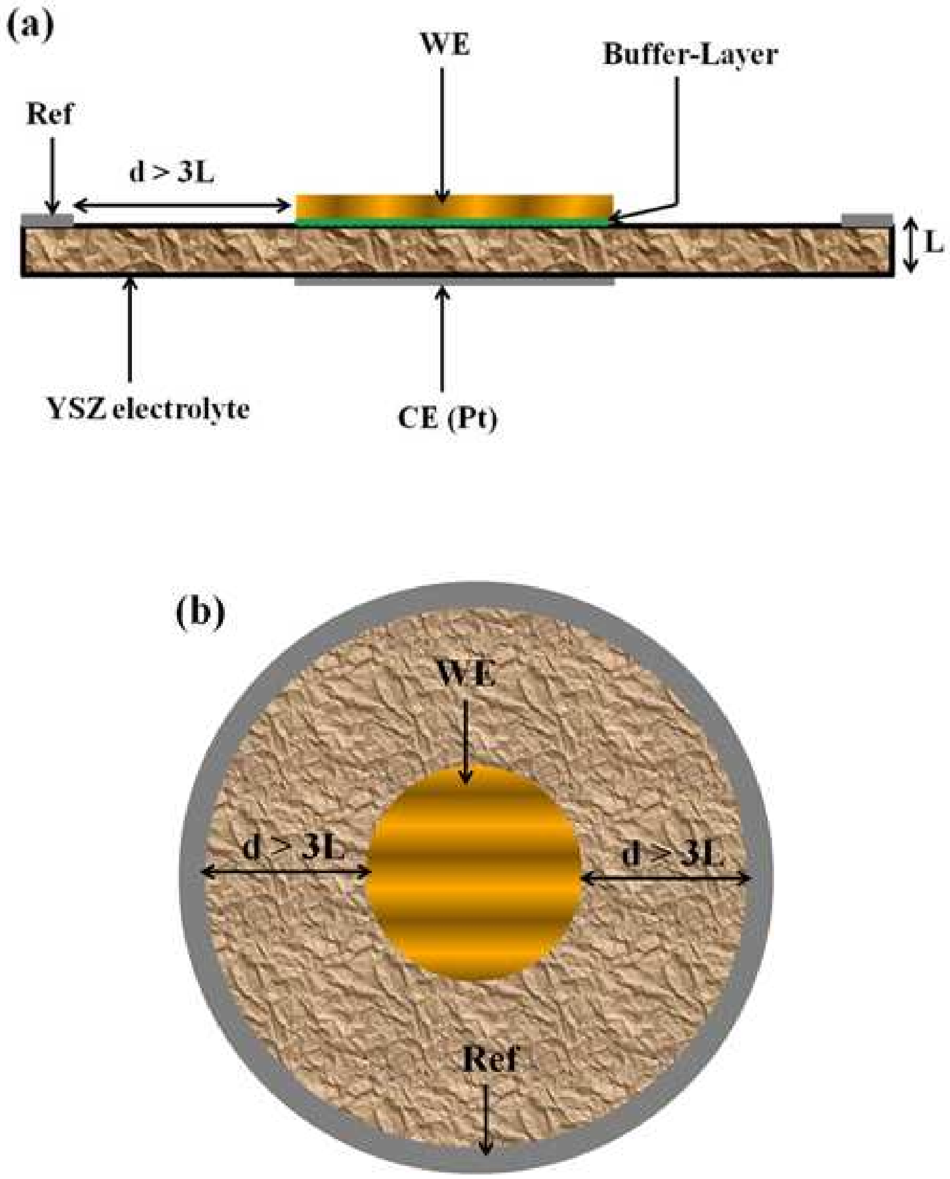

Figure 2.1. Experimental set-up employed for the electrochemical characterization. Working electrode was placed with the counter electrode in symmetrical configuration with an external Pt ring reference electrode to complete the 3-probe configuration. (a) Cross Sectional view and (b) Top view.

2.3. Phase, thermal and microstructural analysis

Powder XRD patterns were recorded to identify the phase purity, crystallite size and lattice parameters of green (after ball milling) and sintered samples using a Rigaku Geigerflex diffractometer (CuK$_\alpha$ radiation.). The lattice parameters were refined by the Rietveld method with the Fullprof program and a correction was made to the experimental full-width at half-maximum for instrumental broadening by using Ni metal as the internal standard. Data were collected over a 2θ range of 20-90° with 0.02° step size and using a counting time of 1 s per step. The densification rate of rectangular green compacts (approximately 3 mm × 5 mm × 15 mm) were studied in Linseis L70 dilatometer with a constant heating rate of 5°C/min.

Surface morphology, cross sectional characterization and elemental analysis were performed by scanning electron microscopy (SEM, Hitachi SU-70) and Energy Dispersive X-ray spectroscopy (EDS) (model Bruker. Quantax-Germany) for sintered ceramics and fractured cells. Transmission Electron Microscopy (TEM) studies of the microstructure and chemical composition of the Co-doped CTO samples were performed in a JEOL JEM 3000F microscope operating at 300 kV. The microscope is fitted with an INCA Energy EDS X-ray microanalysis system and a JEOL Annular Dark Field (ADF) detector for Scanning Transmission Electron Microscopy (STEM) imaging. Electron Energy Loss Spectroscopy (EELS) was done with a Gatan Enfina spectrometer in STEM mode (Spectrum Imaging – SI).

2.4. Measurements of the total electrical conductivity

Total conductivity measurements were performed on dense pellets, (approximately 2 mm thick with diameter of 12 mm), using an Electrochemie-Autolab PGSTAT302N frequency response analyzer in the frequency range of 0.01 Hz - 1 MHz, with amplitude of 50 mV. The pellets were painted on both sides with porous platinum electrodes. Measurements were performed in an isolated chamber under dry nitrogen and oxygen atmospheres, with flow rates of 50 ml/min. All measurements were carried out in the direction of decreasing temperature, from 850 to 100°C at 50°C intervals. At each temperature, stabilization time was 2 hours, with repeated impedance spectra recorded after a further 30 minutes, confirming the attainment of equilibrium. Total conductivity values were calculated from:

$$\sigma = \frac{L}{R \times A} \qquad (2.1)$$

where *L* is the sample length, *R* is the sample resistance and *A* is the sample cross area. Activation energy (E_a) values for the conductivities were calculated by the standard Arrhenius equation:

$$\sigma = \frac{Ao}{T} e^{[-\frac{Ea}{RT}]} \qquad (2.2)$$

where A_o is the pre-exponential factor.

2.5. Measurements of transport number (t_o)

Measurements were performed using an electrochemical cell comprising of an yttria-stabilized zirconia (YSZ) tube. The samples were hermetically fixed onto the YSZ tube, separating the two gas atmospheres, with help of a glass-ceramic sealant. An oxygen chemical potential gradient was achieved by continuous feeding of oxygen or nitrogen to one side of sample and air to the opposing side. Pt wires were used as current collectors. All EMF measurements were performed in the temperature range from 850 to 600°C at 50°C intervals on cooling. An external variable resistance was connected in parallel to the measuring cell in order to increase measurement sensitivity and correct for possible polarization influence in the determination of ion transference numbers. Transport numbers (t_o) were measured using the modified electromotive force (EMF) method first proposed by Gorelov [3]. The measurement procedure and comparison of the external resistance technique with the traditional approach are well documented in the literature [4]. Thus, only a brief description is given below. On the assumption of oxygen concentration cells with negligible polarization resistance of electrodes, the EMF can be calculated by using Wagner and Nernst equations:

$$E_{obs} = \frac{RT}{4F}\int_{p_1}^{p_2} \frac{\sigma_o}{\sigma_o + \sigma_o}\, d\ln p(O_2) = \frac{RT}{4F}\int_{p_1}^{p_2} t_o d\ln p(O_2) = t_o\, E_{th} \qquad (2.3)$$

Where, *R* is the Ideal gas constant, *T* is the Temperature, *F* is the Faraday constant, σ_o and σ_e are the partial oxygen ionic and electronic conductivities and p_1 & p_2 are the values of oxygen partial pressure (pO_2) at the electrodes. Further, non- negligible polarization resistance of electrodes leads to underestimated t_o values, described by the equivalent circuit shown in figure 2.2a,

$$\frac{Eobs}{Eth} = t_o \left[1 + \frac{R\eta}{Ro+Re}\right]^{-1} \qquad (2.4)$$

where R_η is the polarization resistance whilst R_o and R_e are the partial oxygen ionic and electronic resistances of the sample. E_{obs} can be measured as a function of simulating the effect of electronic conductivity, when an external variable resistance included in to the circuit figure 2.2b, therefore;

$$\frac{E_{th}}{E_{obs}} - 1 = (R_o + R_\eta)\left[\frac{1}{R_e} + \frac{1}{R_M}\right] \quad (2.5)$$

At low overpotential, when the overpotential-current dependence is linear, the dependence ($E_{th}/E_{obs} - 1$) versus $1/R_M$ also linear with a slope of ($R_o + R_\eta$). Therefore, the intercept of this dependence over the ($1/R_M$) axis is equal to ($-1/Re$). The values of R_e can be calculated by fitting data to the linear model [4]. Therefore equation 2.5 can be written as;

$$\frac{E_{th}}{E_{obs}} - 1 = A\left[\frac{1}{R_M}\right] + B \quad (2.6)$$

where A and B are regression parameters and $R_e = A/B$. Hence the oxygen ion transference numbers are found as,

$$t_o = 1 - \frac{R_{bulk}}{R_e} \quad (2.7)$$

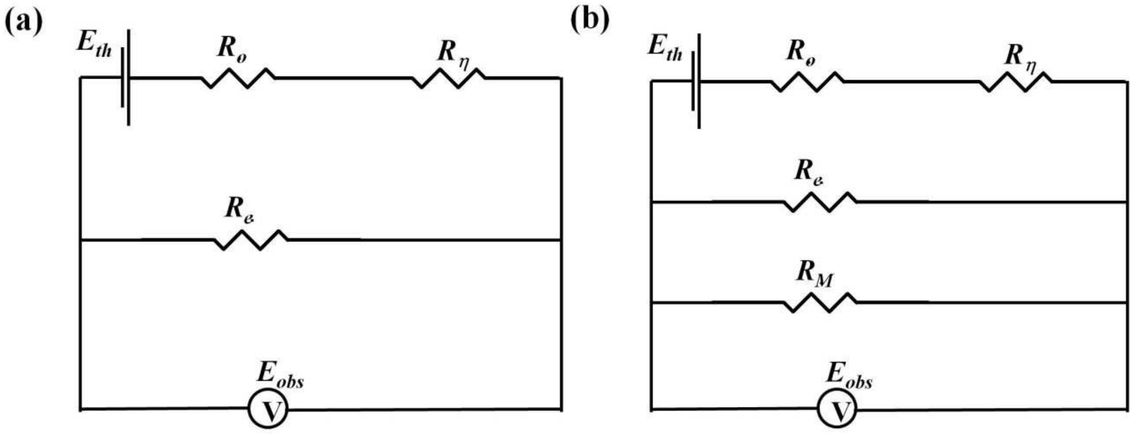

Figure 2.2. Equivalent circuits for (a) classical and (b) modified EMF techniques.

2.6. Measurements of oxygen permeability

Oxygen permeation measurements were performed on dense gas-tight membranes following the procedure reported elsewhere [5]. A 1 mm thick pellet was sealed on the top of the YSZ tube and the bottom of the tube was sealed with YSZ pellet (figure 2.3).

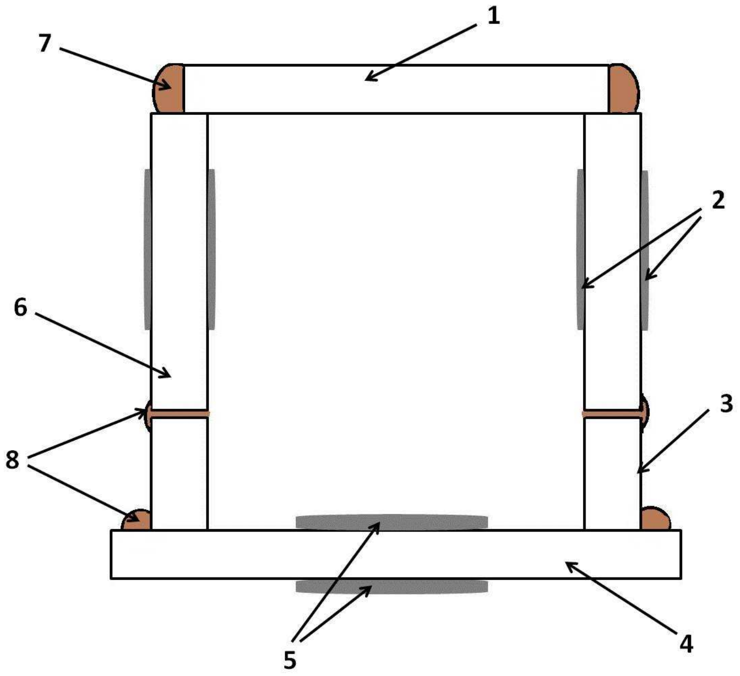

Figure 2.3. Schematic drawing of the electrochemical cell for oxygen permeability measurements: (1) Sample, (2) electrodes of the oxygen sensor, (3) YSZ tube, (4) YSZ pellet (pump), (5) electrodes of the oxygen pump, (6) YSZ tube (sensor), (7) low-temperature glass, (8) high-temperature glass.

Both sides of YSZ tube and YSZ pellet were painted with Pt electrodes, as a sensor and a pump, respectively. An oxygen potential gradient was created between the inner and outer surfaces of the sample by controlling the pump current and was monitored by the sensor. The oxygen flux density values through the sample were calculated from the respective pump current values:

$$j = \frac{I_p}{4FA} \tag{2.8}$$

where I_p is the pump current and A is the area of the membrane (~10 mm diameter). The permeation process is described using the quantities of oxygen flux density, j, and specific oxygen permeability, $J(O_2)$, which are interrelated as

$$J(O_2) = jd[ln\frac{p2}{p1}]^{-1} \tag{2.9}$$

where p_1 is the oxygen partial pressure at the membrane permeate (inner) side and p_2 is the oxygen partial pressure at the membrane feed (outer) side, which remained constant at ~0.21 atm., corresponding to an air atmosphere ($p_1 < p_2$).

2.7. Electrochemical analysis of electrolyte/buffer layer/electrode assemblies

Electrochemical characterization was performed in air using an Electrochemie-Autolab PGSTAT302N. The cell was subjected to DC bias in potentiostatic mode, with potential monitored between working and reference electrodes, from -0.3 V to +0.3V at 0.05V intervals with a dwell time of 30 min at each condition. Polarization was performed in both anodic and cathodic directions to provide information useful for both SOFC and SOEC modes of operation. Open circuit conditions (OPC) were initially measured, followed by the anodic branch. The OPC condition was then re-tested, to ensure no permanent change in performance had occurred, and, subsequently, the cathodic branch was measured. At the end of each dwell, A.C. impedance spectroscopy was performed, superimposed over each potential bias. The measured frequency range was 1 MHz - 0.01 Hz, with signal amplitude 100 mV. Experiments were performed in the temperature range from 850°C to 600°C, in the direction of decreasing temperature. Impedance spectra were fitted to equivalent circuits using ZView software (Scribner Associates).

2.8. References

[1] D. Pérez-Coll, A. Aguadero, M.J. Escudero, L. Daza, Effect of DC current polarization on the electrochemical behaviour of $La_2NiO_{4+\delta}$ and $La_3Ni_2O_{7+\delta}$-based systems, Journal of Power Sources 192 (2009) 2–13.

[2] S.B. Adler, B.T. Henderson, M.A. Wilson, D.M. Taylor, R.E. Richards, Reference electrode placement and seals in electrochemical oxygen generators, Solid State Ionics 134 (2000) 35–42.

[3] V.P. Gorelov, Transference number determination in ionic conductors by the e.m.f. method with active load, Elektrokhimiya 24 (1988) 1380–1381 [in Russian].

[4] V. V Kharton, F.M.B. Marques, Interfacial effects in electrochemical cells for oxygen ionic conduction measurements I. The e.m.f. method, Solid State Ionics 140 (2001) 381–394.

[5] V.V. Kharton, V.N. Tikhonovich, L. Shuangbao, E.N. Naumovich, A.V. Kovalevsky, A.P. Viskup, I.A. Bashmakov, A.A. Yaremchenko, Ceramic microstructure and oxygen permeability of SrCo(Fe, M)$O_{3-\delta}$(M = Cu or Cr) perovskite membranes, Journal of the Electrochemical Society 145 (1998) 1363–1373.

3. Study of the Transport Properties of the Mixed Ionic Electronic Conductor $Ce_{1-x}Tb_xO_{2-\delta}$

3.1. Introduction

Terbium-doped ceria is a promising MIEC fluorite material in both reducing and oxidizing atmospheres that has gained recent interest [1]. Physical and chemical properties of $Ce_{1-x}Tb_xO_{2-\delta}$ have been reported by various authors [2–5], while total, ionic and electronic conductivities of $Ce_{1-x}Tb_xO_{2-\delta}$ (x = 0-0.30) have been provided by Shuk et al. [6]. In general, the total conductivity was shown to increase with increasing Tb content, a trend that was later corroborated by Ye et al. across the whole composition range (x = 0.00-1.00) [7]. For doping levels x = 0.15-0.25, Shuk et al. showed that ~50% electronic contribution to total conductivity was provided at 600-700°C in oxidizing conditions, corresponding to the ideal weighting of ionic and electronic conductivities to attain maximum ambipolar conductivity.

To avoid high sintering temperatures in ceria-based materials many researchers have investigated the addition of small quantities of transition metal oxides as potential sintering additives [8–11]. With respect to terbium doped ceria, Balaguer et al. [1,12], reported that 2 mol% addition of cobalt oxide into $Ce_{1-x}Tb_xO_{2-\delta}$ could improve densification during sintering and could also significantly enhance the total and ambipolar conductivities over that of the Co-free oxide [12]. The observations of Balaguer et al. [1,12] concur well with those reported previously for other doped ceria materials, such as Gd or Pr-doped analogues, $Ce_{0.8}Gd_{0.2}O_{2-\delta}$ and $Ce_{0.8}Pr_{0.2}O_{2-\delta}$, containing equal fractions of Co additive [13–17]. In the case of the Pr and Gd analogues, enhancements in ambipolar conductivity have been related to the presence of a Co network localized at the grain boundary, which can enhance available levels of electronic conductivity [13–17]. In contrast, Balaguer et al. [1,12] noted that a similar grain boundary location of Co was not observed in samples of $Ce_{1-x}Tb_xO_{2-\delta}$+Co (x = 0.1, 0.2) sintered at 1300ºC. Nonetheless, substantial enhancements in ambipolar conductivity could still be obtained. Concerning this observation, it is important to note that improvements in mixed conductivity and faster oxygen exchange have also been outlined for ceria-based materials when the grain size has been reduced to the submicron range [18,19].

In this chapter we assess the enhancement of ambipolar conductivity in Co containing $Ce_{1-x}Tb_xO_{2-\delta}$ materials and examine potential links between this behavior, the resultant oxygen permeation and microstructural factors, with careful attention to the physical location of the sintering additive. In this respect, the sintering temperature has been documented to be an important factor that can negatively impact levels of ambipolar conductivity in the Gd and Pr analogues, when Co containing samples were sintered in excess of 900ºC [13,20–22]. In this work, we analyze the influence of sintering temperature on $Ce_{0.8}Tb_{0.2}O_{2-\delta}$ materials (CTO) containing 2 mol% additions of cobalt oxide sintering aid, through structural and microstructural characterization, conductivity measurements, electromotive force (EMF) and oxygen permeation studies, in order to further understand the behavior of these additives on the properties of CTO MIECs.

3.2. Experimental

Cerium-terbium oxide ($Ce_{0.8}Tb_{0.2}O_{2-\delta}$) materials were prepared by the hydrothermal method that is explained previously in Chapter 2.1. Pellets of cerium terbium oxide (CTO), with and without Co addition, were uniaxially dry pressed at a pressure of 60 MPa followed by isostatic pressing at 200 MPa. Pure CTO pellets were sintered at 1500^{o}C for 10 h. In contrast, Co-doped CTO pellets were sintered at 900^{o}C for 5 h, or at 1200^{o}C for 5 h. In all cases, heating and cooling rates were 2^{o}C/min.

Phase analysis was performed by room temperature XRD and Microstructural characterization was performed by SEM for Co-doped and pure CTO ceramics. TEM studies of the microstructure and chemical composition of the Co-doped CTO samples also were performed as described in Chapter 2.1.

Total conductivity, transport number and oxygen permeability measurements were performed in order to understand the MIECs properties of $Ce_{0.8}Tb_{0.2}O_{2-\delta}$.

3.3. Results and Discussion

Figure 3.1a shows the room temperature XRD pattern of $Ce_{0.8}Tb_{0.2}O_{2-\delta}$ green powder prepared by the hydrothermal method, while Figures 3.1b-d show XRD patterns of final ceramics sintered at 900 and 1200^{o}C with Co additions and at 1500^{o}C without Co, respectively. All XRD patterns can be seen to exhibit the expected cubic defect fluorite structure, without a visible presence of impurity phases.

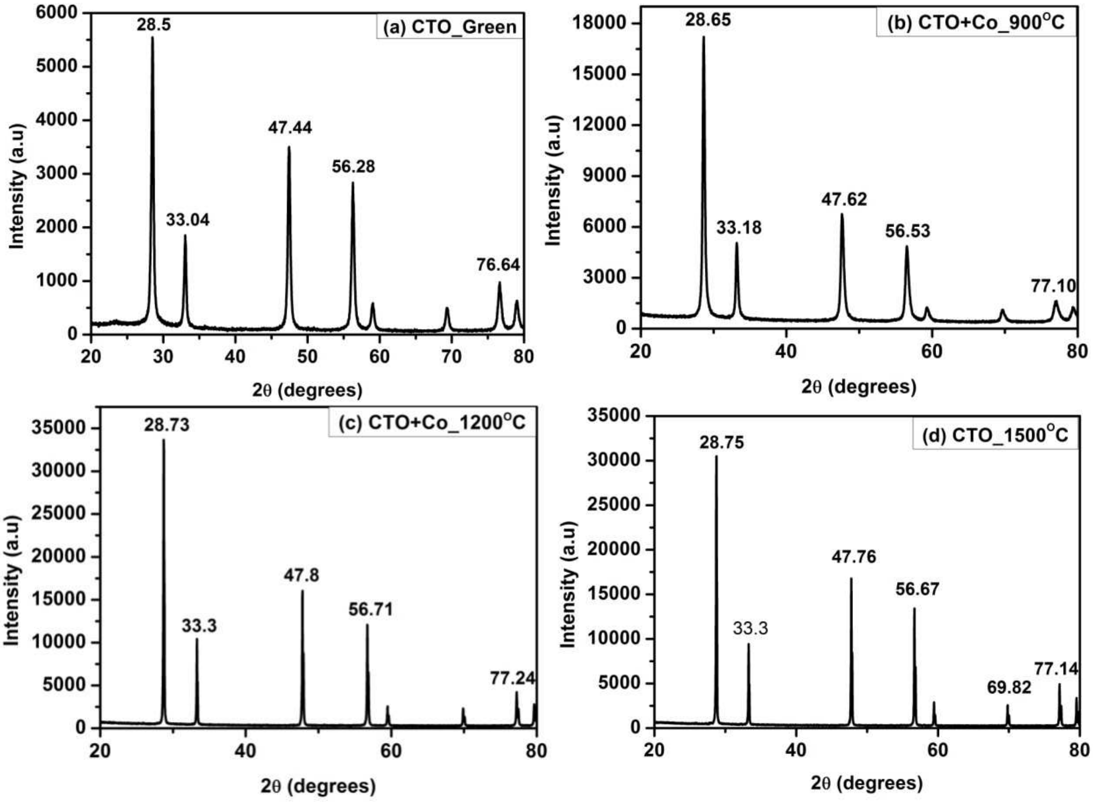

Figure 3.1. X-ray diffraction patterns of as-prepared (a) pure $Ce_{0.8}Tb_{0.2}O_{2-\delta}$ and sintered Co-doped (b, c) and pure (d) $Ce_{0.8}Tb_{0.2}O_{2-\delta}$.

The lattice parameters and crystallite sizes, calculated using the Scherrer formula, are presented in Table 3.1. The diffraction patterns of the as-prepared powder (Figure 3.1a) and CTO+Co ceramics sintered at 900°C (Figure 3.1b) show broader peaks than the other patterns, in agreement with the positive temperature dependence of the crystallite size documented in Table 3.1. The highest lattice parameter is obtained for the green powder while, for sintered ceramics, the lattice parameter is significantly lower in the Co-containing samples. This observation is in agreement with that of Balaguer et al. [1,12], who related lattice contraction to slight solubility of Co in the CTO material.

Table 3.1. Lattice parameters and crystallite sizes of $Ce_{0.8}Tb_{0.2}O_{2-\delta}$ green powder and ceramics.

Material	Lattice parameter (Å)	Average crystallite size

	(±0.0003)	(nm)
CTO_Green	5.4011	30
CTO+Co_900^{o}C	5.3910	32
CTO+Co_1200^{o}C	5.3915	83
CTO_1500^{o}C	5.3940	83

Figure 3.2a shows the shrinkage behavior of green compacts with a constant heating rate of 5^{o}C/min. Intense densification takes place below 1000^{o}C for the sample doped with Co sintering aid, whereas the Co-free sample still continues to sinter at 1500^{o}C (the maximum temperature limit of the dilatometer).

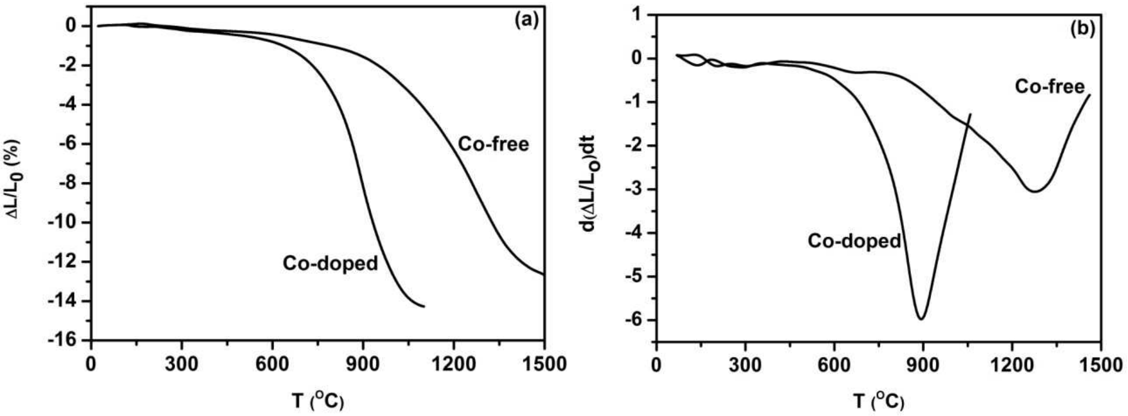

Figure 3.2. Influence of cobalt oxide sintering aid into $Ce_{0.8}Tb_{0.2}O_{2-\delta}$: (a) temperature dependence of the linear shrinkage and (b) linear shrinkage rate.

Figure 3.2b plots the linear shrinkage rate [$d(\Delta L/L_o)/dT$] as a function of temperature . The width of the shrinkage temperature range for the Co-doped material is shown to be much narrower than that of the Co-free green compact and exhibits a maximum in shrinkage rate at approximately 900^{o}C. This phenomenon has been observed in other doped ceria materials [13–17] and is suggested to be due to liquid-phase assisted sintering [11] that allows pellets with densities higher than 90% of the theoretical to be obtained after sintering at 900^{o}C for 5 h. A similar density was attained in the Co-free CTO ceramics only after sintering at a higher temperature of 1500°C for 10 h.

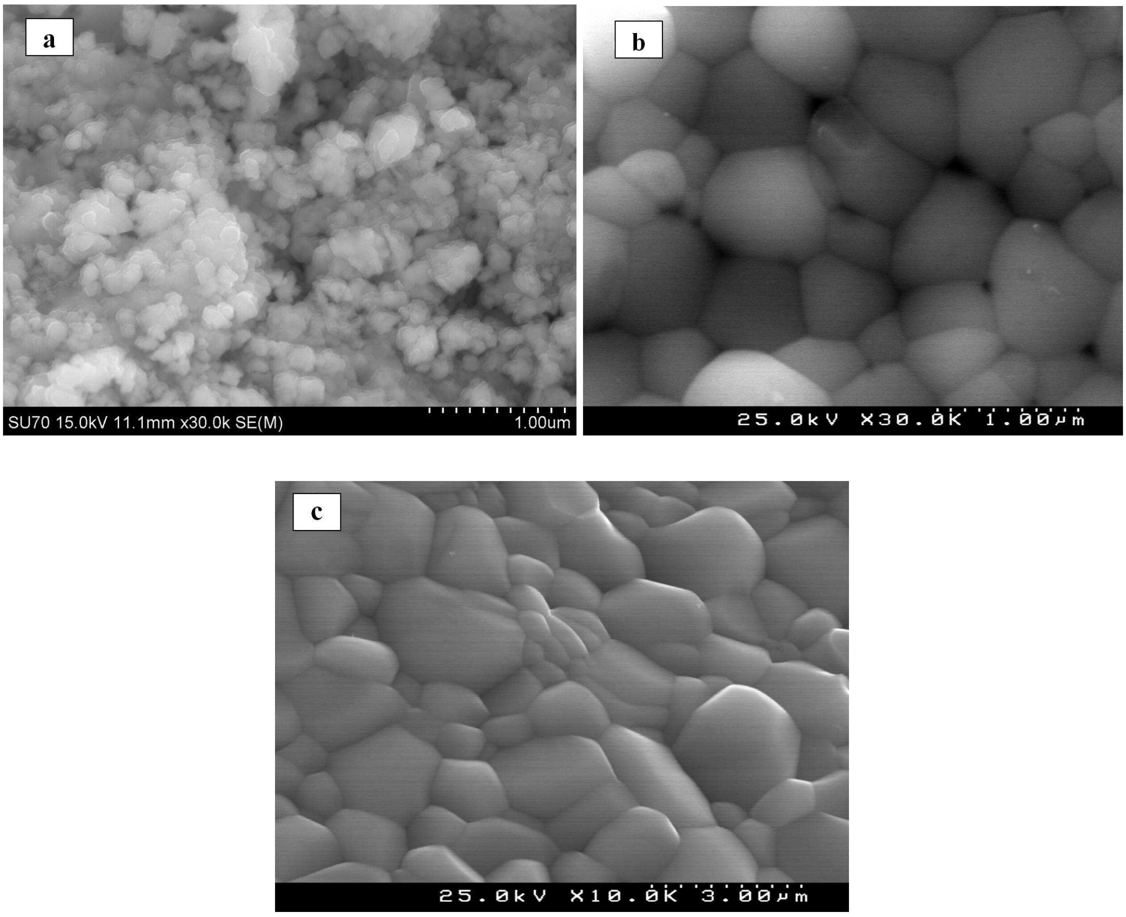

Figure 3.3. SEM micrographs of CTO ceramics: a) sintered at 900°C with Co, b) sintered at 1200°C with Co and c) sintered at 1500°C without Co.

Figure 3.3 shows the morphology of CTO samples sintered at different temperatures with and without Co-sintering aid. The ceramics sintered at highest sintering temperature, 1500°C, Figure 3.3c, without sintering aid show relatively large grains (1.3 ± 0.2μm). Among the Co-doped $Ce_{0.8}Tb_{0.2}O_{2-\delta}$ materials, the oxide sintered at lowest temperature, 900°C, Figure 3.3a, shows a significantly smaller grain size (34 ± 10 nm) than that of the ceramic sintered at 1200°C (0.6 ± 0.1μm). This tendency in grain growth is similar to that previously noted for $Ce_{0.8}Gd_{0.2}O_{2-\delta}$ and $Ce_{0.8}Pr_{0.2}O_{2-\delta}$ ceramics in the literature, where dense materials with sub-micron grain size were obtained after sintering at relatively low temperatures (900-1000°C) by addition of 2 mol% of cobalt oxide as a sintering aid [13,14,17].

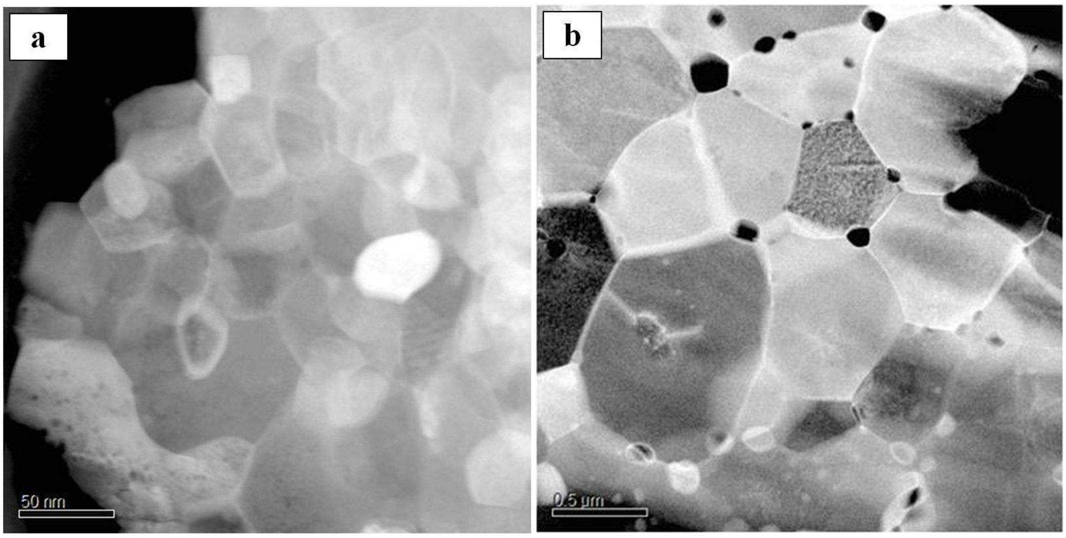

Figure 3.4. ADF-STEM micrographs of Co-doped CTO ceramics sintered at 900 (a) and 1200°C (b) showing grain sizes one order of magnitude larger in the higher temperature sample.

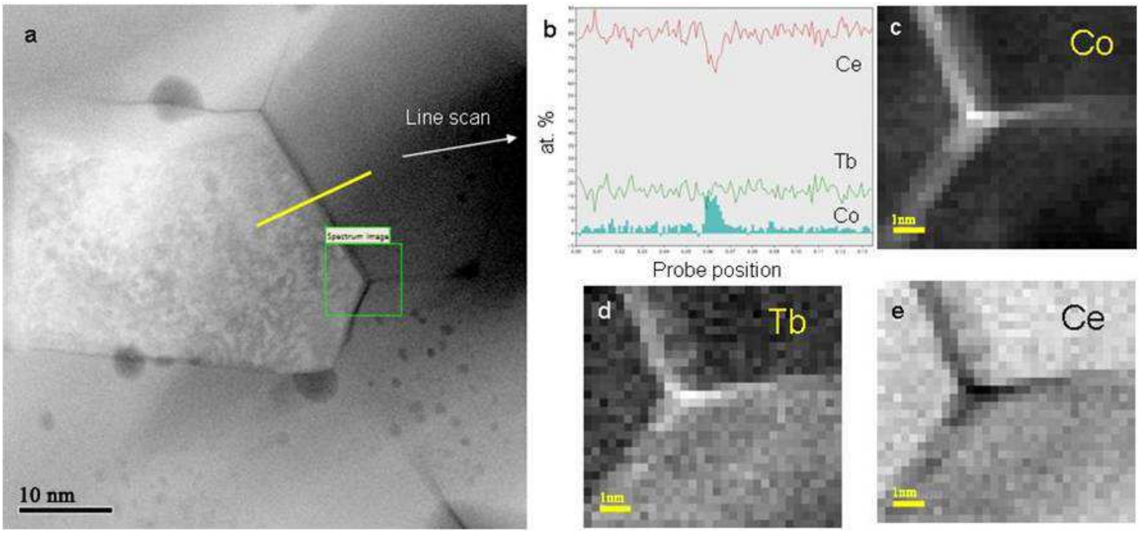

Figure 3.5. a) HAADF STEM image of the Co-doped Ce$_{0.8}$Tb$_{0.2}$O$_{2-\delta}$ ceramic sintered at 900°C. b) Line scan profiles of Ce, Tb and Co across a grain boundary. c-e) Elemental maps determined from the EELS – SI data acquired in a triple point.

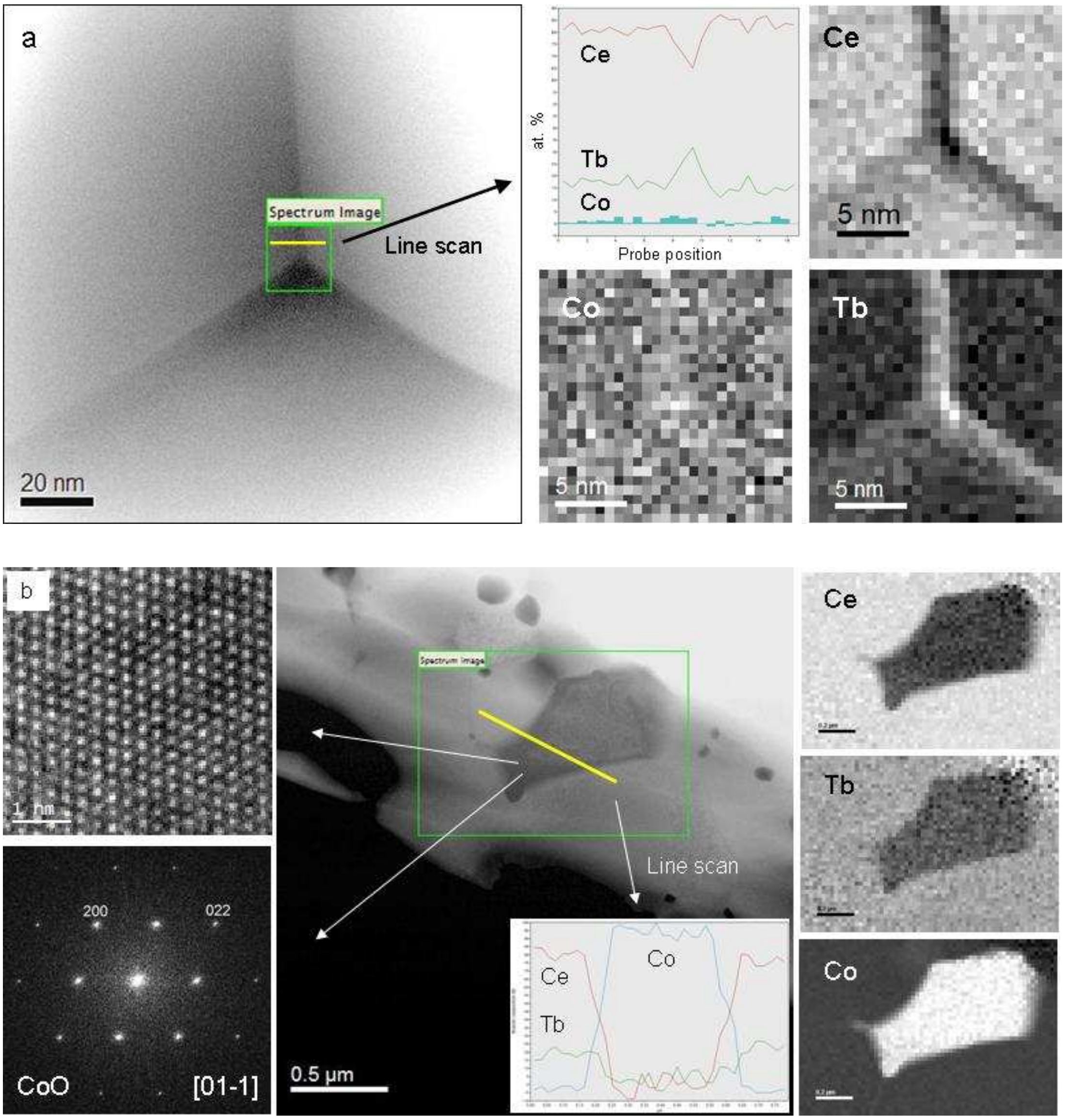

Figure 3.6. a) Triple point in the Co-doped $Ce_{0.8}Tb_{0.2}O_{2-\delta}$ ceramics sintered at 1200°C. HAADF STEM image along with the elemental maps determined from the EELS – SI data. b) Segregated cobalt oxide particle observed in the same sample, a TEM micrograph of this particle and its corresponding digital diffraction pattern are shown on the left side of the figure, the elemental maps determined from the EELS – SI data are shown on the right side.

TEM studies were performed with careful focus at grains and grain boundaries in order to assess the distribution of Co sintering additives after treatment at different sintering temperatures. Figures 3.4a and b show micrographs of the CTO+Co ceramics sintered at 900°C and 1200°C, respectively. The images clearly reveal that increasing sintering temperature leads to substantial grain growth, in agreement with SEM studies, Figure 3.3. Chemical analysis, line scan profiles and elemental maps were obtained from the EELS data with the microscope operated in STEM mode. The results are shown in Figures 3.5 and 3.6 for the CTO+Co ceramics sintered at 900 and 1200^{o}C, respectively. The EELS line scans and elemental maps clearly reveal the Co additive to be segregated to the grain boundaries at the lowest sintering temperature, see Fig. 3.5, in agreement with that previously noted for the Pr and Gd doped analogues [13–17]. At the higher sintering temperature (1200^{o}C), concentrations of cobalt at the grain boundary are shown to be significantly depleted, see Figure 3.6a. Instead of a grain boundary location, accumulation of cobalt is now observed within isolated Co-rich grains, of relatively large size ~0.5 μm, Figure 3.6b. The lattice fringes image taken on this particle and its corresponding digital diffraction pattern are consistent with a cobalt monoxide crystal oriented along the [01-1] zone axis. The analysis clearly reveals that the sintering temperature plays a crucial role in the distribution of the Co sintering aid, with results that mirror those previously reported for Pr and Gd doped analogues [13,20]. The presence of Co-enriched grain boundaries (at lower sintering temperature) or isolated grains (at higher sintering temperature), does not negate the suggestion of some solubility of cobalt in the bulk CTO material. Indeed, as suggested by Balaguer et al. [1,12] the lower lattice parameter noted for the CTO+Co materials in comparison to that of the Co-free composition, Table 3.1, suggests some solubility. However, the current results do highlight that this solubility does not significantly increase with sintering temperature and is shown to be distinctly less than the nominal additive concentration of 2 mol% in both cases. Moreover, the lattice parameters of both the 900 and 1200ºC samples are observed to be similar suggesting similar solubility levels. These low levels of solubility lead to the presence of segregated cobalt in the sintered ceramics, which assumes a different microstructural location depending on sintering temperature.

Conductivity.

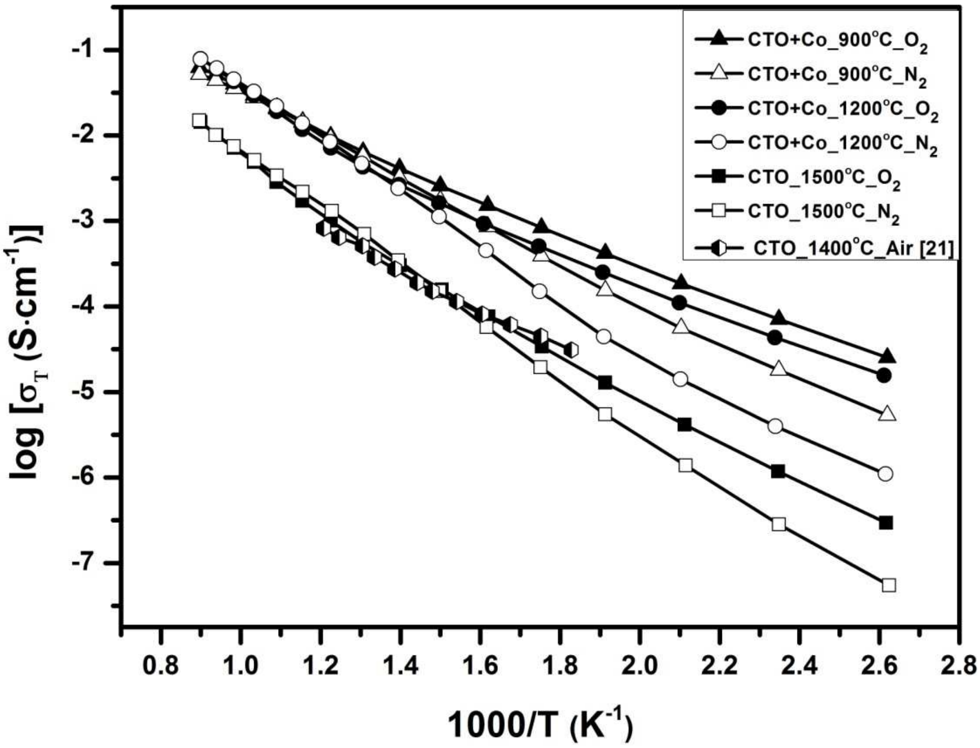

Figure 3.7. Total conductivity of $Ce_{0.8}Tb_{0.2}O_{2-\delta}$ with and without Co sintering aid, measured in dry N_2 or O_2 atmospheres.

Figure 3.7 represents the total conductivity of CTO ceramics sintered at different temperatures with and without cobalt oxide sintering aid, measured under dry atmospheres of O_2 and N_2 gases. In both atmospheres, the oxide sintered at higher temperature (1500°C) without Co shows lower conductivity than the Co-doped CTO sintered at lower temperatures. The total conductivity values for the Co-free sample are shown to correspond well with those reported for pure $Ce_{0.8}Tb_{0.2}O_{2-\delta}$ sintered at 1400°C in the literature [6]. The results of Figure 3.7 clearly demonstrate that minor additions of the Co sintering aid can substantially increase the total conductivity, in agreement with that noted by Balaguer et al. [1,12]. In the lower temperature range, this enhancement of total conductivity is shown to be significantly greater for CTO+Co ceramics sintered at the lower temperature (900°C). A grain boundary network rich in Co additive has been previously shown to enhance total conductivity by reduction of grain boundary resistance [23]. In the 900°C CTO+Co sample similar Co-rich grain boundaries are shown to be present and, thus, can offer an explanation for the higher conductivities observed. At higher measurement temperatures, such effects appear to become negligible, and similar conductivities are obtained for the CTO+Co ceramics sintered at 900 and 1200ºC.

All compositions show higher total conductivities when exposed to more oxidizing environments, i.e. in O_2 rather than N_2, indicating the presence of p-type electronic conductivity. Again, this difference is more pronounced in the lower temperature range, whereas at higher temperatures the total conductivities in O_2 and N_2 are shown to be similar. Table 3.2 summarizes the activation energy values of CTO materials with and without Co in these atmospheres. As temperature increases, all conductivity curves show an increase in gradient, around 400-500^{o}C, most probably reflecting an increase in the significance of the electronic component at lower temperatures due the smaller activation energy of the electronic mobility than that of the ionic [24].

Table 3.2. Activation energy values for the total conductivity of $Ce_{0.8}Tb_{0.2}O_{2-\delta}$ ceramics with and without Co.

Composition	Atmosphere	Activation energy (eV)	
		450-850^{o}C	100-450^{o}C
CTO_1500^{o}C	Oxygen	0.75	0.54
	Nitrogen	0.71	0.66
CTO+Co_1200^{o}C	Oxygen	0.68	0.41
	Nitrogen	0.68	0.60
CTO+Co_900^{o}C	Oxygen	0.55	0.40
	Nitrogen	0.56	0.50

In a similar way, the higher activation energy of the Co-free CTO oxide than Co-doped ceramics can be related to a smaller electronic component. In other words, the addition of Co leads to an increased electronic conductivity and this accounts a decrease in activation energy due to the lower activation energy of the electronic mobility. This is further confirmed by the observation that among Co-doped CTO compositions, the lowest activation energy is characteristic of the oxide sintered at 900°C in which an enhanced electronic conductivity may be offered due to the presence of a Co-rich grain boundary. These suggestions are reinforced in the following section in which the electronic and ionic contributions to total conductivity are separated by the modified EMF technique.

Oxygen ionic and electronic transport.

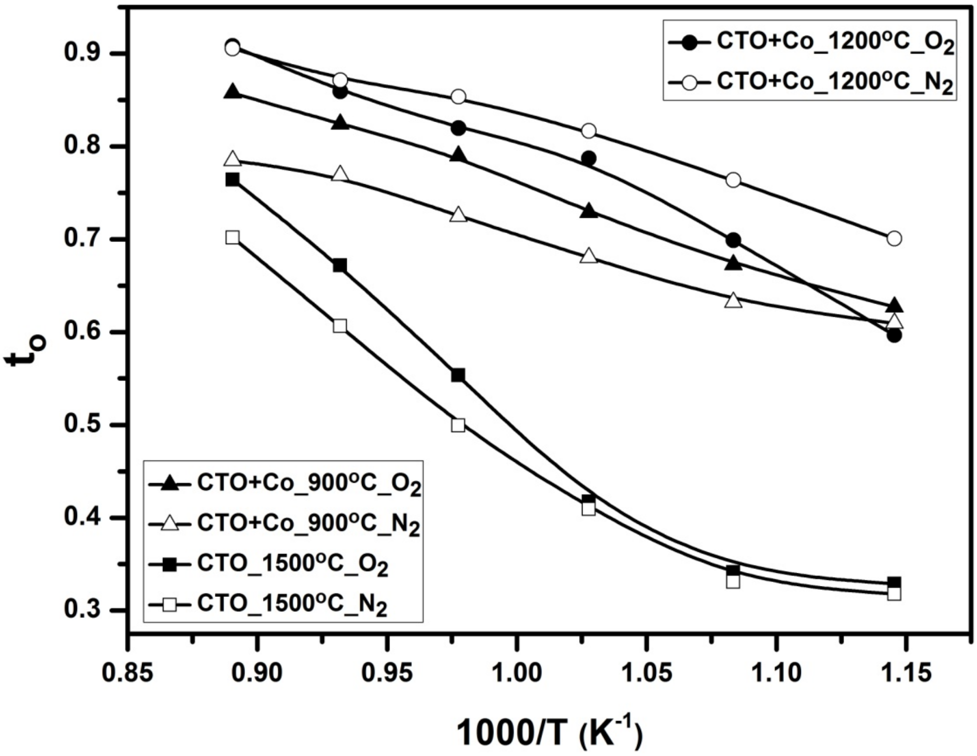

Figure 3.8. Oxide-ion transference numbers of $Ce_{0.8}Tb_{0.2}O_{2-\delta}$ ceramics with and without Co measured in oxygen/air and nitrogen/air gradients, respectively. Labels correspond to active gas.

Figure 3.8 represents the temperature dependence of the oxide-ion transference numbers of $Ce_{0.8}Tb_{0.2}O_{2-\delta}$ with and without Co addition, measured by the modified EMF method. This technique facilitates the separation of the minor contribution of electron-hole conductivity from total conductivity via the elimination of possible electrode polarization effects. The transference numbers were measured across the ceramic membranes under two different pO_2 gradients (oxygen/air and nitrogen/air) in the temperature range from 600 to 850°C. All compositions show positive temperature dependencies of the oxygen ionic transference number. For pure $Ce_{0.8}Tb_{0.2}O_{2-\delta}$, the obtained transference number values are lower as compared to Co-doped CTO, and this difference increases on cooling. Among the CTO+Co ceramics, sintering at higher temperature (1200^{o}C) results in a higher contribution of the ionic conductivity in comparison with that sintered at lower temperature (900^{o}C). This might reflect a loss of the electronic conduction in the Co-doped CTO sintered at 1200^{o}C due to the depletion of a Co-rich grain boundary and the segregation of cobalt as isolated grains, Figure 3.6. In contrast, the lower sintering temperature (900^{o}C) has a potentially higher electronic conductivity due to an increased contribution of cobalt in the grain boundaries, Figure 3.5.

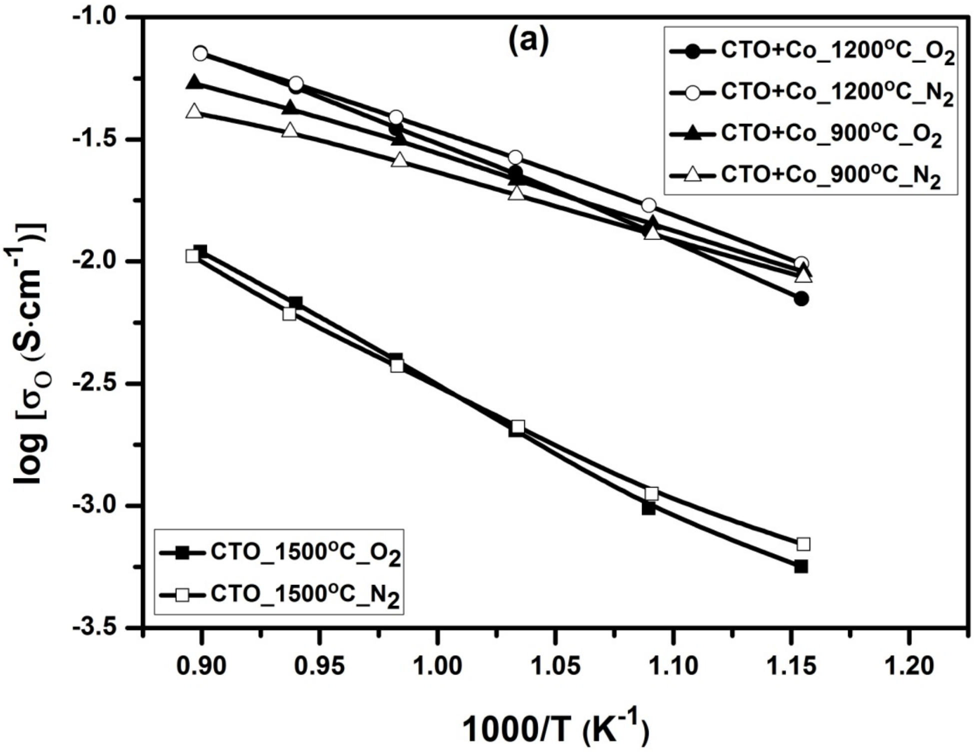

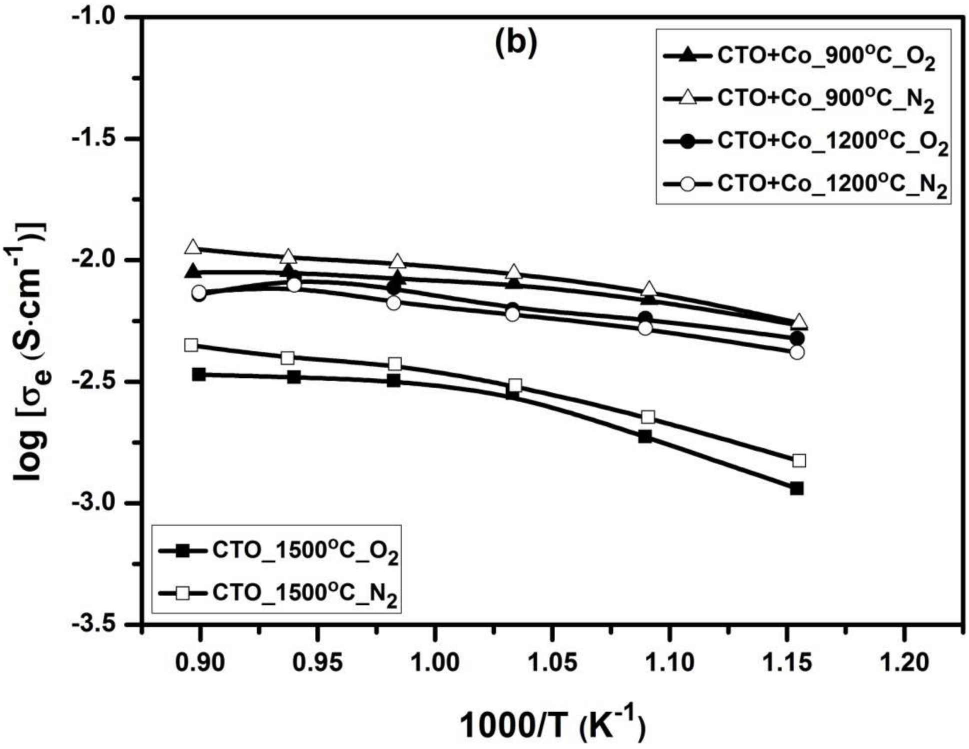

Figure 3.9. (a) Oxygen ionic and (b) electronic conductivities of $Ce_{0.8}Tb_{0.2}O_{2-\delta}$ ceramics with and without Co in N_2 or O_2 atmospheres.

Figure 3.9a shows the temperature dependencies of the partial oxygen ionic conductivity evaluated by the combination of oxygen ionic transference number values with the total conductivity values obtained at identical temperatures:

$$\sigma_o = t_o \sigma_T \qquad (3.1)$$

Note partial conductivities corresponding to oxygen and nitrogen atmospheres were calculated from total conductivity values measured in the respected gases and transference numbers measured obtained under oxygen/air and nitrogen/air gradients, respectively. Thus, to ascribe the calculated partial conductivities to that of pure oxygen or nitrogen atmospheres is an approximation used solely for the purpose of comparison. In this respect, total conductivity values measured at high temperatures were shown to be relatively insensitive to atmosphere, Figure 3.7, thus, potential errors associated with this approximation are minimized.

Pure $Ce_{0.8}Tb_{0.2}O_{2-\delta}$ (sintered at the highest temperature, 1500°C) shows the lowest oxygen ionic conductivity, when compared to CTO+Co ceramics. The CTO samples with cobalt, sintered at both 900 and 1200°C, show similar oxygen ionic conductivities, with very slightly higher ionic conductivity offered by the CTO+Co sample sintered at the higher temperature, 1200ºC. Figure 3.9b represents the partial electronic conductivity values obtained using the equation

$$\sigma_e = (1 - t_o)\sigma_T \tag{3.2}$$

As for oxygen ionic transport, the lowest electronic conductivity is observed for the pure $Ce_{0.8}Tb_{0.2}O_{2-\delta}$ composition. In contrast, the CTO+Co ceramics exhibit significantly higher electronic contributions, with the oxide sintered at the lower temperature (900°C) exhibiting slightly higher values of electronic conductivity throughout the temperature range. This agrees with the suggestion that the presence of cobalt oxide at grain boundaries, Figure 3.5, can lead to an enhancement in electronic conductivity [13–17] and that the beneficial effect of cobalt may be partially spoiled with increasing sintering temperature from 900 to 1200°C. Nonetheless, at these high temperatures these differences in cobalt location cause only minor impact on electrical properties in comparison to that noted at lower temperatures, Figure 3.7. The Co-doped $Ce_{0.8}Tb_{0.2}O_{2-\delta}$ oxides, sintered at 900 and 1200ºC both offer relatively high oxygen ionic and electronic conductivities at elevated temperatures, making them promising materials for MIEC applications [1,12].

Oxygen permeation.

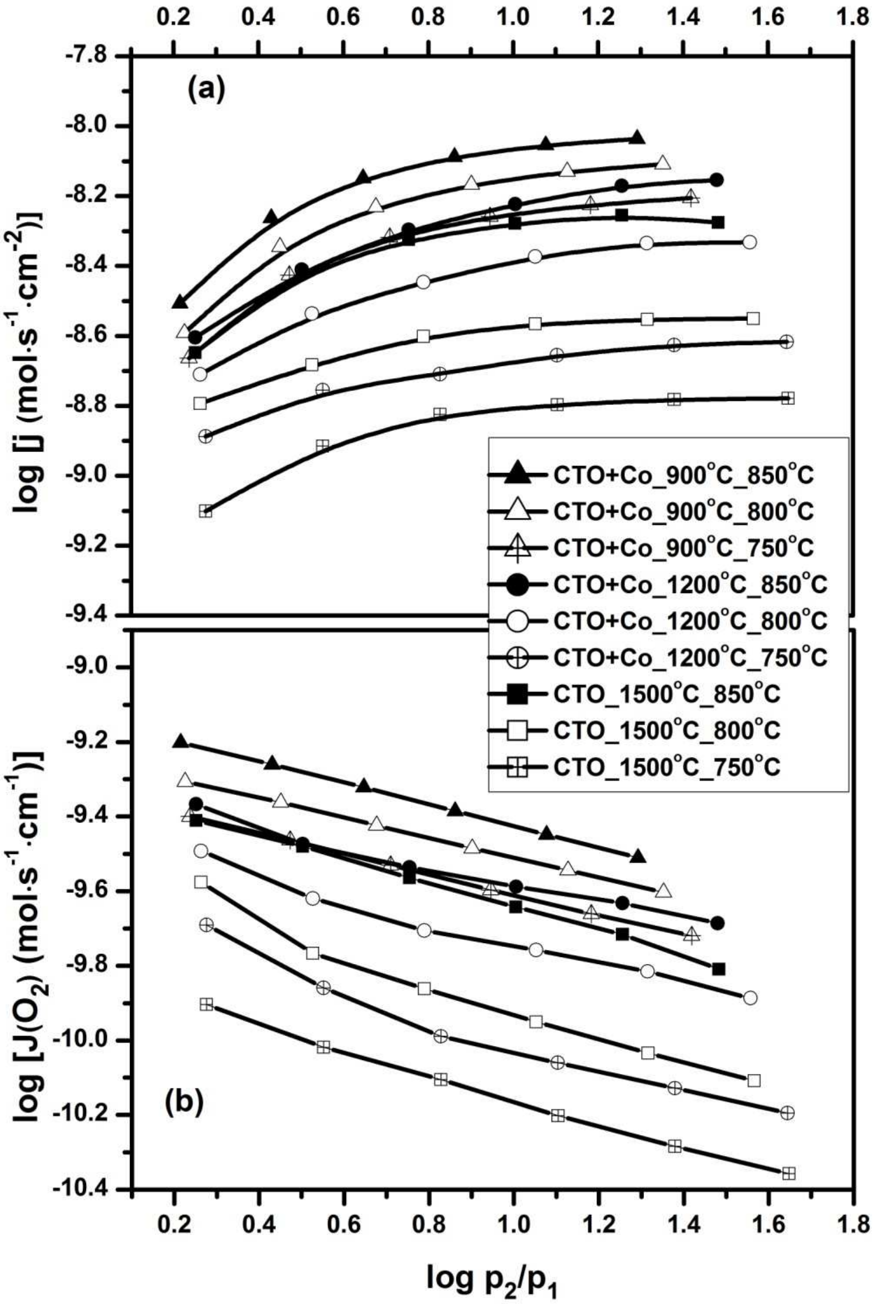

Figure 3.10. (a) The steady state oxygen permeation flux and (b) the specific oxygen permeability values of pure and Co-doped $Ce_{0.8}Tb_{0.2}O_{2-\delta}$ 1 mm thick membranes vs. oxygen partial pressure gradient.

Figures 3.10a and 11b show, respectively, the oxygen flux density, j, and specific oxygen permeability, $J(O_2)$, values of CTO samples with and without Co at different temperatures, as a function of the oxygen partial pressure gradient. The presence of cobalt oxide leads to an enhancement in electronic conductivity as well as in oxygen ionic transport (Figure 3.9) for the CTO+Co ceramics sintered at 900 and 1200ºC. The combination of these effects leads to substantially higher steady state oxygen permeation flux (Figure 3.10a) and corresponding specific oxygen permeability (Figure 3.10b) for cobalt doped CTO samples over that of the Co-free sample sintered at 1500ºC.

The specific oxygen permeability $J(O_2)$ is proportional to the ambipolar conductivity (σ_{amb}) averaged for a given oxygen partial pressure range ($\overline{\sigma_{amb}}$), where t_o is the oxygen ion transference number and σ_T, σ_o and σ_e represent the total, oxygen ionic and electronic conductivities, respectively [17]:

$$J(O_2) = \frac{RT}{16F^2}\overline{\sigma_{amb}} = \frac{RT}{16F^2}\overline{\frac{\sigma_o\sigma_e}{\sigma_o+\sigma_e}} = \frac{RT}{16F^2}\overline{\sigma_T\, t_o(1-t_o)} \qquad (3.3)$$

Using the oxygen ionic transference numbers for oxygen/air gradient (Figure 3.8) and the total conductivity (TC) values in oxygen (Figure 3.7), and the relation between $J(O_2)$ and j (Eq. 2.9), the oxygen permeation flux densities for oxygen/air gradient were calculated. These theoretical and measured oxygen permeation values were used to determine the respective activation energies by the standard Arrhenius equation (see Eq. 2.2 as a model). The activation energy values for experimentally obtained permeation through Co-doped CTO sintered at 1200°C and un-doped CTO are observed to be considerably higher than the respective values for theoretical oxygen fluxes (Table 3.3) and comparable to the activation energies of surface exchange rate of both pure and 2 mol% Co-doped $Ce_{0.8}Tb_{0.2}O_{2-\delta}$ shown in the literature [1]. This means that, in addition to the ionic and electronic conductivities in these oxides, there is an additional process that is limiting oxygen transport through these membranes. This is likely to be slow oxygen surface exchange in Co-doped CTO sintered at 1200°C and un-doped CTO, which limit the observed permeation flux to values below that of the theoretical oxygen permeation calculated from their partial conductivities. Note significant surface exchange limitations have also been reported for both pure and highly (5 mol%) Co-doped $Ce_{0.8}Pr_{0.2}O_{2-\delta}$ in the literature [17]. On the contrary, the activation energy values for experimentally obtained and calculated oxygen permeation through the Co-doped CTO membrane sintered at 900°C are shown to be comparable, indicating that the overall oxygen transport is only governed by the electronic and oxygen ionic conductivities, without significant influence of surface kinetics. The absence of surface exchange limitations in the 900ºC CTO+Co sample is reminiscent of that noted for the 2 mol% Co-doped, Pr analogue, $Ce_{0.8}Pr_{0.2}O_{2-\delta}$ sintered at the same temperature [17].

Table 3.3. Oxygen permeation fluxes and their apparent activation energies.

Activation energy for oxygen permeation				
Material	Calculated from EMF (oxygen/air gradient) and TC		Measured	
	T (^{o}C)	E_a (ev)	T (^{o}C)	E_a (ev)
CTO+Co_900^{o}C	600-850	0.46 ± 0.08	650-850	0.43 ± 0.04
CTO+Co_1200^{o}C	600-850	0.48 ± 0.13	700-850	1.17 ± 0.17
CTO_1500^{o}C	600-850	0.85 ± 0.15	750-850	1.23 ± 0.15

Oxygen permeation flux values					
Material	T (^{o}C)	Calculated from EMF (oxygen/air gradient) and TC		Measured	
		$\log(p_2/p_1)$	j_{theor} ($mol \cdot s^{-1} \cdot cm^{-2}$)	$\log(p_2/p_1)$	j_{exp} ($mol \cdot s^{-1} \cdot cm^{-2}$)
CTO+Co_900^{o}C	850	0.67	7.3×10^{-9}	0.65	7.1×10^{-9}
	800	0.67	6.7×10^{-9}	0.68	5.9×10^{-9}
	750	0.66	5.7×10^{-9}	0.71	4.8×10^{-9}
CTO+Co_1200^{o}C	850	0.68	6.3×10^{-9}	0.75	5.1×10^{-9}
	800	0.68	6.7×10^{-9}	0.79	3.6×10^{-9}
	750	0.67	5.6×10^{-9}	0.83	2.0×10^{-9}

Table 3.3 also compares the theoretical and experimental oxygen permeation fluxes of Co-doped CTO membranes sintered at 900 and 1200°C under similar $p(O_2)$ gradients. Since the oxygen ionic and electronic conductivities of these two materials have been measured to be similar at these temperatures, Figure 3.9, the theoretical oxygen fluxes evaluated on this basis are also shown to be close. Measured and calculated flux densities through the Co-doped CTO membrane sintered at 900°C are shown to coincide, confirming the absence of significant influence of surface exchange kinetics on the oxygen permeation process.

In contrast the measured and calculated oxygen flux values for the Co-doped CTO membrane sintered at 1200°C are shown to deviate from each other and this deviation becomes increasingly more significant with decreasing temperature. At the highest temperature the deviation is shown to be small, albeit larger than that in the 900ºC sintered sample under similar conditions. The small deviation noted at high temperatures suggests that only slight surface exchange limitations are present, where the oxygen flux will still be predominantly governed by the electronic and ionic conductivities. The same conclusion was made on comparison of experimental and calculated oxygen fluxes of $Ce_{0.9}Tb_{0.1}O_{2-\delta}$ with Co (2 mol%) and $Ce_{0.8}Tb_{0.2}O_{2-\delta}$ with Co (2 mol%) measured at 860°C in the literature, for samples sintered at 1300ºC [12]. However, the increasing deviation between experimental and theoretical values of flux density as the measurement temperature decreases, is a strong argument in favor of the presence of oxygen surface exchange limitations in the 1200ºC sintered membrane that have a greater impact on the oxygen permeation at lower temperatures.

Upon reference to the conclusions of the TEM study in Figures 3.5 and 3.6, the presence of significant surface exchange limitations in the 1200ºC sintered CTO+Co sample can be suggested to be due to cobalt depletion of Co-enriched grain boundaries that may serve to promote oxygen surface exchange in the sample sintered at lower temperature. Such an effect would lead to the observed decrease in the measured oxygen permeation flux and an increase in the activation energy. This suggestion is supported by the absence of surface exchange limitations reported for the 2 mol% Co-doped Pr analogue, $Ce_{0.8}Pr_{0.2}O_{2-\delta}$ sintered under similar conditions, where a similar Co-rich grain boundary network had been observed [17]. Note that the effectiveness of the Co-rich grain boundary network to promote oxygen surface exchange was shown to be highly sensitive to its microstructure and was impaired when the grain boundary network became over concentrated in 5 mol% Co doped $Ce_{0.8}Pr_{0.2}O_{2-\delta}$, regardless of a similar ambipolar conductivity [17]. The current results suggest an analogous concept that the concentration of cobalt in the grain boundaries may have become less than its optimal concentration and, thus, fail to adequately prevent oxygen surface exchange limitations in the sample sintered at 1200ºC. In addition, the results concur with that expected from morphological considerations of these samples. Increased mixed conductivity and faster oxygen exchange have been documented for ceria-based materials upon grain size reduction within the submicron range [18,19]. In agreement, the CGO+Co sample sintered at 900ºC, with the smallest sub-micron grain size, is shown to offer the highest mixed conductivity and fastest oxygen exchange of all samples.

3.4. Conclusions

The addition of cobalt decreased the sintering temperature of $Ce_{0.8}Tb_{0.2}O_{2-\delta}$ materials allowing dense, gas-tight CTO ceramics to be formed at 900ºC. The lower sintering temperature resulted in a sub-micron grain size. The transport properties of $Ce_{0.8}Tb_{0.2}O_{2-\delta}$ materials were shown to be significantly influenced by the additions of cobalt oxide sintering aid as well as by sintering temperature. In the lower temperature range, the highest total conductivity was offered by the cobalt containing material sintered at 900ºC. The cobalt containing materials possess substantially higher total, ionic and electronic conductivities than the Co-free sample sintered at 1500ºC. For the Co containing samples further increase of sintering temperature above 900ºC was shown to lead to slight degradation in electronic conductivity. Consequently, the Co-doped $Ce_{0.8}Tb_{0.2}O_{2-\delta}$ material sintered at the lower sintering temperature (900^{o}C) offered the higher oxygen permeation flux when compared to CTO+Co ceramics sintered at higher temperature (1200^{o}C). This was shown to be related to the beneficial effect of Co on surface exchange limitations when cobalt is present in the grain boundary. On sintering at higher temperature, this Co rich grain boundary is shown to be depleted and the cobalt additions are instead manifested as isolated grains. Moreover, the performance of these materials is shown to be inversely dependent on their grain size, with the highest mixed conductivity and surface exchange offered by the sample with the smallest grain size. The current work shows promising transport characteristics of

$Ce_{0.8}Tb_{0.2}O_{2-\delta}$ with minor concentration of Co sintering additive, offering its maximum value for samples sintered at the lower temperature of 900°C.

3.5. References

[1] M. Balaguer, C.-Y. Yoo, H.J.M. Bouwmeester, J.M. Serra, Bulk transport and oxygen surface exchange of the mixed ionic–electronic conductor $Ce_{1-x}Tb_xO_{2-\delta}$ (x = 0.1, 0.2, 0.5), Journal of Materials Chemistry A 1 (2013) 10234.

[2] K.J. de Vries, G.-Y. Meng, Phase formation and thermal stability of fcc (Fluorite) $Ce_{1-x}Tb_xO_{2-\delta}$ solid solutions, Materials Research Bulletin 33 (1998) 357–367.

[3] A.B. Hungría, A. Martínez-Arias, M. Fernández-García, A. Iglesias-Juez, A. Guerrero-Ruiz, J.J. Calvino, J.C. Conesa, J. Soria, Structural, morphological, and oxygen handling properties of nanosized cerium−terbium mixed oxides prepared by microemulsion, Chemistry of Materials 15 (2003) 4309–4316.

[4] X. Wang, J.C. Hanson, G. Liu, J.A. Rodriguez, A. Iglesias-Juez, M. Fernández-García, The behavior of mixed-metal oxides: physical and chemical properties of bulk $Ce_{1-x}Tb_xO_2$ and nanoparticles of $Ce_{1-x}Tb_xO_y$, The Journal of Chemical Physics 121 (2004) 5434–5444.

[5] B.M. Reddy, P. Saikia, P. Bharali, Y. Yamada, T. Kobayashi, M. Muhler, Structural characterization and catalytic activity of nanosized ceria−terbia solid solutions, The Journal of Physical Chemistry C 112 (2008) 16393–16399.

[6] P. Shuk, M. Greenblatt, M. Croft, Hydrothermal synthesis and properties of mixed conducting $Ce_{1-x}Tb_xO_{2-\delta}$ solid solutions, Chemistry of Materials 11 (1999) 473–479.

[7] F. Ye, T. Mori, D.R. Ou, M. Takahashi, J. Zou, J. Drennan, Compositional dependence of electrical conductivity of $Ce_{1-x}Tb_xO_{2-\delta}$ ($0 \leq x \leq 1$), Renewable Energy 33 (2008) 331–335.

[8] Y. Xia, Y. Bai, X. Wu, D. Zhou, Z. Wang, X. Liu, Effect of sintering aids on the electrical properties of $Ce_{0.9}Nd_{0.1}O_{2-\delta}$, Solid State Sciences 14 (2012) 805–808.

[9] M. Balaguer, C. Solís, J.M. Serra, Structural − transport properties relationships on $Ce_{1-x}Ln_xO_{2-\delta}$ system (Ln = Gd, La, Tb, Pr, Eu, Er, Yb, Nd) and effect of cobalt addition, The Journal of Physical Chemistry C 116 (2012) 7975−7982.

[10] T.S. Zhang, J. Ma, Y.J. Leng, S.H. Chan, P. Hing, J.A. Kilner, Effect of transition metal oxides on densification and electrical properties of Si-containing $Ce_{0.8}Gd_{0.2}O_{2-\delta}$ ceramics, Solid State Ionics 168 (2004) 187–195.

[11] C. Kleinlogel, L.J. Gauckler, Sintering and properties of nanosized ceria solid solutions, Solid State Ionics 135 (2000) 567–573.

[12] M. Balaguer, C. Solís, M. Serra, Study of the transport properties of the mixed ionic electronic conductor $Ce_{1-x}Tb_xO_{2-\delta}$ + Co (x = 0.1, 0.2) and evaluation as oxygen-transport membrane, Chemistry of Materials 23 (2011) 2333–2343.

[13] D.P. Fagg, J.C.C. Abrantes, D. Pérez-Coll, P. Núñez, V.V. Kharton, J.R. Frade, The effect of cobalt oxide sintering aid on electronic transport in $Ce_{0.80}Gd_{0.20}O_{2-\delta}$ electrolyte, Electrochimical Acta 48 (2003) 1023–1029.

[14] D.P. Fagg, V.V. Kharton, J.R. Frade, P-Type electronic transport in $Ce_{0.8}Gd_{0.2}O_{2-\delta}$:The effect of transition metal oxide sintering aids, Journal of Electroceramics (2003) 199–207.

[15] D.P. Fagg, V.V. Kharton, J.R. Frade, Transport in ceria electrolytes modified with sintering aids: effects on oxygen reduction kinetics, Journal of Solid State Electrochemistry 8 (2004) 618–625.

[16] D.P. Fagg, A.L. Shaula, V.V. Kharton, J.R. Frade, High oxygen permeability in fluorite-type $Ce_{0.8}Pr_{0.2}O_{2-\delta}$ via the use of sintering aids, Journal of Memberane Science 299 (2007) 1–7.

[17] D.P. Fagg, S. García-martin, V.V. Kharton, J.R. Frade, Transport properties of fluorite-type $Ce_{0.8}Pr_{0.2}O_{2-\delta}$: optimization via the use of cobalt oxide sintering aid, Chemistry of Materials 21 (2009) 381–391.

[18] G.M. Christie, F.P.F. van Berkel, Microstructure—ionic conductivity relationships in ceria-gadolinia electrolytes, Solid State Ionics 83 (1996) 17–27.

[19] I. Kosacki, H.U. Anderson, Microstructure—Property relationships in nanocrystalline oxide thin films, Ionics 6 (2000) 294–311.

[20] M. Balaguer, C. Solís, S. Roitsch, J.M. Serra, Engineering microstructure and redox properties in the mixed conductor $Ce_{(0.9)}Pr_{(0.1)}O_{(2-\delta)}$ + Co 2 mol%., Dalton Trans 43 (2014) 4305–4312.

[21] A. Kaiser, A.S. Prasad, S.P. Foghmoes, S. Ramousse, N. Bonanos, V. Esposito, Sintering process optimization for multi-layer CGO membranes by in situ techniques, Journal of the European Ceramic Society 33 (2013) 549–556.

[22] D. Pérez-Coll, J.C. Ruiz-Morales, D. Marrero-López, P. Núñez, J.R. Frade, Effect of sintering additive and low temperature on the electrode polarization of CGO, Journal of Alloys and Compounds 467 (2009) 533–538.

[23] D. Pérez-Coll, P. Núñez, J.C. Ruiz-Morales, J. Peña-Martínez, J.R. Frade, Re-examination of bulk and grain boundary conductivities of $Ce_{1-x}Gd_xO_{2-\delta}$ ceramics, Electrochimica Acta 52 (2007) 2001–2008.

[24] C. Chatzichristodoulou, P.V. Hendriksen, Electronic and ionic transport in $Ce_{0.8}Pr_xTb_{0.2-x}O_{2-\delta}$ and evaluation of performance as oxygen permeation membranes, Journal of the Electrochemical Society 159 (2012) E162–E170.

4. Comparative study of fluorite-type ceria-based $Ce_{1-x}Ln_xO_{2-\delta}$ (Ln = Tb, Gd and Pr) mixed ionic electronic conductors densified at low temperatures

4.1. Introduction

Significant scientific effort has been devoted to the study of ceria-based oxides, as they can exhibit ionic conducting, electronically conducting, or mixed conducting properties depending on substitution mechanism, rendering them appropriate for a variety of applications, such as electrolytes and electrodes for solid oxide fuel cells (SOFCs),[1,2] oxygen sensors,[3] oxygen permeation membranes[4] and ultraviolet ray absorbents.[5] Although perovskite and perovskite-related structure materials have traditionally been the most widely studied as potential mixed conductors,[6,7] significant levels of ambipolar conductivity can also be obtained in materials of the defect cubic fluorite-type structure by substitution of mixed-valence elements into recognized fast ionic conductors, for example, Nb or Ti substitution into zirconia-based fluorites.,[8,9] or Pr and Tb into ceria-based fluorites [4,10,11]. In the case of the ceria-based materials, such substitution mechanisms can lead to p-type electronic conductivity in oxidizing conditions, via small polaron hopping arising from Pr^{3+}/Pr^{4+} or Tb^{3+}/Tb^{4+},[4,10,11] whereas, under reducing environments n-type electronic conductivity can also be induced due to partial reduction of Ce^{4+} to Ce^{3+}[12–14]. Additional gains in ambipolar conductivity can also be obtained in oxidizing conditions by the presence of small quantities of sintering additives, where preferential segregation of the additive to grain boundaries has been demonstrated to lead to beneficial effects on the level of electronic conductivity [11,15–17]. Several transition elements have been recorded to show this effect e.g. Cu, Co, Fe, with the most studied being that of minor cobalt oxide additions (2 mol%), where significantly enhanced densification and improved ambipolar conductivities have been documented for a wide range of $Ce_{1-x}Ln_xO_{2-\delta}$ systems (Ln = Tb, Pr, Gd, La, Eu, Er, Yb and Nd) [10,11,15,16,18–20].

The concept behind the present study follows from the observation that the sintering temperature of ceria-based materials with Co-sintering additives is a critical factor to obtain the desired enhanced electrical performance. Excessive sintering temperatures are shown to lead to grain growth and significant segregation of cobalt into isolated grains, resulting in decreased ambipolar conductivities and oxygen permeation fluxes [17,20,21]. Therefore, in the current chapter we analyze $Ce_{0.8}Tb_{0.2}O_{2-\delta}$ with small additions (2 mol%) of cobalt oxide sintering aid, sintered at low temperature (<1000ºC) where optimal transport properties are maintained [15,17,21]. Electrical conductivity, EMF and oxygen permeability measurements were performed in order to understand the behavior of CTO mixed ionic electronic conductor and results were compared to the transference numbers, total and partial ionic and electronic conductivities, and oxygen permeability of cobalt doped $Ce_{0.8}Gd_{0.2}O_{2-\delta}$, $Ce_{0.8}Pr_{0.2}O_{2-\delta}$ materials prepared under similar low temperature conditions. In this way, the current article provides a direct appraisal of the peak electrical properties and oxygen permeabilities obtainable from $Ce_{1-x}Ln_xO_{2-\delta}$ (Ln = Tb, Pr, Gd) materials.

4.2. Experimental Section

Cerium-terbium oxide ($Ce_{0.8}Tb_{0.2}O_{2-\delta}$) materials were prepared by the hydrothermal method as previously described in Chapter 2.1. Pellets of the cerium terbium oxide (CTO) with 2 mol% Co addition, were prepared as described in the Chapter 2.1, and subsequently uniaxially dry pressed at a pressure of 60 MPa followed by isostatic pressing at 200 MPa. The pellets were sintered at 900°C for 5 h, heating and cooling rates were 2°C/min.

Phase analysis was performed by room temperature XRD and Microstructural characterization was performed by SEM for Co-doped CTO ceramics. TEM studies of the microstructure and chemical composition of the Co-doped CTO samples also were performed as described in Chapter 2.1.

The total conductivity, transport number and oxygen permeability measurements were performed in order to understand the MIECs properties of $Ce_{0.8}Tb_{0.2}O_{2-\delta}$ with 2mol% Co additions and compared with data for $Ce_{0.8}Pr_{0.2}O_{2-\delta}$ and $Ce_{0.8}Gd_{0.2}O_{2-\delta}$ materials with 2mol% Co additions, prepared under similar conditions [11,16].

4.3. Results and Discussion

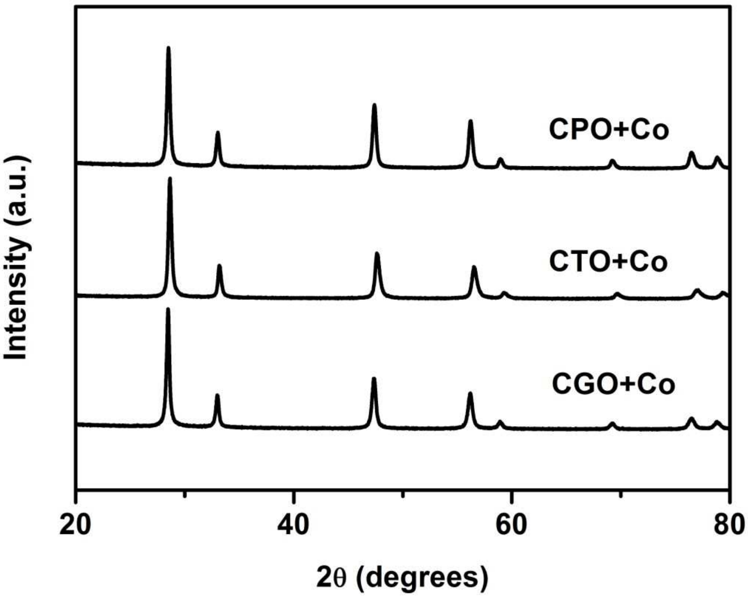

Figure. 4.1. X-ray diffraction patterns of Co-doped $Ce_{1-x}Ln_xO_{2-\delta}$ (Ln = Gd, Tb and Pr) sintered ceramics.

Figure 4.1 shows the XRD patterns of $Ce_{0.8}Ln_{0.2}O_{2-\delta}$ ceramic samples (Ln = Gd, Pr, Tb) sintered at low temperatures ≤1000°C with cobalt oxide (2 mol%) sintering aid. The patterns show broad peaks, reflecting that the formed ceramics are constituted by relatively small grains, Table 4.1. The corresponding lattice parameters (refined from the XRD patterns), average grain sizes (measured by scanning electron microscopy) and densities of the samples are summarized in Table 4.1. The data show that dense materials with sub-micron grain size are obtained after sintering at relatively low temperatures (≤1000°C) by addition of 2 mol% of cobalt oxide as a sintering aid. Although the ionic radii of the lanthanide dopants increases in the sequence Tb < Gd < Pr, for the same 3+ oxidation state, a direct correlation cannot be made with the measured lattice parameters, due to the variable valence of the Tb and Pr dopants [22].

Table 4.1. Lattice parameters and average grain sizes of Co-doped $Ce_{1-x}Ln_xO_{2-\delta}$ (Ln = Gd, Tb and Pr) sintered ceramics.

Composition	Sintering temperature	Lattice parameter (Å)	Average grain size	Densities %

	(°C)	(±0.0003)	(μm)	
CGO+Co	900	5.4275	~ 0.1-0.2	95−99
CTO+Co	900	5.3910	~ 0.34 ± 0.10	93
CPO+Co	1000	5.4106	~ 0.14 ± 0.02	>90

Conductivity

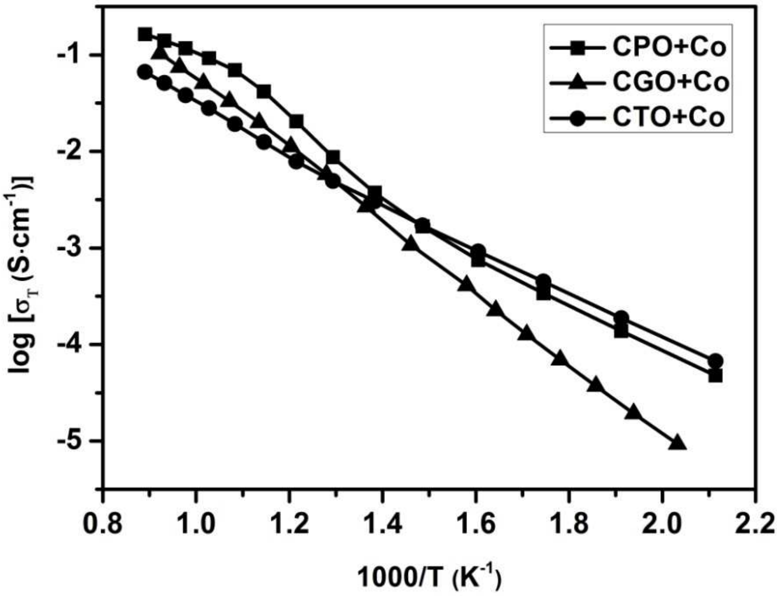

Figure 4.2. Total conductivity of $Ce_{0.8}Ln_{0.2}O_{2-\delta}$ (Ln = Pr, Tb and Gd) ceramics with Co sintering aid in air.

Figure 4.2 shows the total conductivities of $Ce_{0.8}Pr_{0.2}O_{2-\delta}$, $Ce_{0.8}Gd_{0.2}O_{2-\delta}$ and $Ce_{0.8}Tb_{0.2}O_{2-\delta}$ ceramics with Co addition, sintered at low temperatures and measured in air using impedance spectroscopy. At higher temperatures, the largest total conductivity can be observed for CPO+Co ceramics. With respect to the other compositions, CGO+Co shows a more elevated total conductivity than CTO+Co in the higher temperature range, while at lower temperatures this tendency is reversed. The activation energies of the total conductivity of these materials show distinct variations between low and high temperature ranges and this feature is most pronounced for materials containing variable valent dopants, Pr and Tb. For these materials, this effect can be related, predominantly, to the changing oxidation states of Pr and Tb with temperature [23]. On the contrary, in the Gd-doped case this change in activation energy has previously been related to order and disorder transitions of the oxygen sublattice [24].

Table 4.2. Activation energy values for the total conductivity of $Ce_{0.8}Ln_{0.2}O_{2-\delta}$ (Ln = Pr, Tb and Gd) ceramics with Co.

Composition	Atmosphere	Activation energy (eV)	
		500-850°C	200-500°C
CGO+Co	air	0.77 ± 0.02	0.79 ± 0.02
CTO+Co	air	0.64 ± 0.01	0.50 ± 0.01
CPO+Co	air	0.70 ± 0.12	0.59 ± 0.06

EMF:

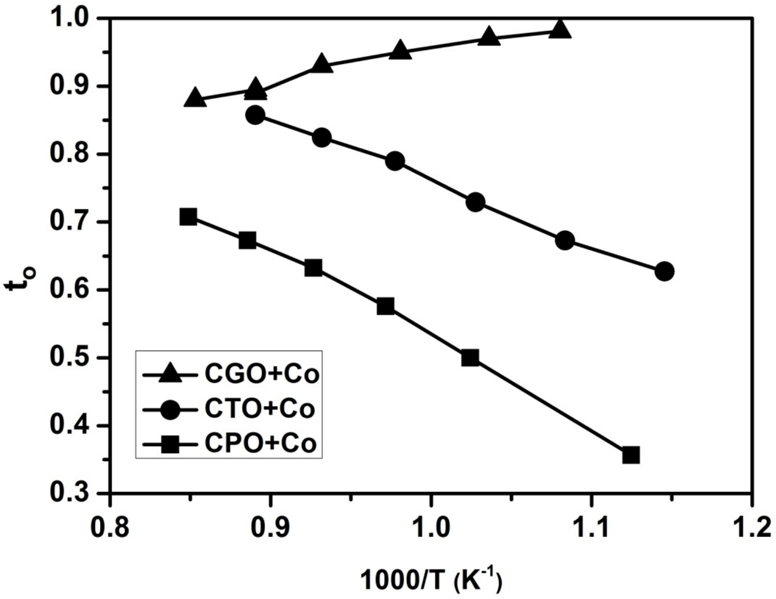

Figure 4.3. Oxygen ionic transference numbers of $Ce_{0.8}Ln_{0.2}O_{2-\delta}$ (Ln = Pr, Tb and Gd) ceramics with Co sintering aid, measured in oxygen/air gradient.

Figure 4.3 represents the behavior of oxygen ionic transference numbers of $Ce_{0.8}Ln_{0.2}O_{2-\delta}$ (Ln = Pr, Tb and Gd) ceramics with Co sintering aid measured by the modified EMF method. This method facilitates the separation of the minor contribution of electronic transport from the total conductivity via the elimination of possible electrode polarization effects. The ionic transference numbers were measured across the membrane under pO_2 gradient (oxygen/air) in the temperature range from 850 to 600°C. Obtained transference numbers show that CGO+Co and CTO+Co ceramics are predominantly oxygen ionic conductors at these temperatures, in contrast with mixed-conducting CPO+Co material. The CGO+Co composition sintered at 900°C displays oxygen ionic transference numbers that increase with decreasing temperature, approaching unity at the lowest temperatures measured. In contrast, the ionic transference numbers of the CPO+Co and CTO+Co compositions are shown to decrease with decreasing temperature.

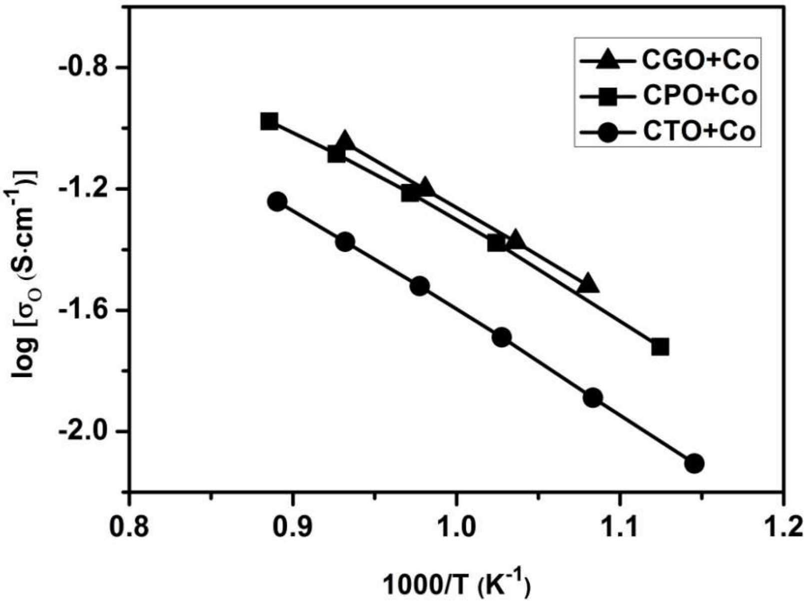

Figure 4.4. Oxygen ionic conductivities of $Ce_{0.8}Ln_{0.2}O_{2-\delta}$ (Ln = Pr, Tb and Gd) ceramics with Co sintering aid in air.

The combination of ionic transference numbers (t_o) with total conductivity (σ_T) measured in air by impedance spectroscopy at corresponding temperatures allows the estimation of ionic conductivity (σ_o) through the following relation,

$$\sigma_o = t_o \sigma_T \tag{4.1}$$

Figure 4.4 summarizes the temperature dependencies of the partial oxygen ionic conductivities of these materials resulting from Eq. (4.1). The compositions CGO+Co and CPO+Co show similar levels of ionic conductivity that are considerably higher than that offered by the terbium doped, CTO+Co, composition. All compositions show similar activation energies for ionic conductivity in the studied temperature range, Table 4.3.

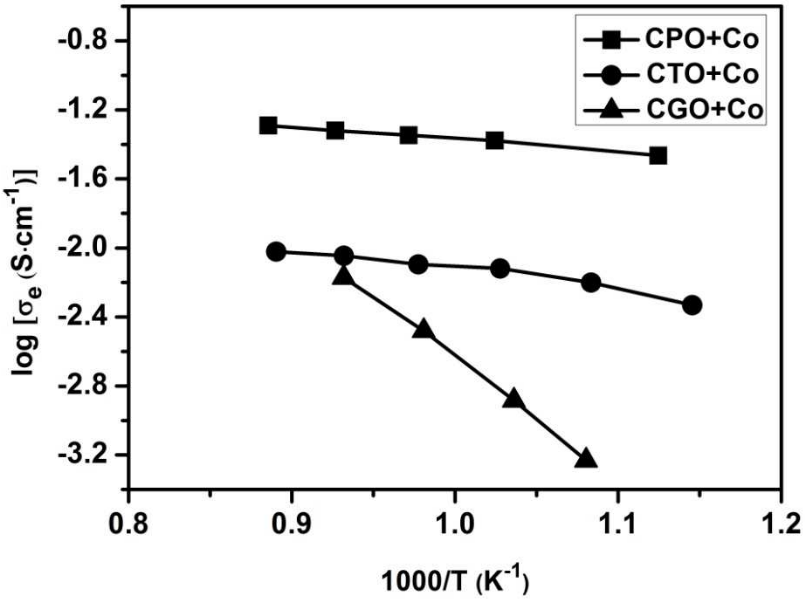

Figure 4.5. Electronic conductivities of $Ce_{0.8}Ln_{0.2}O_{2-\delta}$ (Ln = Pr, Tb and Gd) ceramics with Co sintering aid in air.

In a similar way, the electronic conductivity can be estimated from oxygen ionic transference numbers and total conductivity values at corresponding temperatures as follows,

$$\sigma_e = (1-t_o)\,\sigma_T \qquad (4.2)$$

It has been reported that the addition of 2 mol% CoO into $Ce_{0.8}Gd_{0.2}O_{2-\delta}$, $Ce_{0.8}Tb_{0.2}O_{2-\delta}$ and $Ce_{0.8}Pr_{0.2}O_{2-\delta}$ systems can lead to enhancement of p-type electronic conductivities over the base compositions and this enhancement is greatest for materials sintered at low temperatures (<1000ºC) [17,20,21]. For these peak performing materials, Figure 4.5 shows that the highest electronic conductivities are offered by the compositions containing the variable valent lanthanide dopants, Pr and Tb. The highest electronic contribution of all materials studied is offered by the composition CPO+Co. The activation energies of the electronic conductivity of the CPO+Co and CTO+Co compositions is shown to be similar and to be lower than that of the CGO+Co material, Table 4.3.

Table 4.3. Activation energy values for the ionic and electronic conductivities in air, and oxygen permeation (at log (p_2/p_1) ≈ 0.7) of $Ce_{0.8}Ln_{0.2}O_{2-\delta}$ (Ln = Pr, Tb and Gd) ceramics with Co.

Composition	Activation energy (eV)

	ionic	electronic	oxygen permeation
CGO+Co	0.71 ± 0.01	1.50 ± 0.20	1.56 ± 0.20
CTO+Co	0.75 ± 0.02	0.32 ± 0.08	0.43 ± 0.04
CPO+Co	0.72 ± 0.19	0.33 ± 0.14	0.49 ± 0.09

Oxygen permeability

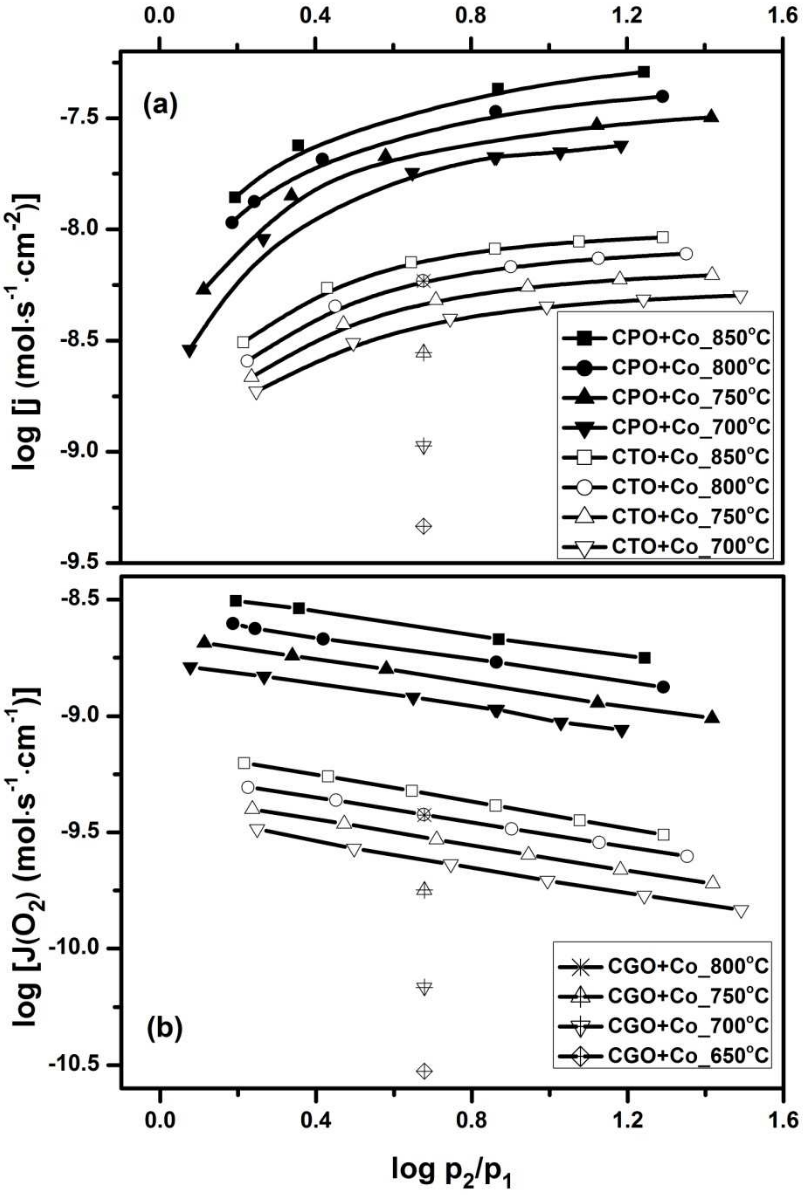

Figure 4.6. The steady state oxygen permeation fluxes (a) and specific oxygen permeability values (b) for Co-doped Ce$_{0.8}$Ln$_{0.2}$O$_{2-\delta}$ (Ln = Pr, Tb and Gd) 1 mm thick membranes vs. oxygen partial pressure gradient (for Pr and Tb – measured, for Gd – calculated).

Figures 4.6a and 4.6b show, respectively, the oxygen flux density, j, and specific oxygen permeability, $J(O_2)$, for the CTO+Co, CPO+Co and CGO+Co compositions at different temperatures, as a function of the oxygen partial pressure gradient. Previous literature has shown that oxygen surface exchange limitations are insignificant for 2 mol% cobalt oxide doped CTO[17,19] and CPO[11] materials, in the studied temperature range. Moreover, considering that increased mixed conductivity and faster oxygen surface exchange has been reported for ceria-based oxides when the grain size decreases to the sub-micron range,[25,26] the surface kinetics of 2 mol% cobalt oxide doped CGO is assumed to not limit significantly the oxygen permeation for the following comparison; in other words, the results presented for this composition in Fig. 4.6 should be considered as a best case scenario. The oxygen permeation flux and, consequently, specific permeability values of Co-doped $Ce_{0.8}Pr_{0.2}O_{2-\delta}$ are substantially higher than those of Co-doped $Ce_{0.8}Tb_{0.2}O_{2-\delta}$ and Co-doped $Ce_{0.8}Gd_{0.2}O_{2-\delta}$ for these peak performing materials sintered at low temperatures. The higher partial oxygen ionic and electronic conductivities result in higher oxygen permeability (assuming negligible surface exchange limitations), achieving a maximum when these conductivities are similar ($t_o \approx 0.5$). Indeed, Co-doped $Ce_{0.8}Pr_{0.2}O_{2-\delta}$ offers a better combination of the oxygen ionic transference number (Fig. 4.3) and partial conductivities (Figs. 4.4 and 4.5), when compared with that offered by CTO+Co and CGO+Co.

At 800°C, the oxygen permeability values of Co-doped $Ce_{0.8}Tb_{0.2}O_{2-\delta}$ and $Ce_{0.8}Gd_{0.2}O_{2-\delta}$ are very close (Fig. 4.6), reflecting that their ambipolar conductivities ($\overline{\sigma_{amb}} = \frac{\sigma_o \sigma_e}{\sigma_o + \sigma_e}$) at this temperature are similar. Thus, even though the oxygen ionic conductivity of CGO+Co is noted to be significantly higher than that of CTO+Co (Fig. 4.4), its ambipolar conductivity is limited by a low level of electronic conduction that is inferior to that offered by the CTO+Co composition under these conditions (Fig. 4.5). On decreasing temperature, the difference in electronic conductivity between these two oxides increases (Fig. 4.5), as the activation energy of electronic conduction for CGO+Co is considerably higher than that of CTO+Co (Table 4.3). Thus, at lower temperatures the lower electronic component in the CGO+Co case can no longer be compensated (in terms of ambipolar conductivity) by ionic conductivity due to the similar activation energies for ionic conductivity of these materials, Table 4.3 (Fig. 4.4). As a consequence, the oxygen permeation of Co-doped $Ce_{0.8}Gd_{0.2}O_{2-\delta}$ becomes progressively lower than that of Co-doped $Ce_{0.8}Tb_{0.2}O_{2-\delta}$, upon decreasing temperature (Fig. 4.6).

On consideration of the definition of ambipolar conductivity ($\overline{\sigma_{amb}} = \frac{\sigma_o \sigma_e}{\sigma_o + \sigma_e}$), it becomes clear that if one of the partial conductivities is significantly lower than the other one (for CGO+Co, $\sigma_e << \sigma_o$), the ambipolar conductivity and, therefore, oxygen permeation, become limited by this contribution (for example in the case of CGO+Co, limitation in ambipolar conductivity is by the level of electronic transport: $\overline{\sigma_{amb}} \approx \sigma_e$). In agreement, the activation energy of oxygen permeation flux through Co-doped $Ce_{0.8}Gd_{0.2}O_{2-\delta}$ membrane, Table 4.3, determined according to the standard Arrhenius equation is very similar to the activation energy of its electronic transport (Table 4.3), further highlighting that the oxygen permeability of CGO+Co is mostly limited by its bulk electronic conduction.

The activation energy values of oxygen permeation flux for Co-doped $Ce_{0.8}Pr_{0.2}O_{2-\delta}$ and $Ce_{0.8}Tb_{0.2}O_{2-\delta}$ lie between their respective activation energy values for oxygen ionic and electronic conductivities, being slightly closer to the activation energy of electronic transport (Table 4.3). This indicates that the oxygen permeability of CPO+Co and CTO+Co, contrary to CGO+Co, is governed by both partial conductivities. The oxygen ionic transference numbers (Fig. 4.3) confirm this assumption, as t_o values of Co-doped $Ce_{0.8}Pr_{0.2}O_{2-\delta}$ and $Ce_{0.8}Tb_{0.2}O_{2-\delta}$ are considerably closer to 0.5, than those of Co-doped $Ce_{0.8}Gd_{0.2}O_{2-\delta}$.

4.4. Conclusions

The introduction of small amount (2 mol%) of cobalt oxide is highly effective as a sintering aid in fluorite $Ce_{1-x}Ln_xO_{2-\delta}$ (Ln = Tb, Gd and Pr) oxides allowing dense materials with sub-micron grain sizes to be formed at sintering temperatures of 1000ºC and below. For the peak performing samples prepared under these conditions, ambipolar conductivities are shown to increase in the order CGO+Co < CTO+Co < CPO+Co. The oxygen ion transference number of CTO+Co, obtained from modified EMF method, increases with temperature, in line with that observed for the praseodymium substituted composition CPO+Co. In contrast, the oxygen ion transference number of the gadolinium substituted analogue, CGO+Co, exhibits negative temperature dependence. The ambipolar conductivities of CTO+Co and CGO+Co compositions are observed to be similar at the highest temperatures studied, 800ºC, while deviating strongly with decreasing temperature due to a much greater activation energy for the electronic conductivity component in the CGO+Co case. The oxygen permabilities obtainable from these materials follow these trends, increasing in the sequence CGO+Co < CTO + Co < CPO + Co. The current work shows that the $Ce_{0.8}Tb_{0.2}O_{2-\delta}$ with low concentration of Co sintering additive can attain relatively high mixed ionic electronic conductivity after sintering at low temperature of 900^oC. Nonetheless, this performance is shown to be significantly inferior to that offered by the praseodymium substituted material, CPO + Co.

4.5. References

[1] T.S. Zhang, J. Ma, Y.J. Leng, S.H. Chan, P. Hing, J.A. Kilner, Effect of transition metal oxides on densification and electrical properties of Si-containing $Ce_{0.8}Gd_{0.2}O_{2-\delta}$ ceramics, Solid State Ionics 168 (2004) 187–195.

[2] A. Martínez-Arias, A.B. Hungría, M. Fernández-García, A. Iglesias-Juez, J.C. Conesa, G.C. Mather, Cerium–terbium mixed oxides as potential materials for anodes in solid oxide fuel cells, Journal of Power Sources 151 (2005) 43–51.

[3] P. Jasinski, T. Suzuki, H.U. Anderson, Nanocrystalline undoped ceria oxygen sensor, Sensors and Actuators B: Chemical 95 (2003) 73–77.

[4] C. Chatzichristodoulou, P.V. Hendriksen, Electronic and ionic transport in $Ce_{0.8}Pr_xTb_{0.2-x}O_{2-\delta}$ and evaluation of performance as oxygen permeation membranes, ECS Transactions 45 (2012) 45–62.

[5] T. Morimoto, H. Tomonaga, A. Mitani, Ultraviolet ray absorbing coatings on glass for automobiles, Thin Solid Films 351 (1999) 61–65.

[6] M.J. Shin, J.H. Yu, Oxygen transport of A-site deficient $Sr_{1-x}Fe_{0.5}Co_{0.5}O_{3-\delta}$ (x = 0–0.3) membranes, Journal of Membrane Science 401-402 (2012) 40–47.

[7] J.J. Kim, M. Kuhn, S.R. Bishop, H.L. Tuller, Cathodic and defect properties of $Ba_xSr_{1-x}Ti_{1-y}Fe_yO_{3-y/2+\delta}$ mixed conducting oxides, Solid State Ionics 230 (2013) 2–6.

[8] D.P. Fagg, A. Feighery, J.T. Irvine, The systems $Zr(Nb,Ti)(R)O_{2-\delta}$, R=Yb, Ca—optimization of mixed conductivity and comparison with results of other systems (R=Y and Gd), Journal of Solid State Chemistry 172 (2003) 277–287.

[9] S. Tao, J.T.S. Irvine, Optimization of Mixed Conducting Properties of Y_2O_3–ZrO_2–TiO_2 and Sc_2O_3–Y_2O_3–ZrO_2–TiO_2 Solid Solutions as Potential SOFC Anode Materials, Journal of Solid State Chemistry 165 (2002) 12–18.

[10] M. Balaguer, C. Solís, J.M. Serra, Structural−transport properties relationships on $Ce_{1-x}Ln_xO_{2-\delta}$ system (Ln = Gd, La, Tb, Pr, Eu, Er, Yb, Nd) and effect of cobalt addition, The Journal of Physical Chemistry C 116 (2012) 7975−7982.

[11] D.P. Fagg, S. García-martin, V.V. Kharton, J.R. Frade, Transport properties of fluorite-type $Ce_{0.8}Pr_{0.2}O_{2-\delta}$: optimization via the use of cobalt oxide sintering aid, Chemistry of Materials 21 (2009) 381–391.

[12] R.N. Blumenthal, R.J. Panlener, Electron mobility in nonstoichiometric cerium dioxide at high temperatures, Journal of Physics and Chemistry of Solids 31 (1970) 1190–1192.

[13] H.L. Tuller, A.S. Nowick, Small polaron electron transport in reduced CeO_2 single crystals, Journal of Physics and Chemistry of Solids 38 (1977) 859–867.

[14] I.K. Naik, T.Y. Tien, Mobility in nonstoichiometric, Journal of Physics and Chemistry of Solids 39 (1978) 311–315.

[15] D.P. Fagg, J.C.C. Abrantes, D. Pérez-Coll, P. Núñez, V.V. Kharton, J.R. Frade, The effect of cobalt oxide sintering aid on electronic transport in $Ce_{0.80}Gd_{0.20}O_{2-\delta}$ electrolyte, Electrochimical Acta 48 (2003) 1023–1029.

[16] D.P. Fagg, V.V. Kharton, J.R. Frade, P-Type electronic transport in $Ce_{0.8}Gd_{0.2}O_{2-\delta}$:The effect of transition metal oxide sintering aids, Journal of Electroceramics 9 (2003) 199–207.

[17] D. Ramasamy, A.L. Shaula, A. Gómez-Herrero, V.V. Kharton, D.P. Fagg, Oxygen permeability of mixed-conducting $Ce_{0.8}Tb_{0.2}O_{2-\delta}$ membranes: Effects of ceramic microstructure and sintering temperature, Journal of Membrane Science 475 (2015) 414–424.

[18] E. Bischoff, Sintering aids for ceria-zirconia alloys, Journal of Materials Science 27 (1992) 2734–2738.

[19] M. Balaguer, C. Solís, M. Serra, Study of the transport properties of the mixed ionic electronic conductor $Ce_{1-x}Tb_xO_{2-\delta}$ + Co (x = 0.1, 0.2) and evaluation as oxygen-transport membrane, Chemistry of Materials 23 (2011) 2333–2343.

[20] D. Perezcoll, P. Nunez, J. Abrantes, D.P. Fagg, V.V. Kharton, J. Frade, Effects of firing conditions and addition of Co on bulk and grain boundary properties of CGO, Solid State Ionics 176 (2005) 2799–2805.

[21] M. Balaguer, C. Solís, S. Roitsch, J.M. Serra, Engineering microstructure and redox properties in the mixed conductor $Ce_{(0.9)}Pr_{(0.1)}O_{(2-\delta)}$ + Co 2 mol%, Dalton Transactions 43 (2014) 4305–12.

[22] D.P. Fagg, V.V. Kharton, A. Shaula, I. Marozau, J. Frade, Mixed conductivity, thermal expansion, and oxygen permeability of Ce(Pr,Zr)O, Solid State Ionics 176 (2005) 1723–1730.

[23] D.P. Fagg, I.P. Marozau, A.L. Shaula, V.V. Kharton, J.R. Frade, Oxygen permeability, thermal expansion and mixed conductivity of $Gd_xCe_{0.8-x}Pr_{0.2}O_{2-\delta}$, x=0, 0.15, 0.2, Journal of Solid State Chemistry 179 (2006) 3347–3356.

[24] A. Hideaki Inaba, B. Hiroaki Tagawa, Ceria-based solid electrolytes, Solid State Ionics 83 (1996) 1–16.

[25] V.V. Kharton, V.N. Tikhonovich, L. Shuangbao, E.N. Naumovich, A.V. Kovalevsky, A.P. Viskup, I.A. Bashmakov, A.A. Yaremchenko, Ceramic microstructure and oxygen permeability of SrCo (Fe, M)$O_{3-\delta}$ (M = Cu or Cr) perovskite membranes, Journal of the Electrochemical Society 145 (1998) 1363–1373.

[26] I. Kosacki, H.U. Anderson, Microstructure-property relationships in nanocrystalline oxide thin films, Ionics 6 (2000) 294–311.

5. Enhancing electrochemical performance by the control of transport properties in buffer layers – SOFC/SOEC

5.1. Introduction

Several limitations are suppressing the development of SOFCs and SOECs. One of the most debilitating is associated with chemical interactions between cell components, which can lead to poor longevities at high working temperatures and/or depleted performance [1]. This problem has often been noted for lanthanide containing electrode materials, due to a high propensity for chemical interactions with the most common electrolyte material, yttria stabilized zirconia (YSZ). Thus, many examples can be found in the literature where thin buffer layers have been implemented in such devices between the electrode/electrolyte layers, in an attempt to mitigate this problem. Typically the buffer layers have been from Y, Sm or Gd doped ceria-based materials, due to their reported ability to successfully minimize such chemical interactions in both SOFC and SOEC devices while offering high oxide-ion conductivities [2–7].

In this thesis work we select a typical scenario of an yttria stabilized zirconia electrolyte combined with a lanthanide containing oxygen electrode. In the present case the Ruddlesdon Popper phase, $Nd_2NiO_{4+\delta}$, was selected to be the "typical" electrode material of study. Interest in such $K_2NiF_{4+\delta}$ structure type oxides as potential oxygen electrodes has blossomed in recent years due to their high levels of mixed ionic and electronic conductivity (see chapter 1.3.2). Due to the prevalence of SOFC research, this materials type has predominately been applied as a potential SOFC cathode [8–10]. Nonetheless, these materials have also shown great promise as oxygen electrodes for SOECs due to the useful property that both the ionic and electronic conductivities increase with increasing oxygen partial pressure; a factor that is documented to offer significant advantages for the SOEC application over that of the more common oxygen deficient perovskite materials [11][12]. However, like many lanthanide containing electrode materials, interaction with the YSZ electrolyte can occur, forming the pyrochlore zirconate, e.g. $Ln_2Zr_2O_7$, where Ln = lanthanide. In the specific case of $Nd_2NiO_{4+\delta}$, this electrode has been documented to exhibit such chemical reaction with YSZ above 900°C [13]. Although this temperature may be above the operating temperatures of many electrochemical cells of interest, such interaction places distinct complications on the fabrication of the electrolyte/electrode assembly due to potential chemical interaction during co-sintering. Thus, the use of ceria based buffer layers is commonly found in the literature as an attempt to prevent this interaction [3,5,6,14].

Traditionally, buffer layers have been fabricated from pure ionic conductors such as Y, Sm or Gd doped ceria-based materials [2][3][5][6][7][15]. To the authors' best knowledge, the possibility to improve electrode kinetics by the tailoring of mixed conductivity in buffer layers has not yet been explored. The doping of buffer layers can, theoretically, allow the higher levels of electronic conductivity to be designed at the electrolyte surface than would be possible by homogenous doping of the electrolyte, due to avoiding limitations associated with electronic leakage. One can find examples where dense mixed conducting "electrode" layers have been formed on the electrolyte, such as a 1μm film of strontium doped lanthanum cobaltite (LSC), sandwiched between a porous electrode of an identical composition [15]. Interestingly, for this mixed conducting layer of high electronic conductivity but low ionic transference number, no improvement in electrode kinetics could be obtained over solely that of the porous electrode. Nonetheless, the opposite has also been documented for a dense 200nm layer of strontium doped lanthanum cobalt ferrate (LSCF); a material offering similar transport properties [16]. Thus it is imperative to evaluate, not only the potential of buffer layers to impact electrode kinetics, but also to investigate the level of mixed conductivity that would be best to induce this effect, while keeping morphology fixed. For this aim, ceria based buffer layers have been assessed, which are predominantly ionic conductors, but where the level of electronic conductivity is increased by doping with the multivalent cation praseodymium. The ability of these layers to offer the desired two-fold function, to resist chemical interaction while impacting electrode kinetics, is also analysed.

5.2. Experimental

Doped-cerium oxide compositions of 20 mol% gadolinium (CGO), or Praseodymium (CPO) were prepared by hydrothermal method and $Nd_2NiO_{4+\delta}$ powder was prepared by the citrate route (see procedure in chapter 2.1). Electrochemical cells with and without buffer layers were prepared by spin coating technique (chapter 2.2).

Powder XRD patterns were recorded to identify the phases present and assess their respective purity. The chemical stability of buffer layers with electrode and electrolyte materials was investigated independently by X-ray diffraction by mixing the powders in a 50:50 wt% ratio and sintering at conditions equal to that used in cell preparation (900°C for 10 h). The cross sectional microstructure and morphology of the cells were analysed by scanning electron microscopy and elemental analysis was performed by Energy Dispersive X-ray spectroscopy (EDS).

Electrochemical characterization was performed using electrochemical cells with and without buffer layers (see procedure in chapter 2.7).

5.3. Results and Discussion

5.3.1 Phase formation and analysis of potential chemical interactions

Figure 5.1a shows the XRD patterns of cobalt doped CGO, and CPO powders prepared by the hydrothermal method. It can be observed that this low temperature preparation method forms single phase crystalline powders with the expected cubic defect fluorite structure, with no observable impurity peaks. Figure 5.1a also presents the XRD pattern of $Nd_2NiO_{4+\delta}$ powder prepared by the citrate method after calcination. No impurity peaks can be observed, indicating the successful preparation of the $Nd_2NiO_{4+\delta}$ electrode materials by this route.

Buffer layers need to offer chemical stability both with the electrode and the electrolyte materials during cell fabrication and operation. Thus, to assess for chemical interaction of the chosen materials, intimate mixtures of the buffer layers with the $Nd_2NiO_{4+\delta}$ electrode and with the YSZ electrolyte were prepared and sintered at 900°C for 10 h.

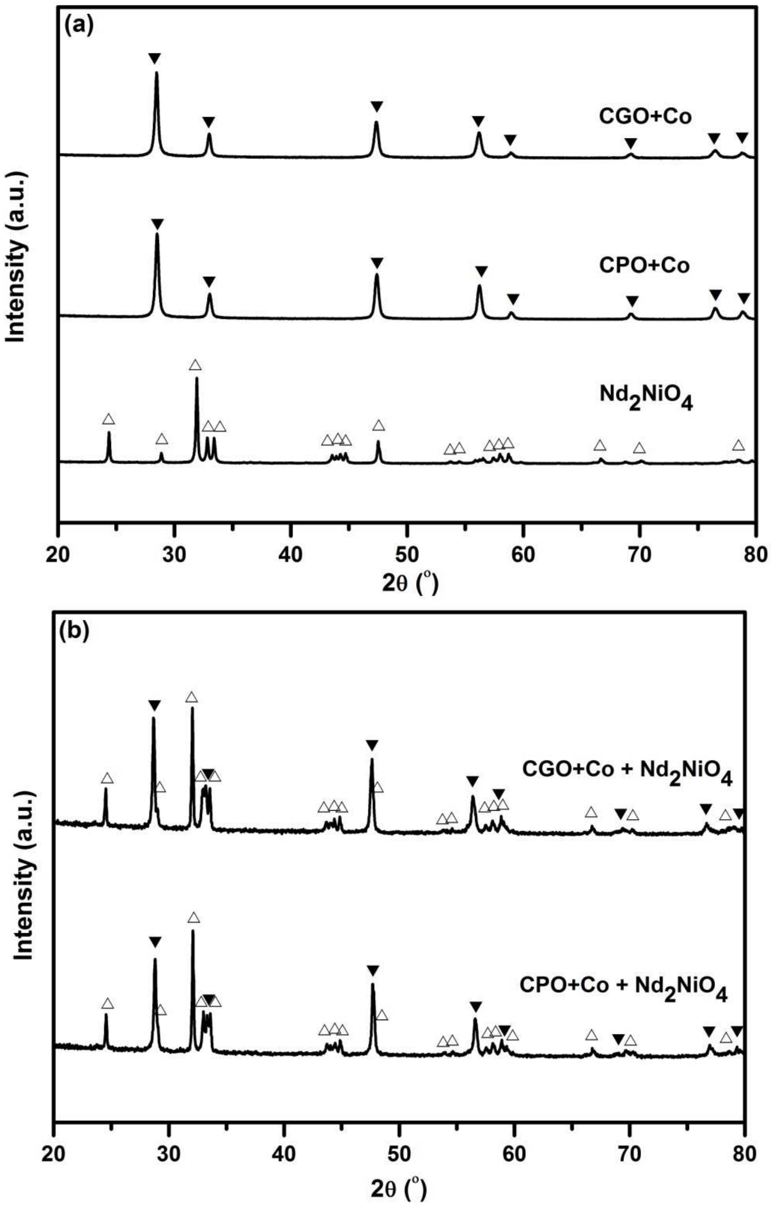
(a)
CGO+Co
CPO+Co
Nd₂NiO₄
Intensity (a.u.)
20
30
40
50
60
70
80
2θ (°)
(b)
CGO+Co + Nd₂NiO₄
CPO+Co + Nd₂NiO₄
Intensity (a.u.)
20
30
40
50
60
70
80
2θ (°)

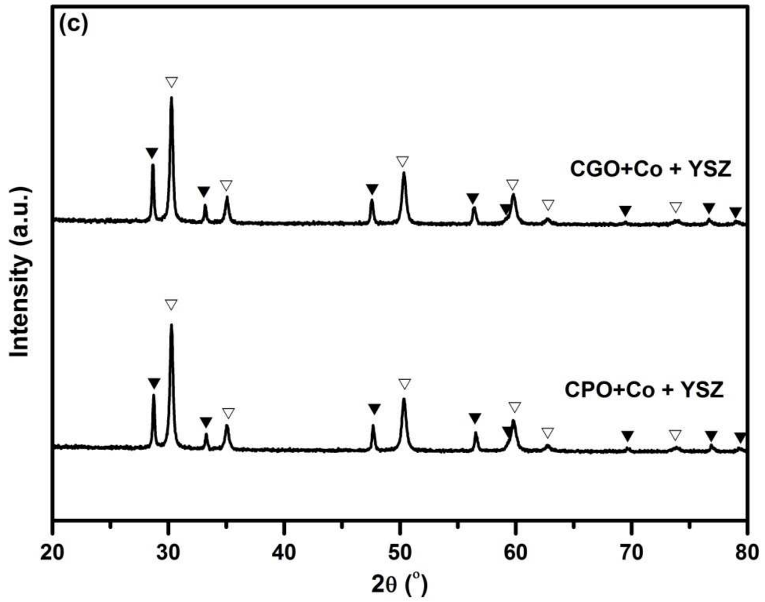

Figure 5.1. XRD patterns of a) prepared phases of CGO+Co, CPO+Co and $Nd_2NiO_{4+\delta}$ b) intimate mixtures of CGO+Co or CPO+Co with $Nd_2NiO_{4+\delta}$ after firing for 10h at 900°C and c) intimate mixtures of CGO+Co or CPO+Co with YSZ after firing for 10h at 900°C.

These conditions emulate the preparation conditions of the electrolyte/buffer layer/electrode assemblies and represent more severe temperatures than that used in subsequent electrochemical operation. The functionality of these materials as potential buffer layers was assessed by XRD and the corresponding patterns are shown in Figure 5.1b and c. Only the desired phase compositions can be noted, with no extra impurity phases observable between buffer layer/electrode and buffer layer/electrolyte mixtures, respectively. For CGO this result corresponds well with that previously documented for this buffer layer material [13]. The current study now extends this knowledge to confirm that all of the proposed doped ceria materials will offer sufficient stability to the surrounding cell components to function as buffer layers under these conditions.

5.3.2. Microstructures of electrolyte/buffer layer/electrode assemblies

Figure 5.2 presents cross sectional micrographs of $Nd_2NiO_{4+\delta}$ electrode and YSZ electrolyte assemblies formed with and without buffer layers. In all cases, the buffer layers are shown to be dense, thin, uniform layers of thickness around 0.5 µm that are well adhered to the YSZ substrate. The thicknesses of the $Nd_2NiO_{4+\delta}$ electrodes are approximately 2 µm in each case and are once more are shown to be well adhered to the supporting layers. The morphologies of the $Nd_2NiO_{4+\delta}$ electrodes are observed to be comparable in each instance.

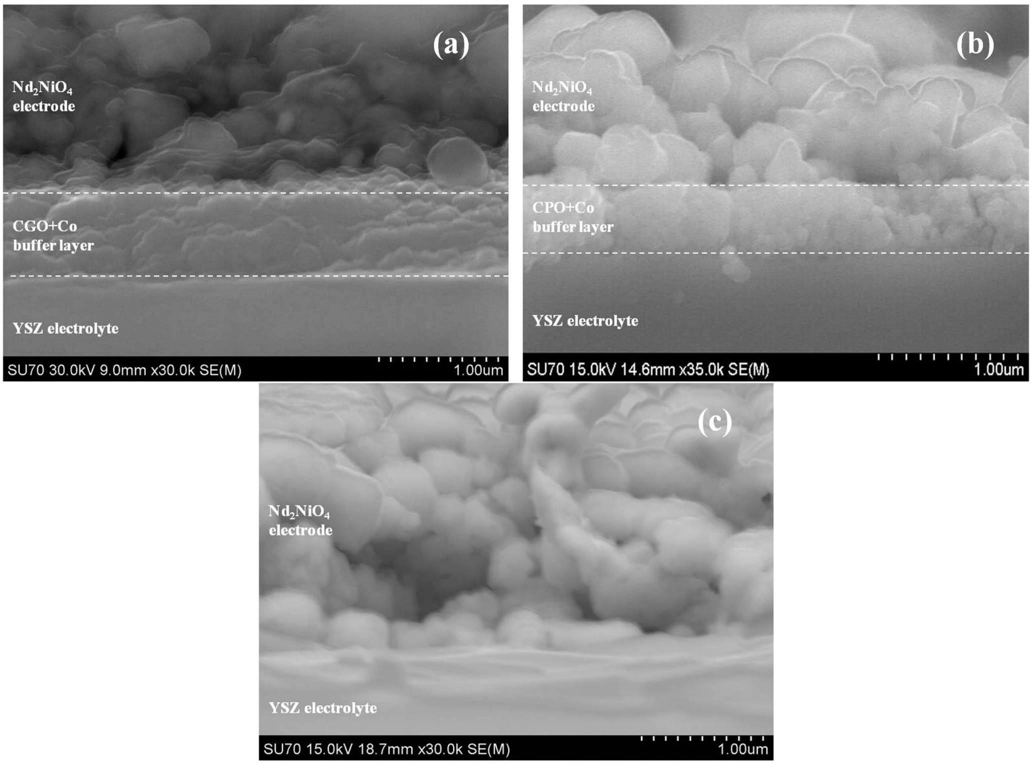

Figure 5.2. Cross-sectional microstructures of electrolyte/electrode assemblies with buffer layers a) CGO+Co, b) CPO+Co and c) without buffer layer.

Figure 5.3 presents compositional analysis of the YSZ/CPO+Co/$Nd_2NiO_{4+\delta}$ assembly by EDS mapping, confirming the clear separation of the $Nd_2NiO_{4+\delta}$ electrode, the buffer layer and the YSZ electrolyte in the architecture, with no notable cation interdiffusion. This result suggests successful fabrication of these electrolyte/buffer layer/electrode assemblies and the absence of chemical interactions between layers, in agreement with the XRD results of section 5.3.1. Assemblies formed using the other buffer layers showed similar results.

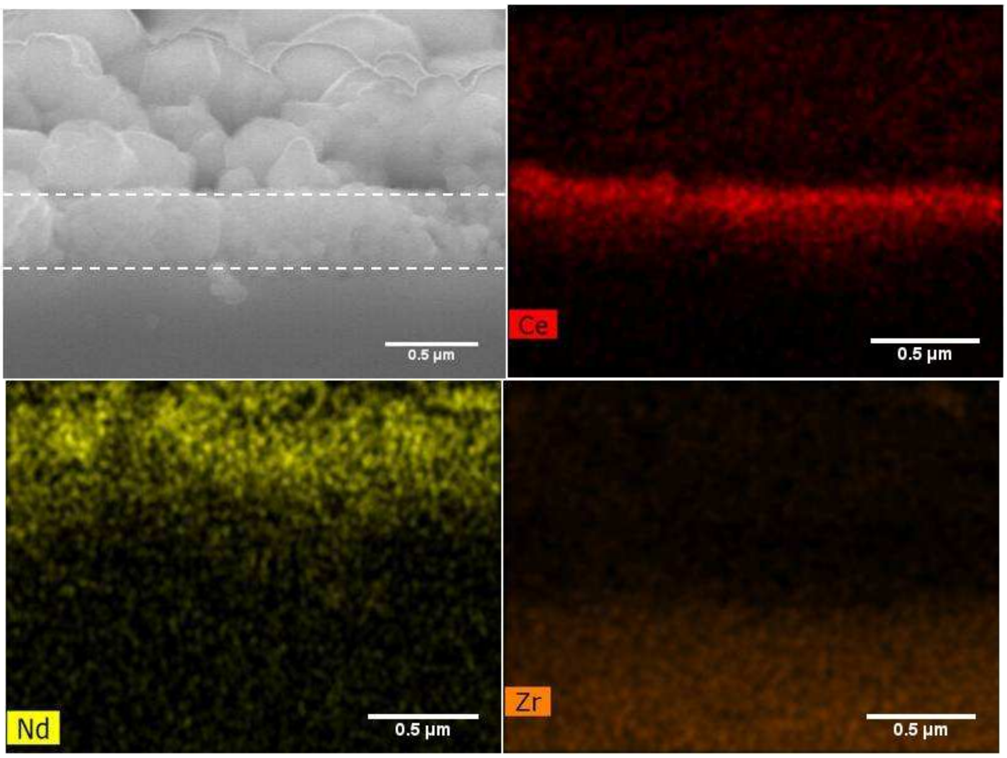

Figure 5.3. SEM-EDS analysis performed across the electrode/electrolyte interface of an YSZ/CPO+Co/$Nd_2NiO_{4+\delta}$ assembly. Assembles formed for the other buffer layers showed similar results.

5.3.3. Ambipolar conductivity of the individual buffer layers

Previous chapters (3 & 4) noted that the presence of Co can lead to important gains in electronic conductivity of approximately 8-30 times in the case of CGO and 2-3 times in the case of CPO in the temperature range 600-900°C, due to the presence of cobalt located at the grain boundaries [17–20]. In contrast, the total conductivities of Co-containing CGO and CPO materials were only slightly raised over that of their Co-free counterparts, due to predominant levels of ionic conductivity that remain virtually unchanged upon Co-addition [17–20]. It has been further noted that the sintering temperature of the Co-containing materials can cause large variations of the relative magnitude of these properties [18,21]. Thus, to ensure relevance between the discussion of transport properties, the proposed buffer layers and the fabrication temperatures of the electrolyte/buffer layer/electrode assemblies, the present study limits itself to compare only transport properties of bulk buffer layer samples that contain 2 mol% Co-additions that have been sintered in temperature ranges relevant to the current study (900-1000°C) [17–20].

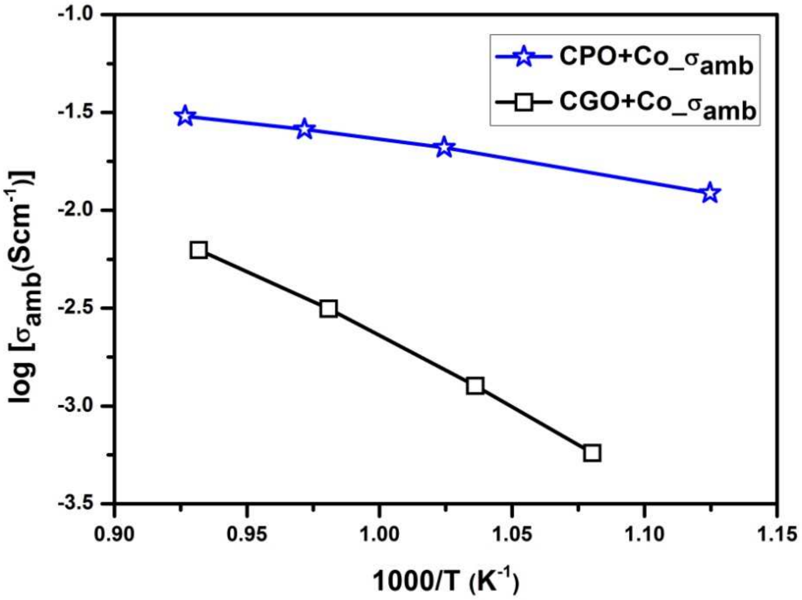

Figure 5.4. Ambipolar conductivities of CGO+Co and CPO+Co.

The ambipolar conductivities of bulk samples of the CPO+Co and CGO+Co samples are compared in Figure 5.4 from figure 4.2 and 4.3 data of these materials [17–20], calculated by the equation 5.1. Respective activation energies are documented in Table 5.1. Ambipolar conductivity values increase in the order CPO+Co > CGO+Co and the activation energy of the ambipolar conductivity of the CGO+Co material is noted to be significantly higher than that of CPO+Co, Table 5.1.

$$\sigma_{amb} = t_o\,(1 - t_o)\,\sigma_T \tag{5.1}$$

Table 5.1. Activation energy of ambipolar conductivities with temperature.

Sample	Activation energy E_a (eV)
	Ambipolar
CGO +Co	1.47 ± 0.11
CPO +Co	0.48 ± 0.06

The global tendencies of the total, the ionic and the electronic conductivities of these materials correspond well with those described in the literature for the respective base materials formed without cobalt [22–24]. The addition of cobalt serves mainly to enhance the respective levels of the electronic component, while the global tendencies between the transport properties of the materials remain intact. To summarize, figures (4.4, 4.5 and 5.4) highlights that the buffer layer materials all possess levels of ionic conductivity that are competitive with the well-known electrolyte material CGO and of similar activation energies. The total conductivities of these materials are also within half an order of magnitude of each other, also with similar activation energies. In contrast, the electronic component is shown to significantly increase in the order CPO+Co > CGO+Co, with a higher activation energy shown in the gadolinium case. The current section, thereby, demonstrates that the chosen buffer layer materials will facilitate the desired experimental plan, by permitting the electrochemical performance of buffer layers with tailorable levels of electronic conductivity and or ambipolar conductivity to be compared and contrasted, whilst maintaining similar, high levels, of ionic conductivity.

5.3.4. Electrochemical behavior of electrolyte/buffer layer/electrode assemblies at OCV

Example impedance spectra measured at open circuit potential (OCV) are shown in Figure 5.5 for all assemblies, prepared and tested with the geometry of Figure 2.1, either with no buffer layer (BL) or containing the buffer layers CGO+Co or CPO+Co. All impedance spectra show an offset along the real Z´ axis at the highest frequencies, followed by the appearance of one or more semicircles at lower frequency. Note the offset resistances (R1) have been subtracted in Figure 5.5 to aid clarity. The impedance spectrum for the $Nd_2NiO_{4+\delta}$ electrode deposited directly on the YSZ electrolyte, without a buffer layer, shows the highest resistance semicircle of the samples analysed and this semicircle exhibits a deformed shape, suggesting that it consists of more than one response.

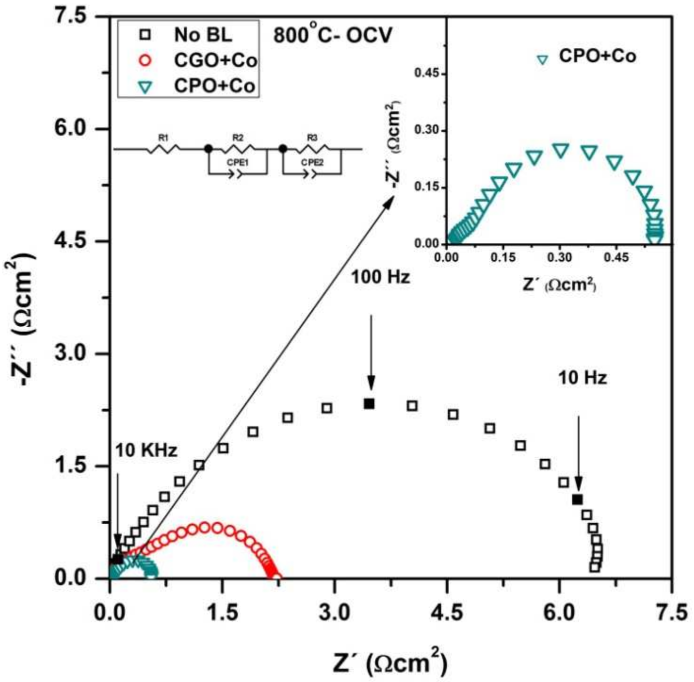

Figure 5.5. Typical impedance spectra measured at OCV, of cells with no buffer layer (BL) or containing the buffer layers CGO+Co or CPO+Co. Ohmic offset, R1, has been subtracted.

In contrast, the CGO+Co buffer layer sample shows the presence of well-defined responses with a significantly lower overall resistance. The samples with CPO+Co buffer layers show further decreases in the overall resistance, while the shape of the impedance spectra for the CPO+Co buffer layer consists of a small semicircle notable at intermediate frequencies followed by a larger semicircle at lower frequency. To show this more clearly the CPO+Co spectra is magnified in the inset of this figure. The capacitance values of these responses will be discussed in detail in the later text. Nonetheless, all responses show capacitance values considerably greater or equal to that of 10^{-5} Fcm^{-2}, and, as such, can be attributed to electrode phenomenon [25].

The study of the electrokinetics of SOFC cathodes has attracted considerable attention in the last 20-30 years, with several reviews available to provide useful collations of this work [26–29]. The main processes suggested to dominate the kinetics of mixed conducting SOFC cathodes are that of diffusion of ionic species through the bulk of the electrode and surface exchange reactions, such as charge transfer and dissociative adsorption of oxygen on the electrode surface, Figure 1.11b [26,29]. These principal limiting phenomena can also be accompanied by additional resistive terms that have been related to electrochemical kinetic limitations at the electrode/electrolyte interface and/or gas phase limitations [26,29]. To simulate these phenomena, a range of potential equivalent circuits have been proposed, such as the series combination of multiple (RQ) elements that involve a resistor (R) and constant phase element (Q) in parallel, to describe each of these phenomenon individually, or the introduction of more specific elements that describe the underlying physics, such as a finite length Warburg element to express bulk ionic diffusion though the electrode, or that of a Gerisher element to describe the co-limitation of the electrode process by bulk diffusion and surface exchange [26,29]. Observation of the impedance spectra of Figure 5.5 shows that the shapes and magnitudes of the impedance response alter dramatically with both the introduction of buffer layers and by varying the electronic conductivity of the buffer layer. For this reason, the simplest equivalent circuit has been chosen with which to preliminarily discuss these results, consisting of a resistor in series with two RQ elements, inset Figure 5.5. At high temperatures the additional series combination of an inductor was also occasionally necessary. This basic equivalent circuit permits a phenomenological discussion of the impact of the buffer layers on the main features of impedance spectra for each of the samples to be presented, without the necessity to make any pre-assumptions of the underlying physical meaning of each response. The fitting parameters extracted for each distributed semicircle are the resistance, R, the pseudo-capacitance, Q, and an additional parameter n which can be related to the true capacitance by the equation

$$C = R^{(1-n)/n} Q^{1/n} \tag{5.2}$$

The higher frequency semicircle (R2) and the lower frequency semicircle (R3) can be attributed to the polarization resistance of the electrodes, where the total polarization resistance is given by Rp = R2 +R3.

Figure 5.6 shows the Arrhenius behavior of the extracted resistances R1, R2, R3, and Rp. The high frequency intercept (R1) exhibits activation energies of approximately 0.8 eV for each sample, Table 5.2, a value that corresponds closely with the expected activation energy of the YSZ electrolyte material [30], thus, reinforcing the association of the R1 term to the ohmic cell resistance.

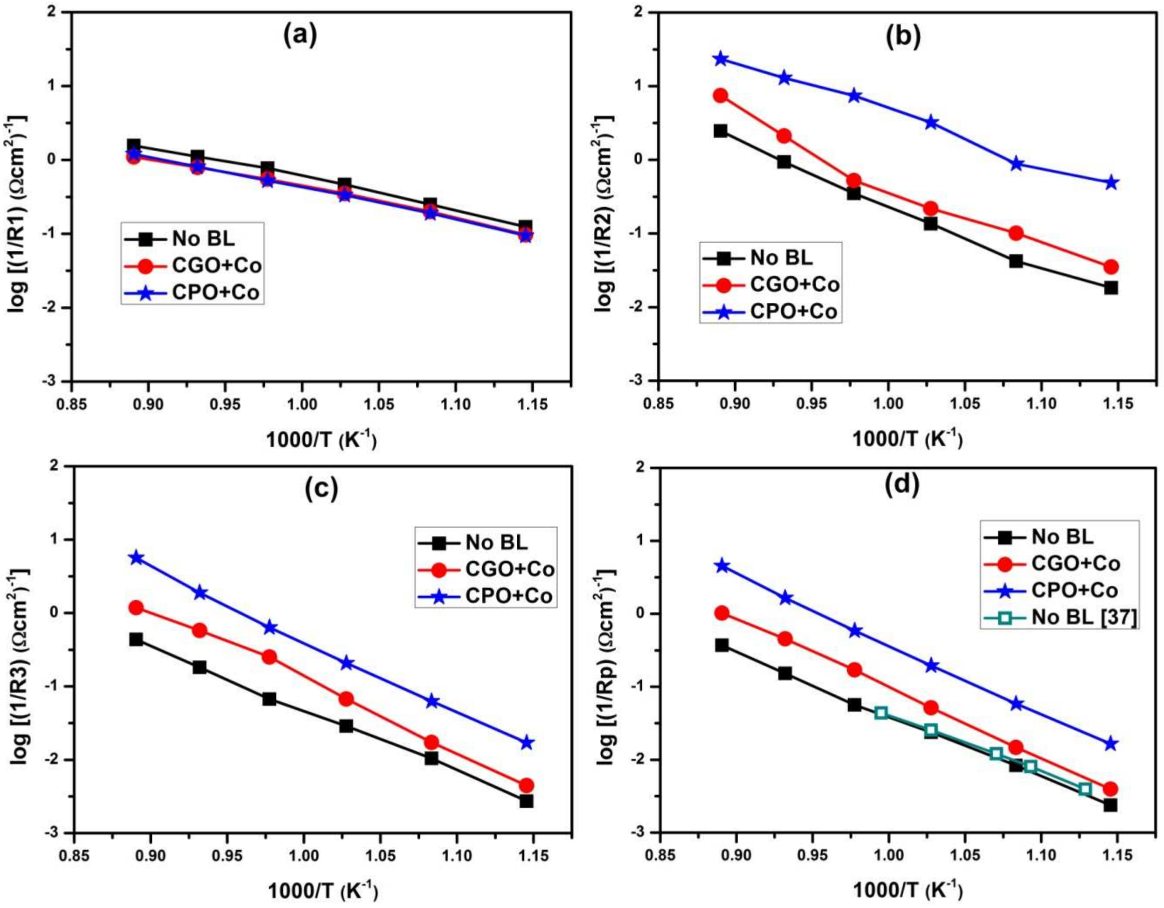

Figure 5.6. The Arrhenius behavior of the polarization resistances a) R1, b) R2, c) R3 and d) Rp, for cells with no buffer layer (BL) or containing the buffer layers CGO+Co or CPO+Co. Figure 5.6d additionally compares results to that of literature data for a $Nd_2NiO_{4+\delta}$ electrode formed without a buffer layer [31].

Table 5.2. Activation energy of OCP with temperature.

Sample	Activation energy E_a (eV)			
	R1	R2	R3	Rp
CGO+Co	0.81 ± 0.03	1.76 ± 0.15	1.93 ± 0.06	1.90 ± 0.02
CPO+Co	0.85 ± 0.02	1.37 ± 0.08	1.95 ± 0.04	1.90 ± 0.03

Empty	0.86 ± 0.03	1.68 ± 0.07	1.68 ± 0.03	1.68 ± 0.03

The values of R1 for samples that contain a buffer layer are shown to be effectively equal, whereas a slightly lower ohmic resistance is recorded for the sample without a buffer layer, Figure 5.6a. The total polarization resistance, Rp, measured for the Nid$_2$NiO$_{4+\delta}$ electrode without a buffer layer is shown to agree very well with that presented in the literature for an identical electrode composition, Figure 5.6d [31]. It has been noted by Mauvi et al. [8] that these values can be further improved by modification of the electrode microstructure by attrition milling. However, as the aim of the current article was to compare the impact of buffer layers on the performance of a typical electrode material, the performance of the Nd$_2$NiO$_{4+\delta}$ electrode was deemed to be sufficient in its as-prepared form, to conform to a representative study case. The values of the polarization resistance R2, R3 and the total polarization resistance, Rp, are shown to increase in the order CPO+Co << CGO+Co < no buffer layer, with the largest gains in performance being notable on moving to the buffer layer CPO+Co, Figures 5.6b, c & d. For example, improvements in performance of around an order of magnitude, for all polarization resistances, R2, R3 and Rp, are noted in samples containing CPO+Co buffer layers, beyond that of a sample without a buffer layer. On comparison to the performance of the sample containing a typical CGO+Co buffer layer, improvements of about 6-times in Rp can be obtained in samples with CPO+Co buffer layers, Figure 5.6b.

When discussing the origin of these improvements, note that i) the electrode material was identical in all cases, ii) that all buffer layers were shown to have comparable levels of ionic conductivity and iii) that samples were free of surface interractions. Thus, this remarkable improvement in electrode kinetics for the cases of buffer layers CPO+Co and CGO+Co can only relate to the manipulation of their transport properties by the predominant increase in their respective electronic conductivities (and, hence, ambipolar conductivities).

5.3.5. Electrochemical behavior of electrolyte/buffer layer/electrode assemblies under polarization

The magnitudes of the impedance arcs, for each sample, were observed to be influenced by anodic and cathodic polarization, generally with a reduced resistance shown as polarization increased. On the other hand, the principal responses of the impedance spectra were observed to be maintained and, thus, were fitted by the same sequence of RQ elements as the equivalent circuit described in Figure 5.5. An exception to this methodology was for the sample CGO+Co where the appearance of an additional semicircle at the lowest frequencies could also be noted under the highest cathodic polarization. Here an additional RQ element was introduced in the equivalent circuit to accommodate this response. Example impedance spectra are shown in Figure 5.7 to highlight these features, obtained under both anodic and cathodic polarization for the samples containing CGO+Co and CPO+Co buffer layers at 800°C under different polarization potentials in air.

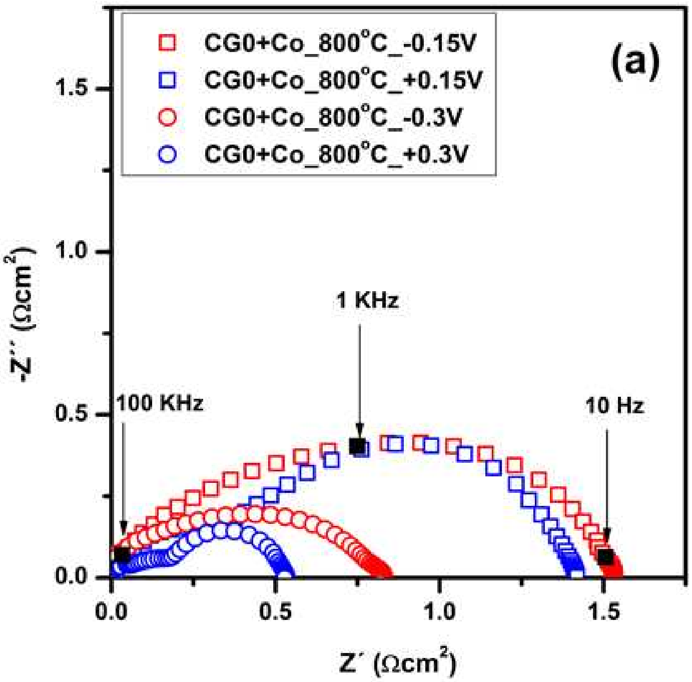

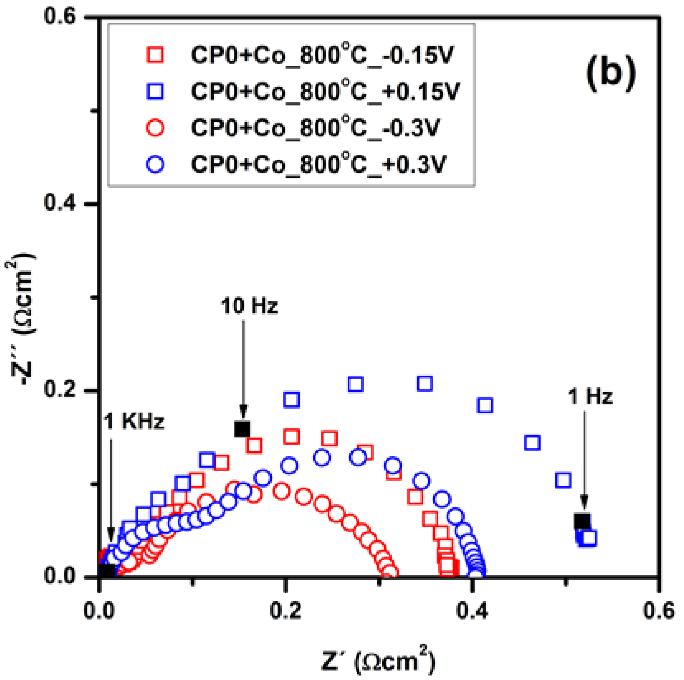

Figure 5.7. Impeadance spectra of cells containing a) CGO+Co and b) CPO+Co buffer layers measured under anodic and cathodic bias in air.

The total polarization resistance, Rp, obtained by the sum of all polarization resistances in the respective equivalent circuits, is plotted in Figure 5.8 as a function of applied potential and temperature for all samples. The global trends in Rp, are shown to mirror those measured at OCV, Figure 5.5, with an increase in Rp shown in the order CPO+Co << CGO+Co < no buffer layer, throughout the polarization range. As previously described, this trend can be principally attributed to the decreasing electronic contribution (and, hence, ambipolar conductivity) of the buffer layer in this sequence, Figure 5.4. At the lowest temperatures, the largest gains in performance are obtained by use of buffer layer CPO+Co.

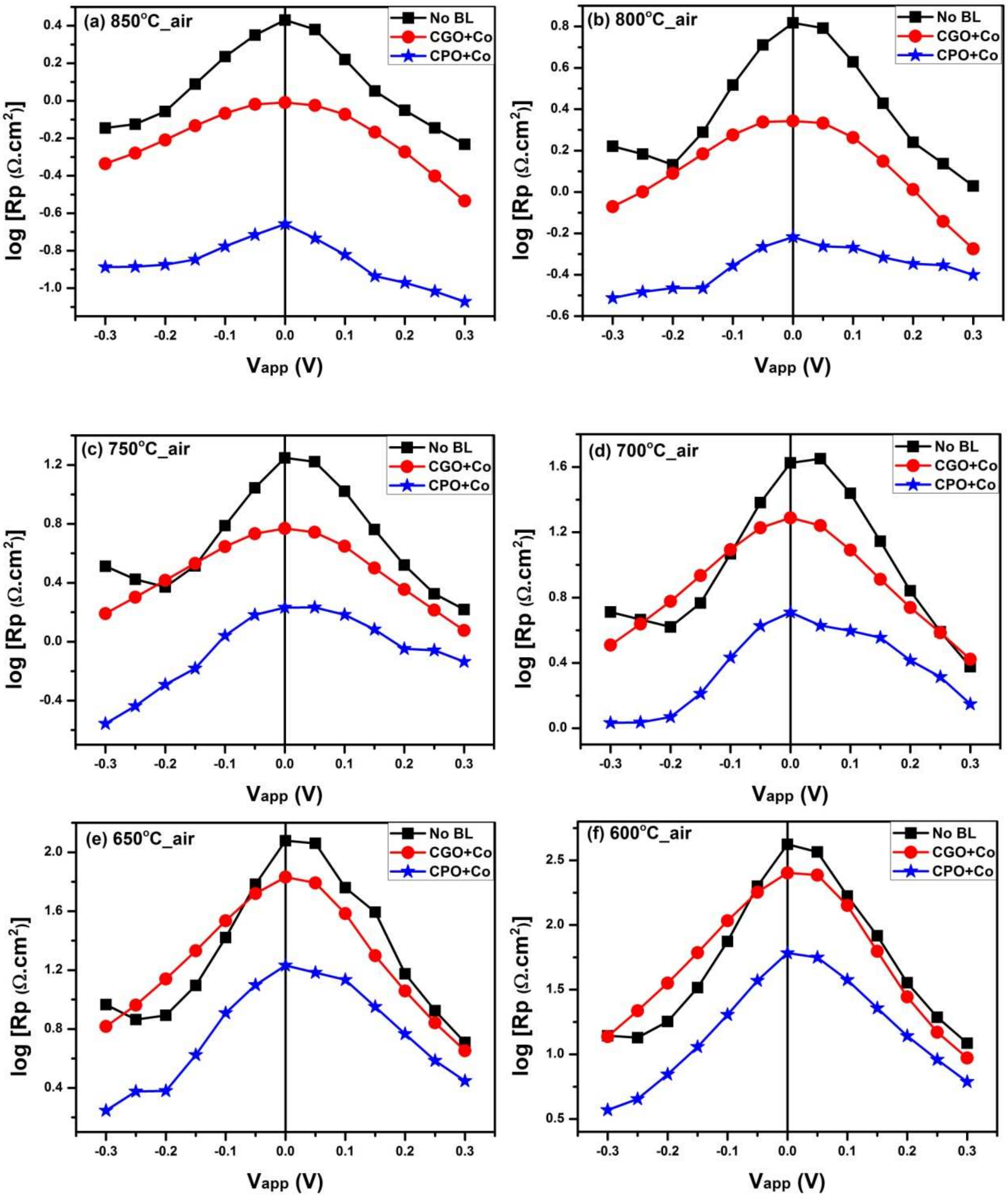

Figure 5.8. Total polarization resistance as a function of applied bias measured in air at different temperatures, for cells with no buffer layer (BL) or containing the buffer layers CGO+Co or CPO+Co.

5.3.6. Discussion of the origin of the improved electrode kinetics

Figure 5.9a plots the capacitance values, C2 and C3, for the higher frequency (R2) and lower frequency (R3) terms, respectively, corresponding to the impedance spectra measured for all samples at OCV calculated from equation 5.2. The capacitance values for CPO+Co buffer layer sample can be observed to be at least two orders of magnitude higher than that obtained for the remaining samples. An increase in capacitance would be in agreement with an increased area for electrochemical reaction provided by an additional surface path, Figure 1.11d. However, if this were a purely geometrical effect, as suggested in the traditional literature [32–37] an equivalent but inverse effect would also be induced on the polarisation resistance, due to the inverse dependencies of capacitance and resistance on area. In order to discuss this point, figure 5.9b plots the respective relaxation frequencies R_f of the R2 and R3 responses, given by the equation,

$$R_f = \frac{1}{2\pi\tau} \tag{5.3}$$

where, τ is the respective time constant given by the product of the resistance and capacitance of each response, τ = RC.

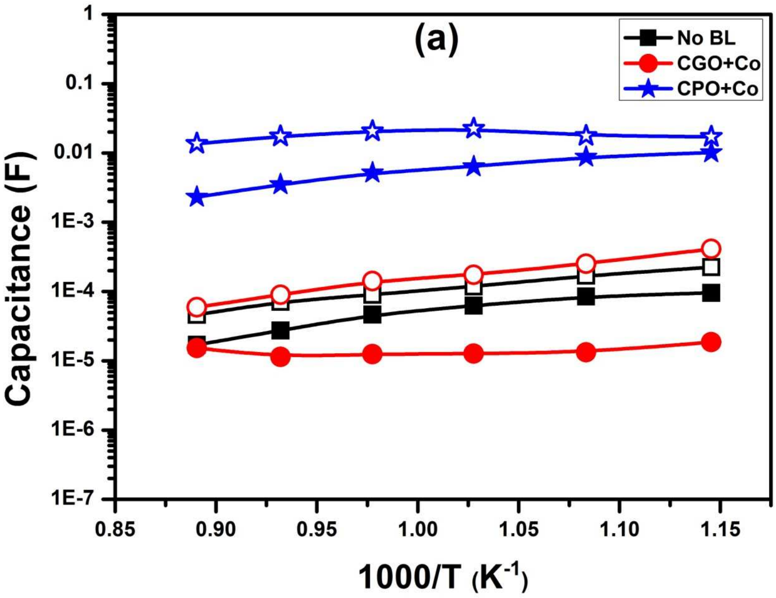

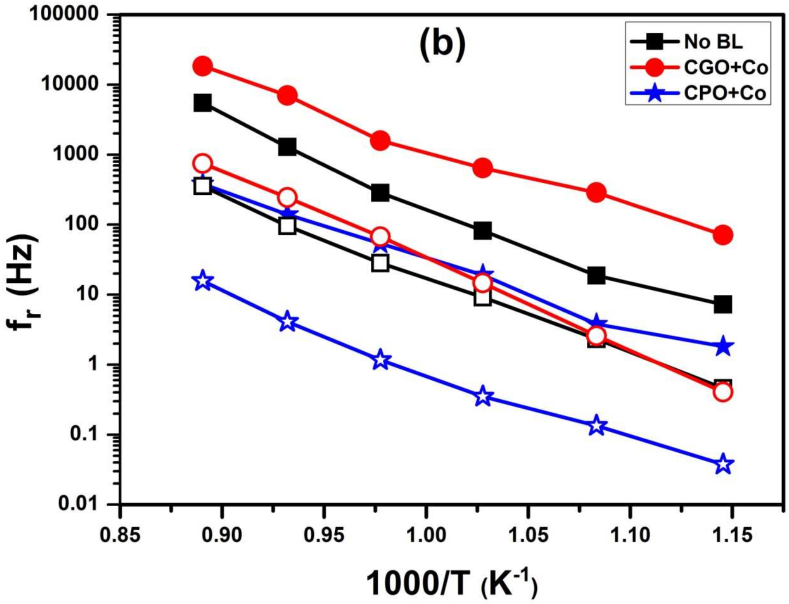

Figure 5.9. Temperature dependence of a) the Capacitance and b) Relaxation frequency. for cells with no buffer layer (BL) or containing the buffer layers CGO+Co or CPO+Co. Filled symbols relate to the higher frequency polarization response (R2), open symbols to the lower frequency response (R3).

If the improvement of electrode kinetic were solely geometric in nature [32–36,38] the time constant of each impedance response, and, thus, the characteristic relaxation frequencies, should remain constant due to the aforementioned, equal, but inverse dependences of the resistive and capacitive terms on area. Figure 5.9b clearly demonstrates that this is not the case, as the relaxation frequencies for the R2 or the R3 responses are significantly higher (by approximately 1.5 orders of magnitude) in samples with no buffer layer or with a CGO+Co buffer layer over that obtained for the CPO+Co buffer layer.

This result can either advocate that the R2 and R3 responses do not correspond to the same phenomenon in every sample, or that a purely geometric improvement by an additional surface path, as suggested in traditional literature, Figure 1.11d, is an over simplification of the current phenomenon.

To test the first hypothesis, figure 5.10, compares the polarization dependences of the R2 and R3 terms for representative samples from each of the two relaxation frequency groups; that of CGO+Co with high relaxation frequencies and CPO+Co buffer layers with low relaxation frequencies. For both buffer layers, the R2 term shows low dependence on polarization for both samples and is notably polarization independent at the highest temperatures, Figure 5.10a. Polarization independence of R2 is feature that is typical of previous results of mixed conducting electrodes and normally associated with solid state mass transfer [8,37].

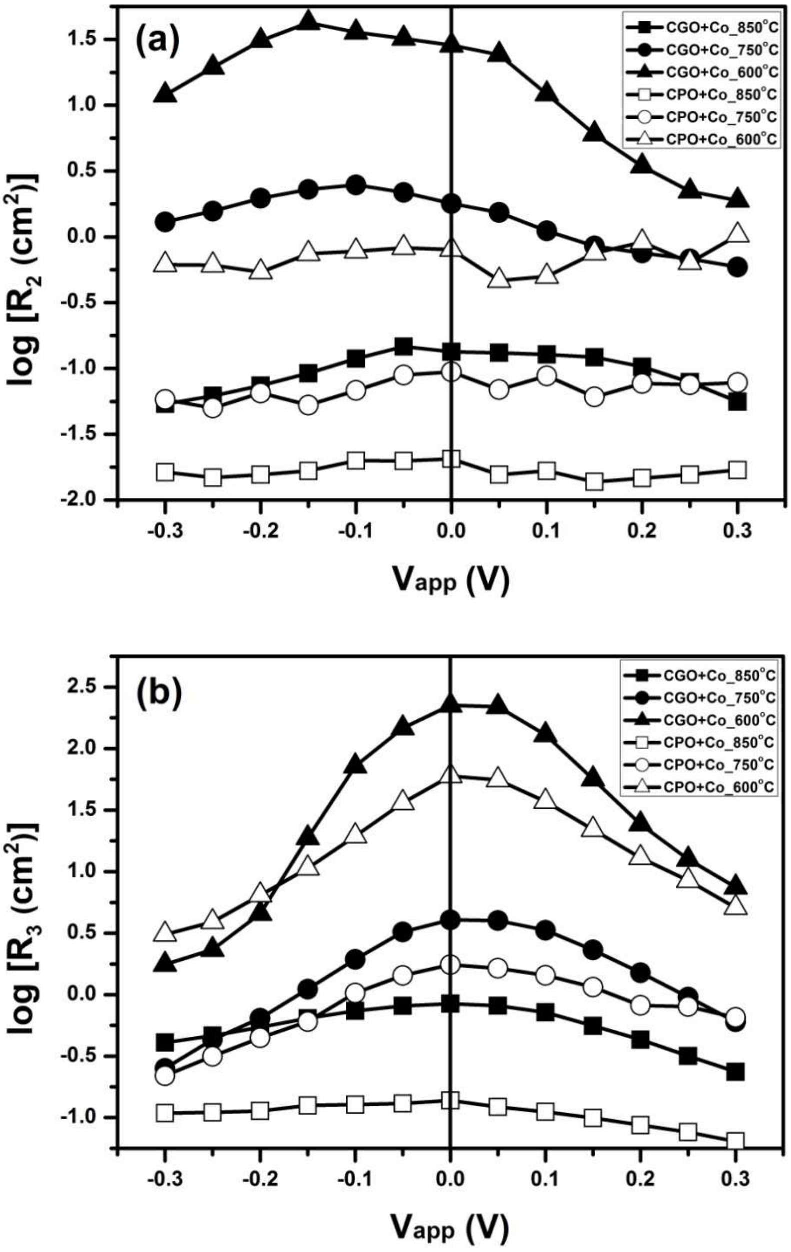

Figure 5.10. Dependence of the polarization resistances a) R2 and b) R3 on applied bias, measured in air at different temperatures for cells containing CGO+Co and CPO+Co buffer layers.

On the contrary, R3 term, Figure 5.10b, demonstrates strong dependences on polarization that appear to be similar in nature for both buffer layers. Note such strong dependences of the lower frequency impedance response on polarization is again characteristic behavior, previously observed for many mixed conducting electrodes [8,37], and normally related to surface exchange reactions, such as charge transfer and dissociative adsorption of oxygen on the electrode surface [26,29,37]. Thus, the polarisation dependences of R2 and R3 for the CGO+Co and CPO+Co buffer layer samples, appear to be both characteristic of those noted in other mixed conducting electrodes in the literature and are also comparable in the two samples, despite their extremely large differences in relative relaxation frequencies, Figure 5.9b. So the question is; if the impedance responses correspond to the same phenomena in both the CPO+Co and CGO+Co cases, how can their relaxation frequencies be so dissimilar?

5.3.7. Extension of the equivalent circuit of Lui [29].

To attempt to answer this question, Figure 5.11a shows the equivalent circuit proposed by Lui, to simulate a typical mixed conducting electrode of high electronic conductivity [29]. Two principal paths are shown in this equivalent circuit that of charge transfer at the TPB, as described by Figure 1.11a, and also that of the bulk path, as described by Figure 1.11b. Lui represents the TPB path with a capacitive term $C_{TPB,}$ a resistive term, R_{ct} and a Warburg impedance that reflects mass transfer both in the solid and gas phases adjacent to the TPB. The bulk path is reflected by a similar combination of elements that in this case reflects both mass transfer and surface exchange for the bulk route through the mixed conductor, given the subscripts MIEC1. Upon provision of an additional surface path by the introduction of a mixed conducting buffer layer, MIEC2, Figure 1.11d, Lui's equivalent circuit would be modified by the addition of another parallel path, involving similar terms of mass transfer and surface exchange, but located at the buffer layer surface, Figure 5.11b.

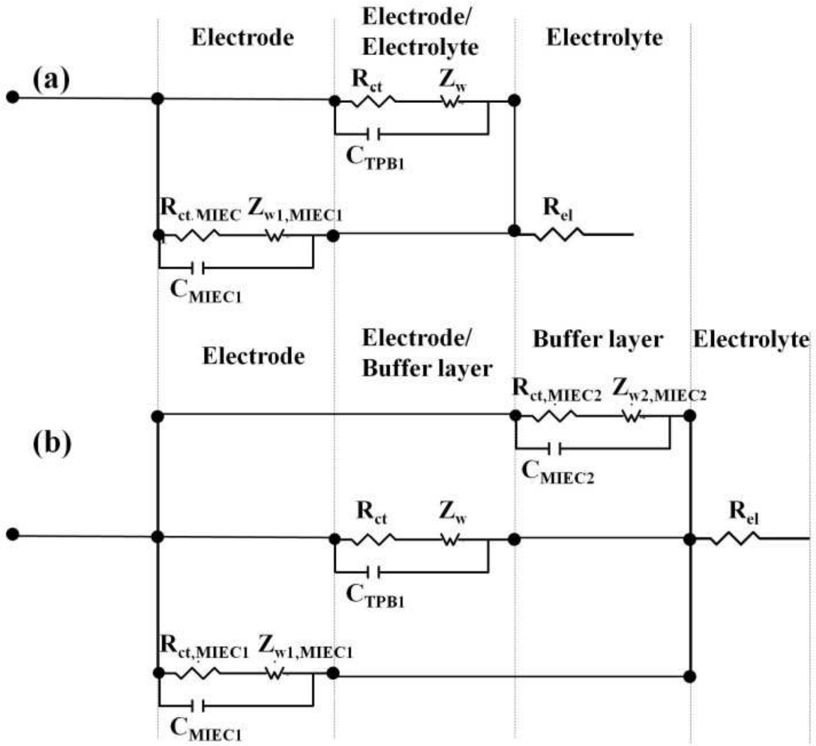

Figure 5.11. a) Equivalent circuit to describe a mixed conducting electrode of high electrical conductivity, as suggested by Lui [29], b) extension of Lui's equivalent circuit with another parallel path to represent the additional existence of a mixed conducting buffer layer.

To fit such an equivalent circuit to the current results would involve prior knowledge of the relative importance of each path and, thus, cannot easily be applied. However, one can estimate the potential effects that an active additional path would have on the overall capacitance and resistance measured for consequent responses. The presence of further capacitive responses in a parallel path would be additive in nature, leading to a higher overall capacitance. Moreover, as noted by Lui, the capacitances values of a MIEC path would be dependent on their surface area [29]. The existence of an additional parallel surface path related to an active buffer layer, Figure 1.11d, therefore, would result in an increase in capacitance for both these reasons and, thus, would correlate with the increase in capacitance noted for the buffer layer CPO+Co in Figure 5.11a. With respect to the resistive terms, the presence of an additional, active parallel path would serve to decrease the total polarization resistance due to the reciprocal additive nature of resistors when in parallel, again in agreement with experimental observations, Figure 5.6d.

At this juncture it should be noted that the resistance to solid state mass transport though a MIEC path was suggested by Liu to be related to the sum of the ionic and electronic resistivities (a factor equivalent to the inverse of the ambipolar conductivity) and also by surface exchange, a factor that has regularly been reported to be improved by increasing ambipolar conductivity [20,26,39]. Moreover, it should be highlighted that the ambipolar conductivity of $Nd_2NiO_{4+\delta}$ is likely to be greatly limited by a low ionic transference number; note in this respect, although the transport properties of $Nd_2NiO_{4+\delta}$ have not been measured to date, they are likely to reflect those of other isostructural compounds, Ln_2NiO_4, in which ionic transference numbers as low as 10^{-2} to 10^{-4} have been estimated [40,41]. Thus, from the total conductivity values of $Nd_2NiO_{4+\delta}$ given by Nakamura et al. [41], ~100Scm^{-1} at ~700°C, one can predict probable ambipolar conductivities for $Nd_2NiO_{4+\delta}$ in the order of 1 to 10^{-2} Scm^{-1}. At the lower end, these are equal to or are exceeded by the level of the ambipolar conductivity measured for the CPO+Co sample in Figure 5.4. Thus, the bulk electrode path, MIEC1, is unlikely to completely short circuit the presence of the additional buffer layer path, MIEC2, Figure 5.11b, and, instead, both paths are likely to be active for the oxygen reduction/oxidation reaction for the current materials, leading to a lower overall polarization resistance, in agreement with the observed results.

Thus, the respective values of capacitance, polarisation resistances and subsequent relaxation frequencies, are shown to not correspond to simple considerations of geometry and an increase in surface area, but are likely to involve a more complex association of potential parallel paths that depend, not only on the relative ambipolar conductivities of the two mixed conducting pathways, but also to their respective levels of surface exchange. What can be learned from the available literature is that these properties are likely to be intricately linked to the level of ambipolar conductivity of the selected buffer layers [26,29,42].

Note, the literature shows CPO+Co materials to offer high levels of oxygen surface exchange and with ambipolar conductivities that can compete with many common mixed conducting perovskites [19–21]. Following the theory of Lui [29] and the equivalent circuit described in Figure 5.11b, the effectiveness of the buffer layer to improve the electrode kinetics would, thus, depend on the balance between the ambipolar conductivities and surface exchange offered by the buffer layer and that of the bulk electrode, and also their relative surface areas. The impact of these features on the effectiveness of buffer layers to improve electrode kinetics must, therefore, be carefully examined in future work.

Nevertheless, as a preliminary demonstration, Figure 5.12 shows some examples of some experimental spectra and the corresponding fittings according to the equivalent circuits presented in Figure 5.11. Although these results should be analyzed with care and are only presented as illustrative, they confirm that the additional path corresponding to the buffer layer can account for the great decrease in total resistance and for the displacement of the apparent processes to a lower range of frequencies.

The tentative fitting was performed as follows. Firstly we have fitted the sample without buffer layer according to the circuit shown in Figure 5.11(a), in which two different paths are considered for the whole electrochemical process, that of the charge transference at the TPB and that corresponding to the bulk path through the mixed conducting electrode (Figure 5.12a). Our starting condition was focused on fixing an estimative value of capacitance ~10^{-6} F/cm^2 for the TPB process according to reported values of true interfacial polarization capacitance in the order of 10^{-5}-10^{-6} F/cm^2 for Pt/YSZ interface [26]. On the other hand, given that the active area of reaction corresponding to triple phase contacts is approximately similar, we have introduced a second approximation in which it was assumed that the TPB process is not considerably affected by the presence of the buffer layer. This assumption may fail, mainly due to some differences in the oxygen exchange and ionic properties of the electrode/electrolyte interface or the electrode/buffer layer interface. However one expects minor differences compared to that exerted by the other path contributions, because the availability of free electrons, coming from the electrode, required for charge transfer at TPB is considered the rate limiting step for the oxygen surface exchange (Figure 1.12a) in YSZ and CGO based electrolytes [43]. In this respect, Horita et al. [44] reported no increase in the surface reaction rate by the use of Y-doped ceria in comparison to YSZ. As a consequence, the fitting of the spectra corresponding to CGO+Co and CPO+Co as buffer layers to the equivalent circuit presented in Figure 5.11b, was performed after fixing the parameters corresponding to the bulk electrode path and the charge transfer at TPB, previously obtained in the fitting of the sample without buffer layer.

The results presented in Figure 5.12b confirm that the presence of the additional parallel path corresponding to the buffer layer in the equivalent circuit of Figure 5.11b can account for the great increase of the overall electrochemical performance.

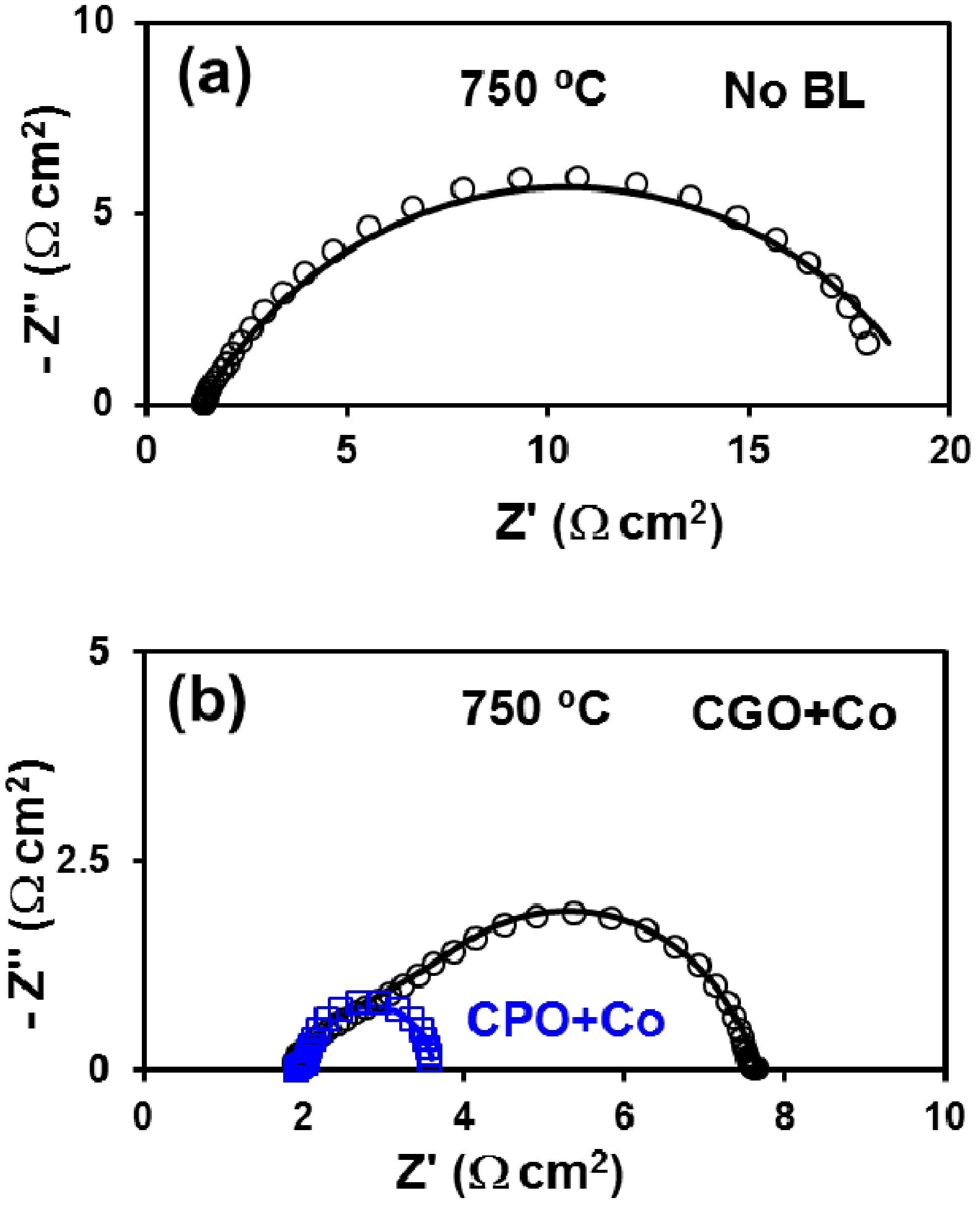

Figure 5.12. Experimental spectra obtained at 750°C at OCP (points) for the studied samples and corresponding fittings (lines) obtained using the equivalent circuits presented in Figure 5.11.

Moreover, the frequency dependence of the impedance results is also well explained by the parallel electroactive path through the buffer layer as it is inferred from Figure 5.13, which shows continued acceptable agreement between the experimental results and the fitting curve obtained by means of the circuit presented in Figure 5.11b. Note the lower peak frequencies in the CPO+Co case in agreement with Figure 5.9b. These results additionally highlight that the vastly superior electrochemical performance of CPO+Co in comparison to CGO+Co (Figure 5.12b) can be accounted for by improvement in both resistive terms affecting the buffer-path performance, that related to the surface exchange and that related to the mass transfer, in agreement with the expected dependence of both contributions on the level of ambipolar transport of ionic and electronic species.

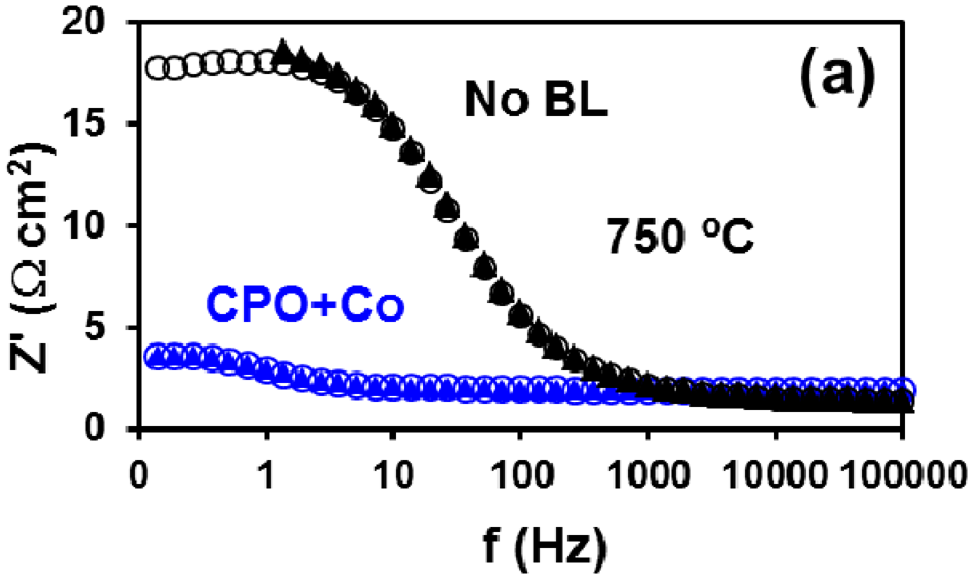

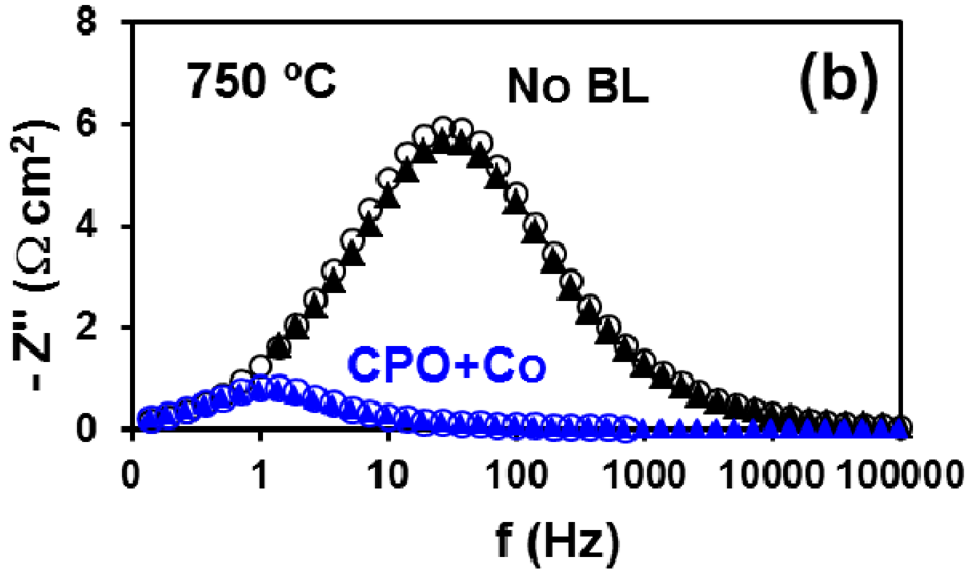

Figure 5.13. Frequency dependence of the impedance data for CPO+Co sample at 750°C (Filled symbols-fitting data and Open symbols-experimental data).

A potential advantage of the current buffer layers is that they are of the same crystallographic structure as the YSZ electrolyte, cubic defect fluorite, a factor that may facilitate ionic motion across the buffer layer/electrolyte boundary due to a continuous oxygen sublattice. It is possible that dense buffer layers from other structural families, such as perovskite, may present additional interfacial resistances due to oxygen sublattice mismatch, a factor again requiring future study. Nevertheless, the current results clearly demonstrate the enormous potential of fluorite buffer layers to improve polarization behavior in SOFC and SOEC devices and the vital role of the ambipolar conductivity in obtaining this effect. The highest performance of the current work is obtained for the CPO+Co buffer layer, which offers the highest ambipolar conductivity of the materials studied, and yields values of polarization resistance that are of an order of magnitude smaller than that of an identical $Nd_2NiO_{4+\delta}$ electrode without a buffer layer.

5.4. Conclusions

The current work has investigated if ceria based buffer layers can offer a twofold role in SOFCs and SOECs to prevent interaction of $Nd_2NiO_{4+\delta}$ electrodes with the YSZ electrolyte and to simultaneously offer improvements in electrode kinetics. Half cells of $Nd_2NiO_{4+\delta}$ electrodes with or without $Ce_{0.8}R_{0.2}O_{2-\delta}$ + 2 mol% Co buffer layers (where R =

Gd, Pr) have been fabricated by spin coating on dense YSZ electrolyte supports and co-sintered at 900°C. Results show the formation of well separated and adhered layers that are absent of observable cation interdiffusion. XRD results of calcined intimate mixtures of the $Nd_2NiO_{4+\delta}$ electrodes and ceria based buffer layers further reinforce the absence of chemical interactions, demonstrating the functionality of all studied buffer layers. Substantial decreases in polarization resistance, Rp, of up to an order of magnitude, can be achieved in the order, no buffer layer > Gd >> Pr. However, the respective values of capacitance, polarisation resistances and subsequent relaxation frequencies, are shown to not correspond to simple considerations of geometry and an increase in surface area. The article outlines how these features may, instead, be explained by a more complex association of potential parallel paths that depend, not only on the resistance to solid state mass transport though the two mixed conducting pathways, but also to their respective levels of surface exchange; factors that can be both related to increased levels of ambipolar conductivity in the mixed conducting buffer layers. This result is important as it shows that the electrochemical performance of the oxygen electrode in SOFC and SOEC devices can be radically improved by tailoring of the transport properties of a thin buffer layer.

5.5. References

[1] M. Shiono, K. Kobayashi, T.L. Nguyen, K. Hosoda, T. Kato, K. Ota, M. Dokiya, Effect of CeO_2 interlayer on ZrO_2 electrolyte/La(Sr)CoO_3 cathode for low-temperature SOFCs, Solid State Ionics 170 (2004) 1–7.

[2] T. Ogier, J.M. Bassat, F. Mauvy, S. Fourcade, J.C. Grenier, K. Couturier, Enhanced performances of structured oxygen electrodes for high temperature steam electrolysis, Fuel Cells 13 (2013) 536–541.

[3] O.A. Marina, L.R. Pederson, M.C. Williams, G.W. Coffey, K.D. Meinhardt, C.D. Nguyen, Electrode performance in reversible solid oxide fuel cells, Journal of Electrochemical Society 154 (2007) B452–B459.

[4] T. Nguyen, K. Kobayashi, T. Honda, Y. Iimura, K. Kato, A. Neghisi, K. Nozaki, F. Tappero, K. Sasaki, H. Shirahama, K. Ota, M. Dokiya, T. Kato, Preparation and evaluation of doped ceria interlayer on supported stabilized zirconia electrolyte SOFCs by wet ceramic processes, Solid State Ionics 174 (2004) 163–174.

[5] D. Wang, J. Wang, C. He, Y. Tao, C. Xu, W.G. Wang, Preparation of a $Gd_{0.1}Ce_{0.9}O_{2-\delta}$ interlayer for intermediate-temperature solid oxide fuel cells by spray coating, Journal of Alloys and Compounds 505 (2010) 118–124.

[6] C. Ferchaud, J.-C. Grenier, Y. Zhang-Steenwinkel, M.M.A. van Tuel, F.P.F. van Berkel, J.-M. Bassat, High performance praseodymium nickelate oxide cathode for low temperature solid oxide fuel cell, Journal of Power Sources 196 (2011) 1872–1879.

[7] J.-J. Choi, D.-S. Park, B.-G. Seong, H.-Y. Bae, Low-temperature preparation of dense $(Gd,Ce)O_{2-\delta}$–Gd_2O_3 composite buffer layer by aerosol deposition for YSZ electrolyte-based SOFC, International Journal of Hydrogen Energy 37 (2012) 9809–9815.

[8] F. Mauvy, C. Lalanne, J.-M. Bassat, J.-C. Grenier, H. Zhao, L. Huo, P. Stevens, Electrode properties of $Ln_2NiO_{4+\delta}$ (Ln=La, Nd, Pr), Journal of Electrochemical Society 153 (2006) A1547–A1553.

[9] J. Wan, J. Goodenough, J. Zhu, $Nd_{2-x}La_xNiO_{4+\delta}$, a mixed ionic/electronic conductor with interstitial oxygen, as a cathode material, Solid State Ionics 178 (2007) 281–286.

[10] V.A.C. Haanappel, C. Lalanne, A. Mai, F. Tietz, Characterization of Anode-Supported Solid Oxide Fuel Cells With Nd_2NiO_4 Cathodes, Journal of Fuel Cell Science and Technology 6 (2009) 041016–041021.

[11] F. Chauveau, J. Mougin, J.M. Bassat, F. Mauvy, J.C. Grenier, A new anode material for solid oxide electrolyser: The neodymium nickelate $Nd_2NiO_{4+\delta}$, Journal of Power Sources 195 (2010) 744–749.

[12] A.M. Svensson, S. Sunde, K.N. Ancioglu, Mathematical modeling of oxygen exchange and transport in air-perovskite-yttria-stabilized zirconia interface regions, Journal of The Electrochemical Society 145 (1998) 1390–1400.

[13] A. Montenegro-Hernández, J. Vega-Castillo, L. Mogni, A. Caneiro, Thermal stability of $Ln_2NiO_{4+\delta}$ (Ln: La, Pr, Nd) and their chemical compatibility with YSZ and CGO solid electrolytes, International Journal of Hydrogen Energy 36 (2011) 15704–15714.

[14] B.A. van Hassel, B. Boukamp, A. Bourggraaf, Electrode polarization at the Au, O_2(g)/Fe implanted yttria-stabilized zirconia interface, Solid State Ionics 51 (1992) 161–174.

[15] A. Endo, S. Wada, C. Wen, H. Komiyama, K. Yamada, Low overvoltage mechanism of high ionic conducting cathode for solid oxide fuel cell, Journal of Electrochemical Society 145 (1998) L35–L37.

[16] N. Hildenbrand, B.A. Boukamp, P. Nammensma, D.H.A. Blank, Improved cathode/electrolyte interface of SOFC, Solid State Ionics 192 (2011) 12–15.

[17] D.P. Fagg, V.V. Kharton, J.R. Frade, P-Type electronic transport in $Ce_{0.8}Gd_{0.2}O_{2-\delta}$: The effect of transition metal oxide sintering aids, Journal of Electroceramics 9 (2002) 199–207.

[18] D.P. Fagg, J.C.C. Abrantes, D. Pérez-Coll, P. Núñez, V.V. Kharton, J.R. Frade, The effect of cobalt oxide sintering aid on electronic transport in $Ce_{0.80}Gd_{0.20}O_{2-\delta}$ electrolyte, Electrochimical Acta 48 (2003) 1023–1029.

[19] D.P. Fagg, A.L. Shaula, V.V. Kharton, J.R. Frade, High oxygen permeability in fluorite-type $Ce_{0.8}Pr_{0.2}O_{2-\delta}$ via the use of sintering aids, Journal of Membrane Science 299 (2007) 1–7.

[20] D.P. Fagg, S. García-martin, V.V. Kharton, J.R. Frade, Transport Properties of Fluorite-Type $Ce_{0.8}Pr_{0.2}O_{2-\delta}$: Optimization via the Use of Cobalt Oxide Sintering Aid, Chemistry of Materials 21 (2009) 381–391.

[21] M. Balaguer, C. Solís, S. Roitsch, J.M. Serra, Engineering microstructure and redox properties in the mixed conductor $Ce_{(0.9)}Pr_{(0.1)}O_{(2-\delta)}$ + Co 2 mol%, Dalton Transactions 43 (2014) 4305–4312.

[22] D.P. Fagg, J.R. Frade, V.V. Kharton, I.P. Marozau, The defect chemistry of Ce(Pr, Zr)$O_{2-\delta}$, Journal of Solid Stat Chemistry 179 (2006) 1469–1477.

[23] C. Chatzichristodoulou, P.V. Hendriksen, Electronic and ionic transport in $Ce_{0.8}Pr_xTb_{0.2-x}O_{2-\delta}$ and evaluation of performance as oxygen permeation membranes, Journal of Electrochemical Society 159 (2012) E162–E170.

[24] C. Chatzichristodoulou, P.V. Hendriksen, Oxygen nonstoichiometry and defect chemistry modeling of $Ce_{0.8}Pr_{0.2}O_{2-\delta}$, Journal of Electrochemical Society 157 (2010) B481–B489.

[25] J.E. Bauerle, Study of solid electrolyte polarization by a complex admittance method, Journal of Physical Chemistry Solids 30 (1969) 2657–2670.

[26] S.B. Adler, Factors governing oxygen reduction in solid oxide fuel cell cathodes, Chemical Review 104 (2004) 4791–4843.

[27] M.M. Kuklja, E.A. Kotomin, R. Merkle, Y.A. Mastrikov, J. Maier, Combined theoretical and experimental analysis of processes determining cathode performance in solid oxide fuel cells., Physical Chemistry Chemical Physics 15 (2013) 5443–5471.

[28] L. Yihong, R. Gemmen, X. Liu, Oxygen reduction and transportation mechanisms in solid oxide fuel cell cathodes, Journal of Power Sources 195 (2010) 3345–3358.

[29] M. Liu, Equivalent circuit approximation to porous mixed-conducting oxygen electrodes in solid-state cells, Journal of Electrochemical Society 145 (1998) 142–153.

[30] I.R. Gibson, G.P. Dransfield, J.T.S. Irvine, Sinterability of commercial 8 mol% yttria-stabilized zirconia powders and the effect of sintered density on the ionic conductivity, Journal of Materials Science 33 (1998) 4297–4305.

[31] F. Mauvy, C. Lalanne, J.M. Bassat, J.C. Grenier, H. Zhao, P. Dordor, Ph. Stevens, Oxygen reduction on porous $Ln_2NiO_{4+\delta}$ electrodes, Journal of European Ceramics Society 25 (2005) 2669–2672.

[32] B.A. van Hassel, B.A. Boukamp, A.J. Burggraaf, Oxygen transfer properties of ion-implanted yttria-stabilized zirconia, Solid State Ionics 53 (1992) 890–903.

[33] P. Bohac, A. Orliukas, L. Gauckler, Lowering of the cathode overpotential of SOFC by electrolyte doping, Electroceramics IV, II, (1994) 771–774.

[34] D.P. Fagg, V.V. Kharton, J.R. Frade, Transport in ceria electrolytes modified with sintering aids: effects on oxygen reduction kinetics, Journal of Solid State Electrochemistry 8 (2004) 618–625.

[35] D. Pérez-Coll, A. Aguadero, M.J. Escudero, P. Núñez, L. Daza, Optimization of the interface polarization of the La_2NiO_4-based cathode working with the $Ce_{1-x}Sm_xO_{2-\delta}$ electrolyte system, Journal of Power Sources 178 (2008) 151–162.

[36] D. Pérez-Coll, A. Aguadero, M.J. Escudero, L. Daza, Effect of DC current polarization on the electrochemical behaviour of $La_2NiO_{4+\delta}$ and $La_3Ni_2O_{7+\delta}$-based systems, Journal of Power Sources 192 (2009) 2–13.

[37] Y.-M. Kim, S.-I. Pyun, J.-S. Kim, G.-J. Lee, Mixed Diffusion and Charge-Transfer-Controlled Oxygen Reduction on Dense $La_{1-x}Sr_xCo_{0.2}Fe_{0.8}O_{3-\delta}$ Electrodes with Various Sr Contents, Journal of Electrochemical Society 154 (2007) B802–B809.

[38] V.V. Kharton, A.P. Viskup, E.N. Naumovich, F.M.B. Marques, Oxygen ion transport in La_2NiO4 based ceramics, Journal of Materials Chemistry 9 (1999) 2623–2629.

[39] E.V. Tsipis, E.N. Naumovich, M.V. Patrakeev, A.A. Yaremchenko, I.P. Marozau, A.V. Kovalevsky, J.C. Waerenborgh, V.V. Kharton, Oxygen deficiency, vacancy clustering and ionic transport in (La,Sr)$CoO_{3-\delta}$, Solid State Ionics 192 (2011) 42–48.

[40] V.V. Kharton, A.P. Viskup, A.V. Kovalevsky, E.N. Naumovich, F.M.B. Marques, Ionic transport in oxygen-hyperstoichiometric phases with K_2NiF_4-type structure, Solid State Ionics 143 (2001) 337–353.

[41] T. Nakamura, K. Yashiro, K. Sato, J. Mizusaki, Electrical conductivity, Seebeck coefficient, and defect structure of oxygen nonstoichiometric $Nd_{2-x}Sr_xNiO_{4+\delta}$, Materials Chemistry Physics 122 (2010) 250–258.

[42] J. Fleig, Solid oxide fuel cell cathodes:polarization mechanisms and modeling of the electrochemical performance, Annual Review Material Research 33 (2003) 361–382.

[43] P.S. Manning, J.D. Sirman, J.A. Kilner, Oxygen self-diffusion and surface exchange studies of oxide electrolytes having the fluorite structure, Solid State Ionics 93 (1996) 125–132.

[44] T. Horita, K. Yamaji, N. Sakai, M. Ishikawa, H. Yokokawa, T. Kawada, M. Dokiya, Oxygen surface exchange of $Y_{0.2}Ce_{0.8}O_{2-x}$ under reducing atmosphere, Electrochemistry Solid-State Letters 1 (1998) 4–6.

6. A new terbium-doped cerium ($Ce_{0.8}Tb_{0.2}O_{2-\delta}$) buffer layer for SOFCs and SOECs

6.1. Introduction

Chapter 5 demonstrated how tailoring the transport properties of ceria based buffer layers can provide necessary phase stability against chemical interaction at the electrode/electrolyte interface, while also providing radical improvements to electrochemical performance. Half cells of CGO and CPO with Co buffer layers with $Nd_2NiO_{4+\delta}$ electrodes were fabricated by spin coating on dense YSZ electrolyte supports and co-sintered at 900°C. Electrochemical measurements showed that valuable decreases in polarization resistancecould be achieved in the order, Rp no buffer layer > Gd >> Pr. The results suggested that one can tune the extension of electrochemically active sites in oxygen electrodes by increasing the ambipolar conductivity of the buffer layer, while continuing to prevent degradation by the physical presence of the buffer layer material between electrode and electrolyte.

Moreover, Chapter 3 assessed the mixed ionic and electronic transport characteristics of the material $Ce_{0.8}Tb_{0.2}O_{2-\delta}$ (CTO) with small additions (2 mol%) of Co sintering additives. It was shown that peak ambipolar conductivity was offered by samples sintered at the lower temperature of 900^{o}C. Building on this information, Chapter 4 compared the mixed conducting properties of a range of ceria-based materials containing Co-additives, CGO+Co CTO+CO and CPO+Co, sintered at similar low temperatures, where peak ambipolar conductivities are documented [1][2]. The comparison highlighted that the CPO+Co material offers the highest ambipolar conductivity of these materials, while the ambipolar conductivity of CTO+Co was slightly lower. Based on this data, the current chapter aims to compare the performance of the new MIEC. $Ce_{0.8}Tb_{0.2}O_{2-\delta}$ + Co (CTO+Co) material with the previously measured CPO+Co composition, as potential buffer layers for an otherwise identical electrochemical cell consisting of a $Nd_2NiO_{4+\delta}$ electrode and YSZ electrolyte.

6.2. Experimental

The terbium-doped (20 mol%) cerium oxide composition was prepared by the hydrothermal method, while $Nd_2NiO_{4+\delta}$ powder was prepared by the citrate route (see procedures in Chapter 2.1). The electrochemical cell with the CTO+Co buffer layer ($Nd_2NiO_{4+\delta}$/CTO+Co/YSZ) was prepared by an identical spin coating technique to that performed for the CPO+Co buffer layer, as described in Chapter 2.2. Both assemblies were fabricated with a maximum co-sintering temperature of 900ºC to retain peak ambipolar conductivities of the buffer layers.

Powder XRD patterns were recorded at room temperature to identify the phase purity of CTO powder prepared by hydrothermal synthesis. In addition, the chemical stability of buffer layer with the respective electrode and electrolyte materials was investigated independently by X-ray diffraction by intimately mixing the powders in 50:50 wt% ratios and calcining at conditions equal to that used in cell preparation (900°C for 10 h). The cross sectional microstructure and morphology of the cell was analysed by scanning electron microscopy with complementary elemental analysis performed by Energy Dispersive X-ray spectroscopy (EDS). Electrochemical characterization was performed by a.c. impedance spectroscopy of the formed electrochemical cell in an identical way to that performed for the CPO+Co buffer layer as described in Chapter 2.7). To better understand the effect of the CTO buffer layer, the electrochemical results are compared to those of composition CPO+Co; the best performing MIEC buffer layer from Chapter 4.

6.3. Results and Discussion

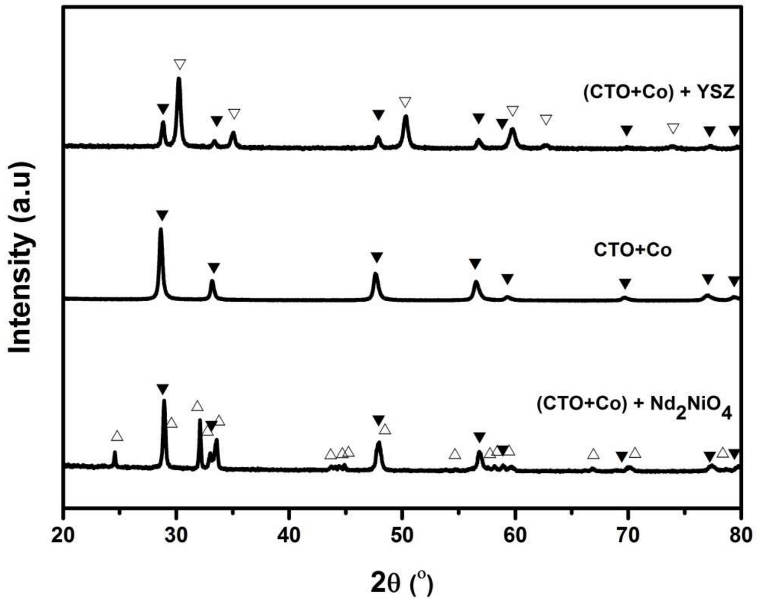

Figure 6.1. XRD phase analysis of Terbium-doped cerium (CTO+Co) buffer layer and with intimate mixtures of $Nd_2NiO_{4+\delta}$ electrode and YSZ electrolyte after firing for 10h at 900°C.

Figure 6.1 shows the XRD patterns of CTO powder with Co-additions prepared by the hydrothermal method. It is observed that the prepared powder is single phase with the expected cubic defect fluorite structure, with no observable impurity peaks. In order to check the chemical stability of the buffer layer, intimate mixtures of the CTO+Co buffer layer with the $Nd_2NiO_{4+\delta}$ electrode and with the YSZ electrolyte were prepared and sintered at 900°C for 10 h. The obtained results show the presence of only the desired phase compositions, with no extra impurity phases observable from potential reactions between buffer layer/electrode and buffer layer/electrolyte mixtures, respectively. This analysis indicates that, similar to the other ceria-based buffer layers assessed in Chapter 5, cobalt containing CTO can serve as a compatible buffer layer to prevent interaction between $Nd_2NiO_{4+\delta}$ electrodes and YSZ electrolytes under these conditions.

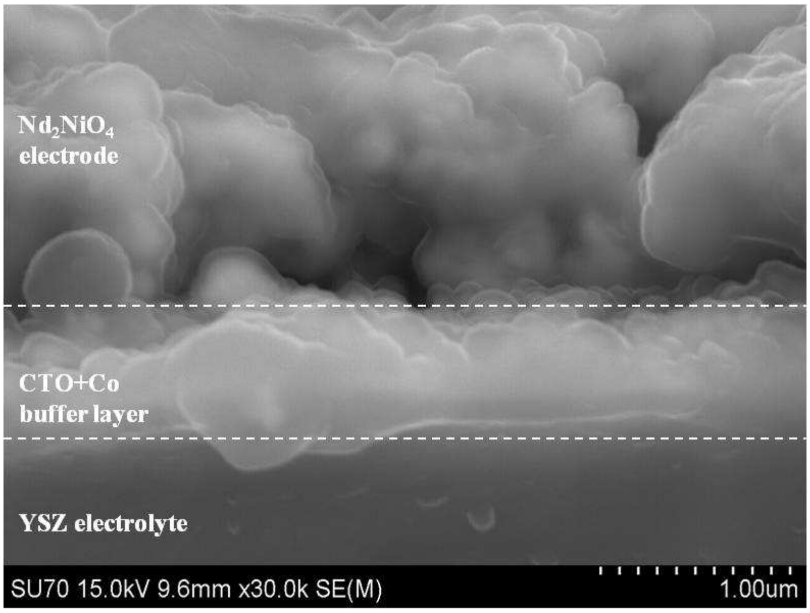

Figure 6.2. Cross-sectional microstructure of CTO+Co buffer layer with electrolyte/electrode assemblies.

Figure 6.2 presents cross sectional micrographs of Nd_2NiO_4 electrode and YSZ electrolyte assemblies formed with the CTO+Co buffer layer. The SEM results show a dense, thin and uniform buffer layer, with thickness around 0.5μm, that is well adhered to the YSZ substrate. The thicknesses of the Nd_2NiO_4 electrodes are approximately 2 μm in each case and are once more shown to be well adhered to the supporting layer. Comparison between the current SEM images and those obtained for the CPO+Co buffer layer in Chapter 5.3, Figures 5.2, suggest a similar morphology for both buffer layers, with analogous cell architectures that subsequently facilitate direct comparison of their electrochemical behaviors.

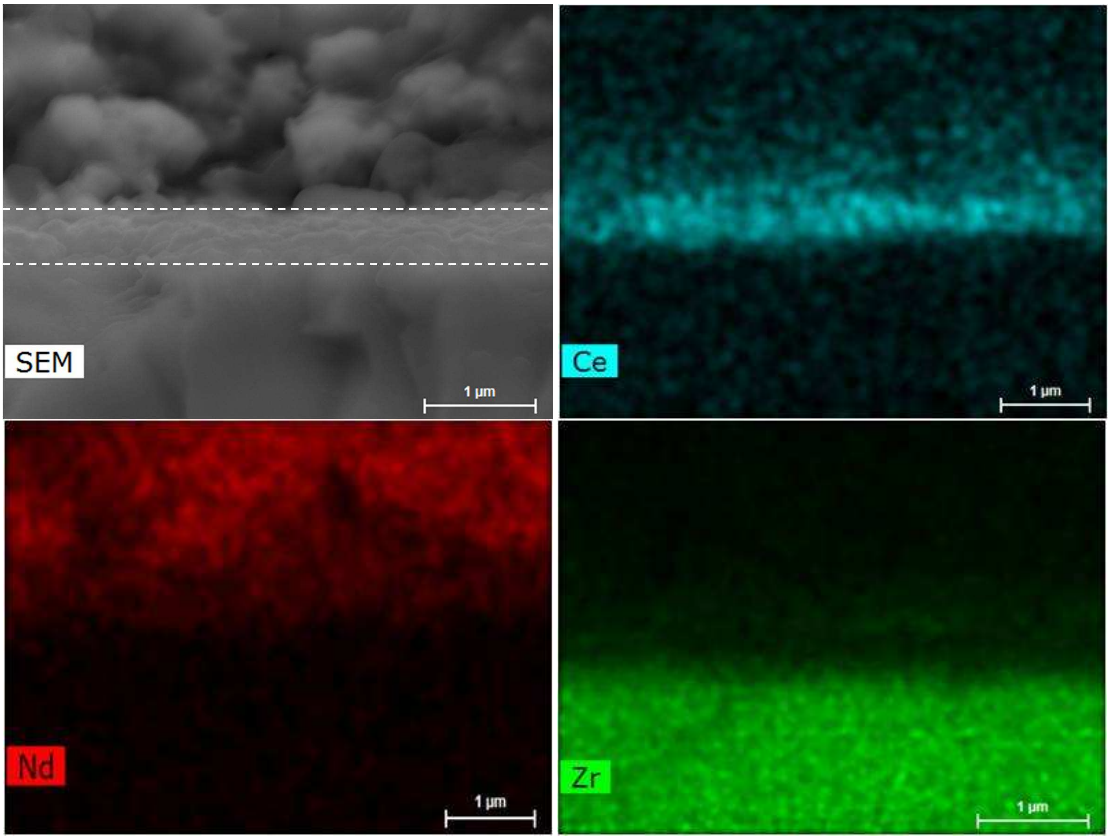

Figure 6.3. SEM-EDS analysis performed across the electrode/electrolyte interface of an Nd_2NiO_4/CTO+Co/YSZ assembly.

Figure 6.3 presents compositional analysis of the Nd_2NiO_4/CTO+Co/YSZ assembly by EDS mapping, confirming a clear separation of the $Nd_2NiO_{4+\delta}$ electrode, the CTO+Co buffer layer and the YSZ electrolyte in the architecture, with no notable cation interdiffusion. This result suggests successful fabrication of the electrolyte/buffer layer/electrode assemblies and the absence of chemical interactions between layers, in agreement with that previously noted for the CPO+Co analogue in Chapter 5.

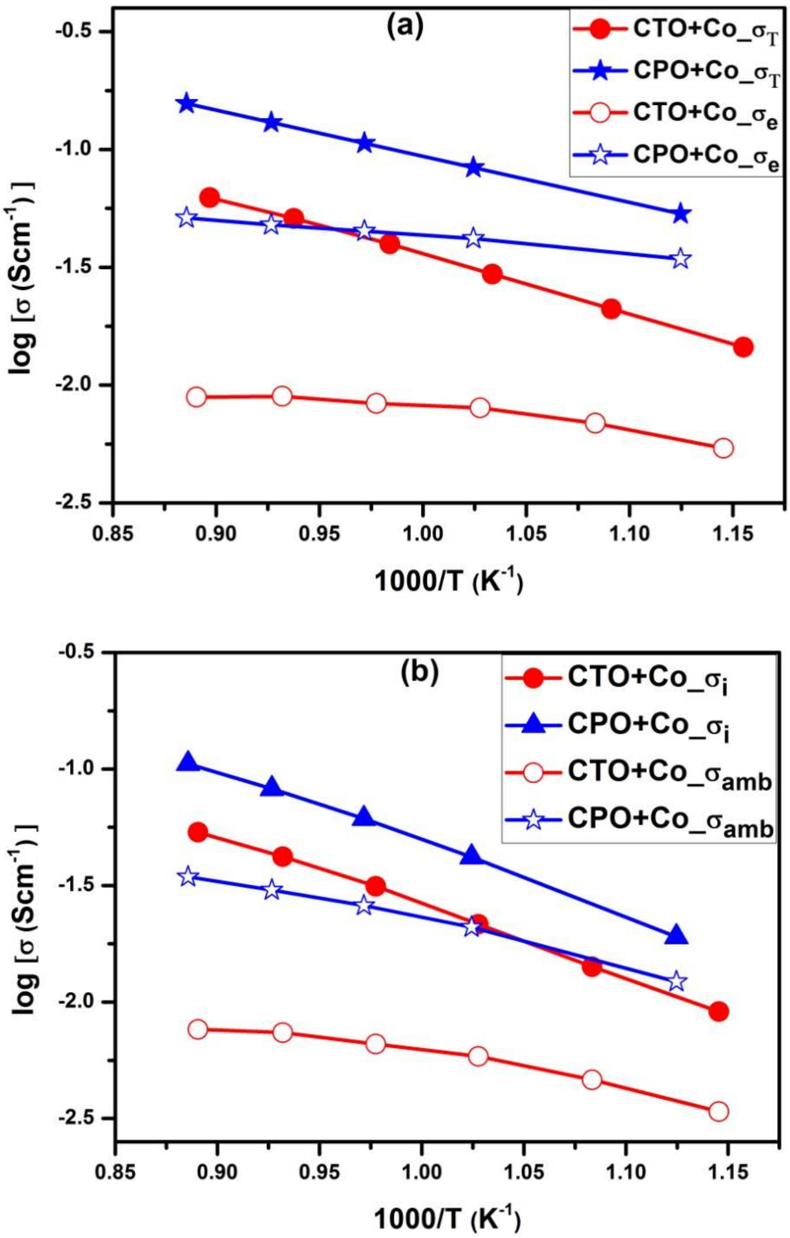

Figure 6.4. Conductivities of CTO+Co and CPO+Co a) total and electronic b) ionic and ambipolar.

For convenience, the transport properties of bulk samples of the CTO+Co (sintered at 900^{o}C) buffer layer material are re-outlined in figure 6.4 and compared to equivalent literature data for CPO+Co cermets analysed by the same technique [3,4]. The respective activation energies for total, ionic, electronic and ambipolar conductivities are documented in Table 6.1. Figure 6.4 shows the total, ionic, electronic and ambipolar conductivities of CTO+Co to be slightly inferior to those measured for CPO+Co. A slightly higher activation energy for ambipolar conductivity is also notable for the CPO+Co composition, Table 6.1.

Table 6.1. Activation energy of CTO+Co and CPO+Co conductivities with temperature

Sample	Activation energy E_a (eV)			
	Total	Ionic	Electronic	Ambipolar
CTO +Co	0.58 ± 0.01	0.68 ± 0.02	0.25 ± 0.07	0.36 ± 0.07
CPO +Co	0.49 ± 0.03	0.72 ± 0.04	0.23 ± 0.02	0.48 ± 0.06

The observed trends in the transport properties of these materials concur with available literature data on their Co-free analogues. The depletion in ionic conductivity in the terbium case can be related to the increasing reducibility of the rare earth dopant, Tb > Pr, with an associated decrease in ionic motion at higher oxygen vacancy concentrations due to vacancy ordering [5–8], while, the slightly inferior total and electronic conductivities of the terbium containing material, in comparison to that of the praseodymium analogue, can be related to a lower mobility of small polarons in the Tb case [6].

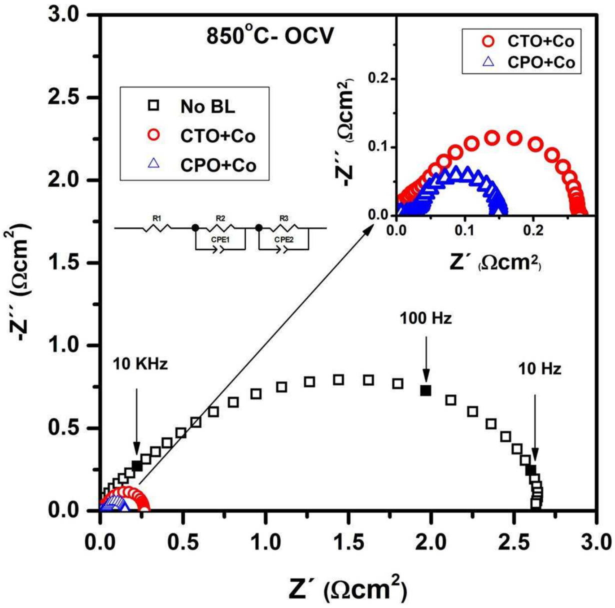

Figure 6.5. Typical impedance spectra of cell with CTO+Co buffer layer measured at OCV, compared to that of cells with no buffer layer (BL) or containing the buffer layer CPO+Co under the same conditions. Ohmic offset, R1, has been subtracted.

Figure 6.5 shows an example impedance spectrum of the cell with the CTO+Co buffer layer measured at 850^{o}C under OCP condition. The spectrum consists of a small semicircle notable at intermediate frequencies followed by a larger semicircle at lower frequency. To show this more clearly the CTO+Co spectra is magnified in the inset of this figure. For comparison, the impedance spectra of cells with no buffer layer or containing a CPO+Co buffer layer measured under the same conditions are also inserted. The samples with buffer layers show significant decreases in overall resistance in comparison to the sample with no buffer layer. Under these conditions, the overall performance of the CPO+Co buffer layer sample is shown to slightly exceed that of the CTO+Co analogue. All impedance spectra were fitted to the simple equivalent circuit shown in Figure 6.5.

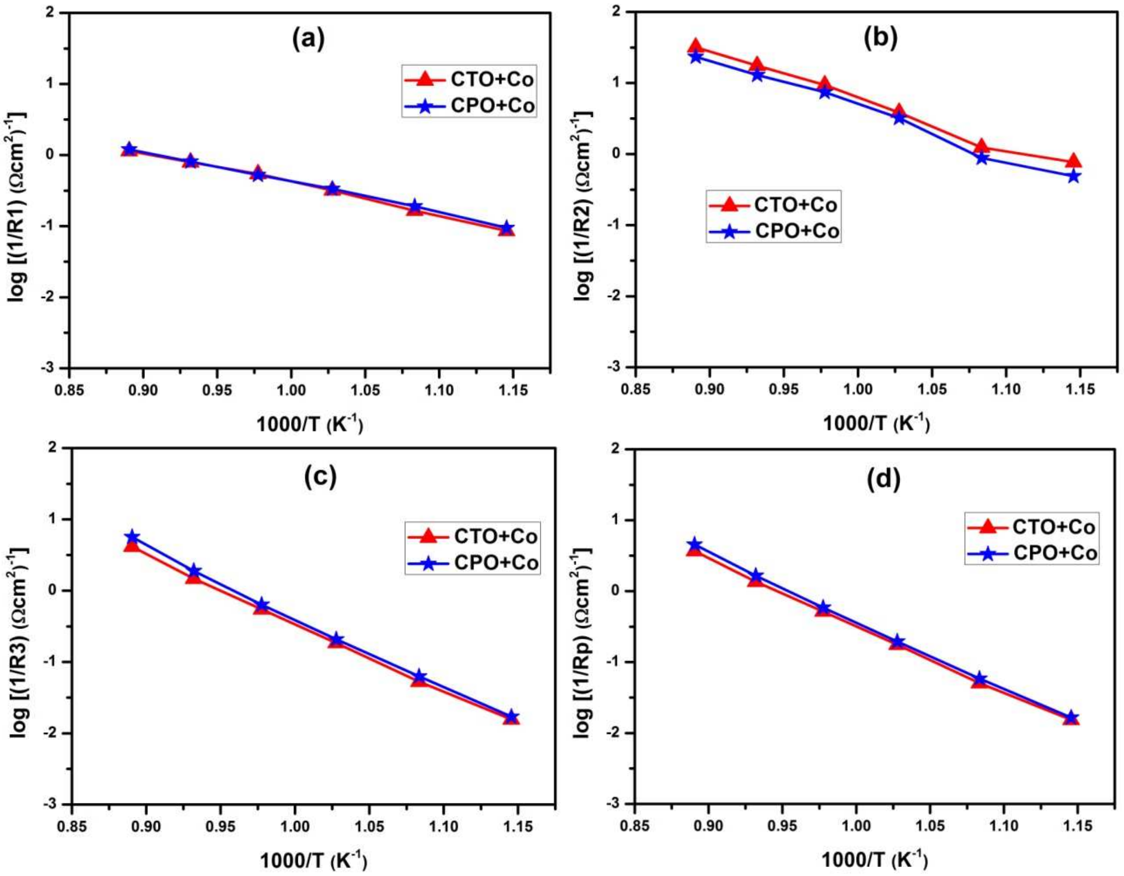

Figure 6.6. The Arrhenius behavior of the polarization resistances a) R1, b) R2, c) R3 and d) Rp, for cells with buffer layers CTO+Co or CPO+Co.

Figure 6.6a and b show the Arrhenius behavior of the extracted resistances R1, and R2 for the buffer layer samples CTO+Co and CPO+Co, with respective active energies documented in Table 6.2. The high frequency intercept (R1) exhibits activation energies of approximately 0.8 eV for CTO+Co and CPO+Co buffer layer samples, corresponding well to that expected for ionic conductivity of the YSZ electrolyte material [9]. For this reason, the R1 response is attributed to cell ohmic resistance and is noted to be comparable to that previously obtained for similar electrochemical cells, without a buffer layer or with CGO+Co buffer layer, in Chapter 5, Table 5.2.

Table 6.2. Activation energies of 1/R1, 1/R2, 1/R3 and 1/R4 for cells containing CTO+Co and CPO+Co buffer layers measured at OCP.

Sample	Activation energy E_a (eV)			
	R1	R2	R3	Rp
CTO +Co	0.88 ± 0.03	1.33 ± 0.07	1.88 ± 0.03	1.85 ± 0.03
CPO +Co	0.85 ± 0.02	1.37 ± 0.08	1.95 ± 0.04	1.90 ± 0.03

The values of the polarization resistance R2 for the CPO+Co and CTO+Co buffer layer cells are shown to be similar and to present comparable activation energies. In both cases, the R3 responses are observed to be approximately an order of magnitude more resistive than that of the R2 responses and, thus, dominate the values of total polarization resistance, Rp, Figure 6.6c and d. With increasing temperature, the values of R3 and total polarization resistance are shown to deviate between the CTO+Co and CPO+Co buffer layers, becoming increasingly more resistive in the CTO+Co case, Fig.6.6c and d. Thus, as temperature increases, the performances of the CPO+Co and CTO+Co materials are noted to diverge, with an increasingly inferior performance provided by the CTO+Co buffer layer. This trend cannot be simply explained by levels of electronic conductivity, as both the CPO+Co and the CTO+Co materials are shown to have similar activation energies for the electronic component (Table 6.1). Nonetheless, it can be directly related to their ambipolar conductivities, which present lower activation energy in the CTO+Co case, Table 6.1. This is an interesting feature that provides support to the discussion of Chapter 5 that suggested, based on the work of Liu [7], that the kinetics of oxygen reduction through a parallel mixed ionic and electronic conducting buffer layer path can be in part related to solid state diffusion given by the sum of the ionic and electronic resistivities integrated throughout the thickness of the electrode, Figure 5.6 in Chapter 5 [10]. Note that a sum of the ionic and electronic resistivities is equivalent to the inverse of the ambipolar conductivity. Thus, in agreement with the suggestion of Liu, the lower activation energy for the ambipolar conductivity of CTO+Co than CPO+Co, Table 6.1, would result in divergence of polarization resistance with increasing temperature, with the lowest polarization resistance provided by the buffer layer composition of the highest ambipolar conductivity, CPO+Co. At this juncture, it should also be mentioned that oxygen reduction kinetics through a mixed conducting buffer layer path also involves oxygen surface exchange [10–12] a factor which has also been shown to depend on ambipolar conductivity [4,13]. Thus, both these considerations based on ambipolar conductivity would correspond to the observed trend in polarization resistance.

Chapter 5 outlined that the presence of a mixed conducting buffer layer and additional parallel path for electrochemical reaction would lead, not only to a reduction in polarization resistance, as described in the previous paragraph, but also to an increase in effective capacitance and reduction in relaxation frequency of the impedance response. Figure 6.7 shows that these phenomena are also obtained for the CTO+Co buffer layer sample, reinforcing the characteristic nature of this behavior for MIEC buffer layers. In the current work, both MIEC buffer layers, CPO+Co and CTO+Co, show similar results, of much greater capacitance values and lower relaxation frequencies than obtained in the cell without a buffer layer, in agreement with that reported in Chapter 5.

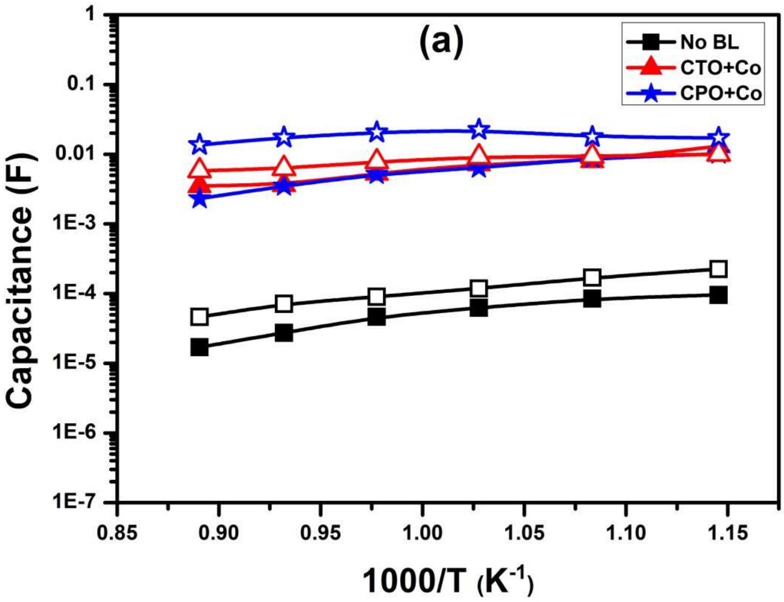

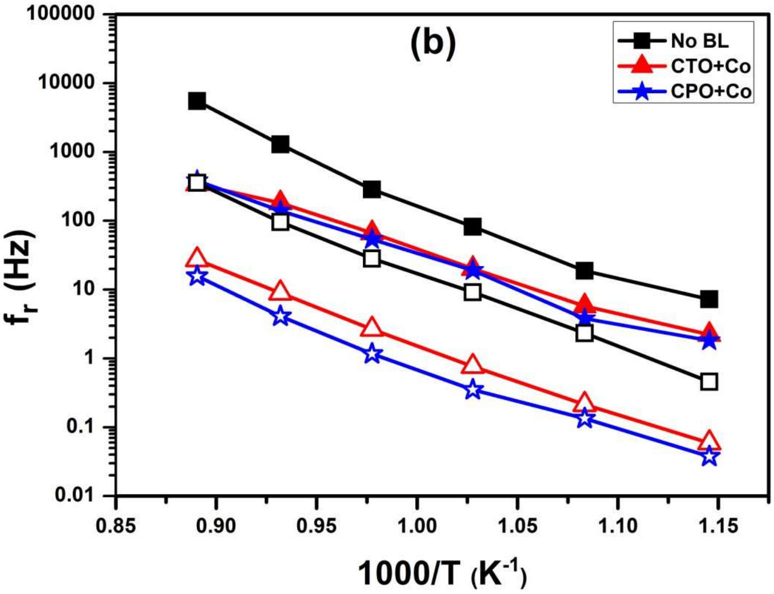

Figure 6.7. Temperature dependence of a) the Capacitance and b) Relaxation frequency, for cells with buffer layers CTO+Co or CPO+Co. Filled symbols relate to the higher frequency polarization response (R2), open symbols to the lower frequency response (R3).

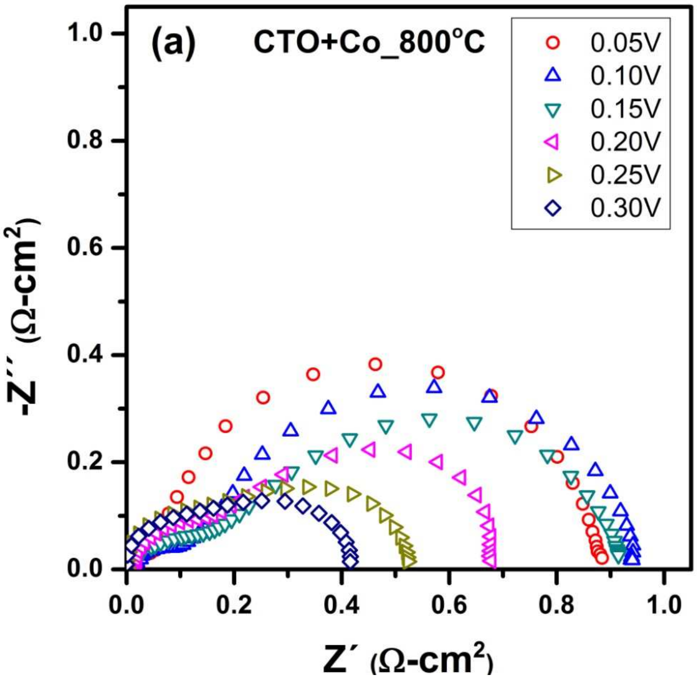

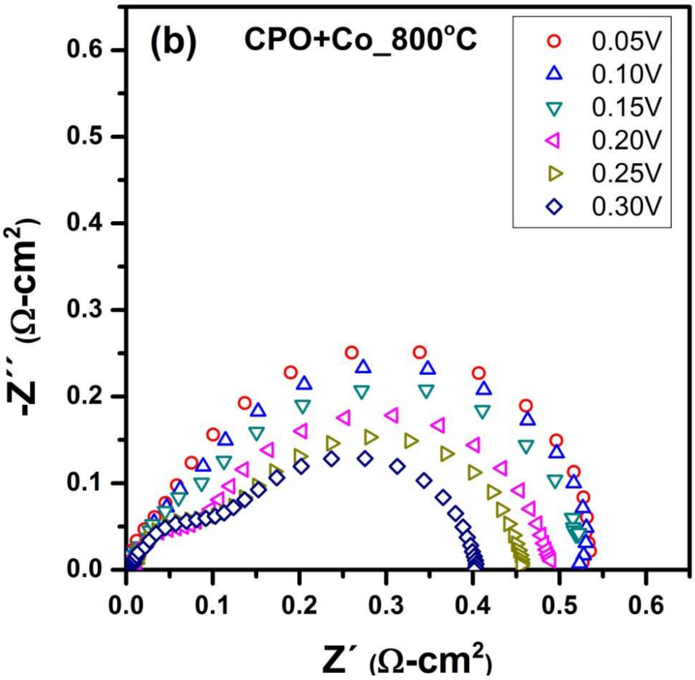

Figure 6.8. Impedance spectra of cells containing a) CTO+Co and b) CPO+Co buffer layers measured under anodic bias in air.

Figure 6.8 shows examples of typical impedance spectra obtained under anodic polarization for the Nd_2NiO_4 electrode with CTO+Co and CPO+Co buffer layers at 800^{o}C in air atmosphere. The impedance spectra change in magnitude upon polarization, while retaining their general shape comprising of two semicircular responses. For this reason all impedance spectra were fitted to a similar equivalent circuit to that use under OPC conditions, as shown in Figure 6.5. The corresponding total polarization resistance, Rp, is shown in Figure 6.9 as a function of applied D.C. potential in the range +0.3 V to -0.3 V with 0.05 V intervals, at different temperatures.

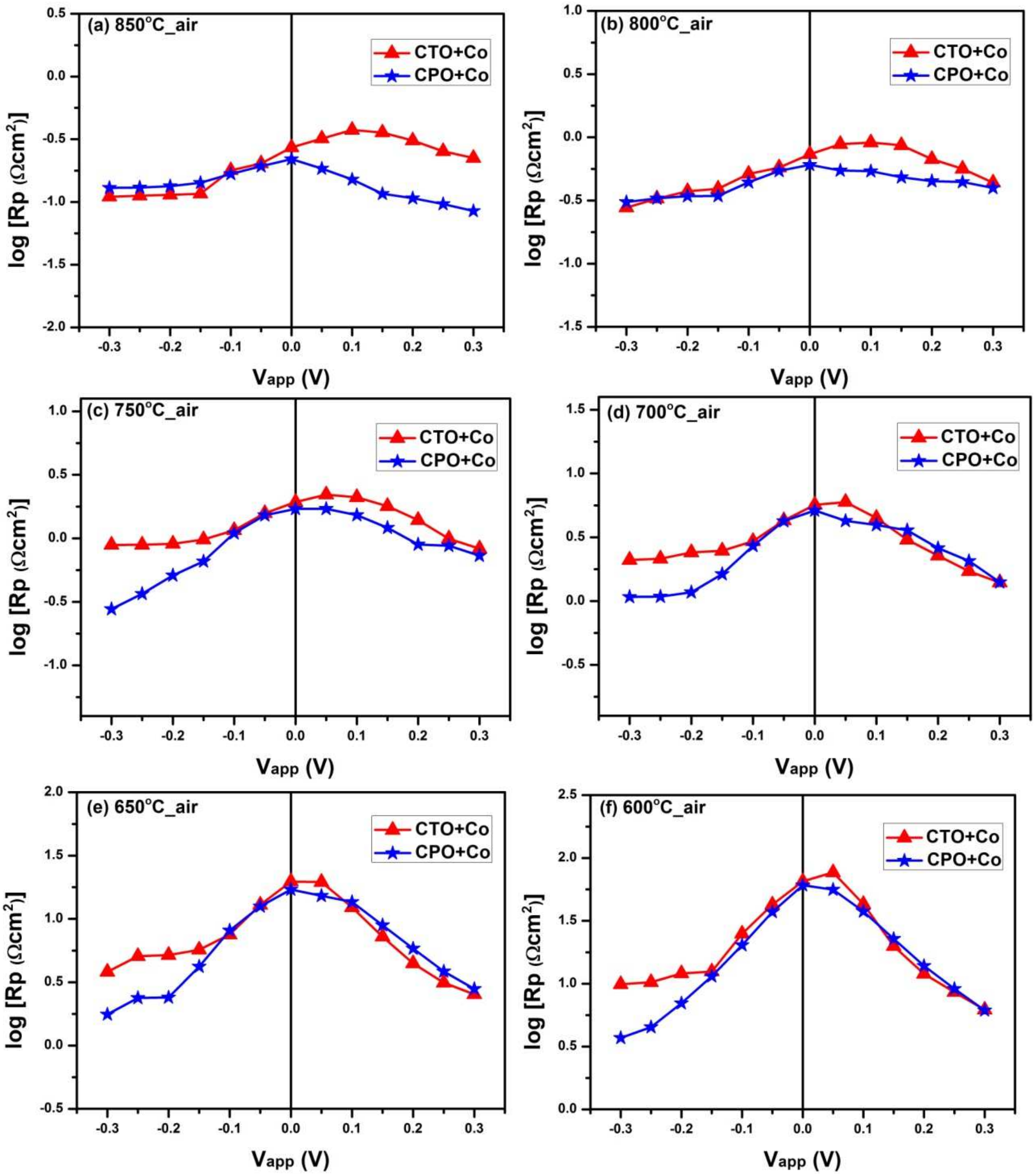

Figure 6.9. Total polarization resistance as a function of applied bias measured in air at different temperatures, for cells containing the buffer layers CTO+Co or CPO+Co.

At the lowest temperatures the total polarization resistances Rp are observed to be similar for CTO+Co and CPO+Co buffer layers over a wide potential range, deviating only under strong cathodic polarization, where limiting behavior becomes notable in the case of CTO+Co. Assuming that performance can be linked to the level of ambipolar conductivity of the buffer layer, in line with the discussion of the previous results, such limiting behavior can be suggested to have route in the lower reported average oxidation state of the terbium containing analogue [14], coupled with related earlier depletions in electronic, ionic and, thus, ambipolar conductivities under cathodic polarization [6]. In this respect, note CPO and CTO materials show a maxima in their electronic conductivity when Pr or Tb achieve the average oxidation state of 3.5+. Moreover, ionic mobility is noted to become impaired upon substantial reduction of these cations due to oxygen vacancy ordering [5,6].

At higher temperatures, the maxima in polarization resistance of the CTO+Co buffer layer sample cease to be observed at OPC, unlike the CPO+Co sample, but are offset towards the anodic polarization branch. Assuming that variations in ambipolar conductivity again may be the principal cause of such effects, one notes that under strongly oxidizing conditions the average oxidation state of Pr and Tb dopants exceeds that of 3.5+ with further oxidation leading to monotonous depletions in conduction. In the CTO+Co buffer layer case this depletion in electronic conductivity may be especially deleterious for cell performance due to a significantly lower initial value of electronic conductivity (and, hence, ambipolar conductivity) than that offered by the CPO+Co analogue, Figure 6.4.

6.4. Conclusions

The electrochemical performance of the oxygen electrode Nd_2NiO_4 has been investigated using a new terbium-doped ceria buffer layer for SOFC and SOEC application. A thin film CTO buffer layer with cobalt additions was successfully prepared on the top of a pre-prepared YSZ electrolyte by a cost effective spin coating method utilizing a low co-sintering temperature (900^{o}C). Results show the formation of well separated and adhered layers that are absent of observable cation interdiffusion.

The YSZ/CTO+Co/Nd_2NiO_4 half cell was characterized by EIS measurements under anodic and cathodic polarization and results were compared to previous data of cells containing no buffer layer or a CPO+Co buffer layer. Both the CPO+Co and CTO+Co buffer layer samples show vastly improved electrokinetic behavior than that obtainable in an equivalent cell without a buffer layer. Such dramatic improvements in polarization resistance are suggested to be due to the existence of a parallel path for electrochemical reaction due to the presence of the MIEC buffer layers. Links between the level of ambipolar conductivity of the buffer layers and polarization behavior have been proposed, both at OPC and also under polarization. At low temperatures, CPO+Co and CTO+Co MIEC buffer layer s are shown to be good candidates to enhance performance of the oxygen electrode under SOEC application, while the performance of the CTO+Co material is shown to be limited for SOFC application at strongly cathodic potentials. At higher operation temperatures, the best performance is offered by the CPO+Co buffer layer under anodic polarization, while under cathodic polarization all buffer layers are shown to exhibit similar performance.

6.5. References

[1] D.P. Fagg, J.C.C. Abrantes, D. Pérez-Coll, P. Núñez, V.V. Kharton, J.R. Frade, The effect of cobalt oxide sintering aid on electronic transport in $Ce_{0.80}Gd_{0.20}O_{2-\delta}$ electrolyte, Electrochimical Acta 48 (2003) 1023–1029.

[2] M. Balaguer, C. Solís, S. Roitsch, J.M. Serra, Engineering microstructure and redox properties in the mixed conductor $Ce_{(0.9)}Pr_{(0.1)}O_{(2-\delta)}$ + Co 2 mol%, Dalton Transactions 43 (2014) 4305–4312.

[3] D.P. Fagg, A.L. Shaula, V.V. Kharton, J.R. Frade, High oxygen permeability in fluorite-type $Ce_{0.8}Pr_{0.2}O_{2-\delta}$ via the use of sintering aids, Journal of Membrane Science 299 (2007) 1–7.

[4] D.P. Fagg, S. García-martin, V.V. Kharton, J.R. Frade, Transport properties of fluorite-type $Ce_{0.8}Pr_{0.2}O_{2-\delta}$: Optimization via the use of cobalt oxide sintering aid, Chemistry of Materials 21 (2009) 381–391.

[5] D.P. Fagg, J.R. Frade, V.V. Kharton, I.P. Marozau, The defect chemistry of Ce(Pr, Zr)$O_{2-\delta}$, Journal of Solid Stat Chemistry 179 (2006) 1469–1477.

[6] C. Chatzichristodoulou, P.V. Hendriksen, Electronic and ionic transport in $Ce_{0.8}Pr_xTb_{0.2-x}O_{2-\delta}$ and evaluation of performance as oxygen permeation membranes, Journal of Electrochemical Society 159 (2012) E162–E170.

[7] C. Chatzichristodoulou, P.V. Hendriksen, Oxygen nonstoichiometry and defect chemistry modeling of $Ce_{0.8}Pr_{0.2}O_{2-\delta}$, Journal of Electrochemical Society 157 (2010) B481–B489.

[8] H. Yahiro, Y. Eguchi, K. Eguchi, H. Arai, Oxygen ion conductivity of the ceria-samarium oxide system with fluorite structure, Journal of Applied Electrochemistry 18 (1988) 527–531.

[9] I.R. Gibson, G.P. Dransfield, J.T.S. Irvine, Sinterability of commercial 8 mol% yttria-stabilized zirconia powders and the effect of sintered density on the ionic conductivity, Journal of Material Science 33 (1998) 4297–4305.

[10] S.B. Adler, Factors governing oxygen reduction in solid oxide fuel cell cathodes, Chemical Review 104 (2004) 4791–4843.

[11] J. Fleig, Solid oxide fuel cell cathodes:polarization mechanisms and modeling of the electrochemical performance, Annual Review Materials Research 33 (2003) 361–382.

[12] M. Liu, Equivalent circuit approximation to porous mixed-conducting oxygen electrodes in solid-state cells, Journal of Electrochemical Society 145 (1998) 142–153.

[13] E.V. Tsipis, E.N. Naumovich, M.V. Patrakeev, A.A. Yaremchenko, I.P. Marozau, A. V. Kovalevsky, J.C. Waerenborgh, V.V. Kharton, Oxygen deficiency, vacancy clustering and ionic transport in (La,Sr)$CoO_{3-\delta}$, Solid State Ionics 192 (2011) 42–48.

[14] C. Chatzichristodoulou, A. Hagen, P.V. Hendriksen, Defect chemistry and thermomechanical properties of $Ce_{0.8}Pr_xTb_{0.2-x}O_{2-\delta}$, Journal of The Electrochemical Society 157 (2010) B299–B307.

7. High performance praseodymium nickelate oxygen electrode with CPO+Co buffer layer for SOFC and SOEC

7.1. Introduction

The previous chapters (5 & 6) highlighted that the Ruddlesden Popper (RP) phase $Nd_2NiO_{4+\delta}$ could be a promising oxygen electrode for SOFC and SOEC devices when deposited on ceria-based, MIEC conducting, buffer layers due to the presence of a beneficial, additional parallel, mixed conducing, path for the electrode reaction. Detail electrochemical measurements showed that the lowest polarization resistances could be achieved for a CPO+Co buffer layer due to its superior ambipolar conductivity. The present chapter builds on these results to focus on a related RP oxygen electrode, Pr_2NiO_4, deposited on the high performing CPO+Co buffer layer.

$Pr_2NiO_{4+\delta}$ with the K_2NiF_4-type structure electrode has been documented to be a promising mixed ionic and electronic conducting oxygen electrode for solid oxide fuel cells [1]. Mauvy et al. [2] measured the electrochemical performance of Ln_2NiO_4 (Ln = La, Nd and Pr) electrodes with an YSZ electrolyte and reported overpotential lossess that were lower than those offered by a traditional LSM electrode. Boehm et al. [3] measured the transport properties of a range of Ln_2NiO_4 materials, Ln = La, Pr, Nd, showing the Pr_2NiO_4 material to exhibit the highest electronic conductivity among the different nickelate compositions with high levels of oxygen diffusion and surface exchange. [3]. Hyodo et al. [4] investigated the effect of Cu and Ga substitution into Ni sites of $Pr_2NiO_{4+\delta}$ on transport properties, showing enhanced ionic conductivity, but depleted hole concentration and mobility. Despite offering attractive MIEC properties, the $Pr_2NiO_{4+\delta}$ orthorhombic structure has been shown to decompose under pure oxygen flow at around 850°C to form the tetragonal $Pr_4Ni_3O_9$ structure and PrO_y [5]. Nonetheless, Kovalevsky et al. [6] demonstrated that this phase change can be reversed by heating above 900°C, reforming the Pr_2NiO_4 phase.

Recently, researchers have also proposed Ln_2NiO_4 electrodes as potential mixed conducting electrodes for proton ceramic fuel cells (PCFC), where in addition to oxide-ion and electron conduction some beneficial proton conduction has also been noted [7–10]. Additionally Dailly et al. [11] investigated a wide range of $AMO_{3-\delta}$ (A = La, Ba, Sr; M=

Mn, Fe, Co, Ni) and $A_2MO_{4-\delta}$ (A = La, Nd, Pr or Sr; M= Ni) type compounds for PCFC application, observing that the lowest area specific resistance (ASR) values were obtained for $Ba_{0.5}Sr_{0.5}Fe_{0.8}Co_{0.2}O_{3-\delta}$ and $Pr_2NiO_{4+\delta}$ cathodes.

Based upon these features $Pr_2NiO_{4+\delta}$ has gained significance as a potential oxygen electrode for SOFC and SOEC applications during the last few years. In this work, electrochemical characterizations of $Pr_2NiO_{4+\delta}$ oxygen electrode with and without CPO+Co buffer layer were analyzed and compared to that of the previously measured Nd_2NiO_4 electrode.

7.2. Experimental

$Pr_2NiO_{4+\delta}$ powder was prepared by a citrate route (see procedure in chapter 2.1) using praseodymium hexahydrate (99.9% pure, Sigma-Aldrich) and nickel nitrate hexahydrate (≥ 96% pure, Sigma-Aldrich). Stoichiometric amounts of the precursors were dissolved in distilled water with a small amount of nitric acid. After addition of citric acid ((≥ 99.5% pure, Sigma-Aldrich) the solution was stirred vigorously for 30 min to obtain a clear solution. The solution was then dehydrated at 120^{o}C and slowly heated until self-combustion of the precipitates. Final calcination was performed at 1100^{o}C for 12 h with 5^{o}C/min heating and cooling rates to obtain the single phase. The powder was then ball-milled at 250 rpm about 5 h to break weak agglomerates. Electrochemical cells with and without CPO+Co buffer layer using $Pr_2NiO_{4+\delta}$ oxygen electrode and YSZ electrolyte were prepared by the spin coating technique (see chapter 2.2).

Powder XRD patterns were recorded at room temperature to identify the phase purity of the prepared $Pr_2NiO_{4+\delta}$ powder. The chemical stability of buffer layer with the electrode material was investigated independently by X-ray diffraction after mixing the powders in a 50:50 wt% ratio and sintering at conditions equal to that used in cell preparation (900°C for 10 h). The cross sectional microstructure and morphology of the cell was analysed by scanning electron microscopy complemented by elemental analysis performed by Energy Dispersive X-ray spectroscopy (EDS). Electrochemical characterization was performed using an electrochemical half cell of the electrode material deposited on a CPO+Co buffer layer (see procedure in chapter 2.7).

7.3. Results and Discussion

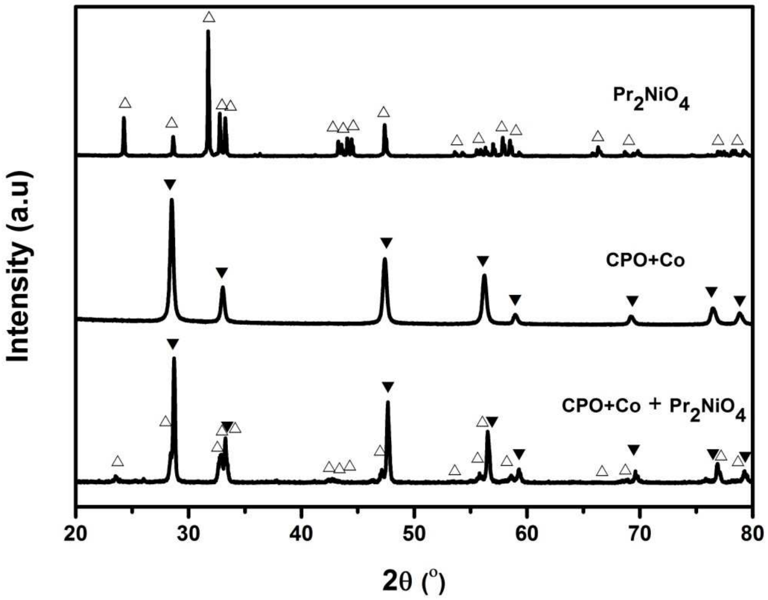

Figure 7.1. XRD phase analysis of $Pr_2NiO_{4+\delta}$ electrode and with intimate mixtures of CPO+Co buffer layer after firing for 10h at 900°C.

Figure 7.1 shows the XRD pattern of $Pr_2NiO_{4+\delta}$ powder prepared by the citrate method after calcinations at 1100°C for 12 h. The obtained patterns indicate the successful preparation of phase pure, $Pr_2NiO_{4+\delta}$, electrode material without any notable impurity peaks. In order to check the chemical stability of the $Pr_2NiO_{4+\delta}$ electrode with the CPO+Co buffer layer, an intimate mixture of the buffer layer and electrode was prepared and sintered at 900°C for 10 h. The obtained result, Figure 7.1, shows the presence of only the desired phase compositions with no extra impurity phases observable between buffer layer/electrode mixtures. This analysis indicates that the $Pr_2NiO_{4+\delta}$ electrode is compatible with the CPO+Co buffer layer under the preparation conditions of the electrochemical cell.

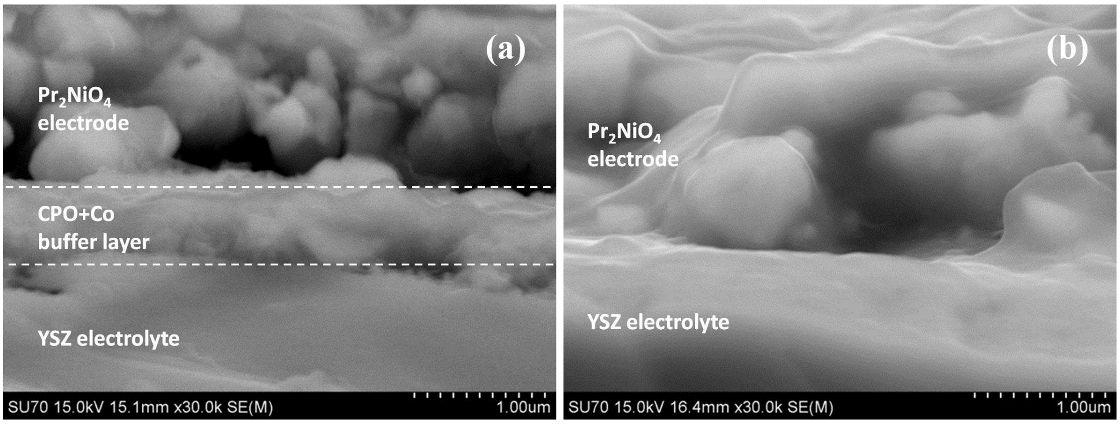

Figure 7.2. Cross-sectional microstructures of electrolyte/electrode assemblies with and without CPO+Co buffer layer.

Figure 7.2 presents cross sectional micrograph of the Pr_2NiO_4 electrode and YSZ electrolyte assembly formed with a CPO+Co buffer layer. The SEM result shows a dense, thin and uniform buffer layer with thickness around 0.5µm that is well adhered to the YSZ substrate. The thickness of the Pr_2NiO_4 electrode is approximately 2 µm and is well adhered to the supporting layer. The observed morphology and cell architecture of the current Pr_2NiO_4/CPO+Co/YSZ half cell is comparable to that of the equivalent half cell formed with the Nd_2NiO_4 oxygen electrode, shown in Chapter 5.3 and Chapter 6.2. Consequently, direct comparison is facilitated between the electrochemical characterizations of the two electrode materials.

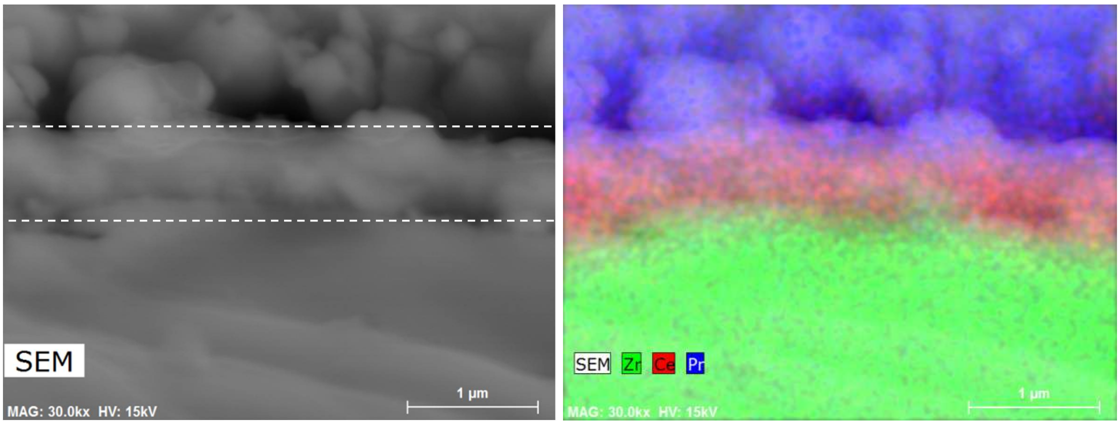

Figure 7.3. SEM-EDS analysis performed across the electrode/electrolyte interface of an Pr_2NiO_4/CPO+Co/YSZ assembly.

Figure 7.3 presents compositional analysis of the Pr_2NiO_4/CPO+Co/YSZ assembly, by EDS mapping, confirming clear separation of the $Pr_2NiO_{4+\delta}$ electrode, CPO+Co buffer layer and the YSZ electrolyte in the architecture, with no notable cation interdiffusion at the fabrication temperature (900ºC). This result suggests successful preparation of the electrolyte/buffer layer/electrode assembly and absence of chemical interactions between layers, in agreement with the XRD results, Fig.7.1.

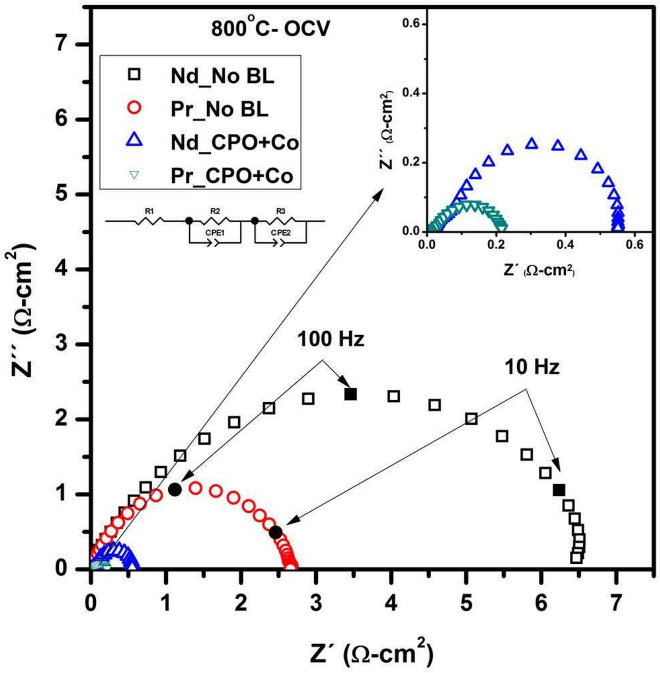

Figure 7.4. Typical impedance spectra of cell with Ln_2NiO_4 electrode (Ln = Nd and Pr) with no buffer layer (BL) or containing CPO+Co buffer layer measured at OCV. Ohmic offset, R1, has been subtracted.

Impedance spectra of cell $Pr_2NiO_{4+\delta}$ electrode with and without CPO+Co buffer layer measured at open circuit potential (OCV) are shown in Figure 6.4. Along with, impedance spectra of cell $Nd_2NiO_{4+\delta}$ electrode with and no CPO+Co buffer layer measured at 800°C inserted for distinguish the effect. All the electrode responses have combinations of two arcs (R2 and R3) along with middle and lower frequency respectively. To show this more clearly the electrodes with CPO+Co buffer layer spectra is magnified in the inset of this figure. The new oxygen electrode $Pr_2NiO_{4+\delta}$ considerably decreasing the total polarization resistance (R2+R3 = Rp) from 6.5 cm^2 to 2.6 cm^2 compared to $Nd_2NiO_{4+\delta}$ oxygen electrode. The samples with CPO+Co buffer layer show further decreases in the overall resistance, especially the sample with $Pr_2NiO_{4+\delta}$ electrode attaining 0.22 cm^2 compared to 0.55 cm^2 of $Nd_2NiO_{4+\delta}$ electrode.

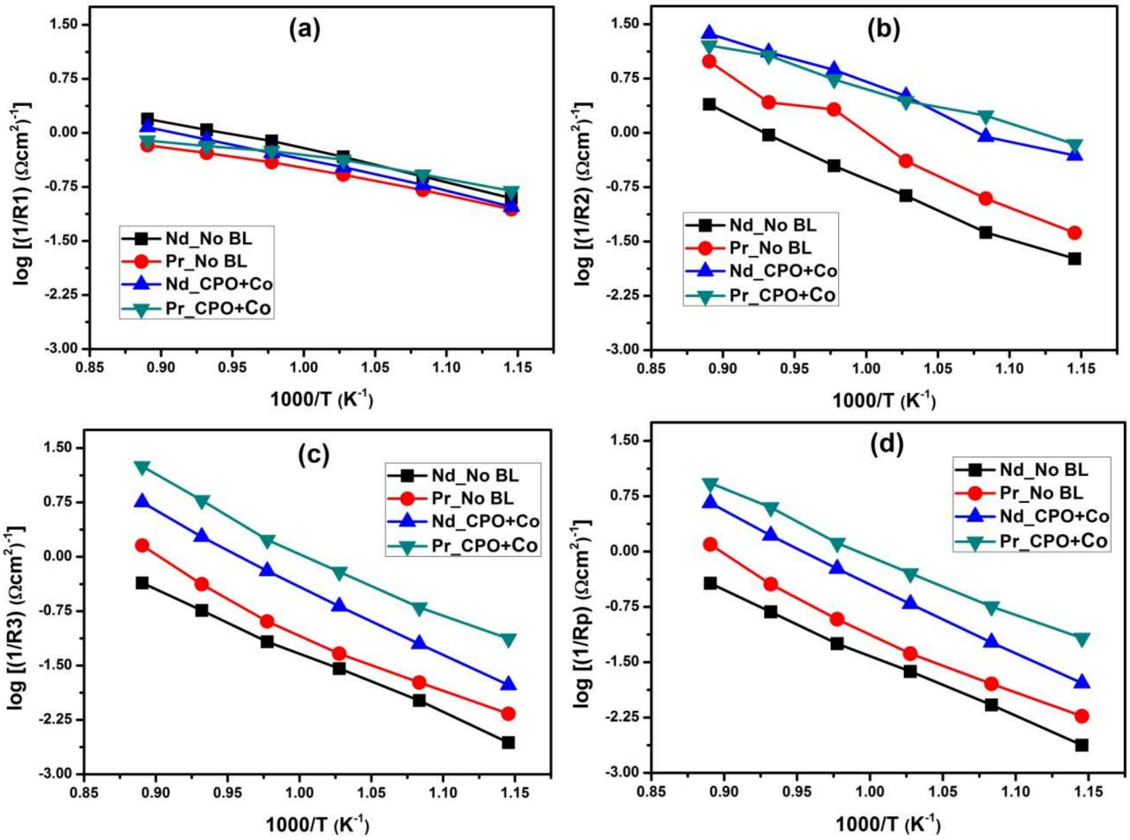

Figure 7.5. The Arrhenius behavior of the polarization resistances a) R1, b) R2, c) R3 and d) Rp, for cells with Ln_2NiO_4 electrode (Ln = Nd and Pr) with no buffer layer (BL) or containing the CPO+Co buffer layer.

Figure 7.5 shows the Arrhenius behavior of the extracted resistances R1, R2, R3, and Rp for Ln_2NiO_4 electrode (Ln = Nd and Pr) with no buffer layer or containing the CPO+Co buffer layer, also respective active energy mentioned the table 7.1 (also see 5.2). The ohmic resistance R1 shows relatively equal for all samples (fig. 7.5a). The resistance of the intermediate frequency contribution R2 significantly decreases for the $Pr_2NiO_{4+\delta}$ electrode than $Nd_2NiO_{4+\delta}$ electrode (fig. 7.5b). Further, it decreases for the samples with CPO+Co buffer layer and seems approximately equal for $Pr_2NiO_{4+\delta}$ and $Nd_2NiO_{4+\delta}$ electrode. Impedance located to this frequency corresponds to ionic transfer at electrode/electrolyte interface, for both samples containing CPO+Co buffer layer at interface [1,10,12]. Therefore, one can define this intermediate frequency response could be the same for both electrodes containing same CPO+Co buffer layer, suggesting that the involved process is similar.

Table 7.1. Activation energy of OCP with temperature.

Sample	Activation energy E_a (eV)			
	R1	R2	R3	Rp
Pr_No BL	0.69 ± 0.03	1.84 ± 0.12	1.78 ± 0.12	1.79 ± 0.10
Pr_CPO +Co	0.54 ± 0.05	1.07 ± 0.04	1.86 ± 0.09	1.66 ± 0.05

The values of the polarization resistance R3 and the total polarization resistance, Rp, are shown to increase in the order Pr_CPO+Co < Nd_CPO+Co < Pr_No BL < Nd_No BL, with the largest gains in performance being notable on moving to the buffer layer CPO+Co with $Pr_2NiO_{4+\delta}$ electrode, Figures 7.5c & d. The large depressed semi circle R3 corresponds to the lower frequency response (fig. 7.4) could be assigned to the oxygen adsorption/dissociation steps overlapped with diffusion processes on porous electrode. Here in our case, the complex phenomenon R3 could be characterized by the combine response of porous electrode and thin buffer layer. The total polarization resistance Rp reduces for $Pr_2NiO_{4+\delta}$ than $Nd_2NiO_{4+\delta}$ electrode, this can be attributed to the increasing electronic conductivity of oxygen electrode $Pr_2NiO_{4+\delta}$ [3].

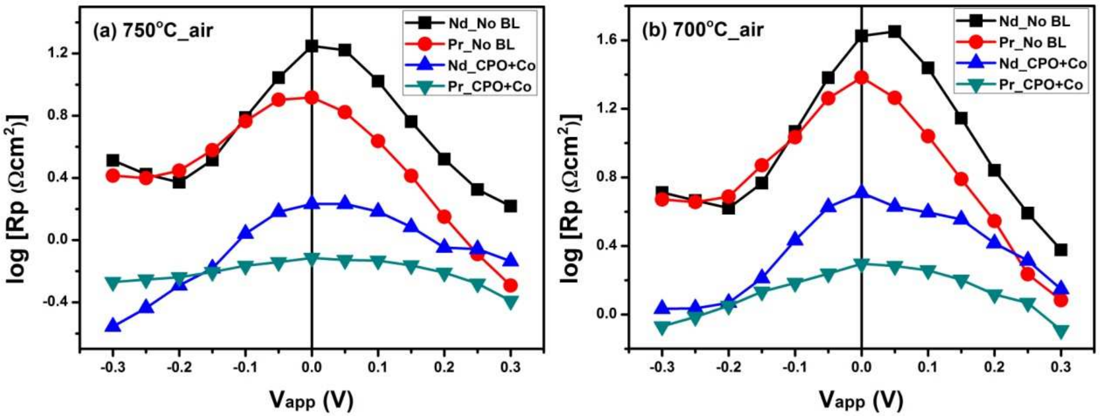

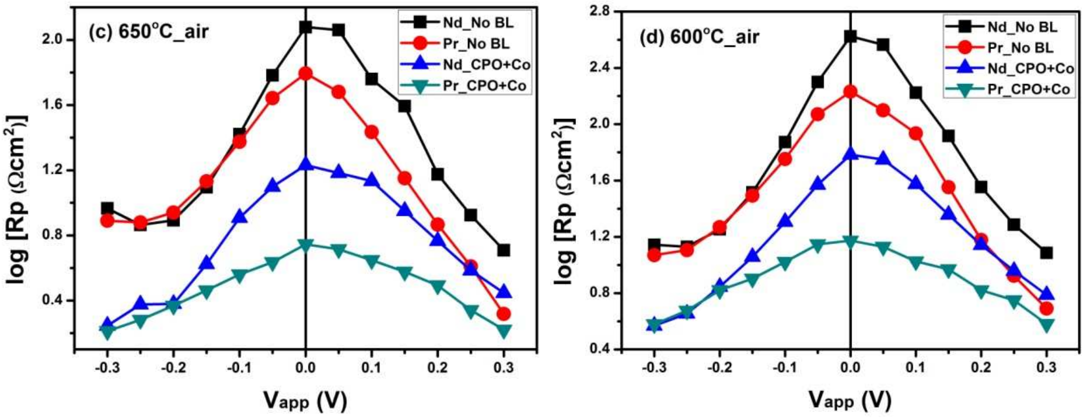

Figure 7.6. Total polarization resistance as a function of applied bias measured in air at different temperatures, for cells with Ln_2NiO_4 electrode (Ln = Nd and Pr) with no buffer layer (BL) or containing the CPO+Co buffer layer.

The electrode polarization process was analyzed under DC current flux at both anodic and cathodic mode. Figure 7.6 shows the response of $Pr_2NiO_{4+\delta}$ and $Nd_2NiO_{4+\delta}$ electrode with and without CPO+Co buffer layer, under DC current flux from the range +0.3 V to -0.3 V with 0.05 V intervals at different temperatures. The $Pr_2NiO_{4+\delta}$ electrode with CPO+Co buffer layer sample exhibit the lower Rp values for entire temperature range along with different DC current flux.

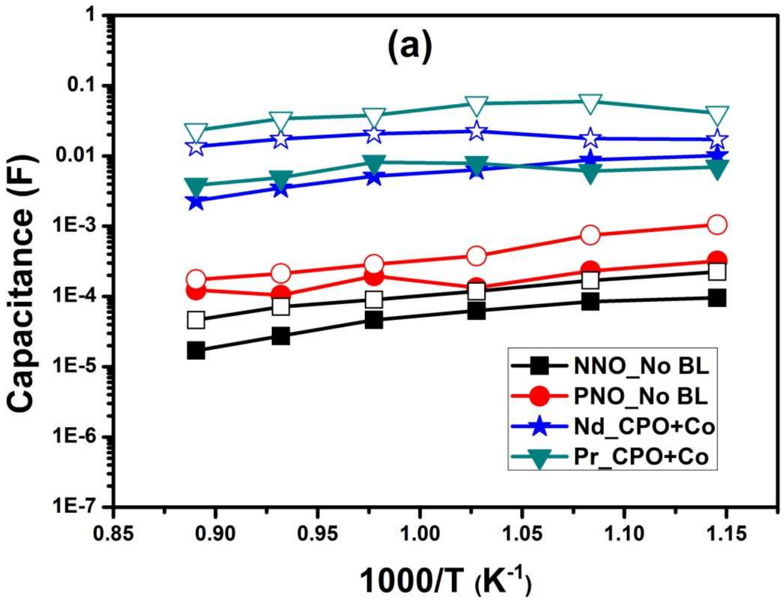

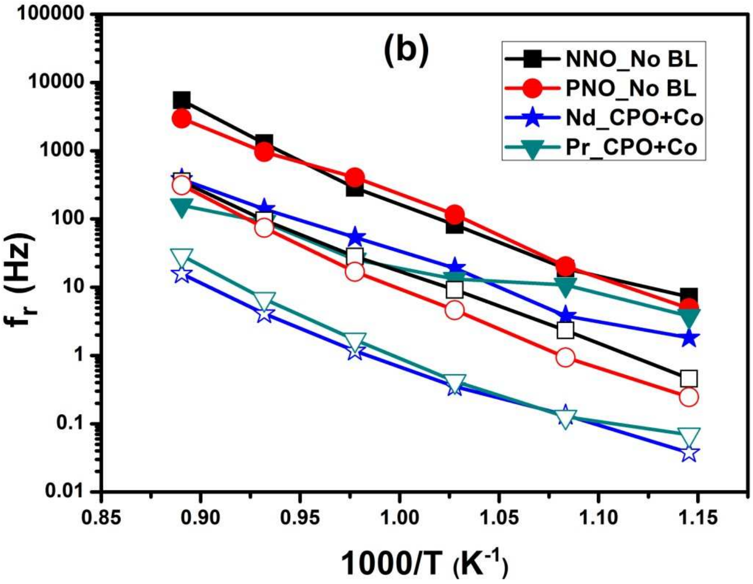

Figure 7.7. Temperature dependence of a) the Capacitance and b) Relaxation frequency, for cells Ln_2NiO_4 electrode (Ln = Nd and Pr) with no buffer layer or containing the CPO+Co buffer layer. Filled symbols relate to the intermediate frequency polarization response (R2), open symbols to the lower frequency response (R3).

The calculated values of capacitance and relaxation frequency accord to intermediate frequency and lower frequency have been plotted as a function of temperature, figure 7.7. According to the figure 6.7a, the capacitance values of $Pr_2NiO_{4+\delta}$ electrode shows close to the $Nd_2NiO_{4+\delta}$ electrode. On the other hand, the capacitance values of CPO+Co buffer layer with $Pr_2NiO_{4+\delta}$ electrode shows more close to the $Nd_2NiO_{4+\delta}$ electrode with same buffer layer. This improved electrode phenomenon indicating that the additional path for electrode kinetics is possible through introducing thin buffer layer between electrode/electrolyte interfaces (see section 5.3.6).

7.4. Conclusions

New Oxygen electrode Pr_2NiO_4 has been investigated with CPO+Co buffer layer for SOFC and SOEC application. Thin film CPO+Co and Pr_2NiO_4 electrode were successfully prepared on the top YSZ electrolyte by cost effective spin coating method. Results show the formation of well separated and adhered layers that are absent of observable cation interdiffusion at this low sintering temperature (900^{o}C) with the help of XRD and SEM-EDS analysis. The half cell with and without buffer layer were characterized by EIS measurements under anodic and cathodic polarization. It is clearly observed that the sample with CPO+Co buffer layer shows decreasing polarization resistance than the sample without buffer layer. The capacitance and relaxation frequency values well agreed with new mechanism interpreted at chapter 4, for improved electrode kinetics through additional path. The electrode performance was increased enormously by the help of CPO+Co buffer layer, shows this kind of MIEC buffer layer material is good candidate for SOFC and SOEC applications. Overall, rare-earth nickelates with the K2NiF4-type structure Pr_2NiO_4 oxygen electrode works more appropriate with CPO+Co buffer layer than Nd_2NiO_4 oxygen electrode.

7.5. References

[1] C. Ferchaud, J.-C. Grenier, Y. Zhang-Steenwinkel, M.M.A. van Tuel, F.P.F. van Berkel, J.-M. Bassat, High performance praseodymium nickelate oxide cathode for low temperature solid oxide fuel cell, Journal of Power Sources 196 (2011) 1872–1879.

[2] F. Mauvy, C. Lalanne, J.M. Bassat, J.C. Grenier, H. Zhao, P. Dordor, Ph. Stevens, Oxygen reduction on porous $Ln_2NiO_{4+\delta}$ electrodes, Journal of the European Ceramic Society 25 (2005) 2669–2672.

[3] E. Boehm, J. Bassat, P. Dordor, F. Mauvy, J. Grenier, P. Stevens, Oxygen diffusion and transport properties in non-stoichiometric $Ln_{2-x}NiO_{4+\delta}$ oxides, Solid State Ionics 176 (2005) 2717–2725.

[4] J. Hyodo, K. Tominaga, Y.-W. Ju, S. Ida, T. Ishihara, Electrical conductivity and oxygen diffusivity in Cu-and Ga-doped Pr_2NiO_4, Solid State Ionics 256 (2014) 5–10.

[5] P. Odier, C. Allançon, J.M. Bassat, Oxygen exchange in $Pr_2NiO_{4+\delta}$ at high temperature and direct formation of $Pr_4Ni_3O_{10-x}$, Journal of Solid State Chemistry 153 (2000) 381–385.

[6] A.V. Kovalevsky, V.V. Kharton, A.A. Yaremchenko, Y.V. Pivak, E.N. Naumovich, J.R. Frade, Stability and oxygen transport properties of $Pr_2NiO_{4+\delta}$ ceramics, Journal of the European Ceramic Society 27 (2007) 4269–4272.

[7] K.V. Kravchyk, E. Quarez, M. Caldes, A. Le Gal La Salle, O. Joubert, Compatibility of $La_{26}O_{27}(BO_3)_8$ electrolyte with standard cathode materials for use in proton conducting solid oxide fuel cells, Journal of Power Sources 196 (2011) 7435–7441.

[8] A. Grimaud, F. Mauvy, J. Marc Bassat, S. Fourcade, M. Marrony, J. Claude Grenier, Hydration and transport properties of the $Pr_{2-x}Sr_xNiO_{4+\delta}$ compounds as H^+-SOFC cathodes, Journal of Materials Chemistry 22 (2012) 16017.

[9] E. Quarez, Y. Oumellal, O. Joubert, Optimization of the lanthanum tungstate/Pr_2NiO_4 half cell for application in proton conducting solid oxide fuel cells, Fuel Cells 13 (2013) 34–41.

[10] P. Batocchi, F. Mauvy, S. Fourcade, M. Parco, Electrical and electrochemical properties of architectured electrodes based on perovskite and A_2MO_4-type oxides for Protonic Ceramic Fuel Cell, Electrochimica Acta 145 (2014) 1–10.

[11] J. Dailly, S. Fourcade, A. Largeteau, F. Mauvy, J.C. Grenier, M. Marrony, Perovskite and A_2MO_4-type oxides as new cathode materials for protonic solid oxide fuel cells, Electrochimica Acta 55 (2010) 5847–5853.

[12] B. Philippeau, F. Mauvy, C. Mazataud, S. Fourcade, J.-C. Grenier, Comparative study of electrochemical properties of mixed conducting $Ln_2NiO_{4+\delta}$ (Ln=La, Pr and Nd) and $La_{0.6}Sr_{0.4}Fe_{0.8}Co_{0.2}O_{3-\delta}$ as SOFC cathodes associated to $Ce_{0.9}Gd_{0.1}O_{2-\delta}$, $La_{0.8}Sr_{0.2}Ga_{0.8}Mg_{0.2}O_{3-\delta}$ and $La_9Sr_1Si_6O_{26.5}$ electrolytes, Solid State Ionics 249-250 (2013) 17–25.

8. Influence of buffer layer parameters on electrochemical performance for SOFC and SOEC

8.1. Introduction

The previous chapters investigated the impact of MIEC, cerium-based buffer layers on the electrocatalytic properties of K_2NiF_4-type structure oxygen electrodes for YSZ electrolyte based SOFC and SOEC devices. Dramatic improvements in electrode kinetics could be induced via the creation of an additional, parallel path for electrochemical reaction, with peak performance being achieved by the use of the CPO+Co buffer layer of highest ambipolar conductivity. Chapter 7 further demonstrated that improved electrocatalytic performance could be obtained by use of the oxygen electrode material $Pr_2NiO_{4+\delta}$ over that offered by the $Nd_2NiO_{4+\delta}$ electrode analogue. Extending these results, the present chapter discusses the influence of the thickness and composition of the CPO+Co buffer layer on the subsequent electrokinetic behavior. In order to investigate this goal, these factors were assessed in otherwise identical electrochemical cells, consisting of the high performing Pr_2NiO_4 electrode, of a fixed morphology, with an yttria stabilized zirconia (YSZ) electrolyte.

Fluorite, lanthanide doped cerium oxides exhibit high ionic conductivity that can exceed that of the well know electrolyte material YSZ in the intermediate temperature range [1]. Mixed oxide-ion and electron conduction can also be introduced into these materials by the presence of multivalent lanthanide dopants, such as praseodymium or terbium [2,3]. In addition, the presence of minor levels of sintering aids, such as cobalt oxide, has also been reported to have a two-fold role to reduce the sintering temperature and to increase the minor electronic contribution to total conductivity [4–6]. The doping of ceria with praseodymium is of particular interest, as this material has been shown to offer the highest ambipolar conductivity and oxygen permeability of any single phase, fluorite material to date, when containing minor amounts of cobalt oxide as a sintering aid [5].

Takasu et al. were first to assess the $Ce_{1-x}Pr_xO_{2-\delta}$ system (x = 0 to 1) and noted a high solubility of Pr in the ceria lattice, with the pure cubic fluorite phase retained up to composition x = 0.7 [5]. Further substitution in excess of this value was shown to create two phases with the cubic defect fluorite structure, of different lattice parameters [7]. In contrast, later works from Shuk et al. [8] and Nauer et al. [7] placed the limit of solid solution at a significantly more modest value of x = 0.3, while a recent work by Luo et al. reported an even lower limit of x = 0.2 [8]. The thermal history of these phases is noted to have significant impact on their resultant lattice parameter due to formation of Pr in different oxidation states [6]. Nonetheless, this factor cannot directly explain the noted discrepancies in the solid solution limits as both Shuk et al. and Nauer et al. reported identical solubility values despite adopting markedly different low and high temperature synthesis routes, respectively. Hence, further work continues to be necessary to be able to fully understand the deviation in reported solid solubilities. Such work should also bear in mind possible improvements in the precision of analytical experimental techniques over time. Takasu et al. showed the highest total conductivity for the composition x = 0.4, while noting low ionic transference numbers of 0.1-0.15 for this material in the temperature range 500-800ºC. Due to the lower solid solubility limit obtained by Shuk et al., the transport properties of materials only up to composition x = 0.3 were measured [6]. Nonetheless, within this compositional range, increasing levels of ionic and electronic conductivities were reported as a function of Pr-content at 700ºC, with corresponding ionic transference numbers being 0.6 and 0.4 for the compositions x = 0.2 and x = 0.3, respectively. Qi et al. [2] studied the total conductivity of $Ce_{0.7}Pr_{0.3}O_{2-\delta}$ as a function of oxygen partial pressure and showed a change between n-type and p-type electrical conductivity behavior with increasing pO_2. Nauer et al. noted the interesting feature that the co-substitution of 3 mol% $NbO_{2.5}$ could further stabilize the single fluorite phase up to 50 mol% of Pr, allowing higher levels of total conductivity to be obtained [9]. In the current work, the quantity of Pr in the CPO+Co buffer layer will be varied to assess for potential links between the ambipolar conductivity of the buffer layer and subsequent electrode kinetics, based on the respective transport properties of the $Ce_{1-x}Pr_xO_{2-\delta}$ materials.

To date, only few articles have addressed the effect of buffer layer thickness on the performance of oxygen electrodes [10,11]. Park et al. [10] investigated the impact of different thicknesses of Gd-doped ceria (GDC) buffer layers between a $Sm_{0.5}Sr_{0.5}CoO_{3-d}$ (SSC) cathode and YSZ electrolyte for potential SOFC use. They noticed that fuel cell performance increased with increasing buffer layer thickness. On the contrary, Kim et al. [11] investigated the same GDC buffer layer of different thicknesses between a $Ba_{0.5}Sr_{0.5}Co_{0.8}Fe_{0.2}O_{3-\delta}$ (BSCF) cathode and YSZ electrolyte and noted performance decreases with increasing GDC buffer layer thickness. Thus, no categorical conclusion can currently be made on the impact of the thickness of the buffer layer on electrochemical behavior. Moreover, no information is presently available on the impact of thickness for buffer layers that offer appreciable mixed conductivity, such as the CPO+Co materials.

Therefore, in this chapter we study the effect of CPO+Co buffer layer with different thickness and with varying Pr contents for the peak performing $Pr_2NiO_{4+\delta}$ oxygen electrode from Chapter 7 deposited on an YSZ electrolyte.

8.2. Experimental

Compositions of praseodymium-doped cerium oxide, $Ce_{1-x}Pr_xO_{2-\delta}$ (x=0.1 to x=0.4), were prepared by hydrothermal synthesis. Electrochemical cells containing these buffer layer compositions with 2 mol% Co-additions, $Pr_2NiO_4/Ce_{1-x}Pr_xO_{2-\delta}$ (x=0.1− 0.4)+Co/YSZ, were prepared by the spin coating technique. Additional electrochemical cells of the fixed buffer layer composition, $Pr_2NiO_4/Ce_{0.8}Pr_{0.2}O_{2-\delta}$+Co/YSZ, were prepared for different buffer layer thicknesss, controlled by the number of spin coating cycles, see preparation procedure in chapter 2.2.

Powder XRD patterns were recorded at room temperature to identify the phase purity of the prepared $Ce_{1-x}Pr_xO_{2-\delta}$ powder as a function of composition. The cross sectional microstructure and morphology of the cells were analyzed by scanning electron microscopy and complementary elemental analysis was performed by Energy Dispersive X-ray spectroscopy (EDS). Electrochemical characterization was performed by A.C. impedance under anodic and cathodic DC bias (see procedure in chapter 2.7).

8.3. Results and Discussion

8.3.1. The impact of Pr-content in the CPO+Co buffer layer

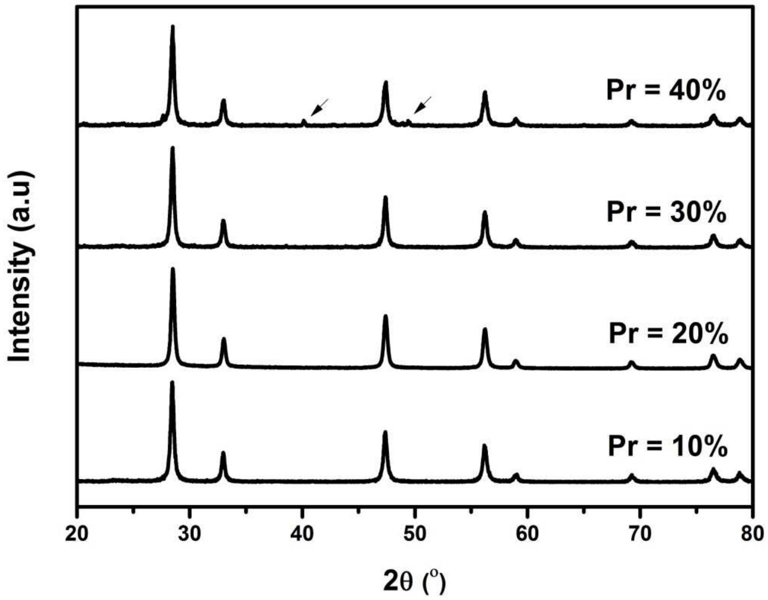

Figure 8.1. XRD patterns of $Ce_{1-x}Pr_xO_{2-\delta}$ (x=0.1− 0.4) powder prepared by hydrothermal method.

Figure 8.1 shows the XRD patterns of $Ce_{1-x}Pr_xO_{2-\delta}$ powder as-prepared by the hydrothermal method. The obtained result shows that the CPO solid solution is formed with the fluorite structure in the range x = 0.1 – 0.3. Further increases in the Pr content (x = 0.4) shows the presence of two phases with the cubic defect fluorite structure, of different lattice parameters, corresponding to ceria and praseodymium rich phases, in agreement with previous literature data of Shuk et al. [8] and Nauer et al. [7].

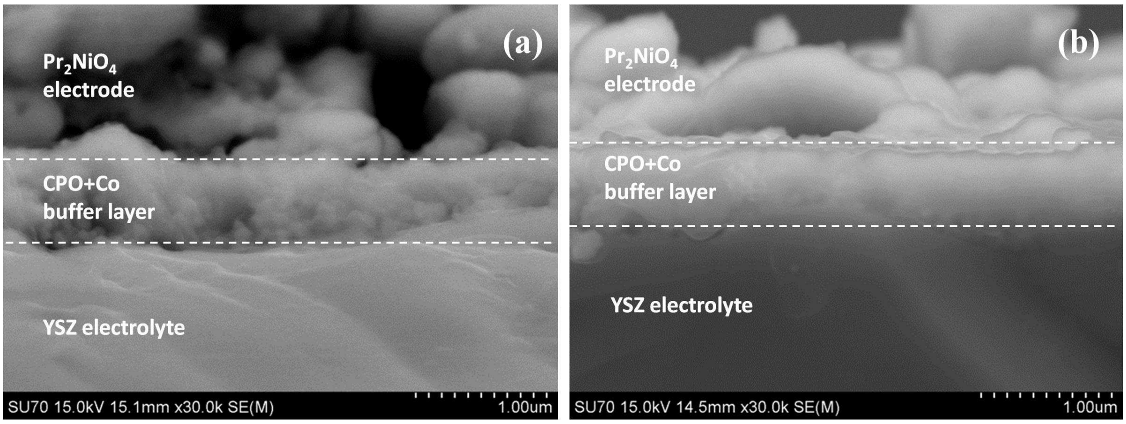

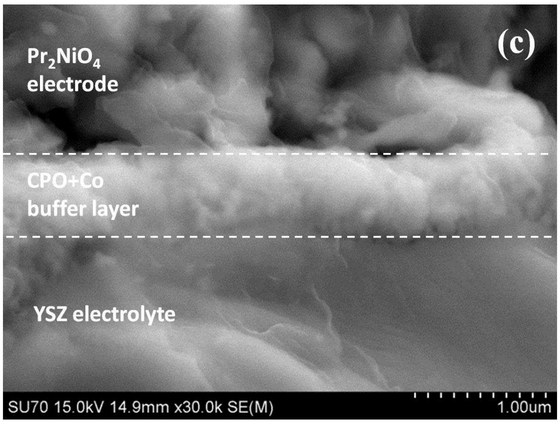

Figure 8.2. Cross-sectional microstructures of electrolyte/electrode assemblies with CPO+Co (Pr= 10, 30 & 40 mol%) buffer layer.

Figure 8.2 presents cross sectional micrographs of Pr_2NiO_4 electrode and YSZ electrolyte assemblies formed with CPO+Co (Pr= 10, 30 & 40%) buffer layer. The morphology of the cell with the buffer layer composition with a Pr content of 20 mol% can be found in Chapter 7, Figure 7.2. The SEM results shows relatively dense buffer layers with thickness around 0.5μm that are well adhered to the YSZ substrate. The thicknesses of the Pr_2NiO_4 electrodes are approximately 2 μm in each case and are once more shown to be well adhered to the supporting layers. The morphologies suggest that the CPO+Co (Pr= 10, 20, 30 & 40%) buffer layer cells have similar architectures facilitating direct comparison of their electrochemical behavior.

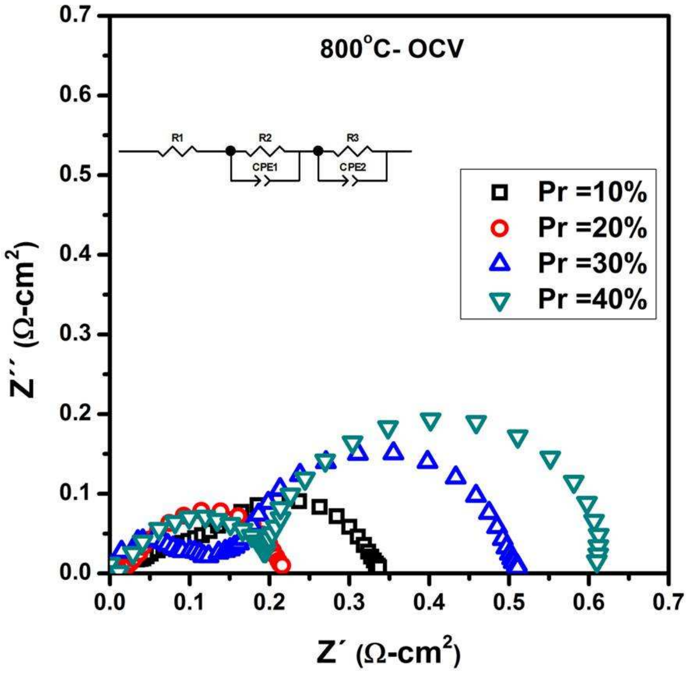

Figure 8.3. Typical impedance spectra of cell with Pr_2NiO_4 electrode and CPO+Co (Pr= 10, 30 & 40 mol%) buffer layer measured at OCV in air. Ohmic offset, R1, has been subtracted.

Impedance spectra of the cells containing $Pr_2NiO_{4+\delta}$ electrodes with CPO+Co (Pr= 10, 30 & 40%) buffer layers measured at open circuit potential (OCV) in air are shown in Figure 8.3. The sample with 20 mol% Pr is also included in figure 8.3, for comparison purposes, from chapter 7, figure 7.4. It can be clearly observed that all electrode responses consist of two arcs (R2 and R3) at intermediate and lower frequency ranges, respectively. The values of the polarization resistance at OCV are shown to increase in a nonlinear fashion in the order of 20 < 10 < 30 < 40 mol % of Pr in the CPO+Co buffer layer.

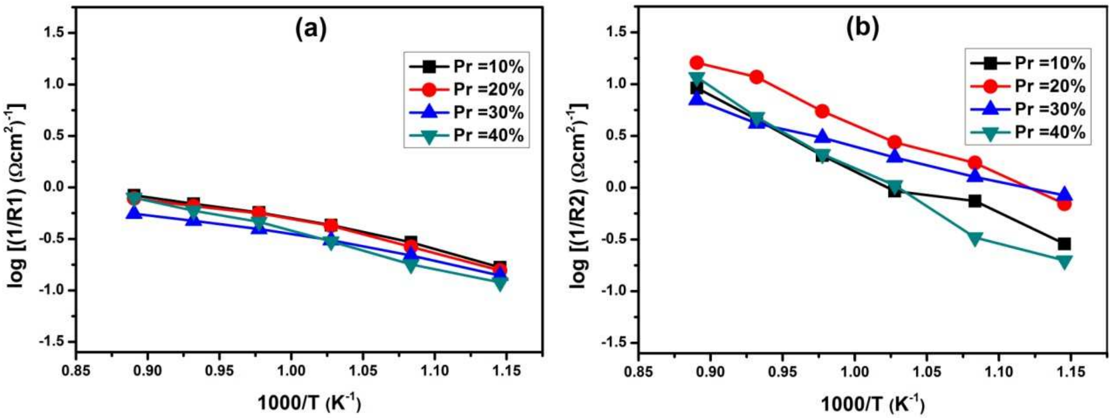

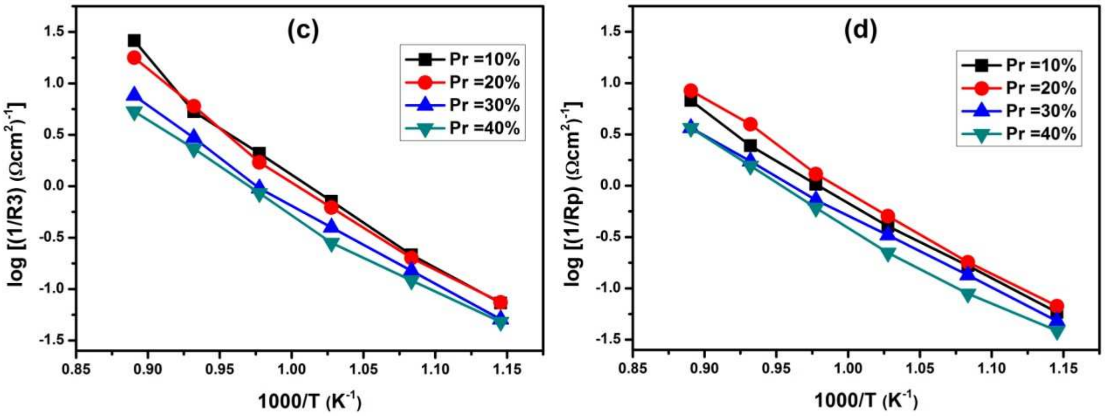

Figure 8.4. The Arrhenius behavior of the polarization resistances a) R1, b) R2, c) R3 and d) Rp, for cells with Pr_2NiO_4 electrode CPO+Co (Pr= 10,30 & 40%) buffer layer.

Figure 8.4 shows the Arrhenius behavior of the extracted resistances 1/R1, 1/R2, 1/R3, and 1/Rp for $Pr_2NiO_{4+\delta}$ electrode with CPO+Co buffer layers containing various Pr levels (10, 20, 30 and 40 mol%), with the respective active energies documented in Table 8.1. The ohmic resistance R1 is shown to be relatively equal for all samples, Fig. 8.4a, in line with their observed comparable cell morphology, Fig.8.2, and equivalent YSZ electrolyte support. The intermediate frequency response R2 is shown to be at its least resistive for the sample with 20 mol% CPO+Co buffer layer across almost all of the measured temperature range, while the lowest performances are offered by the 10 mol% and 40 mol% Pr samples (Fig. 8.4b). In contrast, the performance of the lower frequency response, R3, is shown to separate into two distinct resistance groups, with the lower polarization resistances offered by the buffer layers of lower Pr contents (Pr = 10 and 20 mol%). The total polarization resistance, Rp, shows the lowest value for the sample with 20 mol% Pr in CPO+Co buffer layer, with increases in Rp in the order of 20 < 10 < 30 < 40 mol % Pr across the measured temperature range (600^oC – 850^oC).

Table 8.1. Activation energy of OCP with temperature.

Sample	Activation energy E_a (eV)			
	R1	R2	R3	Rp
Pr = 10%	0.54 ± 0.04	1.13 ± 0.09	1.93 ± 0.11	1.58 ± 0.06
Pr = 20%	0.54 ± 0.04	1.07 ± 0.04	1.86 ± 0.09	1.66 ± 0.05
Pr = 30%	0.46 ± 0.03	0.70 ± 0.03	1.68 ± 0.07	1.46 ± 0.02
Pr = 40%	0.66 ± 0.02	1.40 ± 0.08	1.61 ± 0.07	1.56 ± 0.07

Unfortunately, the transport properties of the full $Ce_{1-x}Pr_xO_{2-\delta}$ + 2 mol% Co series have not been studied to date, with information only currently being available on the 20 mol% Pr material [5]. Moreover, the the non-linear variation of the polarization resistances with Pr-content cannot be explained using estimations based upon the transport properties of pure $Ce_{1-x}Pr_xO_{2-\delta}$ materials published by Takasu et al. [5] and Shuk [6].

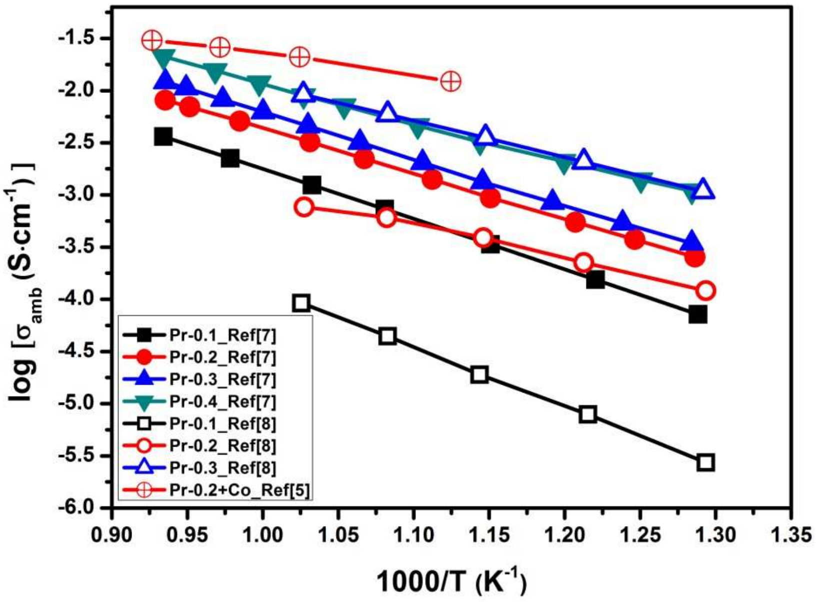

Figure 8.5. The ambipolar conductivity of $Ce_{0.8}Pr_{0.2}O_{2-\delta}$ + 2 mol% Co systems from Fagg et al.[5] and compared to literature data for a pure $Ce_{1-x}Pr_xO_{2-\delta}$ system from Takasu et al.[7] and Shuk et al.[8].

Figure 8.5 collates the results of these authors presented in the form of the Arrhenius dependence of ambipolar conductivity as a function of composition for the pure $Ce_{1-x}Pr_xO_{2-\delta}$ system. It can be seen that both authors report monotonous increases in ambipolar conductivity with increasing Pr-content for the studied compositional range. Moreover, the ambipolar conductivity of the Co containing $Ce_{0.8}Pr_{0.2}O_{2-\delta}$ + 2 mol% Co analogue is also included in Figure 8.5 from the published work of Fagg et al. [5]. The ambipolar conductivity of the Co-containing sample can be seen to be dramatically higher than the Co-free compositions measured by Takasu et al. and Shuk et al.. Figure 8.5, thus, emphasizes the futility of any attempt to use the transport properties of the pure system to predict the current trends in polarization resistance. As reported by Fagg et al., the dramatic enhancement in ambipolar conductivity note in the Co containing analogues is predominantly due to an enhanced electronic contribution that arises due to the segregated presence of cobalt at grain boundaries [5]. It must be further noted that the works of Takasu et al .and Shuk et al. were also performed without taking into account possible errors in the determination of ion transference numbers arising due to electrode polarization, errors that have since been shown to be non-negligible for electrolyte-type materials that possess relatively minor electronic conductivity [12], such as that expected for the current CPO+Co compositions. Hence, for both these reasons, direct comparison of the experimental polarization results with currently available literature information on the transport properties of these materials is not possible. Further work is, therefore, necessary to assess the relevant transport properties of the bulk $Ce_{1-x}Pr_xO_{2-\delta}$ + Co system. This work is in progress.

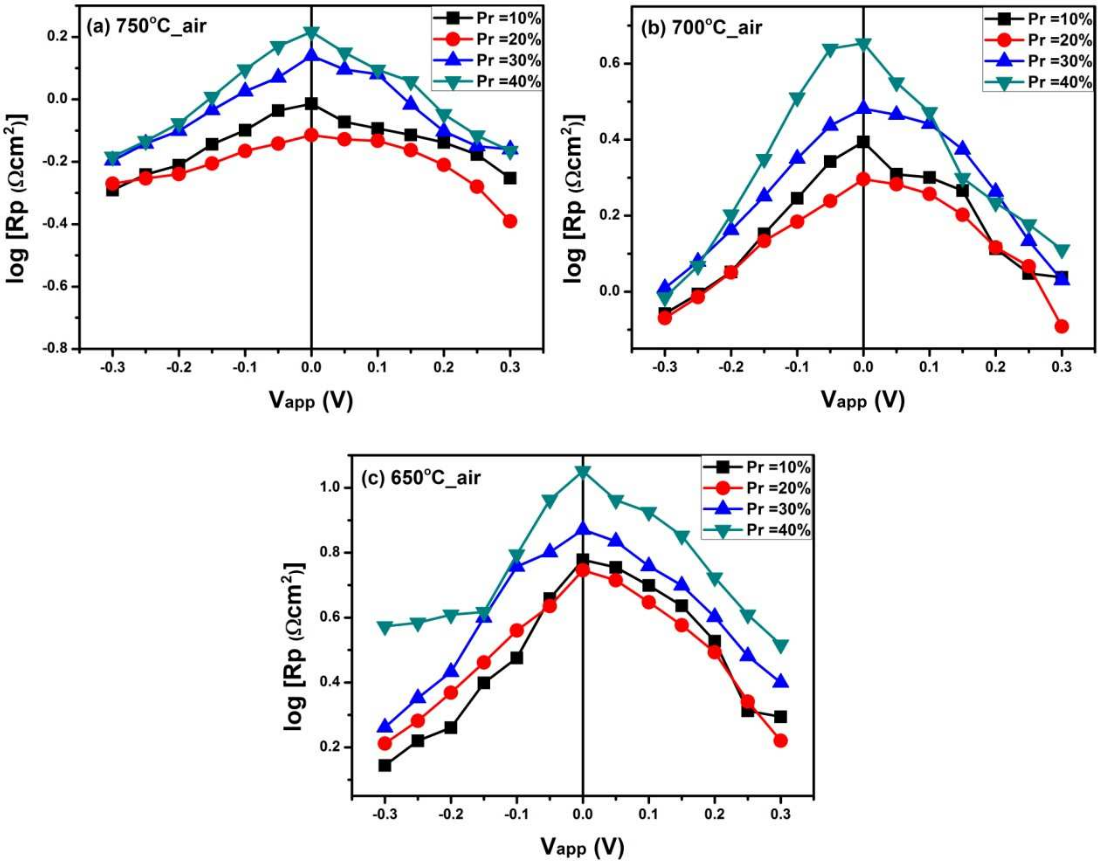

Figure 8.6. Total polarization resistance as a function of applied bias measured in air at different temperatures, for cells containing Pr_2NiO_4 electrode with CPO+Co (Pr= 10,30 & 40%) buffer layer.

The electrode polarization process was analyzed under DC bias in both anodic and cathodic modes of operation. Figure 8.6 shows the polarization response of $Pr_2NiO_{4+\delta}$ electrode with CPO+Co buffer layers containing the various Pr levels (10, 20, 30 and 40 mol%), under DC bias in the range +0.3 V to -0.3 V with 0.05 V intervals at different temperatures. In general, the trends previously documented at OPC are continued throughout the entire polarization range, with increases in Rp in the order of 20 < 10 < 30 < 40 mol %Pr. The total polarization resistance is shown to decrease with increasing DC bias under both anodic and cathodic overpotentials in agreement with that previously observed in chapter 5, 6 & 7, for similar electrochemical cells. Under strong cathodic polarization the values of Rp are shown to converge for all buffer layers, with the exception of composition 40 mol% Pr at 650ºC, where the presence of limiting behavior can be noted.

8.3.2. Various thickness of CPO+Co buffer layer

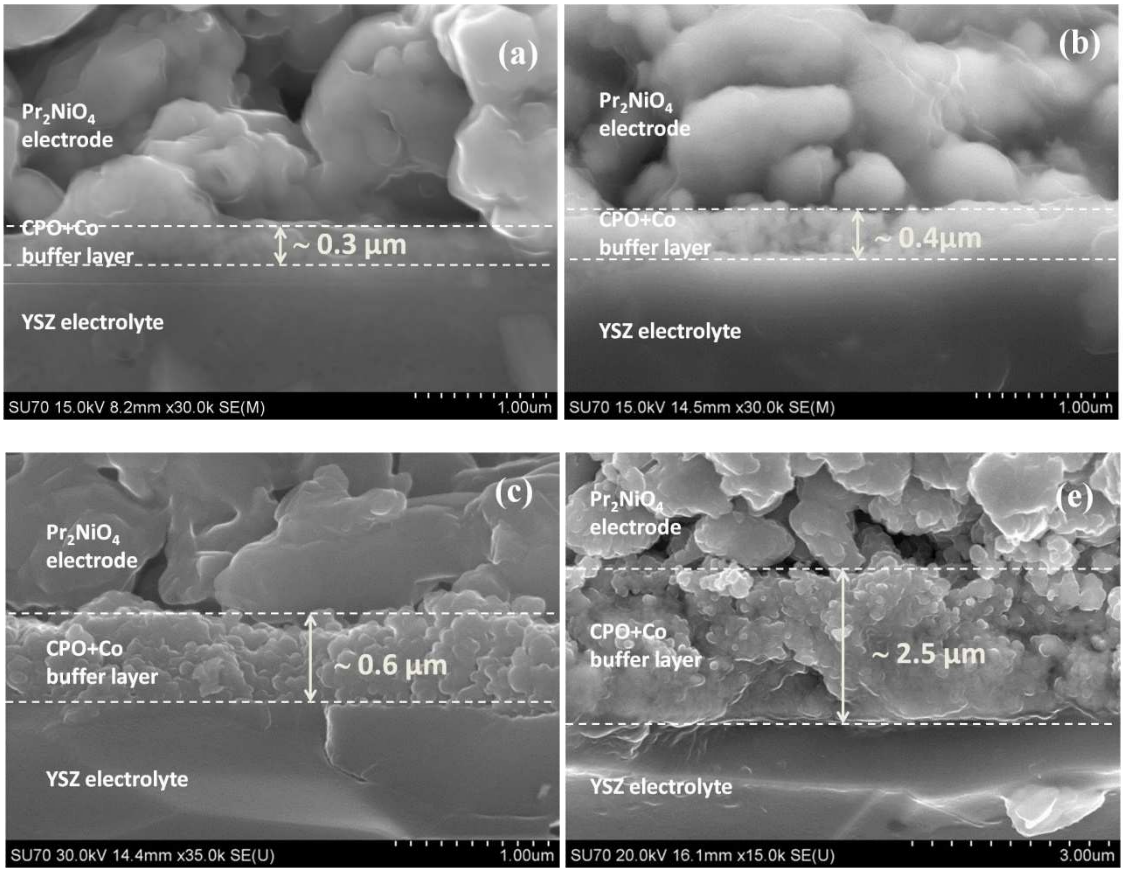

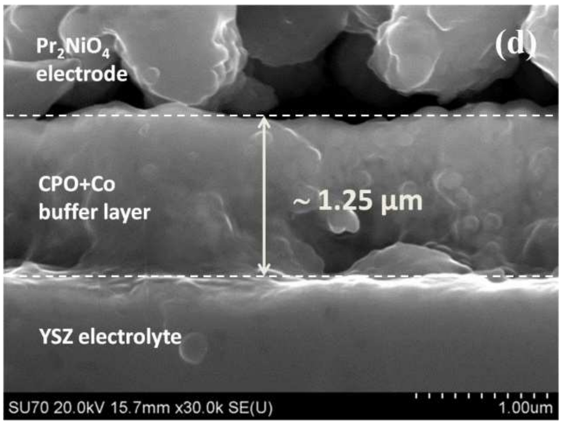

Figure 8.7. Cross-sectional microstructures of electrolyte/electrode assemblies with CPO+Co buffer layer with different thickness.

Figure 8.7 presents cross sectional micrographs of Pr_2NiO_4 electrode and YSZ electrolyte assemblies formed with CPO+Co (Pr = 20 mol%) buffer layer with different thicknesses. The thicknesses of electrode and buffer layers were controlled by number of spin coating steps. The SEM results show relatively dense, thin and uniform buffer layers with a range of thicknesses, approximately 0.3, 0.4, 0.6, 1.25 and 2.5µm, that are well adhered to the YSZ substrate. In order to understand the effect of the different buffer layer thicknesses, the oxygen electrode and electrolyte preparation methods were kept constant for all samples to retain comparable morphology.

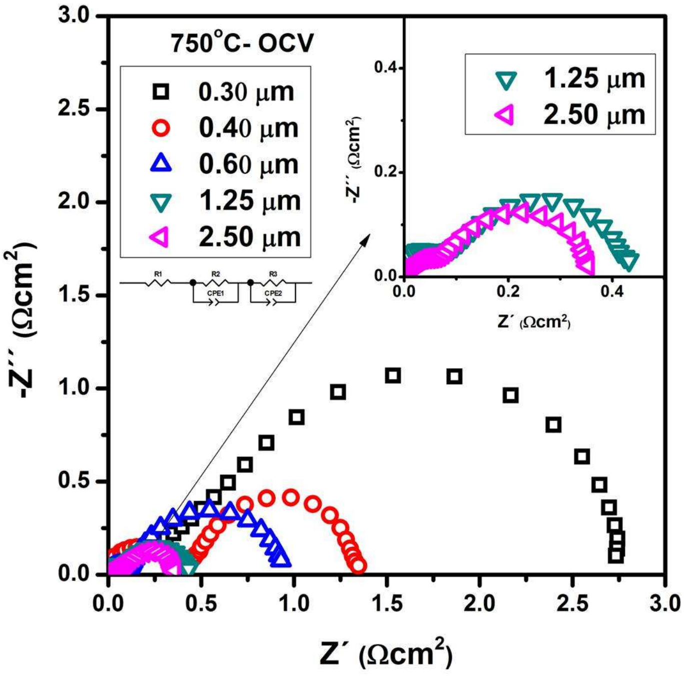

Figure 8.8. Typical impedance spectra of cell with Pr_2NiO_4 electrode and CPO+Co buffer layer with different thickness measured at OCV. Ohmic offset, R1, has been subtracted.

Example impedance spectra measured at 750°C in air under open circuit potential (OCV) are shown in Figure 8.8, as a function of buffer layer thickness. All impedance spectra show the presence of two responses (R2 and R3) at intermediate and low frequency ranges, respectively. The total polarization resistance is observed to decrease with increasing buffer layer thickness.

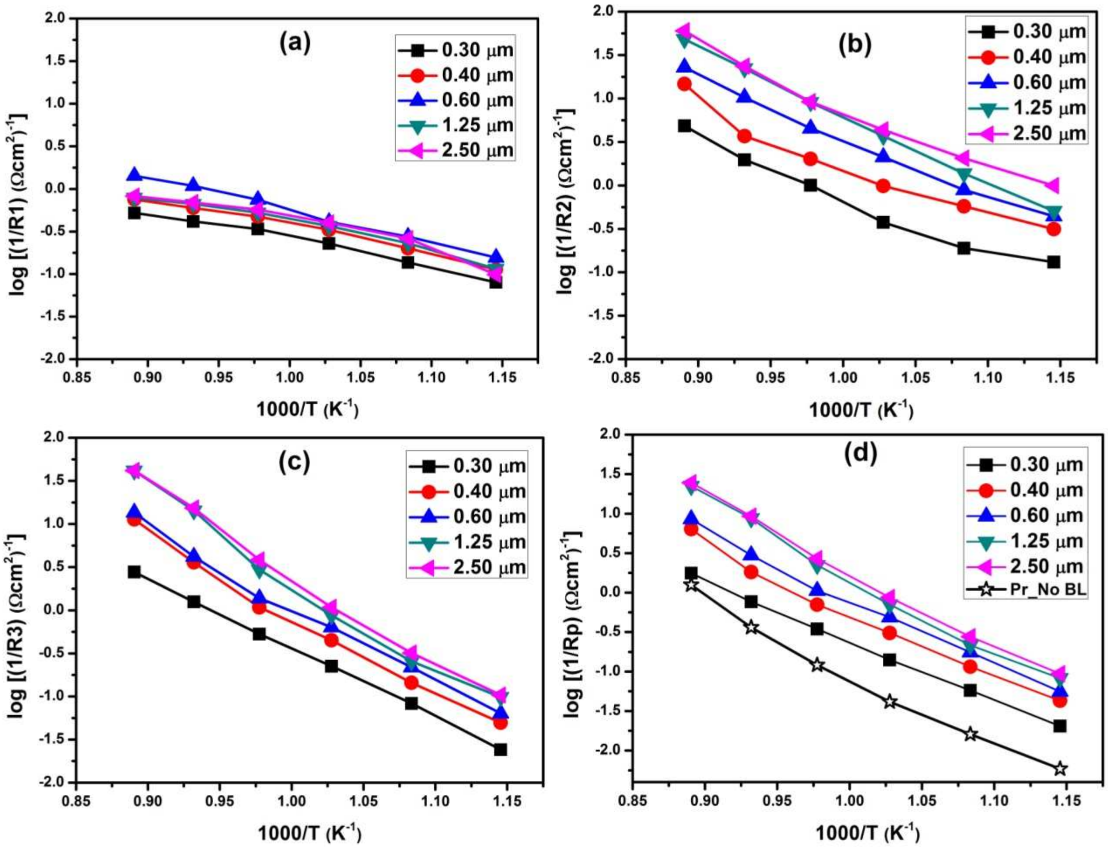

Figure 8.9. The Arrhenius behavior of the polarization resistances a) R1, b) R2, c) R3 and d) Rp, for cells with Pr_2NiO_4 electrode CPO+Co buffer layer with different thickness.

Figure 8.9 shows the Arrhenius behavior of the extracted resistances 1/R1, 1/R2, 1/R3, and 1/Rp for samples containing $Pr_2NiO_{4+\delta}$ electrode with different thickness of CPO+Co buffer layers as a function of temperature. Resistance R1 takes similar values for all samples, Fig. 8.9a, in agreement with the ohmic resistance expected due to the similar YSZ electrolyte composition and morphology used in each case. The intermediate and lower frequency responses, R2 and R3, respectively show a decrease in resistance with increasing buffer layer thickness across the measured temperature range, Figs. 8.9b & c. Hence, the total polarization resistance Rp is also observed to follow the same trend, Fig. 8.9d. To compare these results with a sample with no buffer layer but with an identical Pr_2NiO_4, electrode composition, these results are also inserted in to Figure 8.9d from Chapter 7. One can observe that even a very thin buffer layer (0.3 µm) can substantially reduce total polarization resistance, when compared to an equivalent sample with no buffer layer, with the largest performance gains being obtained at lower temperatures. Very large performance gains can be obtained by an increase in buffer layer thickness between 0.3 µm and 1.25µm, while a further increase of buffer layer thickness to 2.5µm provides only slight improvement. The introducing of MIEC buffer layers has been shown in the previous chapters to induce an additional parallel path for the electrode reaction that can radically decrease polarization resistance. The work of this chapter shows that buffer layer thickness can further modify this improvement with significant gains in performance being offered up to a buffer layer thickness of. 1.25µm.

In this work discussing the kinetics of the oxygen electrode, Adler assumed that the overall reaction could be viewed as a homogeneous chemical reaction occurring over the internal surface area of the MIEC electrode material, where the exchange of neutral oxygen by the mixed conductor converts electronic to ionic current over a finite thickness [13][14]. This thickness represents a penetration depth, δ, that corresponds to the extension of the reaction zone beyond that of the three-phase boundary. This concept of Adler is shown schematically in Fig. 8.10. The penetration depth, δ, was ascribed to the following relationship [15], mirroring that previously proposed for the active region width in porous mixed conducting membranes [16],

$$\delta = \sqrt{\frac{(1-\epsilon)}{\tau}\frac{L_c}{a}} \tag{8.1}$$

where $L_c = D^*/k$ describes a critical length at the transition between diffusion limited and surface reaction limited transport, in which D^* is the chemical diffusion coefficient, k is the surface exchange coefficient, and ε, τ, a are the electrode porosity, tortuosity and surface area, respectively.

It should be noted that a similar concept of an active penetration depth may also be tentatively applied for the buffer layer, due to its suggested role as an additional parallel MIEC path for the electrode reaction, see the equivalent circuit of Figure 5.11. in Chapter 5 (Lui's equivalent circuit adapted for the presence of a buffer layer). In such a case, one can estimate the likely size of the penetration depth by assuming possible values for porosity $\varepsilon = 0.1$, tortuosity $\tau=1$, and surface area $a = 2 \times 10^5$ cm^{-1} (corresponding to a buffer layer particle size of approximately 100nm, as observable in Fig. 8.7) [16]. For this calculation, one also requires estimations of the chemical diffusion coefficient, D*, and surface exchange coefficient, k, of the $Ce_{0.8}Pr_{0.2}O_{2-\delta}$+ Co buffer layer material. Although, these values are available in the literature for the Co free material [17], the previous discussion of Figure 8.5, highlighted that any attempted comparison between Co containing and Co free materials would be futile, due to radically differing ambipolar conductivities. Thus, due to the absence of suitable data for the CPO+Co composition in the current literature, values for the CTO+Co analogue are used in the present calculation, $D^* = 1.6 \times 10^{-3}$ (cm/s), $k = 1.6 \times 10^{-4}$ (cm^2/s) at 700ºC [18]. Entering these values in to equation 8.1 gives an active penetration depth of approximately 6µm. Although this value is notably larger than the buffer layer thickness for peak electrode performance in the current results, 2.5 µm, it can be considered to be a value that is comparable when one takes into account the expected slightly higher ambipolar conductivity (and thus, potentially also surface exchange) of the CPO+Co composition over that of CTO+Co. Moreover, this value becomes even more acceptable as an estimate when one considers that Adler reported values of δ that varied in a range spanning over 4 orders of magnitude for common MIEC materials [15]. It should also be mentioned that equation 8.1 is quite insensitive to the absolute levels of porosity and tortuosity chosen in this simulation.

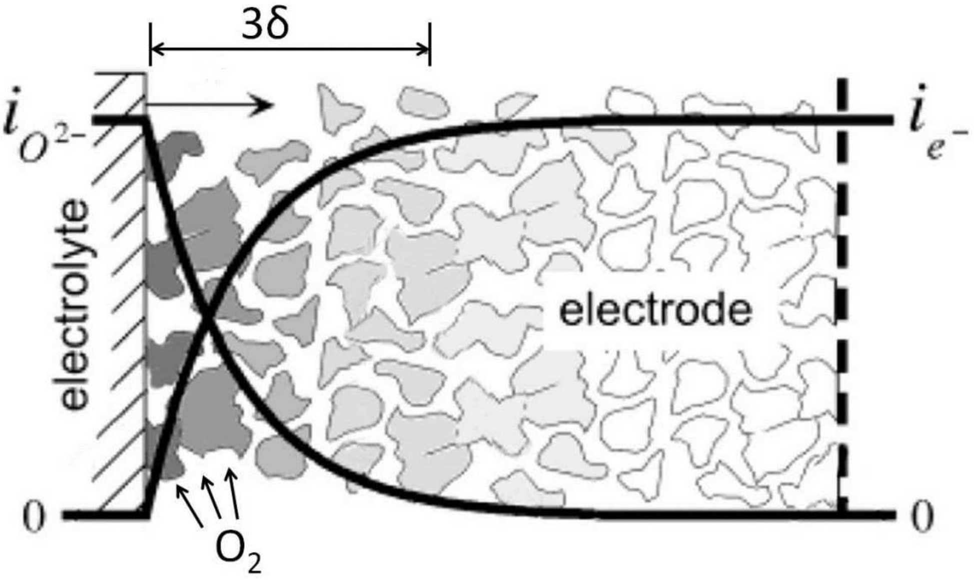

Figure 8.10. 1D model for oxygen reduction active area by Adler [14].

Further support to this discussion is given by Figure 8.11 that presents the respective capacitance values and relaxation frequencies of the impedance responses as a function of buffer layer thickness. In Figure 8.11a the capacitances corresponding to the high and low frequency responses can, respectively, be seen to increase with increasing buffer layer thickness. Large chemical capacitances are known to be characteristic of oxygen electrode mechanisms that involve significant contributions of transport through bulk MIEC paths, arising due to the accumulation of reactive intermediates from both surface species and oxidation and reduction of the bulk MIECs [14]. Adler further noted that the chemical capacitance is proportional to the active penetration depth, δ, and corresponds to the extension of the electrochemical reaction beyond that of the traditional three-phase boundary [14]. The magnitude of the chemical capacitance can, therefore, be expected to increase with increasing MIEC path thickness until the optimal penetration depth is reached. From this point the chemical capacitance would remain constant. Comparison of this theory to the experimental results of Figure 8.11a suggests that the optimal thickness of the buffer layer has not yet been reached due to the noted increasing capacitance with increasing buffer layer thickness. Note that this result coincides with the continued decrease in polarization resistance with increasing buffer layer thickness previously noted in Fig.8.9.

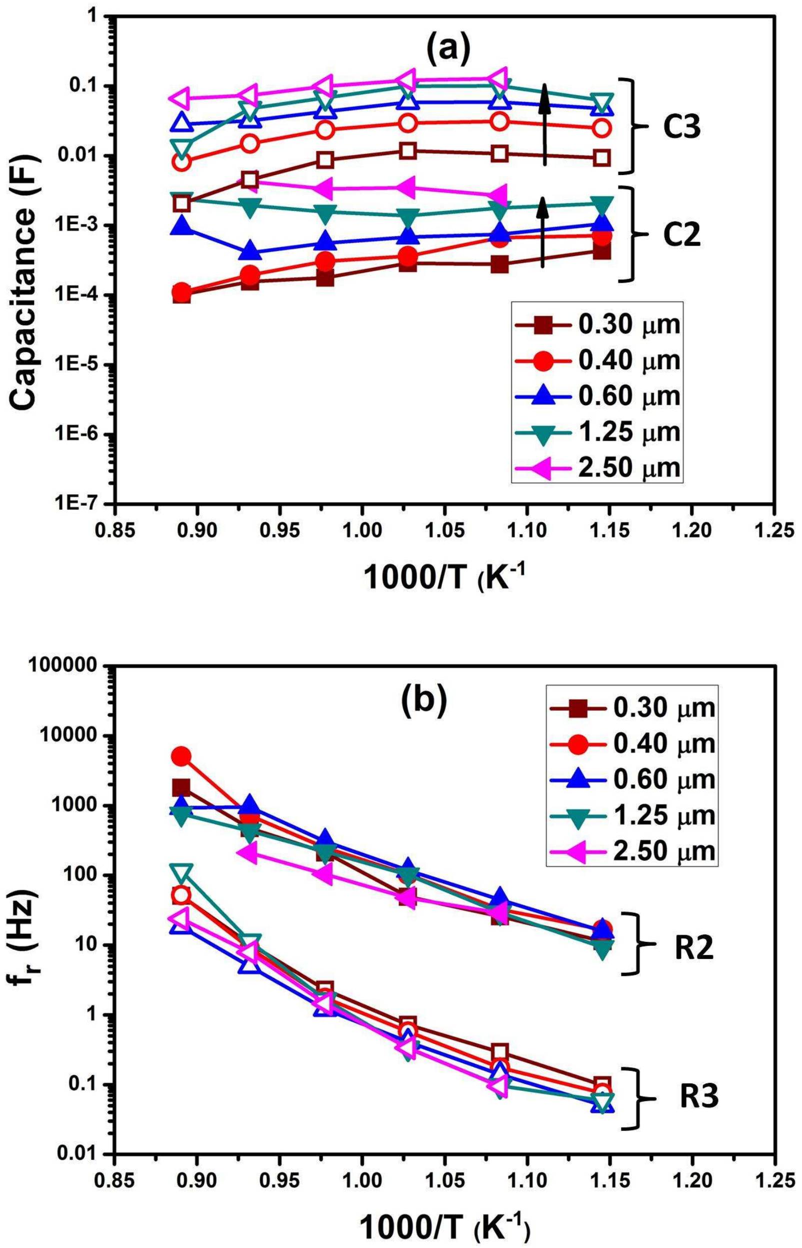

Figure 8.11. Temperature dependence of a) the Capacitance and b) Relaxation frequency. for cells with Pr_2NiO_4 electrode CPO+Co buffer layer with different thickness.

With respect to the relaxation frequencies, Figure 8.11b, it can be observed that effectively constant relaxation frequencies are obtained for the respective R2 and R3 responses with changing buffer layer thickness, suggesting identical oxygen reaction mechanisms in each case. With reference to the previous Chapters, the values of the relaxation frequencies can be described as low and to reflect the availability of a parallel MIEC buffer layer path for the electrode reaction. It can, therefore, be concluded that the parallel buffer layer path continues to demonstrate an important contribution to improved electrode kinetics for all measured buffer layer thicknesses and that this mechanism is also constant.

8.4. Conclusions

The influence of various Pr contents in the CPO+Co buffer layers has been investigated with Pr_2NiO_4 oxygen electrode and YSZ electrolyte. Solid solutions $Ce_{1-x}Pr_xO_{2-\delta}$ (x=0.1 to x=0.3) were successfully synthesized by hydrothermal method. The composition x = 0.4 was shown to be multiphase, consisting of two fluorite phases of different lattice parameters. The buffer layers and Pr_2NiO_4 electrodes were successfully deposited on the top of pre-sintered YSZ electrolytes by the spin coating method. Results show the formation of well separated and adhered layers at the low sintering temperature of 900°C. Samples with different thicknesses of CPO+Co buffer layers were also prepared in order to analyze the effect of buffer layer thickness on polarization resistance. The sample containing the CPO+Co buffer layer with 20 mol% Pr shows the best performances as an oxygen electrode, with lower polarization resistances than the 10, 30 and 40 mol% Pr-doped buffer layers. It was highlighted that further explanation of this behavior requires the additional determination of the transport properties of the CPO+Co buffer layers, while attempts to estimate trends from literature data on the transport properties of Co free analogues are insecure.

Increasing the buffer layer thickness was shown to rapidly decrease polarization resistance until a buffer layer thickness of 1.25 μm. Further increases of buffer layer thickness to 2.5 μm are shown to only provide slight additional improvements in performance. Discussion suggests that this improvement in polarization resistance with increasing thickness in this range may be due to a characteristic penetration depth for the oxygen reaction in the MIEC buffer layer.

8.5. References

[1] K.S. Babu, P. Arunkumar, M. Meena, A review on cerium oxide-based electrolytes for IT-SOFC, Nanomaterials and Energy 1 (2012) 288–305.

[2] X. Qi, Y.S. Lin, Electric conductivity and oxygen permeability of modified cerium oxides, Journal of Materials Science 38 (2003) 1073–1079.

[3] M. Balaguer, C. Solís, J.M. Serra, Structural−transport properties relationships on $Ce_{1-x}Ln_xO_{2-\delta}$ System (Ln = Gd, La, Tb, Pr, Eu, Er, Yb, Nd) and effect of cobalt addition, The Journal of Physical Chemistry C 116 (2012) 7975−7982.

[4] D.P. Fagg, J.C.C. Abrantes, D. Pérez-Coll, P. Núñez, V.V. Kharton, J.R. Frade, The effect of cobalt oxide sintering aid on electronic transport in $Ce_{0.80}Gd_{0.20}O_{2-\delta}$ electrolyte, Electrochimical Acta 48 (2003) 1023–1029.

[5] D.P. Fagg, S. García-martin, V.V. Kharton, J.R. Frade, Transport properties of fluorite-type $Ce_{0.8}Pr_{0.2}O_{2-\delta}$: Optimization via the use of cobalt oxide sintering Aid, Chemistry of Materials 21 (2009) 381–391.

[6] D. Ramasamy, A.L. Shaula, A. Gómez-Herrero, V.V. Kharton, D.P. Fagg, Oxygen permeability of mixed-conducting $Ce_{0.8}Tb_{0.2}O_{2-\delta}$ membranes: Effects of ceramic microstructure and sintering temperature, Journal of Membrane Science 475 (2015) 414–424.

[7] Y. Takasu, T. Sugino, Y. Matsuda, Electrical conductivity of praseodymia doped ceria, Journal of Applied Electrochemistry 14 (1984) 79–81.

[8] P. Shuk, M. Greenblatt, Hydrothermal synthesis and properties of mixed conductors based, Solid State Ionics 116 (1999) 217–223.

[9] M. Nauer, C. Ftikos, B.C.H. Steele, An evaluation of Ce-Pr oxides and Ce-Pr-Nb oxides mixed conductors for cathodes of solid oxide fuel cells: Structure, thermal expansion and electrical conductivity, Journal of the European Ceramic Society 14 (1994) 493–499.

[10] Y. Min Park, H. Kim, Porous Gd-doped ceria barrier layer on solid oxide fuel cell with $Sm_{0.5}Sr_{0.5}CoO_{3-\delta}$ Cathodes, Ceramics International 39 (2013) 2037–2043.

[11] Y.-M. Kim, P. Kim-Lohsoontorn, J. Bae, Effect of unsintered gadolinium-doped ceria buffer layer on performance of metal-supported solid oxide fuel cells using unsintered barium strontium cobalt ferrite cathode, Journal of Power Sources 195 (2010) 6420–6427.

[12] V.V. Kharton, F.M.B. Marques, Interfacial effects in electrochemical cells for oxygen ionic conduction measurements I. The e.m.f. method, Solid State Ionics 140 (2001) 381–394.

[13] S.B. Adler, Mechanism and kinetics of oxygen reduction on porous $La_{1-x}Sr_xCoO_{3-\delta}$ electrodes, Solid State Ionics 111 (1998) 125–134.

[14] S.B. Adler, Factors Governing Oxygen Reduction in Solid Oxide Fuel Cell Cathodes, Chemical Review 104 (2004) 4791–4843.

[15] S.B. Adler, J.A. Lane, B.C.H. Steele, Electrode kinetics of porous mixed-conducting oxygen electrodes, Journal of Electrochemical Society 143 (1996) 3554–3564.

[16] H. Deng, M. Zhou, B. Abeles, Diffusion-reaction in mixed ionic-electronic solid oxide membranes with porous electrodes, Solid State Ionics 74 (1994) 75–84.

[17] D. Chen, S.R. Bishop, H.L. Tuller, Praseodymium-cerium oxide thin film cathodes:Study of oxygen reduction reaction kinetics, Journal of Electroceramics 28 (2012) 62–69.

[18] M. Balaguer, C. Solís, M. Serra, Study of the transport properties of the mixed ionic electronic conductor $Ce_{1-x}Tb_xO_{2-\delta}$ + Co (x = 0.1, 0.2) and evaluation as oxygen-transport membrane, Chemistry of Materials 23 (2011) 2333–2343.

9. Conclusions and Future work

The current thesis described tailoring of the transport properties of ceria-based buffer layers to offer a twofold role in SOFCs and SOECs to prevent interreaction between oxygen electrode/electrolyte and to simultaneously offer improvements in electrode kinetics. In order to investigate these phenomena, the bulk transport properties of a range of ceria-based cubic defect fluorite materials $Ce_{1-x}Ln_xO_{2-\delta}$ (Ln = Gd, Tb and Pr, given the nomenclature CGO, CTO and CPO, respectively) with minor additions of cobalt sintering aid were electrochemically studied.

The introduction of small amount (2 mol%) of cobalt oxide is highly effective as a sintering aid in ceria-based fluorite oxides allowing relatively dense materials with sub-micron grain sizes to be formed at low sintering temperatures ($\leq 1000^oC$). The conductivity studies showed that the transport properties of $Ce_{1-x}Ln_xO_{2-\delta}$ (Ln = Tb, Gd and Pr) are significantly influenced by the additions of minor level cobalt oxide sintering aid as well as by their final sintering temperature, with depleted performance being offered by samples sintered in excess of 1000ºC. The cobalt containing ceramic materials offered higher total and electronic conductivities than their Co-free analogues sintered at higher temperatures, while original high levels of ionic conductivity are maintained. The ambipolar conductivities of these buffer layer materials were shown to increase in the order of CGO+Co < CTO+Co < CPO+Co. The oxygen ion transference number obtained from modified EMF method showed increases with temperature for CTO+Co and CPO+Co samples in contrast to the negative temperature dependence shown by CGO+Co. A higher oxygen permeation flux was shown by the sample containing cobalt oxide sintering aid, while an increasing oxygen permeation flux was given in the order CGO+Co < CTO + Co < CPO + Co.

Electrochemical half cells of $Nd_2NiO_{4+\delta}$ oxygen electrodes with or without $Ce_{0.8}R_{0.2}O_{2-\delta}$ + 2 mol% Co buffer layers (where R = Gd, Pr) were successfully fabricated by spin coating on dense YSZ electrolyte supports and co-sintered at 900°C. The SEM and EDS results showed the formation of well separated and adhered layers that were absent of observable cation interdiffusion. Moreover, the XRD results of calcined intimate mixtures of the

$Nd_2NiO_{4+\delta}$ electrodes and ceria based buffer layers further reinforced the absence of chemical interactions, demonstrating the functionality of all studied buffer layers. All samples were characterized by EIS measurements under anodic and cathodic polarization, and exhibited significant decreases in polarization resistance, Rp, of up to an order of magnitude, in the order, no buffer layer > Gd >> Pr. The samples with buffer layers showed impressive decreases in polarization resistance that are suggested to be due to the existence of a parallel path for electrochemical reaction due to the presence of the MIEC buffer layers. Preliminary modeling was performed where the equivalent circuit of Liu was extended to accommodate this parallel buffer layer path and was shown to be able to describe the noted higher capacitance values of the polarization responses of the buffer layer samples and their lower relaxation frequencies.

Comparison of the utility of the new terbium-doped ceria ($Ce_{0.8}Tb_{0.2}O_{2-\delta}$) material with cobalt additions as a potential buffer layer was also electrochemically tested and successfully fabricated between $Nd_2NiO_{4+\delta}$ and dense YSZ electrolyte. The XRD, SEM and EDS analyses again exhibited the formation of well separated and adhered layers with no observable cation interdiffusion. The EIS measurements showed similar large improvements in polarization resistance as offered by the previous CPO+Co buffer layer, and were, hence, again attributed to the existence of a parallel buffer layer path for electrochemical reaction. Nonetheless, the performance of the CTO+Co buffer layer was shown to be slightly inferior to that of CPO+Co . Overall, CPO+Co and CTO+Co MIEC buffer layers are good candidates to substantially enhance performance of the oxygen electrode.

The electrochemical performance and compatibility of the oxygen electrode Pr_2NiO_4 was investigated with CPO+Co buffer layer under SOFC and SOEC modes and compared to that of Nd_2NiO_4. The EIS measurement showed that the greatest performance enhancement could be obtained for the Pr_2NiO_4 rare-earth nickelate electrode than that of the Nd_2NiO_4 analogue.

Finally, the influence of various Pr levels (Pr = 10, 20, 30 and 40 mol%) in the CPO+Co buffer layer was investigated using the peak performing Pr_2NiO_4 oxygen electrode and YSZ electrolyte. The EIS measurements showed the sample containing the CPO+Co buffer layer with 20 mol% Pr to exhibit the lowest polarization resistance than the other compositions tested, 10, 30 and 40 mol% Pr-doped buffer layers. Moreover, a study of the impact of different thickness of CPO+Co buffer layer with Pr_2NiO_4 oxygen electrodes and YSZ electrolyte on electrode kinetics was investigated by their preparation by spin coating, followed by electrochemical examination by EIS. Results showed the performance to increase with increasing thickness of the CPO+Co buffer layer with the most marked gains being obtained up to a buffer layer thickness of 1.25 μm.

This thesis work, therefore, demonstrates how tailoring the transport properties of thin ceria-based buffer layers in solid oxide fuel or electrolyser cells can provide the necessary phase stability against chemical inter-reaction at the electrolyte/electrode interface, while also providing radical improvements in the electrochemical performance of the oxygen electrode. It is further shown how this improvement can be related to increased levels of ambipolar conductivity in the mixed conducting buffer layer, which provides an additional parallel path for electrochemical reaction. This thesis work is an important breakthrough as it shows how electrode polarization resistance can be substantially improved, in otherwise identical electrochemical cells, solely by tailoring the transport properties of thin intermediate buffer layers.

Future work will be focused on studying the transport properties of $Ce_{1-x}Pr_xO_{2-\delta}$ ($x = 0.1 - 0.4$) materials containing minor cobalt addition and comparison of this data to the measured electrode properties of electrochemical cells containing these buffer layers. In addition, one proposes to analyze the effect of electrochemical performance by doping Nb in to $Ce_{1-x}Pr_xO_{2-\delta}$ system, where extension of the solid solution to higher Pr-contents has been reported, that may have a beneficial effect on the subsequent electrode properties of electrochemical cells containing this buffer layer. Such work will provided a wider compositional range of the CPO+CO system where the transport properties can be manipulated substantially and, hence, further clear links between ambipolar conductivity in buffer layers and resultant electrode kinetics can be made. Additional work on MIEC buffer layers of other structural families, such as perovskite, can also be suggested to investigate possible additional resistance terms at the electrolyte/buffer layer interface due to crystallographic lattice mismatch. Similar studies can also be suggested to investigate if similar improvements in electrode kinetics can be induced in protonic ceramic fuel cell (PCFC) applications by the introduction of mixed conducting buffer layers.

Simultaneously, future work will also aim to fabricate complete SOFC and SOEC anode/electrolyte/cathode assembiles with optimized buffer layers to consequently investigating overall electrochemical cell performance.